

The Deep Roots of Volcanoes: Models of Magma Dynamics with Applications to Subduction Zones

Richard Foa Katz

Submitted in partial fulfillment of the
requirements for the degree
of Doctor of Philosophy
in the Graduate School of Arts and Sciences

COLUMBIA UNIVERSITY

2005

© 2005

Richard Foa Katz

All Rights Reserved

ABSTRACT

The Deep Roots of Volcanoes: Models of Magma Dynamics with Applications to Subduction Zones

Richard Foa Katz

In this thesis I present research on the dynamics of the partially molten mantle with applications to magma genesis and transport in subduction zones. Subduction zones are the most complex tectonic setting for magma genesis on Earth. To model and understand them requires a study of the fundamental physics and chemistry of the mantle beneath their associated volcanoes where melting occurs and magma migrates through the pores of the rock toward the surface. These partially molten regions of the mantle control the overall chemical evolution of the Earth as well as the characteristics of the volcanic systems that they feed. At tectonic boundaries, the mechanical interaction of partially molten mantle with lithospheric plates, and with large-scale mantle convection, influences the dynamics and organization of plate tectonics. These interactions can be described within the framework of the magma dynamics equations derived by *McKenzie* (1984).

One important question concerns how partially molten regions are organized. It is generally accepted that magma resides in the interconnected pores between crystals that make up mantle rock. Less well understood, however, is the spatial distribution of porosity: is it uniform or localized? To address this issue, chapters 2 and 5 consider mechanical and chemical interactions in the fluid–solid system of the partially molten mantle that, through instabilities, produce heterogeneous, localized distributions of fluid from an initially uniform mixture. The mechanical instability results from porosity-weakening of the solid matrix (*Stevenson*, 1989; *Spiegelman*, 2003), however the orientation of bands of high porosity is shown here to be controlled by the balance between porosity and strain-rate weakening. The chemical instability results from reactive dissolution of mantle matrix by upwelling fluids (*Aharonov et al.*,

1997; *Spiegelman et al.*, 2001). Using a new, parameterized pseudo-phase diagram for the generic rock–water system, I show that hydrous fluids rising off the slab in a simple subduction zone model channelize and locally modify the temperature field. These two chapters demonstrate that, relative to predictions by homogeneous models, localization of melt in the mantle can radically alter permeability structure, melt transport rates, thermal structure, chemical transport and even large-scale deformation of the magma/mantle system in subduction zones and other settings of magma genesis.

Subduction zones represent the most complex instance of partial melting in a tectonic/volcanic system. Observations of arc volcanoes raise a suite of questions about the dynamics active at depth below them. To address these questions requires comprehensive, self-consistent models of magma genesis and transport in subduction zones. Even a basic model that incorporates fluid and solid flow, reaction and temperature evolution will be complex, challenging to construct, and require advanced computational resources. In Chapter 2 I describe a computational approach for fluid flow in a deforming mantle matrix; in chapter 3 for modeling mantle flow with highly variable non-Newtonian viscosity; in Chapter 4 for melting systematics of the hydrous magma/mantle system; and in chapter 5 for temperature-dependent reactive flow of hydrous fluids/magma. Each of these contributes to the development of a comprehensive model of subduction by addressing computational challenges and exposing complex behavior such as sharp viscosity gradients and strong localization phenomena.

The central themes of this thesis are localization phenomena and the effects of complex rheology on the magma–mantle system. Calculations presented here demonstrate that both of these are likely to play an important role in shaping the processes of magma genesis and transport in partially molten regions of the mantle and, particularly, in subduction zones. Many questions are raised by this work, especially regarding the observable signature of predicted localizations. This work represents fundamental progress on understanding the generation and organization of magma in the mantle.

Contents

Table of Contents	i
List of Tables	vi
List of Figures	vii
Acknowledgments	xviii
Dedication	xxi
1 Introduction	1
1.1 Modern challenges in understanding subduction	3
1.2 Theoretical framework	6
1.3 Computational framework	9
1.4 The content of this thesis	12
2 The Dynamics of Melt and Shear Localization in Partially Molten	
Aggregates	17
2.1 Introduction	17
2.1.1 Past work with magma dynamics theory	20

2.2	Coupling shear deformation and fluid flow	21
2.2.1	Linear analysis	21
2.2.2	Numerical solutions	31
2.3	Comparison with data	34
2.4	Discussion	35
2.5	Conclusion	36
3	Mantle Flow and Thermal Structure in a Kinematic Subduction	
	Zone Model	37
3.1	Introduction	37
3.2	Governing equations and numerical solution	38
3.3	Results	41
3.4	Discussion	46
3.4.1	Magma genesis in subduction zones	46
3.4.2	Magma focusing in subduction zones	48
3.5	Conclusions	52
4	A New Parameterization of Hydrous Mantle Melting	55
4.1	Introduction	55
4.1.1	Basic structure of the parameterization	57
4.2	Mathematical Formulation	58
4.2.1	Anhydrous Melting	58
4.2.2	Hydrous Melting Extension	60
4.3	Experimental Database	68

4.3.1	Anhydrous	68
4.3.2	Hydrous	70
4.4	Model Calibration	71
4.4.1	Anhydrous melting	71
4.4.2	Hydrous melting	72
4.4.3	Free Parameters and Missing Constraints	73
4.5	Comparison with other models	75
4.6	Testing and validation	76
4.6.1	Adiabatic upwelling beneath mid-ocean ridges	76
4.6.2	Arc Melting	81
4.7	Summary	82
5	Reactive hydrous melting and channelized melt transport in arcs	89
5.1	Introduction	89
5.2	Reactive melting	91
5.2.1	Chemistry	91
5.2.2	Physics	96
5.3	Results	99
5.3.1	Flow from the slab surface to the core of the mantle wedge . .	100
5.3.2	Flow from the slab surface to the lithosphere overlying the wedge	102
5.4	Discussion	106
5.5	Future work	110
5.6	Conclusion	112

6	Discussion	114
6.1	Summary	114
6.2	Open questions	116
6.2.1	Buoyancy effects	116
6.2.2	Rheological effects	117
6.2.3	Experimental constraints	117
6.2.4	Magmatic focusing	118
6.3	Conclusions	119
	Bibliography	121
A	Ridge Migration, Asthenospheric Flow and the Origin of Magmatic Segmentation in the Global Mid-Ocean Ridge System	136
A.1	Introduction	136
A.2	Model description and solution	139
A.3	Melting and melt focusing	141
A.4	Results	142
A.5	Discussion	143
A.6	Conclusions	145
B	A Semi-Lagrangian Crank-Nicolson Algorithm for the Numerical Solution of Advection-Diffusion Problems	148
B.1	Introduction	148
B.2	Algorithms	149

B.2.1	Basic Algorithms	150
B.2.2	Hybrid Schemes	152
B.3	An analytic test problem	154
B.4	Results	157
B.5	Discussion	162
B.5.1	Adaptive Interpolation Method	163
B.6	Conclusions	166

List of Tables

3.1	Empirically determined parameters for diffusion and dislocation creep (<i>Karato and Wu</i> , 1993; <i>Hirth and Kohlstedt</i> , 2003) used in equation (3.5).	40
4.1	Summary of experimental peridotites (anhydrous experiments only). ^a Modal cpx not known or not available. The mean of the other peridotites, 16%, is assumed for computations here. ^b Constructed by combining mineral separates from the Kilbourne Hole Xenolith.	69
4.2	Summary of parameters and values.	74
4.3	Summary of variance reduction. ^a Using data from anhydrous experiments below 4 GPa and below 40% melting. The use of the entire data set yields lower variance reduction for all parameterizations.	77

List of Figures

- 1-1 A schematic diagram of plate tectonics. A mid-ocean ridge/spreading center is illustrated at left where two plates of oceanic lithosphere are diverging. A subduction zone is illustrated at right where the oceanic lithosphere is colliding and sinking beneath continental lithosphere. Orange represents partially molten regions. 16
- 2-1 A comparison of experimental & numerical results. (a) An example cross section of an experiment (PI-1096) adapted from Figure 1a of *Holtzman et al.* (2005) (experimental details are given by *Holtzman et al.* (2003a)). The melt-rich bands are the sloping darker gray regions at angle θ to the shear direction. (b) The porosity and (c) perturbation vorticity from a numerical simulation with $n = 6$ and $\alpha = -27$ at shear strain γ of 2.79. The domain is five by one compaction lengths. The perturbation vorticity, $\nabla \times [\mathbf{V} - \dot{\gamma}y\mathbf{i}]/\dot{\gamma}$, is the total vorticity minus the constant vorticity $\dot{\gamma}$ due to simple shear (here normalized by $\dot{\gamma}$). Black lines in **b** and **c** show the position of passive tracer particles that were arrayed in vertical lines at $\gamma = 0$; white dotted lines show the expected position of the tracers due only to simple shear. The linear, low-angle red bands in **c** are weak regions associated with high porosity and enhanced shear while the linear, subvertical blue regions are regions of reversed shear. (d) Histograms comparing band angle distributions in experiments and numerical solution shown in panel b. 19

2-2	The position of the maxima of \dot{s} as a function of n . Curves are obtained by plotting equation (2.21) for different ratios of the bulk to shear viscosity ζ_0/η_0 . Neglecting the effect of compaction on viscosity gives a result indistinguishable from the black curve. These curves predict the angles at which bands will have the highest instantaneous porosity growth rate. To undergo significant accumulated growth, a band must remain near one of these favored angles. High angle bands represented by the upper branch of the curves in this figure are rapidly advected away from the angle of peak instantaneous growth to angles near and above 90° where they cease to grow and begin to compact. Low angle bands represented by the lower branch are not rotated strongly by advection (see passive advection trajectories in Figure 2-5c, for example) and thus remain longer in a favorable position for growth of porosity. The amplitude $e^{s(t)}$ of low angle bands thus increases faster than the amplitude of high angle bands.	27
2-3	Results from linear analysis showing the effect of stress exponent n on the angular dependence and rate of growth of porosity perturbations (with $k \gg 1$). (a) The initial growth rate \dot{s} of porosity from equation (2.22) as a function of band angle θ and n . (b) The normalized amplitude of perturbations as a function of θ for $\gamma = 1$. Advection by simple shear preferentially rotates higher angle bands out of favorable orientation for growth. Panels c and d show the normalized amplitude of porosity perturbations, $e^{s(t)}$, as a function of strain γ and angle θ for $n = 1$ and $n = 4$ respectively. Black lines are passive advection trajectories that show the rotational effect of unperturbed simple shear on initial band angles. The angle with peak amplitude as a function of strain is determined by both the growth rate (shown in panel a) and passive rotation, hence the line through the maximum amplitude (darkest red regions) crosses passive advection trajectories.	29
2-4	Two descriptions of the perturbation velocity field from linear analysis. Panel a shows the relative sizes of the shear and volumetric components of the perturbation flow field for $n = 1, 4$. The velocities for $n = 4$ are four times greater than those for $n = 1$ (as can be seen in panel b) but are scaled down to fit on the graph. It is evident from this panel that the volumetric component of strain goes to zero at 0° and 90° while the shear component goes to zero at 45° and 135° . The shear component is always maximized at 0° and 90° to the shear plane. Panel b shows the shear component of the perturbation velocity field as a function of band angle and n . The amplitude of the perturbation scales with n . Curves for higher n show greater enhancement of shear near 0° and 90° than the sine wave that represents $n = 1$	30

2-5	Evolution of band angle in numerical simulations, experiments and linear analysis. Panels a , b and c show the evolution of angle distribution averaged over four simulations for $n = 1$, 4 and 6, respectively. In b and c simulations do not reach the maximum strains achieved in experiments and hence results from linear analysis are used to extend them to $\gamma = 3.6$. For panels a–c, in the part of the plot derived from simulation results, each row at each step of strain represents a single histogram of the porosity field like the one in Figure 2-1d. These panels should be compared to Figure 2-3c and d. Panel d summarizes panels a , b and c as well as simulation results for $n = 2$ by plotting only the angle with <i>maximum</i> amplitude as a function of strain. This represents the dominant band angle and is generally consistent with a visual estimate from the porosity field. Black symbols in all four panels represent mean band angles from independent experiments to different strain. Characteristics of porosity bands in experimental cross-sections were quantified by hand-measurement (not FFTs). A key question remains as to the behavior of the full non-linear calculations for high strain at $n > 3$	33
3-1	A schematic diagram of the computational domain showing the slab, crust and wedge subdomains.	40
3-2	Representative results from the numerical solution of equations with full diffusion/dislocation creep viscosity, slab dip of 45° , convergence rate of 8 cm/year, crustal thickness of 35 km and a fault depth of 50 km. Depths and distance from the trench are given in km on the y and x axes respectively. The domain is 350 km wide by 300 km deep and the resolution is < 2 km in both directions. The viscosity field is shown in Figure 3-3. (a) Dimensionless pressure. Note that this panel is on a different scale than the others; The pressures are large and non-zero only very close to the base of the fault. (b) Potential temperature in degrees centigrade. Note the relatively high temperatures near the wedge corner. (c) Vertical component of the velocity field in cm/yr. Note the strong upwelling toward the wedge corner. (d) Horizontal velocity in cm/yr.	42
3-3	The \log_{10} of viscosity field from the same simulation as shown in Figure 3-2. Depths and distance from the trench are given in km on the y and x axes respectively. The effect of the stress dependence of viscosity can be seen most clearly in the diagonal band of dark blue sub-parallel to the slab where mantle shear is strongest.	44

3-4	A comparison of temperature fields from simulations with (a) isoviscous, (b) diffusion creep and (c) combined dislocation/diffusion creep viscosity. Panel (d) shows the temperature field in panel (b), T_b , minus the temperature field in panel (a), T_a . Panel (e) shows $T_c - T_b$. Panel (f) shows $T_c - T_a$. Panels (a)–(c) share a single (diagonal) color bar. Note the large temperature differences above the slab between variable viscosity and constant viscosity simulations in panels (d) and (f). Variable viscosity flow prevents cold mantle from being advected around the wedge corner and onto the surface of the slab. Panel (e) shows a significant difference between Newtonian and non-Newtonian viscosity for temperatures in the wedge corner with colder temperatures for the non-Newtonian case. This results from strain rate-weakening flow of colder mantle.	45
3-5	Slab surface temperature profiles for simulations shown in Figure 3-4a–c. These simulations all have a mantle potential temperature of 1300° C. The isoviscous flow model produces a slab surface temperature that is much lower than that of Newtonian and non-Newtonian temperature dependent viscosities.	49
3-6	Simplified estimates of fluid flow in subduction zones. Following <i>Spiegelman and McKenzie</i> (1987), these calculations assume constant and uniform porosity and no melting and the following parameter values: $\phi = 0.01$, $\mu = 10^2$ Pa-s, $k_0 = 10^{-11}$ m ² , Blake-Kozeny-Carmen exponent $n = 2$ and $\Delta\rho = 500$ kg/m ³ . Together these parameters give a ratio of buoyancy-driven fluid velocity to slab-driven solid velocity, w_0/U_0 , of approximately 20 (although results are qualitatively similar for $10^{-12} \leq k_0 \leq 10^{-10}$). The left column shows the viscosity field and the right column shows the base-10 logarithm of the dimensionless pressure. Fluid flow streamlines are shown in blue. Fluid upwelling far from the pressure gradients of the wedge corner rises at about 15 cm/yr. (a)-(b) Isoviscous 10^{21} Pa-s solid flow and corresponding fluid flow. (c)-(d) Diffusion (T and P dependent) creep viscosity solid flow. (e)-(f) Full diffusion/dislocation creep viscosity.	51
3-7	A comparison of two possible proxies for volcano position derived from numerical simulations with data from <i>England et al.</i> (2004). (a) Depth from the volcanic arc to the slab assuming that the arc is directly above the location of the maximum degree of melting, F_{max} . F_{max} is computed using the parameterization described in chapter 4 assuming a constant bulk water content everywhere in the domain. (b) Depth from the volcanic arc to the slab assuming that the arc is directly above the “nose” of the 1225°C isotherm. The nose is the point on the isotherm with the shortest horizontal distance to the trench. Its position may provide a proxy for the limit to lateral melt transport toward the wedge corner.	53

4-1	The anhydrous solidus, lherzolite liquidus (see text) and liquidus. Also shown, for comparison, the anhydrous solidi of <i>Hirschmann</i> (2000), <i>Langmuir et al.</i> (1992) and <i>McKenzie and Bickle</i> (1988).	61
4-2	Isobaric anhydrous melting curves at different pressures with modal cpx of the unmelted rock at 15 wt%. For a comparison of these calculations to data, see Figure 4-6.	62
4-3	The solidus for different bulk water contents of the system. Solidus depression is linear with dissolved water. It is bounded by the saturation of water in the melt, a function of pressure.	65
4-4	Isobaric melting curves (for 1 GPa) with different bulk water contents. The 0.3 wt% melting curve is saturated at the solidus.	67
4-5	Degree of melting as a function of the water in the system, holding the temperature (see figure) and pressure (1.5 GPa) constant. Modal cpx is 17% in the unmelted solid. (a) F as a function of $X_{\text{H}_2\text{O}}^{\text{bulk}}$. Compare to <i>Gaetani and Grove</i> (1998) figure 13a. (b) F as a function of water dissolved in the melt. Bulk distribution coefficient of water is assumed to be 0.01.	77
4-6	The melting model with modal cpx at 15 wt% compared to isobaric subsets from the experimental database. Note that experimental results represent a range of starting compositions in terms of modal mineralogy and mineral fertility. Commonly used KLB-1 has 15 wt% cpx. Note the variability among nominally comparable experiments in P , T and composition. (a) 0 GPa (b) 1 GPa (c) 1.5 GPa (d) 3 GPa. . . .	78
4-7	A plot of experimentally determined degree of melting as a function of pressure and temperature. The chosen solidus has an A_1 35 °C below that of <i>Hirschmann</i> (2000) to better fit the low melt fraction experiments but uses the same A_2 and A_3 that he reported. The 29 experiments within 10 °C of the <i>Hirschmann</i> solidus have an average degree of melting of 10 wt%. Of the 29, only 5 have no melting. This is due in part to our inclusion of experiments with more fertile source compositions (<i>e.g.</i> PHN-1611 and MPY) in the database.	79
4-8	(a) The calibration of $\Delta T(X_{\text{H}_2\text{O}})$ for the parameters K and γ from equation 4.16. Data is derived from the experiments of <i>Hirose and Kawamoto</i> (1995), <i>Kawamoto and Holloway</i> (1997), <i>Gaetani and Grove</i> (1998), and <i>Grove</i> (2001). Result is given in table 4.2. (b) The saturation water content in wt% of the melt as a function of pressure from equation 4.17. Points are from <i>Dixon et al.</i> (1995), who report a regular solution model for basalt up to 0.5 GPa based on their and other experiments, and <i>Mysen and Wheeler</i> (2000), who report the saturation water content for three haploandesitic compositions (shown are results from the aluminum free composition that is 79% SiO ₂). . .	84

4-9	A comparison of the results of several parameterizations of dry melting and pMELTS calculations at 1 (in blue) and 3 (in green) GPa. The parameterizations are described by <i>Langmuir et al.</i> (1992), <i>McKenzie and Bickle</i> (1988) and <i>Iwamori et al.</i> (1995). pMELTS is described by <i>Ghiorso et al.</i> (2002). A commonly used parameterization by <i>Kinzler and Grove</i> (1992) is not considered because it requires the input of chemical information.	85
4-10	A comparison of parameterizations of mantle melting in the presence of water at 1 and 3 GPa. <i>Asimow and Langmuir</i> (2003) use a hydrous extension of the anhydrous parameterization described by <i>Langmuir et al.</i> (1992). <i>Davies and Bickle</i> (1991) extends the <i>McKenzie and Bickle</i> (1988) parameterization to handle wet melting. (a) For bulk water content of 0.1 wt%. (b) For bulk water content of 0.5 wt%. . .	86
4-11	Results of the numerical integration of equations 4.20 and 4.23 for a mantle with bulk water ranging from 0 to 200 wt ppm and modal cpx of 10 wt%. Values of all melting model parameters are as given in table 4.2. Some of the curves show a kink due to cpx-out. (a) $F(P)$. (b) $T(P)$. (c) A quantification of the water induced low- F tails on adiabats. The pressure interval over which the first one percent of melting occurs is plotted as a function of bulk water in the system and potential temperature.	87
4-12	A representative example of a two dimensional static arc melting calculation. Bulk water of 0.5 wt% is applied only over the corner of the wedge shown in (b). The potential temperature of the mantle is taken to be 1350 °C. (a) Temperature of equilibration. (b) Equilibrium degree of melting in percent melt by mass. Maximum is 9.3%.	88

- 5-1 **(a)-(c)** Phase relations in the model system albite-H₂O along geothermal gradients in which P and T increase after *Manning* (2004), justifying the simple parameterization of hydrous mantle melting adopted in the initial stages of this study. Abbreviations: Ab, albite; L, liquid; Q, quartz; Fl, fluid; V, vapor. (a) and (b) illustrate relations along paths crossing respectively below and above the second critical end point in the system (*Shen and Keppler, 1997; Stalder et al., 2000; Manning, 2004*). The consequence of a critical end point is the change from a discrete solidus to a continuous melting interval. As shown in (c), this can be expressed in water-poor systems (dark-shaded compositions in (a) and (b)) in terms of the change in dissolved silicate in the fluid phase (H₂O-rich vapor or melt) with P and T. Comparison of the two paths indicates that there is little difference in the shape of these solubility curves. Our strategy has been to adopt a parameterization, shown in panel (d), that assumes melting behavior like that of a supercritical system. The resulting curves are then calibrated to the *Katz et al. (2003)* melting parameterization (points in panels (d) and (e)). There is a discrepancy between the two parameterizations in silicate content at low temperature because the melting parameterization of *Katz et al. (2003)* does not consider the small solubility of rock into water at temperatures below the solidus. 94
- 5-2 Two initial condition of vertical distribution of temperature and the resulting equilibrium content of rock in the fluid and dimensionless melting rate. The green line shows the initial condition for the calculation shown in Figure 5-3 and the red line shows the initial condition for Figure 5-4. **(a)** Imposed vertical temperature profile. The green line is a crude representation of the temperature field immediately above the slab: temperatures increase upward. The red line represents the temperature field between the slab and the bottom of the lithosphere. Both of these are simple approximations to a more realistic geotherm shown in Figure 5-6. **(b)** Equilibrium concentration of rock in the fluid given the temperature-pressure curve in panel (a). **(c)** Dimensionless melting rate given the temperature-pressure curve in panel (a). Note that precipitation is occurring at the bottom of the lithosphere in the simulation initiated with the red temperature profile. The curves in panels (b) and (c) are calculated by solving the steady-state, zero compaction length approximation of the governing equations. 97
- 5-3 Results from one time-step of a simulation of hydrous reactive flow through the inverted thermal boundary layer in the mantle wedge above the subducting slab. **(a)** Schematic diagram illustrating position and orientation of the computational domain with respect to the trench and subducting slab. **(b)** Snapshot of porosity (colors) and weight fraction of water in the fluid (contours). **(c)** Vertical fluid velocity in cm/year (color) and temperature in degrees centigrade (contours).101

5-4	Porosity (color) and temperature (contours) at four non-dimensional times in a hydrous reactive melting simulation. Temperature increases above the bottom of the domain into the wedge core and then, unlike in Figure 5-3, decreases with height toward the surface. Channels form and immediately begin to coalesce into bundles that tighten with time. These channel bundles carry a large flux of melt and are able to significantly perturb the temperature field. Freezing melt near the top boundary lowers the permeability and confines outflow to narrow, high porosity gaps. Below these gaps, melt pools in high porosity zones. We are exploring hypotheses for the mechanism of coalescence.	104
5-5	Results from the same calculation as in Figure 5-4 comparing porosity, fluid composition, vertical fluid velocity and temperature fields. (a) Porosity field (color) with overlayed contours of water concentration in the fluid. Rapid flow through the channel bundles leads to high water concentrations in the bottom half of the domain and that can persist through to the top of the domain. (b) Vertical fluid velocity (color) with overlayed contours of temperature. Fluid velocities are calculated assuming a velocity scale w_0 of 1 m/yr after <i>Spiegelman et al.</i> (2001). This is a conservative estimate and may be low by 2 orders of magnitude. (Since time in this calculation is scaled by δ/w_0 , all rates scale with this ratio as well. So the input flux, the melting rate and the melt velocity all vary together with changes in w_0 .) Note the stagnation of melt in the high porosity “pods” at the base of the cold thermal boundary layer.	105
5-6	Subduction zone geotherm (blue) and solidus (red, assuming 1 wt% bulk water) taken at 100 km from the “trench” from the temperature field shown in Figure 3-2b. The thick section of the blue line marks the section of the geotherm that passes through viscosities below 10^{22} Pa-s in the wedge. The open circle on the blue line marks the point where the geotherm crosses the slab surface.	107
5-7	A schematic illustration of the proposed magmatic focusing instability. The blue regions represent cold, compact mantle. The pink areas represent hot, porous mantle. Red arrows represent highly porous channels. Channels impinge on the thermal boundary layer and perturb its topography. Melt follows upward along the sloping boundary by the mechanism proposed by <i>Sparks and Parmentier</i> (1991). This focusing produces more efficient thermal erosion of the boundary layer and coalescence of channels. As localized thermal erosion advances upward, regions between the channel bundles compact and become almost impermeable, pushing the coalescence point downward and forcing horizontal melt transport into the high-flux channel bundles.	109

- A-1 (a) Schematic diagram illustrating a discontinuity in the spreading ridge modified from *Carbotte et al.* (2004). The ridge-normal rate of ridge migration is given by the vector U_r . The leading segment is labeled **L** and the trailing one **T**. Black arrows show assumed paths of melt focusing beneath the lithosphere. Grey arrows show lithospheric motion. Focusing regions Ω_+ and Ω_- used in equation (A.3) are dashed rectangles with sides of length h and $2h$. (b) Schematic diagram illustrating the model domain and boundary conditions. Half spreading rate is U_0 138
- A-2 Model results and observations of morphological asymmetry versus offset length of discontinuities in the MOR. **Symbols:** difference in axial depth of two adjacent ridge segments across ridge-axis discontinuities (Δd) restricted to those cases where the leading ridge segment is shallower than the trailing segment. Data for fast and intermediate spreading ridges from *Carbotte et al.* (2004). Also shown are previously unpublished data from the slow spreading southern MAR 23°-36°S measured as the difference in axis elevation at mid-points of adjacent segments. Along the 11000 km of MOR examined in the combined data set, the leading ridge segments are shallower at 76% of all discontinuities with offsets greater than 5 km. Symbols for each ridge are colored to correspond to the closest model half rate. Mean half rates in cm/year are 1.9 (southern MAR), 2.8 (Juan de Fuca), 3.7 (Southeast Indian), 4.3 (Pacific Antarctic), 4.6 (northern EPR) and 7.0 (southern EPR) (*DeMets et al.*, 1994). **Curves:** Δd from equation (A.3) for a range of spreading rates. Solid curves represent a conservative estimate of 670 km for the asthenospheric depth and recover a reasonable melt focusing region, Ω (shown in Figure A-1a), determined by approximate “by eye” fitting of the curves to the data. This procedure gives a characteristic dimension h of 24 km, although this solution is non-unique (see text). Dotted curves were computed for an asthenospheric depth limit of 300 km and the same focusing region. 140
- A-3 Output from a sample calculation with $U_0 = U_r = 1$ cm/year and domain size of 200 km depth by 1200 km width. (a) Colored field is \log_{10} of the viscosity field. Vectors represent the flow pattern beneath the migrating ridge. (b) Colored field as in (a). Vectors represent the perturbations of the solid flow field caused by ridge migration. *The scaling of the vectors is slightly different in (a) and (b).* (c) Colored field is W' , the vertical component of the velocity perturbation field in km/Ma. The red contour shows the boundary of the melting region and black contours map Γ' , the melting rate perturbation, in $\text{kg m}^{-3} \text{Ma}^{-1}$. White lines mark the location of the maximal values of W' as a function of depth, as in Figure A-4a. 144

A-4	Results from a simplified model for the perturbed flow, showing the effect of spreading rate on the position and magnitude of the peak upwelling perturbation. Model domain is 200 km deep by 800 km wide. (a) Dashed curves show the position of the bottom of the lithosphere for calculations at different spreading rates and $U_r=7$ cm/year (see legend in b). Solid curves show the position, at each depth, of the maximum and minimum in the vertical component of the velocity perturbation field (e.g see Fig. 3). Note that the W' field contracts slightly with decreasing spreading rate which explains the change in the maxima seen in Figure A-2. (b) Heavy curves represent the maximum in W' as a function of depth for a fixed rate of ridge migration, $U_r = 7$ cm/yr. Light curves are the maxima in W' for $U_r = U_0$	146
B-1	Results of an example calculation using the combined operator SLCN scheme. (a) The u field at model time $t = 2.8$. (b) The residual, analytic minus numerical, at the same time. (c) The residual over model time. The red curve shows the maximum residual normalized by the L2 norm of the discrete analytic solution. The blue curve is the grid averaged L2 norm of the residual, normalized in the same way. .	155
B-2	L_∞ percent error as a function of Peclet number for CNCS, operator split SLCN and operator combined SLCN. The time step is set according to equation (B.15), with $\beta = 0.7$ and $\alpha = 6$ for the semi-Lagrangian algorithms and $\alpha = 1$ for the CNCS scheme.	159
B-3	L_∞ % Error (as defined in Eq. (B.24)) as a function of courant number, $\frac{Pe v_{max} \Delta t}{\Delta x}$. Each graph represents a different grid spacing. These are, in terms of grid points per wavelength of the initial q field: (a) 6 (b) 9 (c) 12 (d) 19 (e) 25 (f) 38	160
B-4	Computational time (in seconds) as a function of Courant number, $\frac{Pe v_{max} \Delta t}{\Delta x}$. All computations performed on a Sun Blade 100 with 250 KB RAM and a 500 MHz processor. Each graph represents a different grid spacing. These are, in terms of grid points per wavelength of the initial q field: (a) 6 (b) 9 (c) 12 (d) 19 (e) 25 (f) 38	161
B-5	Two examples of adaptive interpolation with overshoot detection, both with $x = 1.3$. The green lines delineate the tolerance envelope, the thickness of which is exaggerated for clarity. (a) In this case, assuming that the field is smooth, the cubic interpolant is a better approximation than the linear one. The overshoot detection algorithm correctly returns false. (b) This figure shows the overshoots that characterize the cubic interpolant near an edge. The overshoot detection algorithm returns true and thus the linear interpolant is chosen.	164

B-6	Results for three interpolation methods for the semi-Lagrangian advection scheme, compared with the analytic solution after three full rotations. (a) Analytic solution. (b) Bilinear interpolation (c) Bicubic interpolation (d) Adaptive interpolation. (e) Profiles across the box after 1 (solid line), 3 (dashed line) and 9 (dash-dotted line) full revolutions.	165
-----	---	-----

Acknowledgments

Although the cover of this thesis bears only my name, the contributions of many others enabled and shaped the work that is presented here. Foremost among these is Marc Spiegelman, my academic adviser and mentor for the past five years. Over this period, Marc has been patient and generous with his time. The ideas that form the backbone of this thesis emerged through our countless discussions. Although creativity is Marc's most significant contribution to this work, it is only one of many. In every step of the development of my research, from debugging code, to analyzing results, to preparing presentations and papers, Marc has offered his expertise and insight. Marc will modestly assert that he was merely fulfilling his role as adviser, however his teaching and mentoring awards attest to the efforts that he devotes to these activities. It has been a pleasure to work with him and I am grateful for his help. More importantly, I am grateful for the constant challenge of meeting his expectations.

Three other scientists have made significant contributions to the development of my doctoral thesis. Charlie Langmuir worked with me during my first two years at Columbia, helping me to understand and parameterize the complex hydrous mantle melting system. Suzanne Carbotte shared with me her bathymetry data and her ideas about mantle dynamics. Discussions with Marc and Suzanne lead to my publication about depth asymmetry across offsets in the mid-ocean ridge. The help and insight of Peter Kelemen over the past year has been valuable. He encouraged me to pursue my notion that non-Newtonian viscosity could play a role in the process of melt localization in partially molten aggregates under shear, which resulted in my obtaining the most exciting results of this thesis.

The summer of 2003 spent at Argonne National Lab in Chicago was a turning point in my the research for my thesis. With help from Barry Smith and Matt Knepley, I learned to use the their ingenious Portable Extensible Toolkit for Scientific computation (PETSc). Developing code in the PETSc framework enabled me to obtain solutions to problems that would have otherwise been inaccessible, and to do so with an ease that I had not previously known. Through my interactions with Barry

and Matt, I learned how to think about the numerical solution of partial differential equations. PETSc is the foundation on which this thesis is built.

Many others offered advice, ideas and help. It has been a pleasure to work with Ben Holtzman and Craig Manning on different projects. Liz Cottrell became interested in my research and attempted a set of difficult experiments to better constrain my models. Peter van Keken, Paul Asimow, Terry Plank, David Walker, Paul Tackley, David Bercovici, Marc Hirschmann and Roger Buck all responded to my questions, read my manuscripts, shared code or listened to my ideas and provided useful suggestions.

I am grateful to Dave Lentricia, Mahdad Parsi, Doug Shearer, Bob Bookbinder, Gus Correa and Satish Balay for their help resolving computer issues on my desktop, as well as on the clusters at Argonne and Lamont. I am also grateful to the seismology office (Bonnie Bonkowski, Mary Russell and Stacey Gander), and the DEES office (Mia Leo, Missy Pinkert, Carol Mountain and Bree Burns) for creating an environment in which students are allowed to think almost exclusively about their research and academic progress, with minimal consideration for administrative issues.

The past five years have frequently been a thrilling adventure. They have taught me much outside the confines of academia. For this I must thank my friends, who shared their time and interests with me. Among these are many Lamonters, most of whom I will not mention here, but to whom I am grateful nonetheless. I do want to specially thank to Dick Kuczkowski and Mia Leo, who included me in their trips to the Brooklyn Academy of Music each season. Kevin Wheeler deserves special thanks for being an dependable friend whose help, at a critical time, was invaluable. I am grateful to my parents, Martin and Helen Katz, and to my grandparents, Piero and Naomi Foa, for the love, encouragement and support they have provided. And I thank my brother David and our parents for their many visits to New York and for the spectacular dinners that we shared.

Finally, many thanks are due to the Office of Science and the National Nuclear Security Administration of the US Department of Energy, to the Krell Institute, and to advisory board of the Computational Science Graduate Fellowship for four years

of generous funding of my graduate work and attendance at annual conferences as a fellow. It was the CSGF practicum program that sent me to Argonne National Laboratory in Chicago where I established a collaboration with the PETSc team. The skills, concepts and connections that I acquired as a fellow shaped the research presented here and will be of great value to me well into the future.

Dedication

To my scientist-ancestors, Piero, Carlo and Pio Foá, who set an example of integrity and excellence in research, teaching and life.



Chapter 1

Introduction

Subduction zone/island arc volcanoes are among the most dramatic and hazardous features on the surface of Earth. Most of the characteristics of arc volcanoes such as their location and spacing, their eruptive style (explosive or quiescent) and the chemistry of their lavas are determined at depth in the mantle where rock partially melts and the resulting magma rises toward the surface. Despite the societal relevance of volcanoes and the importance of their source regions, very little is known about the inaccessible places deep in the Earth where magma genesis occurs. The goal of this thesis is to develop theoretical and computational tools and insights that contribute to the developing understanding of the deep roots of volcanoes, especially those associated with subduction zones. It is necessary to address fundamental issues of magmatic organization in the partially molten mantle to enable the development of tectonic-scale models of magmatism.

The behavior of magma in the Earth's mantle is fundamentally a problem of two-phase fluid dynamics. The magma which feeds volcanoes is a liquid. The mantle, located between the Earth's crust and core, is a crystalline solid. Over time-scales longer than the period of a seismic wave, the mantle moves as an extremely viscous fluid and can be modeled using the equations of fluid dynamics. The two fluids, magma and mantle rock, coexist in partially molten regions of the mantle and interact chemically and physically. Because the mantle is composed of angular interlocking crystals, magma can reside in or move through the pores between crystals. *McKenzie* (1984) and others derived a set of fluid dynamics equations that are used to describe

the creeping motion of mantle rock, the porous flow of magma and the interactions between them. The equations, reviewed in section 1.2 below, express the conservation of mass, momentum and energy for a two-phase continuum. To describe magma/mantle dynamics in a specific physical context one must find a solution to these equations under the relevant conditions. Due to the complexity of the governing equations and constitutive laws, however, solutions are not easily obtained. The research in this thesis is centered around finding and interpreting solutions to the magma dynamics equations using computational and analytic approaches.

Although much of the research presented here addresses general questions about melting and magma dynamics, I have chosen to focus attention on the applications of this work to subduction zones. Subduction zones are one of the three major categories of volcanic systems on Earth¹. Subduction zones are the most important of these systems because they control the long-term geochemical evolution of the planet as well as the geometry and kinematics of plate tectonics. Hence research into the dynamics of subduction volcanism will help us to understand some of the most fundamental features of the Earth.

Subduction zones, shown schematically in Figure 1-1, represent the descending leg of mantle convection. Lithosphere formed at oceanic spreading centers cools as it migrates away from these ridges. At some distance from the ridge old, dense lithosphere is subducted and sinks back into the mantle, driving downward flow in the surrounding rock. To the scientists working shortly after the discovery of plate tectonics, it was far from obvious why a cold, downwelling environment is invariably associated with volcanism. Much work went into resolving this apparent paradox. Early work suggested that the solution has two parts. Experimental studies (*Kushiro et al.*, 1968; *Kushiro*, 1972; *Green*, 1973) showed that melting of mantle rock in the presence of water occurs at a much lower temperature than dry melting of the same rocks. At about the same time, *McKenzie* (1969) applied the corner-flow solution of *Batchelor* (1967) and demonstrated that the subducting slab could drive a flow of solid mantle, advecting hot peridotite into the wedge corner. Metamorphic reactions

¹Mid-ocean ridges, hot spots volcanoes and subduction related arc volcanoes

in the slab were known to release water-rich fluids into the overlying mantle. Together these ideas represent a crude recipe for arc volcanism and the basis for much later work.

1.1 Modern challenges in understanding subduction

Today, the challenge lies in refining this understanding by elucidating the connections between the wealth of observations available at the surface and the underlying properties and dynamic processes occurring at depth. In particular there is a set of zeroth-order observations that are diagnostic of subduction zone processes, yet their causes are still not well understood. For example

Arc location and geometry. Surface magmatism is localized in a volcanic front that is invariably 110 ± 40 km above the earthquakes in the slab (e.g. *Gill*, 1981; *Tatsumi*, 1986; *Jarrard*, 1986). Recent work suggests that the depth to earthquakes is actually *anti*-correlated with subduction rate and dip-angle, but otherwise insensitive to most subduction parameters (*England et al.*, 2004).

Thermal constraints. Temperatures of primitive arc magmas are known to range from <1100 °C to >1300 °C (*Tatsumi et al.*, 1983; *Sisson and Bronto*, 1998; *Tanton et al.*, 2001; *Kelemen et al.*, 2003). Furthermore, almost the entire range of estimated temperature can be found among primitive lavas from individual volcanoes (e.g. *Baker and Price*, 1994). Heat flow observations (e.g. *Furukawa*, 1993b; *Blackwell et al.*, 1982) show high values along the volcanic arc.

The role of volatiles. Arc magmas show a range of volatile contents, from considerably higher than MORB and OIB (e.g. $\gtrsim 3\text{wt}\%$ H₂O in primitive arc basalts) (e.g. *Gill*, 1981; *Stolper and Newman*, 1994; *Sisson and Layne*, 1993; *Sobolev and Chaussidon*, 1996; *Plank et al.*, 2004) down to near anhydrous concentrations in some primitive arc basalts (e.g. *Sisson and Bronto*, 1998). Water and other

volatiles are clearly important in the source region of many arc magmas and back-arcs, however, their precise role in melting is still only poorly understood.

The role of sediments. Arc magmas also show distinctive chemical signatures in trace elements and short lived radioisotopes such as the U-series nuclides and ^{10}Be (e.g. *Morris et al.*, 1990; *Hawkesworth et al.*, 1993; *Plank and Langmuir*, 1993; *Miller et al.*, 1994; *Turner et al.*, 2001; *George et al.*, 2003; *Bourdon et al.*, 2003; *Turner et al.*, 2004)) suggesting some interaction of subducted sediments and fluids in the melting process. These tracers may provide important information on rates, paths and interactions of slab components through the slab-wedge-arc system, but relating element fluxes to mass fluxes and process can be quite challenging (e.g. *Elliott et al.*, 1997; *Clark et al.*, 1998).

While these features are generally well accepted, there are many specific questions which still remain:

- Where does melting occur in subduction zones and what processes control the location and volcanic flux of island arcs? Do these characteristics reflect the water flux off the slab or a combination of flux variations, mantle thermal structure and mantle plumbing (*Spiegelman and McKenzie*, 1987; *Davies and Stevenson*, 1992; *Iwamori*, 1998; *Conder et al.*, 2002b; *Kelemen et al.*, 2002)?
- Can we distinguish or quantify the roles of these different processes, e.g. the relative contributions of hydrous flux melting and decompression melting?
- How can we use thermal observations to constrain processes? E.g. What is the nature of the melt transport system that can create and preserve disparate temperatures in mantle-derived melts? What are the relative contributions of solid flow and melt transport to the observed heat flow in arcs?
- How can geochemical data be used to constrain processes in the arc? Can we determine how much subducted material returns to the surface through the arc and how much gets entrained in the mantle? Most generally, how do we

reconcile the complex chemical histories recorded by trace elements and short lived isotopes in a single consistent physical model?

In general, finding answers to these questions will require a concerted, collaborative effort between observationalists, theorists and experimentalists. An important part of this collaboration, however, will be a theoretical/computational framework that can quantify and test ideas of how processes relate to observations. All of the questions and, indeed, all of the observations above are linked to patterns of melting and flow of fluids/magma from the slab to the volcano. A model that could be used to address the observations would ideally consider the coupled two-phase dynamics and geochemical transport of reactive fluid magma in the solid mantle. In other words, the model should calculate time-dependent fluid and solid velocity fields; thermal structure; reactive dehydration, melting and freezing; and the transport of trace, major and radiogenic elements from the slab to the volcano. Such a model will be a significant challenge to construct as well as to interpret. Before it is even feasible, many smaller research problems must be solved to develop and understand the petrological, geodynamical and computational infrastructure required. Some of these problems and their solutions comprise the chapters of this thesis.

Most of the results contained here, as well as the lessons learned, are applicable much more broadly than the limited context of subduction zone volcanism, however. First, they are applicable to magma dynamics in other volcanic settings where much of the same physics, if somewhat different chemistry, still applies. For example, in appendix A, I describe a model developed to address a particular set of observations of a different volcanic system, mid-ocean ridges. Second, insights gained through this work may prove useful in developing theories about other instances of two-phase flow in Earth science such as migration of fluids in subterranean reservoirs, sea-ice formation, hydrothermal fluid flow and the erosional formation of channelized surface drainage networks. Finally, methods and codes developed in this thesis for the study of magma dynamics will provide a basis for more sophisticated models including, perhaps, a comprehensive model of magma genesis and transport in a subduction zone.

In the rest of this chapter I provide a brief outline of the theoretical and computation framework in which my research was conducted. Both the theory of viscous flow in a deformable porous matrix and the computational tools that I use to obtain solutions to the governing equations have been developed and described in many papers available in the scientific literature. The review provided here is cursory and intended only to inform the reader unfamiliar with these fields. Following this background material is a section outlining the chapters of the thesis and their main conclusions.

1.2 Theoretical framework

The equations that have been used to describe the dynamics of magma in the asthenospheric mantle were first derived by *McKenzie* (1984). These equations were later derived in slightly different form by several authors (*Scott and Stevenson*, 1984, 1986; *Fowler*, 1985). *Fowler* (1990) provides a review of these theories and highlights the differences between them, which are, in most cases, subtle. *Bercovici et al.* (2001) derived a set of equations from first principals that account for surface interactions and “damage”. The formulation of *McKenzie* (1984) is the version that is used here. It is a set of conservation equations for mass, momentum and energy for a two-phase continuum composed of the solid, granular phase and a fluid phase that resides in the pore space on the grain boundaries of the solid. The equations imply the assumption that this two-phase system can be described by continuous functions of space and time at scales larger than the scale of a Representative Volume Element (RVE). The RVE is a fictitious parcel of fluid and solid that contains a large enough number of grains that it can be well-characterized by its average quantities, e.g. grain-scale variations can be effectively averaged out. The RVE must be small enough that the averages defined over its volume do not vary by “much” between one RVE and its neighbors, e.g. large-scale gradients in the medium must be well-resolved by a sufficient set of RVEs. Since the mean grain size of the mantle is assumed to be $\sim 0.1\text{-}10$ cm, an RVE for the mantle might be about 1-100 cubic meters. The continuum differential equations are written in the limit of a vanishingly small RVE however, and since all of the

quantities used in the equations are defined as averages over an RVE, the equations are valid only at scales much larger than the grain scale.

Conservation of mass The conservation of mass for both the solid and fluid phases is expressed with the following two equations, respectively:

$$\frac{\partial \rho_s(1 - \phi)}{\partial t} + \nabla \cdot [\rho_s(1 - \phi)\mathbf{V}] = -\Gamma, \quad (1.1)$$

$$\frac{\partial \rho_f \phi}{\partial t} + \nabla \cdot [\rho_f \phi \mathbf{v}] = \Gamma, \quad (1.2)$$

where ϕ is the porosity, the volume fraction over a vanishingly small RVE that is fluid. \mathbf{V} and \mathbf{v} are the solid and fluid velocities, ρ_s and ρ_f are the solid and fluid densities, t is time and Γ is the mass transfer rate from the solid to the fluid (the melting rate). These equations state that a change in the mass of either phase at a point is the result of mass transfer between the phases or of the divergence of advective transport of that phase at that point. Expanding equation (1.1) one obtains,

$$\frac{\partial \phi}{\partial t} + \mathbf{V} \cdot \nabla \phi = (1 - \phi)\nabla \cdot \mathbf{V} - \Gamma/\rho_s, \quad (1.3)$$

which states that changes in porosity are due to advection, compaction and melting. In deriving equation (1.3) it is assumed that the solid density is constant. The assumption of constant fluid and solid density is made throughout this thesis.

Conservation of solid momentum Convection of the mantle is generally considered to be well described by the Stokes equation for a highly viscous creeping fluid with a Reynolds number much smaller than one. The conservation of momentum for the solid phase in the equations of magma dynamics should thus reduce to the Stokes equation in the limit of constant porosity and no melting. In general, however, it should allow for viscous compaction and dilation. *McKenzie* (1984) expressed this in the following form

$$\nabla P = \nabla \cdot \eta (\nabla \mathbf{V} + \nabla \mathbf{V}^T) + \nabla (\zeta - 2\eta/3) \nabla \cdot \mathbf{V} + \bar{\rho} \mathbf{g}, \quad (1.4)$$

where P is the total pressure, η is the shear viscosity and ζ is the bulk viscosity. The quantity $(\zeta + 4\eta/3)$ is the viscosity that resists compaction and dilation of the mantle matrix, although this is not obvious from the form of equation (1.4) above (*McKenzie*, 1984; *Spiegelman*, 1993a). Variable viscosity and its effect on the coupled fluid-solid system is a recurring theme in this thesis. The compaction term in equation (1.4) containing $\nabla \cdot \mathbf{V}$ is often neglected in calculations of magma migration (e.g. *Scott and Stevenson*, 1986; *Iwamori*, 1998) although it controls much of the interesting physics (e.g. *Spiegelman*, 1993c; *Spiegelman et al.*, 2001). The phase-averaged density is given by $\bar{\rho} = \rho_f \phi + \rho_s(1 - \phi)$ and \mathbf{g} is the downward-pointing gravity vector. As written, equation (1.4) states that pressure gradients are balanced by gradients in viscous strain and compaction as well as by buoyancy. In this thesis, buoyancy-driven solid flow is neglected. Other studies have shown that thermal (e.g. *Su and Buck*, 1993; *Kelemen et al.*, 2002) and porous buoyancy (e.g. *Buck and Su*, 1989) may be important in the shallow, partially molten mantle.

Conservation of fluid momentum Because fluid in the mantle is presumed to reside in the connected pore network on the grain boundaries of the crystals it is natural to expect its motion to be described by a modified Darcy’s law. *McKenzie* (1984) and others have shown that, with an appropriate choice for the form of the interphase drag force, the balance of stresses for the fluid can be written as

$$\phi(\mathbf{v} - \mathbf{V}) = -\frac{k_\phi}{\mu} [\nabla P - \rho_f \mathbf{g}], \quad (1.5)$$

where μ is the fluid viscosity (typically assumed to be a constant) and k_ϕ is the porosity-dependent permeability. The permeability is given by the a simplified Kozeny-Carmen relationship (*Bear*, 1972),

$$k_\phi = \frac{d^2 \phi^n}{c} \quad (1.6)$$

where d is the grain size in meters and c is a constant of proportionality. For the mantle, n is estimated to be between 2 and 3 (*von Bargaen and Waff*, 1986; *Cheadle*,

1989; *Wark and Watson*, 1998; *Zhu and Hirth*, 2003; *Renner et al.*, 2003; *Cheadle et al.*, 2004). Equation (1.5) states that the separation flux of fluid and solid is driven by dynamic and lithostatic pressure gradients and is proportional to the permeability of the medium.

Conservation of energy The conservation of energy equation derived by *McKenzie* (1984) is

$$\begin{aligned} \overline{\rho c_P} \frac{\partial T}{\partial t} - T \left(\Delta S \Gamma - \bar{\alpha} \frac{\partial P}{\partial t} \right) + (1 - \phi) \rho_s c_P^s \mathbf{V} \cdot \left(\nabla T - \frac{T \alpha_s \nabla P}{\rho_s c_P^s} \right) + \\ \phi \rho_f c_P^f \mathbf{v} \cdot \left(\nabla T - \frac{T \alpha_f \nabla P}{\rho_f c_P^f} \right) = \nabla \cdot k_T \nabla T + H + D, \end{aligned} \quad (1.7)$$

where T is the temperature in Kelvin, ΔS is the entropy difference between the fluid and the solid, α is the thermal diffusivity, c_P is the specific heat at constant pressure, k_T is the thermal conductivity, H represents internal heat sources and D represents viscous dissipation. Overlined quantities are phase averaged. See *McKenzie* (1984) for details. This equation states that changes in the enthalpy at a point in the two-phase continuum are balanced by latent heat, advected heat, adiabatic heat, internal heat sources and viscous dissipation. In chapter 5 a simplified version of this equation is solved for a coupled reactive flow system where the equilibrium fluid composition, and hence the melting rate, is a function of temperature.

It can be shown that in the limit of zero porosity and zero melting, and neglecting small terms, equation (1.7) reduces to the advection/diffusion equation for potential temperature θ

$$\frac{D \mathbf{V} \theta}{Dt} = \kappa_T \nabla^2 \theta, \quad (1.8)$$

where \mathbf{V} is the solid velocity field and κ_T is the thermal diffusivity.

1.3 Computational framework

The computational solution of the equations described above, whether in the limit of zero porosity (chapter 3 and appendix A) or with dynamically evolving porosity

(chapters 2 and 5), is a significant challenge for two main reasons. First, these equations contain non-linearities in their constitutive laws (permeability, viscosity) that lead to non-linearities in the discretized equations to be solved. Stress-dependent (non-Newtonian) viscosity is particularly challenging from the point of view of computational solutions. Second, these non-linearities result in the evolution of highly localized flow structures and sharp gradients in material properties. The resolution of small scale features associated with localization phenomena requires refined grids that, when associated with Krylov solvers, result in poor performance on single processors. The use of advanced numerical software that combines linear and non-linear equation solvers with inherent parallel scalability to tens of processors is a convenient way to address this challenge².

Fortunately, such software exists and is freely available. The Portable Extensible Toolkit for Scientific computation (PETSc, *Balay et al. (2002, 1997, 2001)*) is a well supported, evolving set of libraries that provide a framework for the development of parallel, PDE-based simulations on structured and unstructured grids. Two important design features of PETSc are (1) the structured interface that it provides to the user that enforces a complete separation of application and solver code and (2) an inherent parallelism that allows the same code to run on a laptop and a cluster of thousands of nodes. These features allow the user to write a scalable application code with minimal concern for parallel communication and test the code with a large set of linear solvers provided by PETSc.

In all of the simulations described here the magma dynamics equations are discretized on a regular, Cartesian, two-dimensional grid with a finite volume technique (*Knepley et al., 2006*). Staggering of variables is used when the horizontal and vertical components of velocity are computed explicitly (e.g. chapters 3 and 2 and appendix A). When only the compaction potential is needed (chapter 5) then a cell-centered mesh is used. The equations are solved to user-specified tolerances on a set of norms on the discrete residual. The residual is the point-wise measure of the extent to which

²Although much progress has been made using Picard iteration on linear multigrid methods (e.g. *Spiegelman et al., 2001*).

the solution vector does not satisfy the discrete equations.

Much of the work on this system of equations has concentrated on isoviscous problems where the potential form equations are particularly convenient as they remove pressure from the system (e.g. *Spiegelman*, 1993a,b). Variable viscosity problems benefit from a primitive variable formulation which we have implemented for the first time. The primitive variable form requires that the Stokes equation be discretized directly. The Stokes equation is singular, however, because it is invariant to the addition of any constant pressure field. This does not represent a problem under PETSc because it solves the linear system iteratively to a finite tolerance with a Krylov method, so that the pressure singularity does not affect the solution. Furthermore, PETSc jointly inverts the Stokes equation and the incompressibility constraint (or compaction rate equation) to simultaneously enforce conservation of mass and momentum. In fact, PETSc enables the user to invert for all field variables simultaneously. In mantle flow problems such as the arc calculations discussed in chapter 3, this means that all four degrees of freedom (DOF) at each grid point (pressure, temperature, and horizontal and vertical velocities) are determined by solving a set of sparse, non-linear algebraic equations. Viscosity is not stored as a DOF in these calculations, it is computed “on-the-fly”. Storage of the viscosity as a DOF increases the memory requirement of the code, the amount of communication between processors and the amount of communication between processor cache and memory. More importantly, for non-Newtonian rheology, storing the viscosity separately allows it to be varied (by the Newton scheme) as an independent variable in calculating a finite difference Jacobian matrix, when in fact viscosity is *not* an independent variable. This actually reduces the convergence rate of the solver.

Advection terms are discretized with an upwind Fromm scheme used by *Trompert and Hansen* (1996) and *Albers* (2000). A semi-Lagrangian algorithm for advection by the method of characteristics has been described by *Spiegelman and Katz* (2005) (appendix B of this thesis) however a parallel version of this code is not yet available under PETSc³. One advantage of characteristics-based schemes over grid-based ad-

³Although see www.ldeo.columbia.edu/~katz/SemiLagrangian_PETSc/.

vection is the lack of a stability condition on the length of the time step. Another is the removal of asymmetric terms from the system of discrete equations. A problem with these schemes is the complexity of communication in parallel and the cost of high-order interpolation schemes that are necessary to minimize numerical diffusion.

1.4 The content of this thesis

The main content of this thesis is organized into four chapters and two appendices. Chapter 2 discusses fundamental physics of localization by mechanical instability in the two-phase system. This is complemented by chapter 5 that discusses chemical instability expected from hydrous reactive flow in subduction zones. Chapters 3 and 4 are also concerned with subduction zones and provide important components required of a more comprehensive model of subduction zone magma genesis. Appendix A, published in *Geophysical Research Letters*, describes a model of magma genesis beneath a migrating mid-ocean ridge developed to address a set of observations by *Carbotte et al.* (2004). An important connection, however, between this appendix and the calculations of solid flow in a subduction zone in chapter 3 is the way in which the temperature dependence of viscosity sets up a self-consistent flow boundary that directs mantle flow.

Chapter 2. Experiments by *Holtzman et al.* (2003a) on partially molten aggregates under simple shear show the emergence of a banded porosity structure with bands at a low angle to the shear plane. Previous attempts to model these bands (e.g. *Spiegelman*, 2003) using the two-phase magma dynamics equations have reproduced their emergence but failed to match the angle of bands. *In this chapter we show, using linear analysis and non-linear numerical simulations, that to couple the reorganization of porosity to shear and match the experiments requires a strain rate dependent rheology.*

Chapter 3. This chapter describes calculations of the flow field and thermal structure induced by subduction of oceanic lithosphere into a variable viscosity man-

tle. The results obtained from these calculations are consistent with numerous other cited studies on subduction and hence are not reported in detail. However, these models were essential for developing and testing the primitive variable approach to solving the Stokes equation with PETSc. They are part of a larger subduction zone benchmarking project (*van Keken, 2003b*). *These results reinforce the conclusion that temperature-dependent viscosity, at a minimum, is required to simulate reasonable flow and temperature fields for subduction zones.*

Chapter 4. In this chapter, published in *Geochemistry Geophysics Geosystems*, I describe a simple mathematical formulation developed to permit rapid and approximate calculation of the degree of melting of an equilibrium system of water, mantle rock (peridotite) and silicate melt given information on the temperature, pressure and composition of that system. The parameterization is calibrated using experimental data from the literature and is validated using melting calculations relevant to ridges and arcs. *This work produced a piece of geodynamic modeling infrastructure used in later chapters and by other authors.*

Chapter 5. I explore the consequences of reactive fluid flow in a simplified subduction zone context. Above the slab, an aqueous fluid traverses increasing temperatures and decreasing pressures on its way to the core of the wedge. Dissolution of rock leads to strong channelization of the fluid flux above the slab thermal boundary layer. Another set of calculations takes an initially water-rich fluid through the inverted temperature gradient above the slab, through the core of the wedge and finally through the colder temperatures at the base of the lithosphere. The inclusion of the cold lithospheric boundary layer causes coalescence of channels into widely spaced “channel bundles” that pierce the lithosphere by transporting heat. *This chapter demonstrated the plausibility of channelized melt flow beneath volcanic arcs and the possibility of melt focusing by interaction with a cold thermal boundary layer.*

Appendix A. Observations of systematically asymmetric depth of ridge segments across offsets in the mid-ocean ridge system by *Carbotte et al. (2004)* motivated

the research described in this chapter. The flow field and thermal structure beneath the two spreading plates of a migrating mid-ocean ridge is calculated and demonstrated to be asymmetric, leading to an imbalance in magma production rates across the ridge. A parameterized model of melt focusing maps this imbalance onto the depth difference of segments across an offset. The results are shown to be in agreement with the data. *This work explains an important set of observations and shows quantitatively that ridge migration can affect the distribution of melting beneath a mid-ocean ridge.*

Appendix B Grid-based discretizations of the advection-diffusion equation, whether finite volume, up-wind or pseudo-spectral based, have stability criteria that limit their time-step size. Furthermore, these methods can produce severe numerical artifacts, especially in the presence of steep gradients in the advected quantity. We describe a characteristics-based semi-Lagrangian advection scheme that has no stability limit. When combined with a Crank-Nicolson discretization of the diffusion operator the resulting discretization is efficient and accurate. *This chapter provides a description and analysis of a useful numerical scheme for solving the advection-diffusion equation.*

The chapters of this thesis represent progress in the development of a numerical simulation of magma genesis and transport in a subduction zone. They separately address many of the challenges that will need to be overcome to assemble a comprehensive, self-consistent model. For example, recent work by *Kelemen et al.* (2002) has demonstrated the importance of including variable viscosity in subduction zone thermal models; experiments by *Holtzman et al.* (2003a) (and models in *Spiegelman* (2003) and chapter 2) indicate the importance of porosity and stress-dependence of rheology in calculating melt/solid interactions; and chemical interactions between magma and the mantle have been shown to be important in determining the physical and chemical organization of melt transport (*Spiegelman et al.*, 2001; *Jull et al.*, 2002; *Spiegelman and Kelemen*, 2003). Beyond the complexity inherent in the equations of magma/mantle dynamics, each of these features adds additional complexity to the

system and presents additional challenges to the modeler. The feasibility and interpretation of a comprehensive model depends on a careful examination of all of its components.

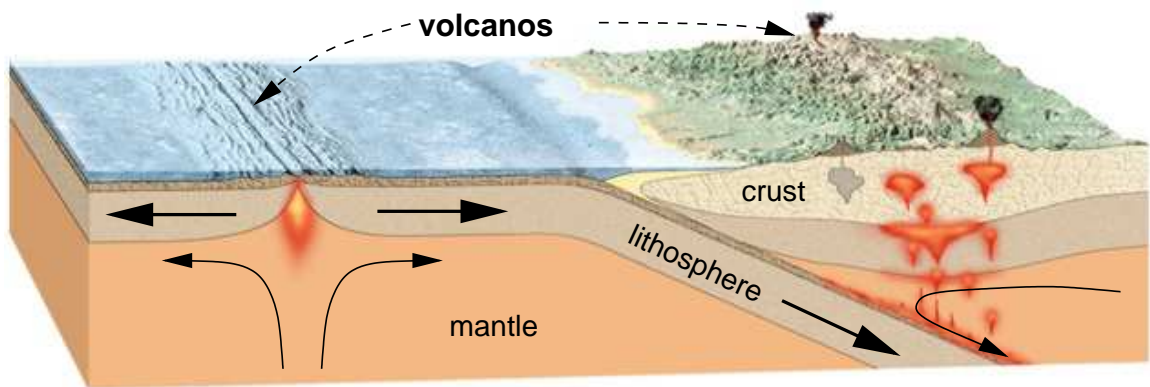


Figure 1-1: A schematic diagram of plate tectonics. A mid-ocean ridge/spreading center is illustrated at left where two plates of oceanic lithosphere are diverging. A subduction zone is illustrated at right where the oceanic lithosphere is colliding and sinking beneath continental lithosphere. Orange represents partially molten regions.

Chapter 2

The Dynamics of Melt and Shear Localization in Partially Molten Aggregates

Abstract

The emergence of patterns of melt distribution in experiments on partially molten aggregates under simple shear (*Daines and Kohlstedt, 1997; Zimmerman et al., 1999; Holtzman et al., 2003a,b*) provide a rare opportunity to test magma migration theory (*McKenzie, 1984; Scott and Stevenson, 1984, 1986; Fowler, 1985; Bercovici et al., 2001*) by directly comparing experiments and calculations. The fundamental observation is the emergence and persistence to large strains of bands of high porosity and concentrated deformation oriented at about 15-25° to the plane of shear (*Holtzman et al., 2005*). We report results from linear analysis and numerical solutions that suggest that band angle in experiments is controlled by a balance between porosity and strain rate-weakening mechanisms. Lower angles are predicted for stronger strain rate-weakening. For the specific model considered here, a power-law stress-dependent rheology, calculations with $n \approx 6$ are consistent with the observations. These results suggest that partially molten aggregates deforming under shear may have a greater sensitivity to strain rate than previously believed (*Hirth and Kohlstedt, 1995a,b*)

2.1 Introduction

Recent experiments on deformation of partially molten aggregates (*Daines and Kohlstedt, 1997; Zimmerman et al., 1999; Holtzman et al., 2003a,b*) provide a rare opportunity to directly test the predominant theory for magma migration in the Earth's mantle (*McKenzie, 1984; Scott and Stevenson, 1984, 1986; Fowler, 1985; Bercovici et al., 2001*). Unlike most experiments that measure bulk material properties, these

experiments develop quantifiable patterns (Figure 2-1a) that have proved challenging to model. The fundamental observation is the emergence and persistence to large strains of bands of high porosity and concentrated deformation oriented at about $15\text{--}25^\circ$ to the plane of shear (*Holtzman et al.*, 2005). Here we present linear analysis (Figure 2-3) and fully non-linear numerical simulations (Figures 2-1b–c, 2-5) that calculate the evolution of a partially molten aggregate matrix undergoing simple shear. These calculations show that magma migration theory can reproduce the distribution of band angles if the viscosity of the aggregate is *both* porosity and strain rate-weakening. Moreover, the balance of these weakening mechanisms controls the preferred angle. We derive these results using a non-Newtonian power-law viscosity because it is a commonly accepted constitutive relation for high temperature creep of mantle materials (*Karato and Wu*, 1993; *Hirth and Kohlstedt*, 2003). Using a stress exponent of $n \sim 4 - 6$, our calculations can reproduce band angles observed in experiments. We suggest that these results should hold for a more general strain rate dependence and discuss their implications for the rheology of partially molten mantle.

In the experiments, an olivine-basalt-chromite aggregate is deformed in simple shear to large strains (e.g. $\gamma \sim 3.6$) at a pressure and temperature where the basalt is molten and resides in the pores of the crystalline matrix. A detailed description of these experiments has been previously published (*Zimmerman et al.*, 1999; *Holtzman et al.*, 2003a). Figure 2-1a shows a section through an experiment with well developed melt-rich bands. These bands form spontaneously at or before strains of $\gamma \sim 1$ at low angles to the plane of shear and remain at low angles to the shear plane even at large strains. The histogram in Figure 2-1d (red bars) shows that the distribution of measured band angles is dominated by bands at about 20° for a sample strained to $\gamma = 3.4$. *Holtzman et al.* (2005) have developed an approximate scaling argument based on steady-state energy dissipation and suggest that for a Newtonian, porosity-weakening viscosity, energy dissipation is minimized when deformation is concentrated into low-angle melt bands. This analysis, however, says little about the formation and evolution of the melt bands.

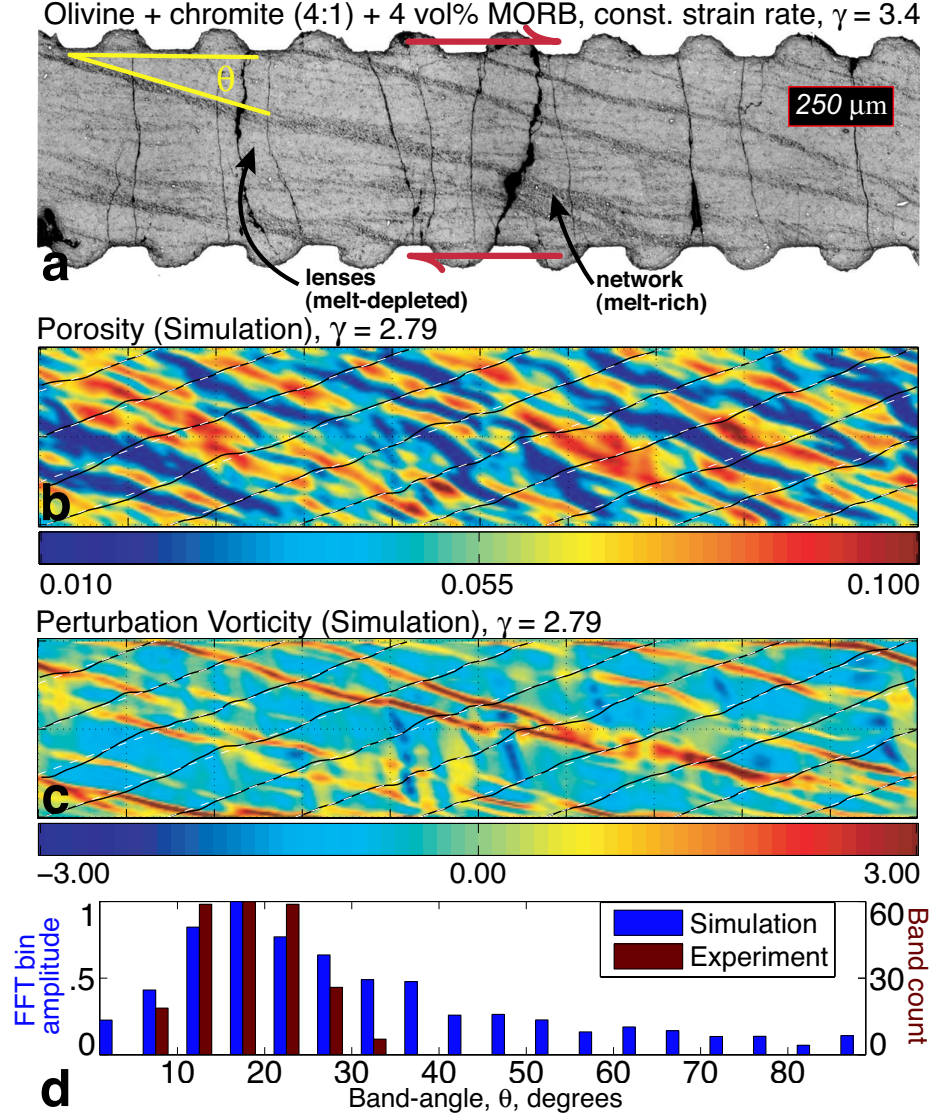


Figure 2-1: A comparison of experimental & numerical results. (a) An example cross section of an experiment (PI-1096) adapted from Figure 1a of *Holtzman et al.* (2005) (experimental details are given by *Holtzman et al.* (2003a)). The melt-rich bands are the sloping darker gray regions at angle θ to the shear direction. (b) The porosity and (c) perturbation vorticity from a numerical simulation with $n = 6$ and $\alpha = -27$ at shear strain γ of 2.79. The domain is five by one compaction lengths. The perturbation vorticity, $\nabla \times [\mathbf{V} - \dot{\gamma}y\mathbf{i}]/\dot{\gamma}$, is the total vorticity minus the constant vorticity $\dot{\gamma}$ due to simple shear (here normalized by $\dot{\gamma}$). Black lines in **b** and **c** show the position of passive tracer particles that were arrayed in vertical lines at $\gamma = 0$; white dotted lines show the expected position of the tracers due only to simple shear. The linear, low-angle red bands in **c** are weak regions associated with high porosity and enhanced shear while the linear, subvertical blue regions are regions of reversed shear. (d) Histograms comparing band angle distributions in experiments and numerical solution shown in panel b.

2.1.1 Past work with magma dynamics theory

These experiments should be well described by continuum theories because both the system size (~ 1 mm) and the size of melt bands ($\sim 100 \mu\text{m}$) are large compared to the grain size ($\sim 10 \mu\text{m}$). Moreover, by controlling grain size and composition, the experiments are designed so that the sample thickness is slightly larger than the “compaction length” $\delta = \sqrt{k_\phi(\zeta + 4\eta/3)/\mu}$ which is the intrinsic length-scale in magma dynamics theory (McKenzie, 1984; Spiegelman, 1993a). The compaction length depends on the permeability k_ϕ , matrix shear and bulk viscosities (η and ζ respectively) and the viscosity of the pore fluid μ . Previous results suggest that localization instabilities occur on scales smaller than the compaction length (e.g. (Stevenson, 1989; Spiegelman et al., 2001; Spiegelman, 2003)).

Magma dynamics theory couples viscous creep of the crystalline mantle to porous flow of low viscosity magma in the pores between crystals (McKenzie, 1984). This physics is described by a set of continuum conservation equations for mass, momentum and energy of both phases and has been considered by many authors (Scott and Stevenson, 1984; Fowler, 1985; Scott and Stevenson, 1986; Spiegelman, 1993a,b, e.g.). These equations are described in Chapter 1 of this thesis. Stevenson (1989) presented the first work on mechanical localization in this system and showed that a porosity-weakening viscous material (Hirth and Kohlstedt, 2003) undergoing extension is unstable: tension across a weak, high porosity region leads to low pressure that, in turn, causes convergence of melt flow into that region, raising its porosity and further weakening it. Stevenson and others showed that perturbations with wavelengths shorter than the compaction length grow at equal rate (Stevenson, 1989; Richardson, 1998; Hall and Parmentier, 2000).

Spiegelman (2003) extends Stevenson’s analysis to include advection of porosity due to simple shear. This analysis shows that all plane-wave perturbations of porosity between 0 and 90° to the direction of shear will grow while perturbations with angles greater than 90° will compact. The maximum growth rate is achieved at 45° while shear is enhanced for angles less than 45° . The variation of compaction and shear

with band angle are shown in Figure 2-4. *Spiegelman* (2003) and *Holtzman et al.* (2003a) speculate that only bands that grow *and* concentrate shear will be favored. However, in the linear analysis for a solely porosity-weakening material, localized shear deformation does not couple to the pressure gradients that drive fluid flow.

2.2 Coupling shear deformation and fluid flow

To achieve a coupling between shear and fluid flow requires that the solid viscosity include both porosity and strain rate-weakening. Specifically, we use a constitutive relation for viscosity consistent with experiments (*Karato and Wu*, 1993; *Mei et al.*, 2002; *Hirth and Kohlstedt*, 2003, e.g.)

$$\eta(\phi, \dot{\epsilon}) = \eta_0 e^{\alpha(\phi - \phi_0)} f(\dot{\epsilon})^{\frac{1-n}{n}} \quad (2.1)$$

where η_0 is the viscosity at reference porosity ϕ_0 and strain rate. $\alpha = -28 \pm 3$ is an experimentally derived porosity-weakening coefficient (*Kelemen et al.*, 1995a; *Mei et al.*, 2002), f is a function of the first and second invariants of the strain rate tensor and n defines the power-law dependence of viscosity on stress. This viscosity is Newtonian when $n = 1$ and is a standard non-Newtonian power-law viscosity when $\phi = 0$ and f is the second invariant of the strain rate tensor.

2.2.1 Linear analysis

Linearized viscosity

To understand the effect of this modification we extend the linear analysis developed for Newtonian viscosity by *Spiegelman* (2003). The key component in this extension is to linearize the viscosity given in equation (2.1) by expanding the ϕ -dependence in a Taylor series for $\phi = \phi_0 + \varepsilon\phi_1$

$$e^{\alpha(\phi - \phi_0)} \approx 1 + \varepsilon\alpha\phi_1. \quad (2.2)$$

Here ε is a number that is small compared with unity such that terms of order ε^2 can be neglected.

We also need to linearize the strain rate dependence of viscosity. To do this it is convenient to write the matrix velocity as a background simple shear flow plus a small perturbation. The perturbation can then be split into incompressible and volumetric flow components represented by a vector potential ψ_1 and a scalar potential \mathcal{U}_1 :

$$\mathbf{V} = \dot{\gamma}y\mathbf{i} + \varepsilon (\nabla \times \psi_1\mathbf{k} + \nabla\mathcal{U}_1) \quad (2.3)$$

For convenience we assume the simplest physically reasonable choice for f , $f(\dot{\epsilon}) = \dot{\epsilon}_{II} = \sqrt{\dot{\epsilon}_{ij}\dot{\epsilon}_{ij}/2}$. Using equation (2.3), the second invariant can be recast in terms of the velocity potentials

$$\dot{\epsilon}_{II}^{\frac{1-n}{n}} \approx \left(\frac{\dot{\gamma}}{2}\right)^{\frac{1-n}{n}} \left(1 + 2\varepsilon\frac{\Psi}{\dot{\gamma}}\right)^{\frac{1-n}{2n}}. \quad (2.4)$$

where

$$\Psi = \left(2\frac{\partial^2\mathcal{U}_1}{\partial x\partial y} + \frac{\partial^2\psi_1}{\partial y^2} - \frac{\partial^2\psi_1}{\partial x^2}\right) \quad (2.5)$$

and terms of order ε^2 have been neglected. It is important to note that Ψ contains contributions from both the incompressible and compressible components of the velocity field. It remains unclear whether the compressible component of velocity should contribute to weakening of the material. We have decided to include the compressible part in the derivation for generality but we show results neglecting its contribution. We show that for the ratio of bulk to shear viscosity in the experimentally estimated range (*Cooper*, 1990; *Renner et al.*, 2003), the effect of including volumetric strain in the calculation of the second invariant of the strain rate tensor is small.

Using the fact that $2\varepsilon\frac{\Psi}{\dot{\gamma}} \ll 1$ we can apply Taylor expansion to equation (2.4) and keep terms up to first order in ε

$$\left(1 + 2\varepsilon\frac{\Psi}{\dot{\gamma}}\right)^{\frac{1-n}{2n}} \approx 1 + \varepsilon\frac{1-n}{n}\frac{\Psi}{\dot{\gamma}}, \quad (2.6)$$

and then combine equations (2.6), (2.4), (2.2) and (2.1) to give the linearized viscosity

$$\eta(\phi_1, \mathbf{V}_1) \approx \eta_0 \left(1 + \varepsilon \alpha \phi_1 + \varepsilon \frac{1-n}{n} \frac{\Psi}{\dot{\gamma}} \right), \quad (2.7)$$

where the constant $\frac{\dot{\gamma}}{2} \frac{1-n}{n}$ has been absorbed into the viscosity prefactor η_0 and we have neglected $O(\varepsilon^2)$ terms. From equation (2.7) we can see that the first order perturbation to the background viscosity is given by

$$\eta_1(\phi_1, \mathbf{V}_1) = \eta_0 \left(\alpha \phi_1 + \frac{1-n}{n} \frac{\Psi}{\dot{\gamma}} \right). \quad (2.8)$$

Linearized magma dynamics, scaling and a trial solution

Having obtained a linearized form of the strain rate-dependent viscosity, η_1 , we follow the steps performed by *Spiegelman* (2003), who derives the dimensionless, linearized magma dynamics equations

$$\frac{\partial \phi_1}{\partial t} + y \frac{\partial \phi_1}{\partial x} = (1 - \phi_0) \mathcal{C}_1, \quad (2.9)$$

$$-\nabla^2 \mathcal{C}_1 + \mathcal{C}_1 = 2\xi \frac{\partial^2 \eta_1}{\partial x \partial y}, \quad (2.10)$$

$$\nabla^2 \mathcal{U}_1 = \mathcal{C}_1, \quad (2.11)$$

$$\nabla^4 \psi_1 = \frac{\partial^2 \eta_1}{\partial x^2} - \frac{\partial^2 \eta_1}{\partial y^2} \quad (2.12)$$

where \mathcal{C}_1 is the dimensionless perturbation compaction rate, $\mathcal{C}_1 = \nabla \cdot \mathbf{V}_1$, $\xi = \eta_0 / (\zeta_0 + 4\eta_0/3)$ and ζ_0 and η_0 are the background bulk and shear viscosity, respectively. In these equations, time is non-dimensionalized by the background strain rate such that $t = \gamma$, the total strain. Lengths are non-dimensionalized by the compaction length at porosity $\phi = \phi_0$, i.e. $\delta = \sqrt{k_0(\zeta_0 + 4\eta_0/3)/\mu}$, which is the intrinsic length scale that arises from the magma dynamics equations (*McKenzie*, 1984; *Spiegelman*, 1993a). See paragraphs 8 and 10 in *Spiegelman* (2003) for details. To complete the linear

analysis we assume trial solutions $\mathcal{C}_1 = \mathcal{C}^*(t)\phi_1$, $\mathcal{U}_1 = \mathcal{U}^*(t)\phi_1$, $\psi_1 = \psi^*(t)\phi_1$ and

$$\phi_1 = \exp [i\mathbf{k}(t) \cdot \mathbf{x} + s(t)] \quad (2.13)$$

where the \mathcal{C}_1^* , ψ_1^* and \mathcal{U}_1^* are scalar, possibly complex function of time only. $\mathbf{k}(t)$ is the time-dependent vector wavenumber

$$\mathbf{k}(t) = k_x \mathbf{i} + k_y(t) \mathbf{j} = k_x^0 \mathbf{i} + (k_y^0 - k_x^0 t) \mathbf{j} \quad (2.14)$$

that gives the evolution of a wave vector evolving passively under advection by unperturbed simple shear flow (see *Spiegelman* (2003) paragraph 13 for details). Equation (2.14) can be recast to find the passively advected band angle as a function of time,

$$\theta(t) = \tan^{-1} \left[\frac{\sin \theta_0}{\cos \theta_0 - t \sin \theta_0} \right], \quad (2.15)$$

where $\theta_0 = \tan^{-1}[k_x^0/k_y^0]$ is the initial angle and t is dimensionless time.

Solutions to the linearized magma dynamics equations

Given the trial solutions for ϕ_1 , \mathcal{U}_1 and ψ_1 , we can write the dimensionless, first order viscosity as

$$\eta_1(\mathbf{x}, t) = \left[\alpha + \frac{1-n}{n} (k_x^2 \psi^* - 2k_x k_y \mathcal{U}^* - k_y^2 \psi^*) \right] \phi_1. \quad (2.16)$$

Substituting equations (2.13), (2.16) and the other trial solutions into equations (2.9)-(2.12) and performing some algebra we obtain

$$\mathcal{C}^* = -2\xi\alpha \frac{k_x k_y k^4}{(k^2 + 1) \left[k^4 + \frac{1-n}{n} (k_x^2 - k_y^2)^2 \right] + 4 \frac{1-n}{n} \xi k_x^2 k_y^2 k^2}, \quad (2.17)$$

where $k^2 = \mathbf{k} \cdot \mathbf{k}$. In the Newtonian limit ($n = 1$), equation (2.17) reduces to the solution obtained in *Spiegelman* (2003),

$$\mathcal{C}^* = -2\xi\alpha \frac{k_x k_y}{k^2 + 1}. \quad (2.18)$$

Inspection of equation (2.17) shows that for wavenumbers $k^2 \ll 1$ (dimensionally, wavelengths much longer than the compaction length), $\mathcal{C}^* \rightarrow 0$ approximately as k^2 . This means that perturbations larger than the compaction length do not grow and we can concern ourselves with short wavelength perturbations where $k^2 \gg 1$. In this case we can rewrite equation (2.17) as a function of the angle, θ , between perturbation wavefronts and the shear plane:

$$\mathcal{C}^* = -\frac{\alpha\xi \sin(2\theta)}{1 + \frac{1-n}{n} [\cos^2(2\theta) + \xi \sin^2(2\theta)]} \quad (2.19)$$

by using the geometric relations $k_x = |\mathbf{k}(t)| \sin \theta(t)$ and $k_y = |\mathbf{k}(t)| \cos \theta(t)$ and trigonometric identities. The velocity potential factors ψ^* and \mathcal{U}^* can similarly be expressed in terms of θ . If we had chosen a form for f independent of volumetric strain then the $\sin^2(2\theta)$ term in the denominator of equation (2.19) would not appear in this expression. This change has the effect of collapsing all four curves in Figure 2-3a to the same value at 45° .

Using equation (2.17), the growth rate of the porosity perturbation as a function of time is

$$s(\theta, t) = -\int_0^t \frac{\alpha\xi(1-\phi_0) \sin(2\theta)}{1 + \frac{1-n}{n} [\cos^2(2\theta) + \xi \sin^2(2\theta)]} dt. \quad (2.20)$$

At small times $\delta t \ll 1$, the log of the amplitude of porosity is approximately $s(\theta, \delta t) \approx \dot{s}\delta t$ and the maxima of $s(\theta, \delta t)$ are the same as the maxima of \dot{s} .

Taking the derivative of equation (2.19) with respect to θ , setting to zero and solving gives three solutions for $0 \leq \theta \leq 90$. For $n \leq (2-\xi)/(1-\xi)$, only the solution $\theta = \pi/4$ is real valued and represents the sole maximum at 45° . When n increases past this bound however, two other solutions become pure real and represent the symmetric maxima of s

$$\theta_{max} = \frac{1}{2} \tan^{-1} [\pm(-2 + n + \xi - n\xi)^{-1/2}] \quad (2.21)$$

and the solution at 45° becomes a local minimum. This pattern, already evident in Figure 2-3a, is shown for a continuous range of n in Figure 2-2. The assumption

that compaction contributes to viscosity variations means that different values of the ratio of bulk to shear viscosity correspond to different curves. The result without this assumption is indistinguishable from the black curve. Experiments by *Cooper* (1990); *Renner et al.* (2003) have roughly constrained the bulk viscosity to lie between 1 and 10 times the shear viscosity. Even if the bulk viscosity is within this range, for a given band angle (say 20°) there is significant difference between the n required along the blue curve and the green curve in Figure 2-2. For the results of numerical simulations plotted in Figure 2-5, a value of $\zeta_0/\eta_0 = 10$ has been assumed. If compaction strain does not contribute to determining the local shear viscosity there is little change in the preferred value of n . If, however, compaction strain is important and the ratio of bulk to shear viscosity is on the low end of expected values, $\zeta_0/\eta_0 \sim 1$, then linear analysis would predict that a higher n is needed to make simulations consistent with data (see Figure 2-5 for a comparison). This is an important point to resolve in future work because it affects both the value of n preferred by our model as well as the behavior of the magma/mantle dynamics system in other contexts (such as reactive melting calculations (*Spiegelman et al.*, 2001)).

Linear analysis results

In this new analysis the exponential growth rate of plane-wave perturbations in porosity \dot{s} is given by

$$\dot{s}(\theta, n) = -\frac{\alpha\xi(1 - \phi_0)\sin(2\theta)}{1 + \frac{1-n}{n}\cos^2(2\theta)}. \quad (2.22)$$

Here we have neglected the contribution of matrix dilation to weakening. The parameter $\xi = 1/(\zeta_0/\eta_0 + 4/3)$ controls the growth rate of porosity perturbations through the product $\alpha\xi$.¹ The amplitude of porosity perturbations at time t is given by $e^{s(t)}$. In the limit of Newtonian viscosity ($n = 1$), equation (2.22) reduces to that derived

¹Because the ratio of bulk to shear viscosity ζ_0/η_0 must be positive, ξ is constrained to lie between 0 and $\frac{3}{4}$. Only the zeroth order bulk viscosity term ζ_0 appears in the linear analysis solutions. For simplicity and due to a lack of experimental constraints, we consider ζ a constant ranging from one to ten times η_0 (*Cooper*, 1990; *Renner et al.*, 2003) in numerical simulations reported here. Simulations where ζ varies with porosity have been carried out and are indistinguishable from those with ζ constant.

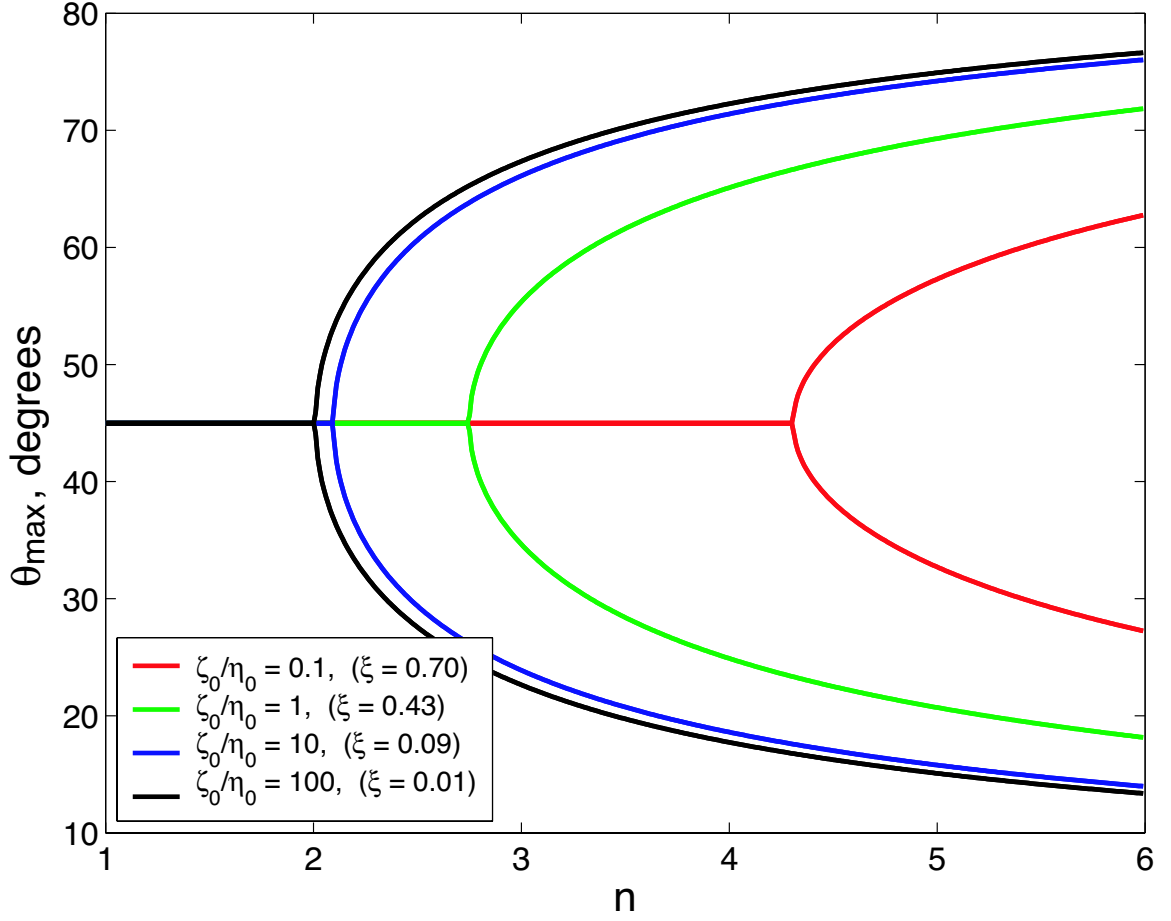


Figure 2-2: The position of the maxima of \dot{s} as a function of n . Curves are obtained by plotting equation (2.21) for different ratios of the bulk to shear viscosity ζ_0/η_0 . Neglecting the effect of compaction on viscosity gives a result indistinguishable from the black curve. These curves predict the angles at which bands will have the highest instantaneous porosity growth rate. To undergo significant accumulated growth, a band must remain near one of these favored angles. High angle bands represented by the upper branch of the curves in this figure are rapidly advected away from the angle of peak instantaneous growth to angles near and above 90° where they cease to grow and begin to compact. Low angle bands represented by the lower branch are not rotated strongly by advection (see passive advection trajectories in Figure 2-5c, for example) and thus remain longer in a favorable position for growth of porosity. The amplitude $e^{s(t)}$ of low angle bands thus increases faster than the amplitude of high angle bands.

by *Spiegelman* (2003).

Figure 2-3a shows the *instantaneous* growth rate of porosity perturbations \dot{s} as a function of θ and n . For $n = 1$ there is a single peak at 45° . Increasing n leads to a broadening and division of this peak into two distinct peaks, one at low angle and one at high angle. To understand this behavior it is instructive to examine equation (2.22). For solely porosity weakening viscosity ($n = 1$), the growth rate is proportional to $\sin(2\theta)$, which has a maximum at 45° . This represents the angle of largest instantaneous extension in simple shear. For $n > 1$, increased shear in high porosity regions further decreases their viscosity. Enhanced shear is largest for perturbations oriented at 0 and 90° and goes to zero at 45° , as shown in Figure 2-4. This is manifest as $\cos^2(2\theta)$ in equation (2.22). At any given orientation between 0 and 90° , a larger viscosity contrast will result in larger pressure gradients driving fluid flow. The balance between favorable orientation for opening (45°) and favorable orientation for concentrating shear (0 and 90°) is controlled by the factor $(1 - n)/n$.

Figure 2-3a shows symmetric peaks in the instantaneous growth rate at low ($\sim 15^\circ$) and high ($\sim 75^\circ$) angles. However, these preferred angles do not evolve equally over time. Due to the effect of advection of porosity by simple shear, high angle bands are rotated² rapidly with strain out of an orientation that is favorable for growth (bands oriented at angles greater than 90° actually decrease in amplitude). On the other hand, low angle bands are rotated relatively slowly away from their initial angles and remain in a favorable orientation for growth up to large strains. The preferred growth of low angle bands at high n is illustrated in Figure 2-3b, which shows the amplitude of porosity perturbations $e^{s(t)}$ as a function of θ and n at a strain of $\gamma = 1$.³ Figure 2-3c and d show the full evolution of amplitude as a function of θ up to a strain of $\gamma = 2$ for $n = 1$ and $n = 4$. In the case of $n = 1$ the peak amplitude begins at 45° and

²They are actually sheared. The effect of this shear, however, appears as a rotation whose rate depends on angle. Passive advection trajectories for $\theta(t)$ are discussed in the Appendix (equation (2.15)) and shown as black lines in Figure 2-3c–d and Figure 2-5.

³The amount of strain over which the linear analysis remains valid depends partly on $\alpha\xi$. For typical parameter values, predictions of amplitude break down by strains of $\gamma \lesssim 1$. However, comparison to numerical solutions, suggests that predictions of angular distributions are surprisingly good to large strains.

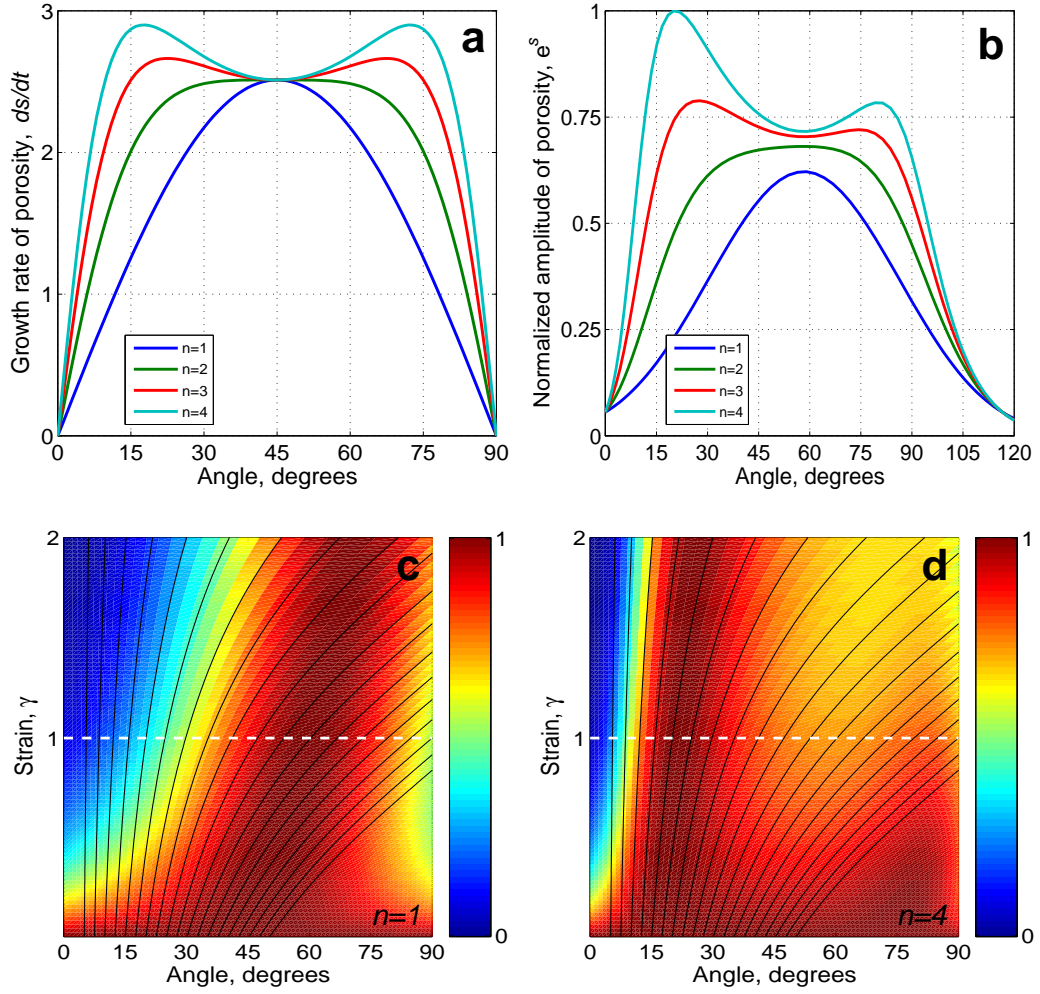


Figure 2-3: Results from linear analysis showing the effect of stress exponent n on the angular dependence and rate of growth of porosity perturbations (with $k \gg 1$). (a) The initial growth rate \dot{s} of porosity from equation (2.22) as a function of band angle θ and n . (b) The normalized amplitude of perturbations as a function of θ for $\gamma = 1$. Advection by simple shear preferentially rotates higher angle bands out of favorable orientation for growth. Panels c and d show the normalized amplitude of porosity perturbations, $e^{s(t)}$, as a function of strain γ and angle θ for $n = 1$ and $n = 4$ respectively. Black lines are passive advection trajectories that show the rotational effect of unperturbed simple shear on initial band angles. The angle with peak amplitude as a function of strain is determined by both the growth rate (shown in panel a) and passive rotation, hence the line through the maximum amplitude (darkest red regions) crosses passive advection trajectories.

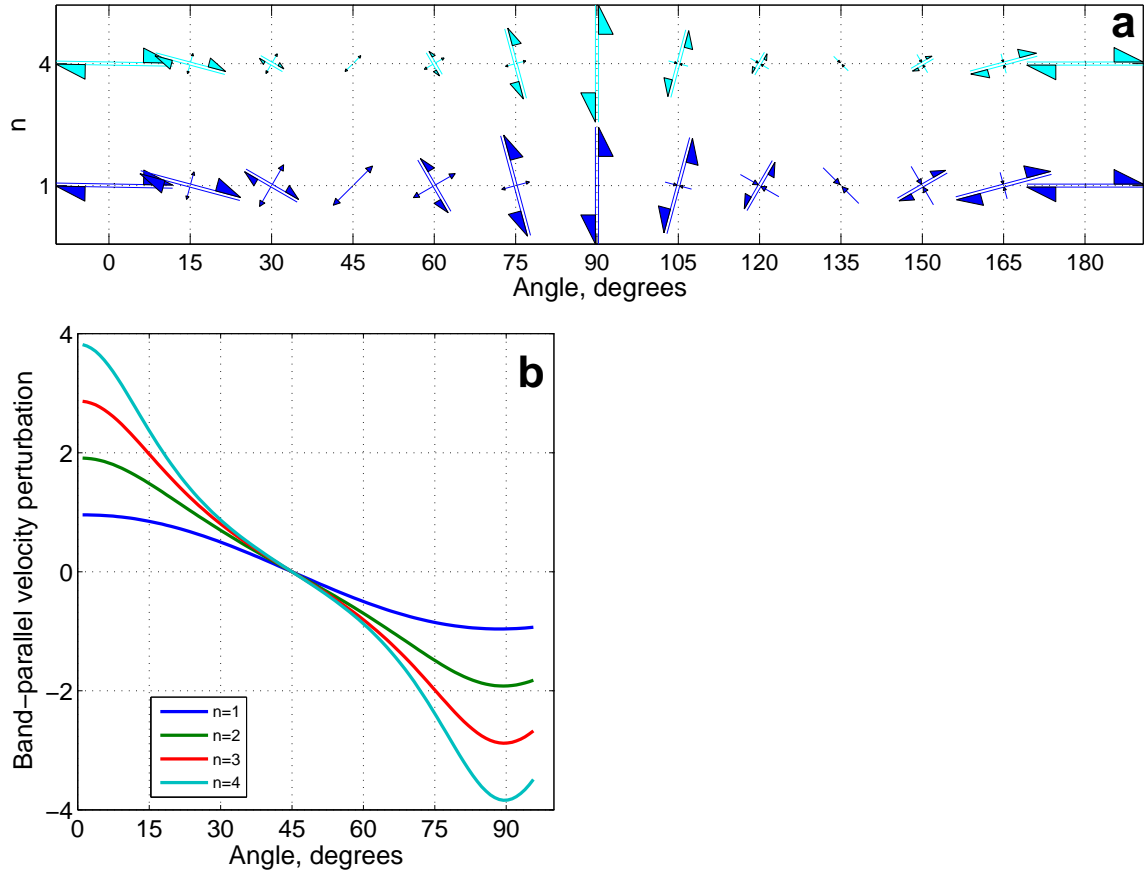


Figure 2-4: Two descriptions of the perturbation velocity field from linear analysis. Panel **a** shows the relative sizes of the shear and volumetric components of the perturbation flow field for $n = 1, 4$. The velocities for $n = 4$ are four times greater than those for $n = 1$ (as can be seen in panel **b**) but are scaled down to fit on the graph. It is evident from this panel that the volumetric component of strain goes to zero at 0° and 90° while the shear component goes to zero at 45° and 135° . The shear component is always maximized at 0° and 90° to the shear plane. Panel **b** shows the shear component of the perturbation velocity field as a function of band angle and n . The amplitude of the perturbation scales with n . Curves for higher n show greater enhancement of shear near 0° and 90° than the sine wave that represents $n = 1$.

increases with increasing strain to about 65° at $\gamma = 2$. For $n = 4$, there is initially a symmetric bimodal distribution of amplitude at 15 and 75° but with increasing strain the amplitude of low angle bands grows much more rapidly than that of high angle bands. To validate these results requires numerical solutions of the full non-linear equations.

2.2.2 Numerical solutions

The equations governing the two-phase aggregate are reviewed in the introduction of this thesis. Some rearrangement puts them into the following form, convenient for numerical solution,

$$\frac{\partial \phi}{\partial t} + \mathbf{V} \cdot \nabla \phi = (1 - \phi) \nabla \cdot \mathbf{V}, \quad (2.23)$$

$$\nabla \cdot \mathbf{V} = \nabla \cdot \frac{k_\phi}{\mu} \nabla P, \quad (2.24)$$

$$\nabla P = \nabla \cdot [\eta (\nabla \mathbf{V} + \nabla \mathbf{V}^T)] + \nabla \left[\left(\zeta - \frac{2\eta}{3} \right) \nabla \cdot \mathbf{V} \right], \quad (2.25)$$

where ϕ is porosity, \mathbf{V} is solid velocity, P is the dynamic pressure, k_ϕ is permeability ($k_\phi \propto \phi^n$), μ is the melt viscosity, η is the shear viscosity of the solid and ζ is the bulk viscosity of the solid. Terms representing the buoyancy force and mass transfer between solid and fluid are not included because they are negligible in the experiments. The equations are discretized using a semi-implicit finite volume scheme on a staggered mesh. The domain is periodic in the horizontal. On the top and bottom boundaries the matrix velocity is required to satisfy $\mathbf{V} = \pm U_0 \mathbf{i} + 0 \mathbf{j}$ and vertical gradients in pressure and porosity are required to equal zero.

Due to strong non-linearities and localization phenomena, computational solutions to the full differential equations are challenging to obtain. However, we have made significant progress using the Portable Extensible Toolkit for Scientific computation (PETSc, (*Knepley et al.*, 2006; *Balay et al.*, 2001)) which provides a suite of tools for the numerical solution of non-linear PDEs. The system of discrete non-linear equations is solved using a Newton-Krylov-Schwarz method (*Cai et al.*, 1997; *Gropp et al.*, 1998) with GMRES and an incomplete LU factorization preconditioner.

To investigate the effect of varying the stress-dependence of viscosity we ran 4 groups of simulations at $n = 1, 2, 4, 6$. Each group consisted of 4 model runs at different grid resolutions from 50 to 80 cells per compaction length on a domain of 4×2 compaction lengths. Each run was initiated with 5 vol% background porosity with 0.05 vol% white noise perturbation. The simulations were run until they failed to converge, which typically occurred when inter-band porosities reached zero.

Output from a representative run with $n = 6$ is shown in Figure 2-1b–c at a strain of $\gamma = 2.79$. The simulations are initiated with a small amount of random noise added to a uniform background porosity field ($< 1\%$ of ϕ_0). Sharp gradients in material properties due to localization cause convergence rates to degrade such that we have not consistently been able to integrate the equations with high n beyond a strain of about $\gamma = 2.5$.

To quantify the band angle distributions in these simulations, histograms are calculated by taking the 2D FFT of the porosity field and integrating the amplitude response within 5° bins in band angle θ . Figure 2-1d shows the histogram derived from Figure 2-1b. At each step of strain, similar histograms are produced from ensembles of simulations with different seeds for initial noise. The power spectrum of the initial noise field controls the wavelength of the emergent band pattern but does not affect the angle. This is consistent with the prediction from linear analysis that all perturbation wavelengths shorter than the compaction length grow. We have typically initiated simulations with white noise. Figure 2-5a–b shows the evolution of histograms with increasing strain for $n = 1$ and $n = 4$. The qualitative similarity of these results to those shown in Figure 2-3c–d is striking. One salient difference is that in simulations, even at small strain, high-angle bands do not grow.

Colored circles in Figure 2-5d chart the evolution of the preferred angle taken from the histograms as a function of strain and n . Consistent with the linear analysis, a more non-linear viscosity (higher n) results in a lower initial peak band angle. Furthermore, peak band angle increases with strain for all n . However, this increase in angle is not simply passive rotation by unperturbed shear flow. If it were, the symbols would follow the passive advection trajectories shown by black lines in Figures 2-3c–d

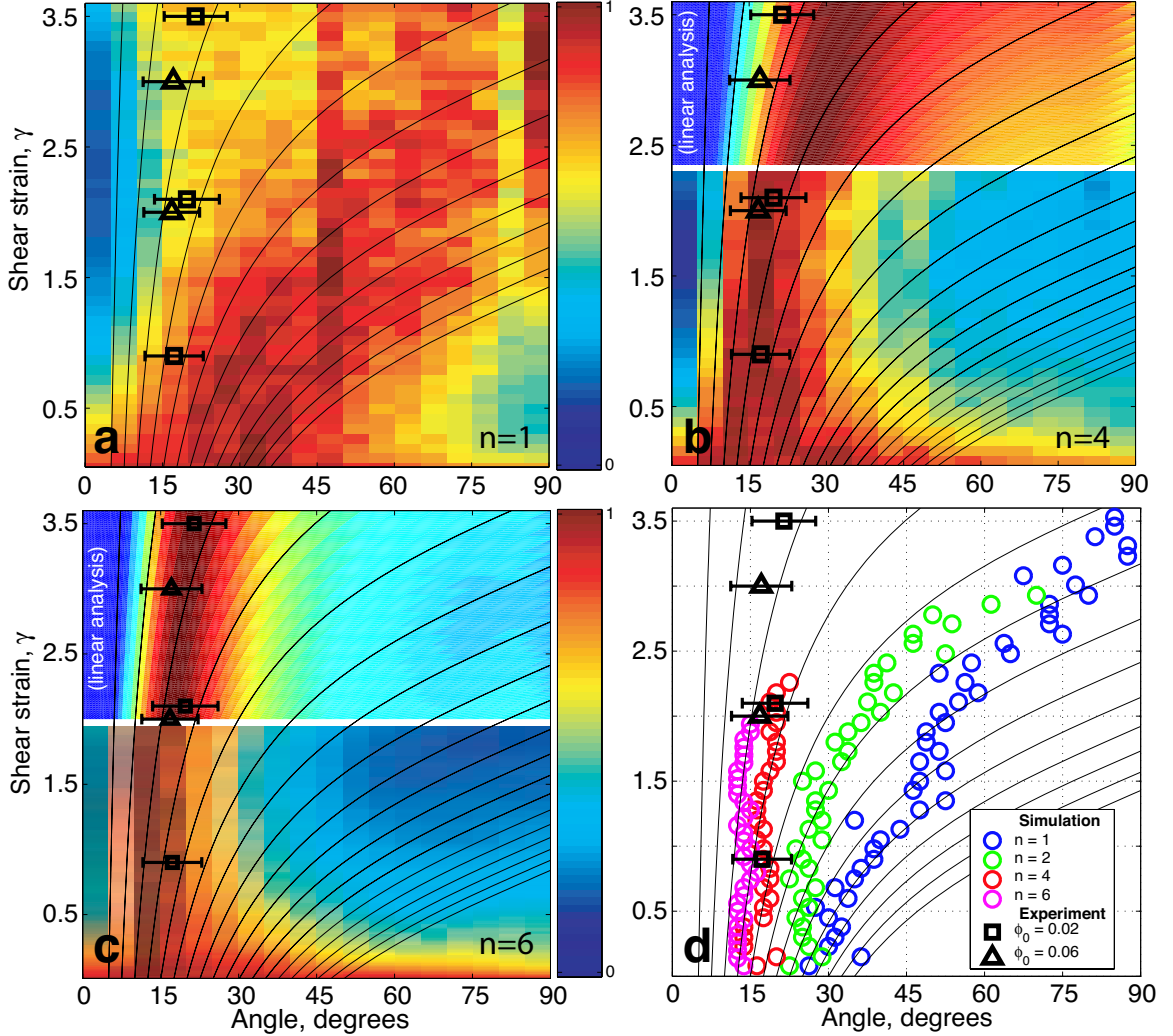


Figure 2-5: Evolution of band angle in numerical simulations, experiments and linear analysis. Panels **a**, **b** and **c** show the evolution of angle distribution averaged over four simulations for $n = 1$, 4 and 6, respectively. In **b** and **c** simulations do not reach the maximum strains achieved in experiments and hence results from linear analysis are used to extend them to $\gamma = 3.6$. For panels a–c, in the part of the plot derived from simulation results, each row at each step of strain represents a single histogram of the porosity field like the one in Figure 2-1d. These panels should be compared to Figure 2-3c and d. Panel **d** summarizes panels **a**, **b** and **c** as well as simulation results for $n = 2$ by plotting only the angle with *maximum* amplitude as a function of strain. This represents the dominant band angle and is generally consistent with a visual estimate from the porosity field. Black symbols in all four panels represent mean band angles from independent experiments to different strain. Characteristics of porosity bands in experimental cross-sections were quantified by hand-measurement (not FFTs). A key question remains as to the behavior of the full non-linear calculations for high strain at $n > 3$.

and 2-5a–d and expressed analytically in equation (2.15). For example, a plane wave initially oriented at 25° to the shear plane will rotate to 90° by a strain of $\gamma \sim 2.25$ under passive advection. For $n = 2$, the peak band angle begins and remains at 25° to a strain of about $\gamma \sim 1.5$. It then appears to follow the passive advection trajectory that initiated at about 16° . Similar patterns are seen for higher n , however because they initiate with lower peak band angle, the deviation from a passive advection trajectory is more subtle. This behavior is also seen in the linear analysis (Figure 2-3c–d) and is the result of the interplay of instantaneous growth of bands in favored orientation and the rotation of these bands out of this orientation by advection due to simple shear.

2.3 Comparison with data

Data from experiments are shown by black symbols in Figure 2-5 and can be directly compared to model results. Each point represents the mean of the distribution of band angles measured in an individual experiment (see Figure 2-1a, d) (*Holtzman et al.*, 2003a). This data shows that the peak band angle is roughly constant at 10 – 20° up to large strain. Up to a strain of about $\gamma \sim 2$, the data are consistent with simulations with $n = 4$ or 6 . Unfortunately our current numerical techniques have not been able to consistently take these simulations to higher strain. If linear analysis is an accurate means for extending band angle evolution to higher strain than achieved in simulations (Figure 2-5b–c) then results for $n = 6$ are most consistent with the data. The open question is what mechanism is active in experiments at high strain that maintains the low band angle.

Spiegelman (2003) suggests one mechanism for maintaining low angle in which bands act as strain guides for matrix shear. These strain guides are assumed to modify the solid flow field significantly from simple shear, reducing the amount of rotation. Strain concentrations are observed in experiments (*Holtzman et al.*, 2003a) and in simulations (Figure 2-1b–c) where strain markers are offset across porosity bands. However, comparison of strain markers to their positions predicted by simple

shear in Figure 2-1b–c shows that the deviation from simple shear is small.

Holtzman et al. (2005) propose another scenario in which a pumping mechanism forces transfer of fluid from bands being rotated to higher angles to newly forming bands at low angles. We note that in calculations reported here, some form of porosity reorganization is constantly occurring, evidenced in Figure 2-5 by the observation that the evolution of peak band angle does not follow passive advection trajectories. Furthermore, an animation of calculations at large n (Movie S1) shows reconnection of porosity bands, maintaining the dominance of those at low angle. This reorganization is manifest in Figure 2-5b–c in that the standard deviation of the distribution does not increase with strain.

2.4 Discussion

In all calculations some amount of porosity band reconnection is occurring. However the dominant angle and standard deviation are ultimately controlled by the magnitude of the strain rate dependence of viscosity (e.g. the size of n). Within the context of the power-law viscosity used here, values of $n \sim 4 - 6$ (Figure 2-5b–d) are required to match observed band angles. These values are somewhat higher than the values between 3 and 4 for partially molten aggregates undergoing dislocation creep or dislocation-accommodated grain-boundary sliding inferred from uniaxial deformation experiments at small strains $\leq 25\%$ (*Hirth and Kohlstedt*, 1995a,b). One suggestion is that this discrepancy is due to the different deformation geometry between compression and shear configurations. An experimentally testable prediction from our model is that deformation of a partially molten aggregate in simple shear will have a larger strain rate dependence of viscosity than one deformed in uniaxial compression. It should be emphasized, however, that the n that we predict is the “material” n , valid at every point in the medium, and not the “effective” n that can be calculated from stress–strain rate measurements taken through the course of an evolving experimental run.

It should be noted that in these calculations, we *assume* a power-law viscosity

and treat n as a control parameter. The key feature of this rheology is the strain rate-weakening mechanism that couples localized shear to the organization of porosity bands. We suggest that any rheology that has a strain rate-weakening mechanism would give similar results. Another example of such a rheology is plasticity, which can also lead to strain localization (*Rudnicki and Rice, 1975; Buck et al., 2005, e.g.*). Visco-plasticity can be approximated by a power-law stress dependence with large n (*Jellinek et al., 2005*), however plastic rheologies typically prescribe an internal friction angle which determines the angle of shear bands. A pleasing feature of our calculations is that the band angle emerges naturally from the balance of two weakening mechanisms with no *a priori* assumptions about angles.

2.5 Conclusion

In the analysis described here we have demonstrated how a non-Newtonian, strain rate-weakening solid viscosity affects the dynamics of pattern formation in partially molten aggregates. Our results show how the balance of stress and porosity-weakening controls the angle at which porosity bands emerge and evolve in simulations. The patterns developed in our calculations are quantitatively consistent with those observed in experiments. There are, however, discrepancies between experiments and calculations such as the aspect ratio and spacing of bands and the steep porosity gradients at their edges. It is possible that models that use other strain rate dependent rheologies can resolve these differences. On the other hand, these discrepancies may point to physics that is missing from magma migration theory. Exploration of these ideas provides opportunities and challenges for theorists and experimentalists.

Chapter 3

Mantle Flow and Thermal Structure in a Kinematic Subduction Zone Model

3.1 Introduction

Models of the creeping solid flow of the mantle wedge and the associated arc thermal structure are fundamental for understanding the context in which subduction zone melting occurs. Two categories of these models exist and many investigators have contributed to their development: “kinematic” models where the position of the slab is fixed and drives a corner-flow in the adjacent wedge (*Furukawa, 1993a; Kincaid and Sacks, 1997; King, 2001; van Keken et al., 2002; Kelemen et al., 2002; Conder et al., 2002b; Gerya and Yuen, 2003; van Keken, 2003a; Gutscher and Peacock, 2003; Currie et al., 2004; Kincaid and Griffiths, 2004*), and “dynamic models” in which the slab’s position is determined by viscous stresses and buoyancy forces (*Hager and O’Connell, 1978; Becker et al., 1999; Billen and Gurnis, 2001; Gurnis et al., 2004; Billen and Hirth, 2004*). While the latter category of model is very important to our understanding of the mechanics of subduction and its role in plate tectonics, a study of arc magma genesis does not require computing a dynamically self-consistent slab geometry. Recent models in the first category are broadly similar to each other and emphasize the importance of including (at least) a temperature-dependent mantle viscosity.

We have developed a kinematic model that employs a pressure, temperature and stress dependent viscosity. This viscosity is consistent with experiments on dry, melt-free mantle rocks (*Karato and Wu, 1993; Hirth and Kohlstedt, 2003*). As in simulations with only temperature dependence of viscosity, our simulations show a more focused mantle flow in the wedge corner, leading to a hotter mantle nose and slab surface than in earlier constant viscosity flow/thermal models. Moreover, variable viscosity solutions produce a component of solid upwelling. Output from representative calculations are shown in Figures 3-2 and 3-3. These results have been submitted to a benchmark project for subduction zone thermal models (*van Keken, 2003b*) and are nearly the same as results obtained by other approaches.

3.2 Governing equations and numerical solution

In the limit of zero porosity, no melting, and neglecting buoyancy forces the equations of magma dynamics reduce to the incompressible Stokes equation and a steady-state advection-diffusion equation for potential temperature θ ,

$$\nabla P = \nabla \cdot [\eta (\nabla \mathbf{V} + \nabla \mathbf{V}^T)] , \quad \text{s.t. } \nabla \cdot \mathbf{V} = 0, \quad (3.1)$$

$$\mathbf{V} \cdot \nabla \theta = \kappa \nabla^2 \theta, \quad (3.2)$$

where \mathbf{V} is the solid velocity, P is the dynamic pressure and κ is the thermal diffusivity. The true temperature is given by

$$T = T_0 \theta \exp \left(\frac{\alpha g}{c_P} z \right) \quad (3.3)$$

where T_0 is a reference temperature, α is the thermal expansivity, g represents gravity, c_P is the specific heat and z is the depth.

The dynamic viscosity in equation (3.1) can be chosen as a constant (isoviscous), diffusion creep (pressure and temperature dependent) or combined diffusion/dislocation creep (non-Newtonian pressure, temperature and stress dependent). For the latter,

diffusion and dislocation viscosities are combined to give an effective viscosity,

$$\eta_{eff} = \frac{2}{\eta_{disl}^{-1} + \eta_{diff}^{-1}}. \quad (3.4)$$

Independently, the dislocation and diffusion creep viscosities are given by

$$\eta_{disl,diff} = A_0 \exp\left(\frac{E^* + PV^*}{nRT}\right) \dot{\epsilon}_{II}^{\frac{1-n}{n}} \quad (3.5)$$

where A_0 , E^* , V^* , and n are material constants that are different for diffusion and dislocation creep (their values are given in Table 3.1). R is the universal gas constant, P is the total pressure (approximately equal to the lithostatic pressure), T is the absolute temperature and $\dot{\epsilon}_{II}$ is the second invariant of the strain-rate tensor. For numerical stability, viscosity is truncated at 10^{24} Pa-s, which is sufficient to preserve the rigid behavior of the cold lithosphere [van Keken, *pers. comm.* 2003].

Equations (3.1), (3.2) and the boundary conditions are discretized using a finite volume approach on a fully staggered grid and solved within the PETSc framework using a Newton-Krylov-Schwarz method (Cai *et al.*, 1997; Gropp *et al.*, 1998), typically GMRES with an ILU preconditioner (see chapter 1 for details). The software and application are described in detail by Knepley *et al.* (2006). The computational domain is divided into subdomains where different equations for the velocity are solved. A schematic layout is shown in Figure 3-1. Below the slab surface, velocity is prescribed to be equal to the convergence rate resolved into its vertical and horizontal components, according to a prescribed slab dip. The crustal velocity is prescribed to be zero and in the wedge the velocity is the solution of equation (3.1). The depth of the base of the crust is independent of the fault depth, however the fault depth can be no smaller than the crustal thickness. Cells in the wedge that border the fault “see” a velocity of zero across the fault. This would be better implemented with a stress-free boundary condition on the fault (or with a set of weak, visco-plastic cells).

With a full non-Newtonian viscosity, this system is highly ill-conditioned, even singular, unless a very good initial guess at the solution is given. Because vari-

<i>Parameter</i>	<i>Value</i>	<i>Value</i>	
<i>Name</i>	<i>Diffusion Creep</i>	<i>Dislocation Creep</i>	<i>Units</i>
Prefactor, A_0	1.8×10^7	2.9×10^4	Pa sec
Activation energy, E^*	375	530	kJ mol ⁻¹
Activation volume, V^*	5×10^{-3}	14×10^{-6}	m ³ mol ⁻¹
Stress exponent, n	1	3.5	

Table 3.1: Empirically determined parameters for diffusion and dislocation creep (Karato and Wu, 1993; Hirth and Kohlstedt, 2003) used in equation (3.5).

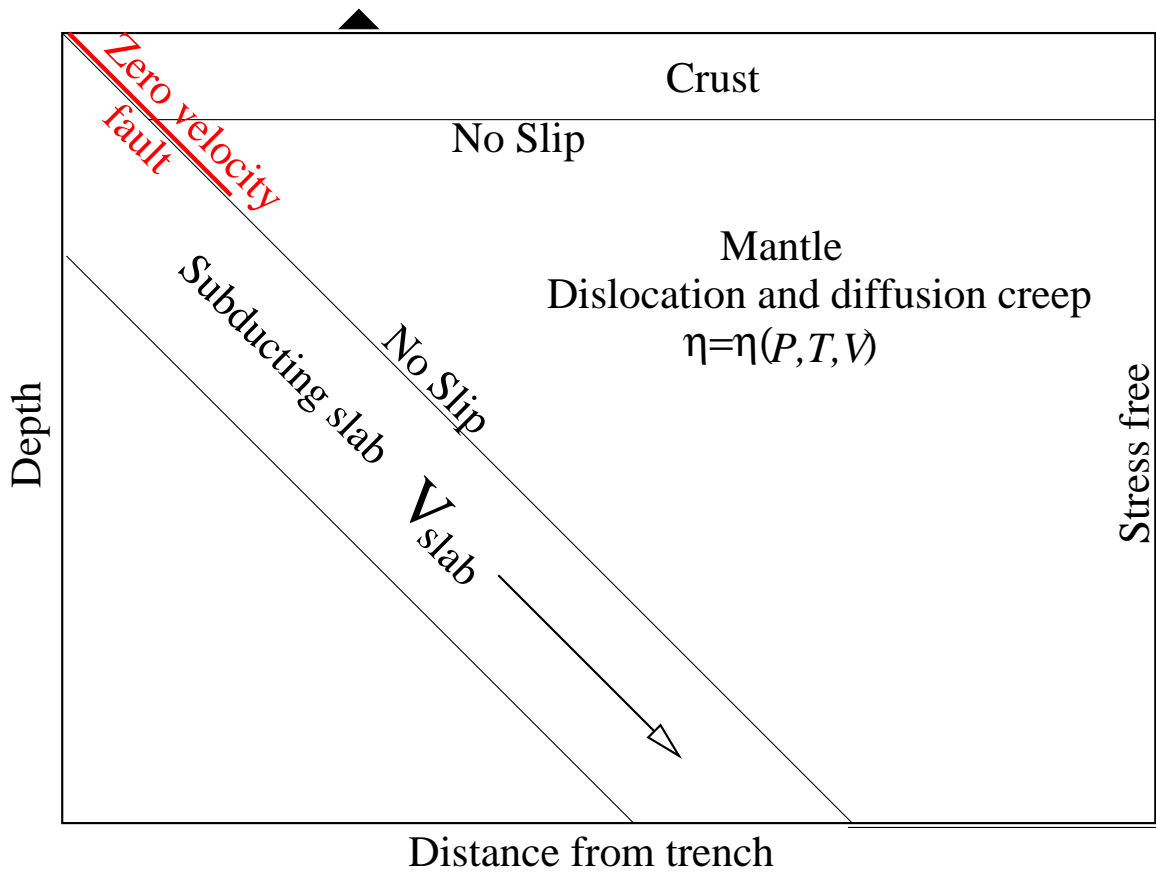


Figure 3-1: A schematic diagram of the computational domain showing the slab, crust and wedge subdomains.

able viscosity solutions are not available analytically we have adopted a continuation method to gradually approach the full variation in viscosity from initially constant viscosity. Specifically, we modify the normalized viscosity

$$\eta \rightarrow \eta^\beta \quad (3.6)$$

where β is the continuation variable and is constrained to fall between zero and one. For each simulation, a full solution is first obtained with $\beta = 0$ (constant viscosity). This solution becomes the initial guess for the next solution step and β is increased by a constant amount. Iteration leads eventually to a solution where $\beta = 1$, which represents full variation of viscosity. If a step fails to converge, β is reduced by a set fraction and the solve is repeated. A typical solution with full viscosity variation requires 10-15 continuation steps, depending on other parameters such as slab dip. This method can be very slow (100-1000 times longer than to obtain the solution for a constant viscosity) but has proved robust.

3.3 Results

A set of representative results from a simulation with full diffusion/dislocation creep viscosity and 45° slab dip is given in Figure 3-2. The viscosity field for this simulation is shown in Figure 3-3. It is evident from Figure 3-2a that the pressure gradients very close to the singularity at the base of the fault are large but that these gradients do not extend far into the wedge. Increased grid resolution would possibly lead to a large negative pressure spike near the singularity but would not resolve any more fine-scale structure. Diffusive cooling of the lithosphere from above produces a thick thermal boundary layer that is too viscous to flow. Slab-wedge coupling, however, drags the mantle constantly downward from the wedge corner and requires a counterflow from the wedge to satisfy incompressibility. This flow is constrained by the lithosphere above and the slab below and is hence highly localized relative to isoviscous corner flow, as is evident in Figures 3-2c-d and 3-4a-c. Furthermore, the counterflow has a

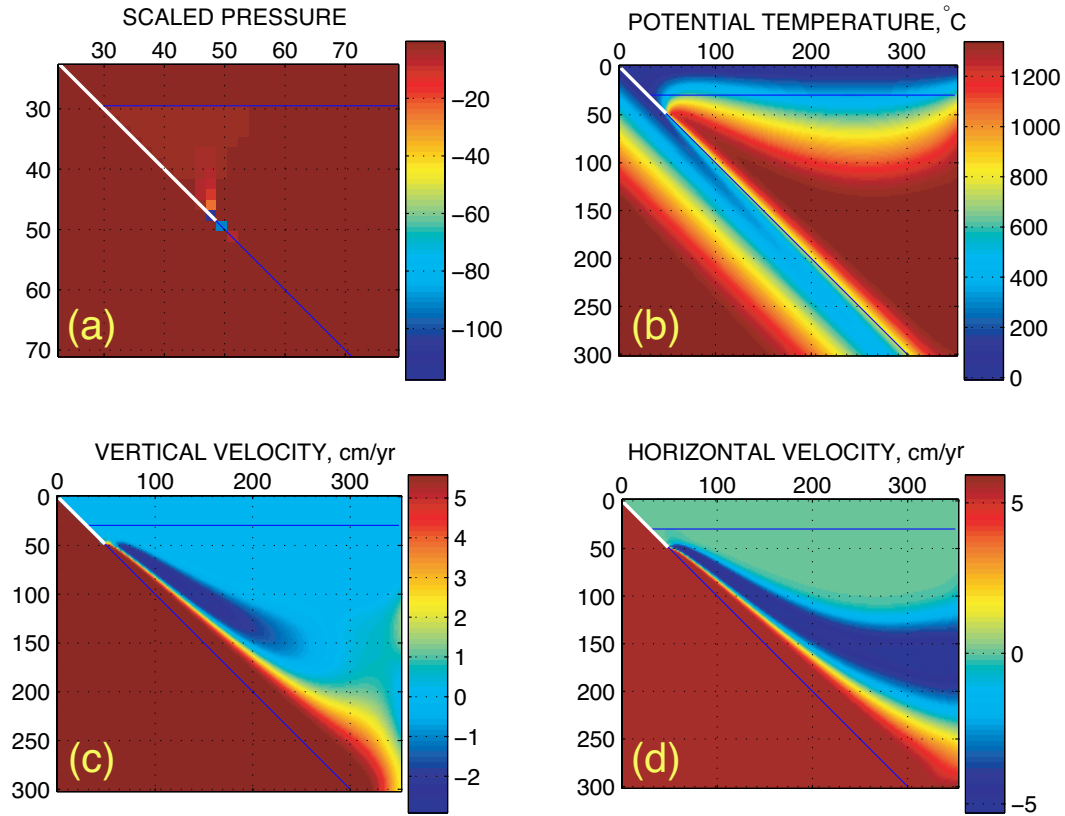


Figure 3-2: Representative results from the numerical solution of equations with full diffusion/dislocation creep viscosity, slab dip of 45° , convergence rate of 8 cm/year, crustal thickness of 35 km and a fault depth of 50 km. Depths and distance from the trench are given in km on the y and x axes respectively. The domain is 350 km wide by 300 km deep and the resolution is < 2 km in both directions. The viscosity field is shown in Figure 3-3. **(a)** Dimensionless pressure. Note that this panel is on a different scale than the others; The pressures are large and non-zero only very close to the base of the fault. **(b)** Potential temperature in degrees centigrade. Note the relatively high temperatures near the wedge corner. **(c)** Vertical component of the velocity field in cm/yr. Note the strong upwelling toward the wedge corner. **(d)** Horizontal velocity in cm/yr.

strong vertical component with important implications for adiabatic melt generation.

As shown in Figure 3-4, the temperature field difference between isoviscous flow and pressure/temperature dependent flow is much greater than the difference between temperature/pressure dependent flow and *non-Newtonian* temperature/pressure dependent flow. Isoviscous models allow cold mantle to flow as readily as hot mantle resulting in advection of colder rock along the base of the crust, into the corner and onto the slab surface. Giving viscosity a temperature dependence prevents this by requiring the thermal lithosphere to be resistant to flow. The stress dependence of viscosity actually lowers the temperature of the nose of the wedge because it allows for reduced viscosity of cold, high-stress lithosphere, making it possible to advect some colder rock into the wedge corner.

Inspection of the flow fields in Figure 3-2c–d reveals that the strong counterflow is directed toward the bottom of the fault where the slab-wedge interface is fully coupled. The depth of this point, the base of the interplate fault, is a critical and poorly constrained parameter in these simulations. *Conder* (2005) makes a case for assigning its position dynamically based on a yield stress criterion. The depth of the fault controls the distance to the surface to which hot mantle solid will penetrate. Besides the obvious effects on surface heat flow, hot shallow mantle will tend to melt extensively and this would contribute to the magma budget of the arc. Seismicity on the plate interface extends to about 35 km in most arcs and this depth provides a lower bound on the slab-mantle coupling depth. Water release from the slab could hydrate the mantle at the slab–wedge interface and cause the formation of a narrow, fault-like shear zone that would aseismically extend the fault deeper into the mantle. Such an extension of the fault would reduce the advection of cold mantle rock out of the nose of wedge and hence stabilize the fault’s depth extent.

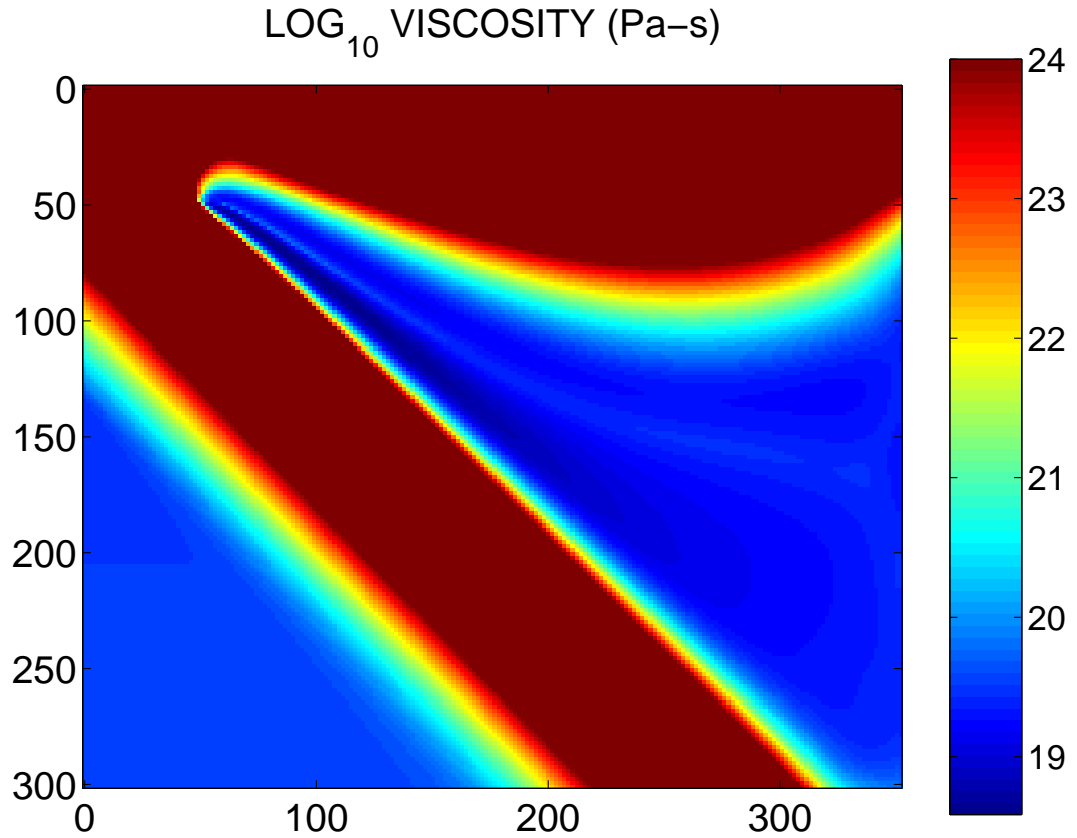


Figure 3-3: The \log_{10} of viscosity field from the same simulation as shown in Figure 3-2. Depths and distance from the trench are given in km on the y and x axes respectively. The effect of the stress dependence of viscosity can be seen most clearly in the diagonal band of dark blue sub-parallel to the slab where mantle shear is strongest.

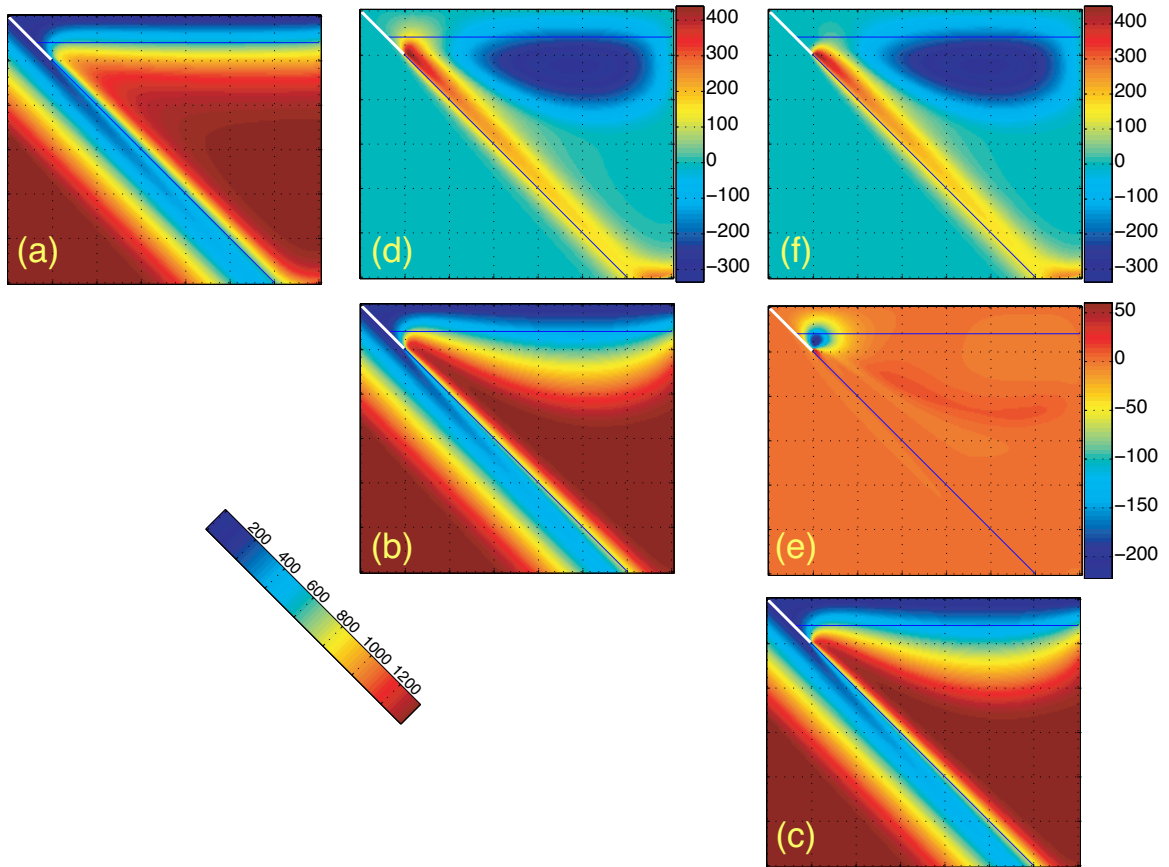


Figure 3-4: A comparison of temperature fields from simulations with **(a)** isoviscous, **(b)** diffusion creep and **(c)** combined dislocation/diffusion creep viscosity. Panel **(d)** shows the temperature field in panel (b), T_b , minus the temperature field in panel (a), T_a . Panel **(e)** shows $T_c - T_b$. Panel **(f)** shows $T_c - T_a$. Panels (a)–(c) share a single (diagonal) color bar. Note the large temperature differences above the slab between variable viscosity and constant viscosity simulations in panels (d) and (f). Variable viscosity flow prevents cold mantle from being advected around the wedge corner and onto the surface of the slab. Panel (e) shows a significant difference between Newtonian and non-Newtonian viscosity for temperatures in the wedge corner with colder temperatures for the non-Newtonian case. This results from strain rate-weakening flow of colder mantle.

3.4 Discussion

3.4.1 Magma genesis in subduction zones

There are three general, independent mechanisms for the generation of molten rock in subduction zones: reactive hydrous melting of the mantle, adiabatic decompression melting of the mantle, and hydrous melting of the downwelling slab’s crust and/or sediments. While the calculations described in this chapter do not explicitly predict melting by any of these mechanisms, thermal structure and mantle flow form the context for all melting that occurs in a subduction zones. Hence the simulations described in this chapter can be interpreted in terms of the constraints that they place on melting (or lack thereof).

Hydrous reactive mantle melting. Hydrous reactive melting of mantle rock is generally expected to be the major source of arc volcanic material. Arc magmas show a range of volatile contents, from considerably higher than MORB and OIB (e.g. $\gtrsim 3\text{wt}\%$ H_2O in primitive arc basalts) (e.g. *Gill*, 1981; *Stolper and Newman*, 1994; *Sisson and Layne*, 1993; *Sobolev and Chaussidon*, 1996; *Plank et al.*, 2004) down to near anhydrous concentrations in some primitive arc basalts (e.g. *Sisson and Bronto*, 1998). This water in arc lavas is carried to depth by hydrous minerals in the subducting slab and released as a silicate rich fluid in metamorphic reactions (*Schmidt and Poli*, 1998; *Forneris and Holloway*, 2003; *Manning*, 2004). As the fluid rises through the mantle it experiences increasing temperature and decreasing pressure with height and hence a rapid increase in the solubility of silicate components leading to “dissolution” of the mantle matrix by the fluid. *Katz and Spiegelman* (2004) showed that this process leads to channelized flux of hydrous magma in a model of hydrous reactive melt transport. While this process requires only an inverted thermal gradient above the slab (which is present in all thermal structure models), the details of fluid reaction distribution and melt flow trajectories will depend heavily on the thermal structure. The details of this process are considered in chapter 5.

Adiabatic decompression mantle melting. Anhydrous lavas are found among volcanics at some subduction zones; these lavas appear to be the product of decompression melting, much like mid-ocean ridge lavas. *Sisson and Bronto* (1998) showed an example of this from Galunggung, Indonesia. *Kelley et al.* (2004) later showed that the lavas from this region form two groups with respect to water content, one clearly the product of hydrous melting and the other nominally anhydrous. Flow simulations described here and elsewhere (e.g. *van Keken et al.*, 2002; *Kelemen et al.*, 2002; *Conder et al.*, 2002b) demonstrate that passive upwelling of mantle flow is a robust prediction of calculations with temperature dependent viscosity. Calculations by *Gerya and Yuen* (2003) have shown that active upwelling due to compositional buoyancy may produce decompression melts however these melts are unlikely to have the composition of MORB because dry mantle peridotite is not compositionally buoyant.

Slab melting. Slab melting has long been invoked by petrologists to explain the geochemical signature of arc volcanic rocks called Adakites (*Kay*, 1978; *Kelemen et al.*, 1990; *Kay et al.*, 1993; *Martin et al.*, 2005). The debate on whether slab melting occurs today has focused on whether kinematic simulations of arc thermal structure can produce slab-surface temperatures hot enough for slab melting (*Peacock*, 1990). While isoviscous models typically have slabs that are too cold to melt, *Kelemen et al.* (2002) showed that slab surface temperatures in a model with temperature dependent viscosity are significantly hotter and may be high enough to cause melting. This work also considered thermal constraints provided by heat flow and observed metamorphic facies and concluded that they are inconsistent with isoviscous models but agree with variable viscosity simulations. While the addition of stress dependence of viscosity from the dislocation creep mechanism may cool the corner relative to diffusion creep viscosity, the slab surface remains at about the same temperature, as shown in Figure 3-4e. A comparison of slab surface temperatures from simulations presented here is given in Figure 3-5. These curves show hotter temperatures than the those calculated by *Kelemen et al.* (2002) although they are similar to curves obtained by *van Keken et al.* (2002). In fact, curves representing variable viscosity simulations cross the

fluid-saturated basalt solidi given by *Kelemen et al.* (2002) at about 3.5 GPa. These simulations indicate that slab melting may contribute to magma genesis in arcs.

3.4.2 Magma focusing in subduction zones

Spiegelman and McKenzie (1987) investigated pressure gradients caused by isoviscous corner flow as a mechanism for melt focusing in arcs and ridges. For fluid flow to deviate from vertical percolation driven by buoyancy, horizontal pressure gradients must be approximately equal to or greater than buoyancy. As *Spiegelman and McKenzie* (1987) showed, for reasonable mantle porosities and crustal production rates, viscosities of $\sim 10^{21}$ are required in an isoviscous corner-flow model. Variable viscosity models described here (see Figure 3-3) demonstrate that experimentally constrained viscosities may be much lower than this in the mantle wedge beneath subduction zones. *Sparks and Parmentier* (1991) argued that these low viscosities would reduce pressure gradient forces well below the level of the buoyancy force acting on the melt and hence preclude pressure-driven focusing of melt into the wedge corner.

The results of fluid flow calculations similar to that of *Spiegelman and McKenzie* (1987) are shown by streamlines in Figure 3-6. Not surprisingly, constant 10^{21} Pa-s viscosity corner-flow (panels a and b) has significant flow focusing. The fluid flow lines in a simulation with combined diffusion/dislocation creep viscosity (panels e and f) are vertical where viscosities are low, except in the wedge corner above the the interplate fault. Here strain is very large and produces strong pressure gradients. This is different from the case where viscosity is temperature and pressure dependent only, shown in Figure 3-6c-d. Here viscosity is higher in the mantle wedge, coupling stress more efficiently between the slab and the lithosphere and driving a broader convergence of melt streamlines. Small amounts of deformation in the cold lithosphere and in the layer of cold mantle accreted to the slab surface produce strong pressure gradients that draw in fluid in horizontally from a large region of the wedge. It is interesting to note that although the viscosity fields of diffusion and combined diffusion-dislocation creep are nearly identical, there is a large difference in the fluid flow fields in each case, predicted by this model. All else being equal (or nearly so),

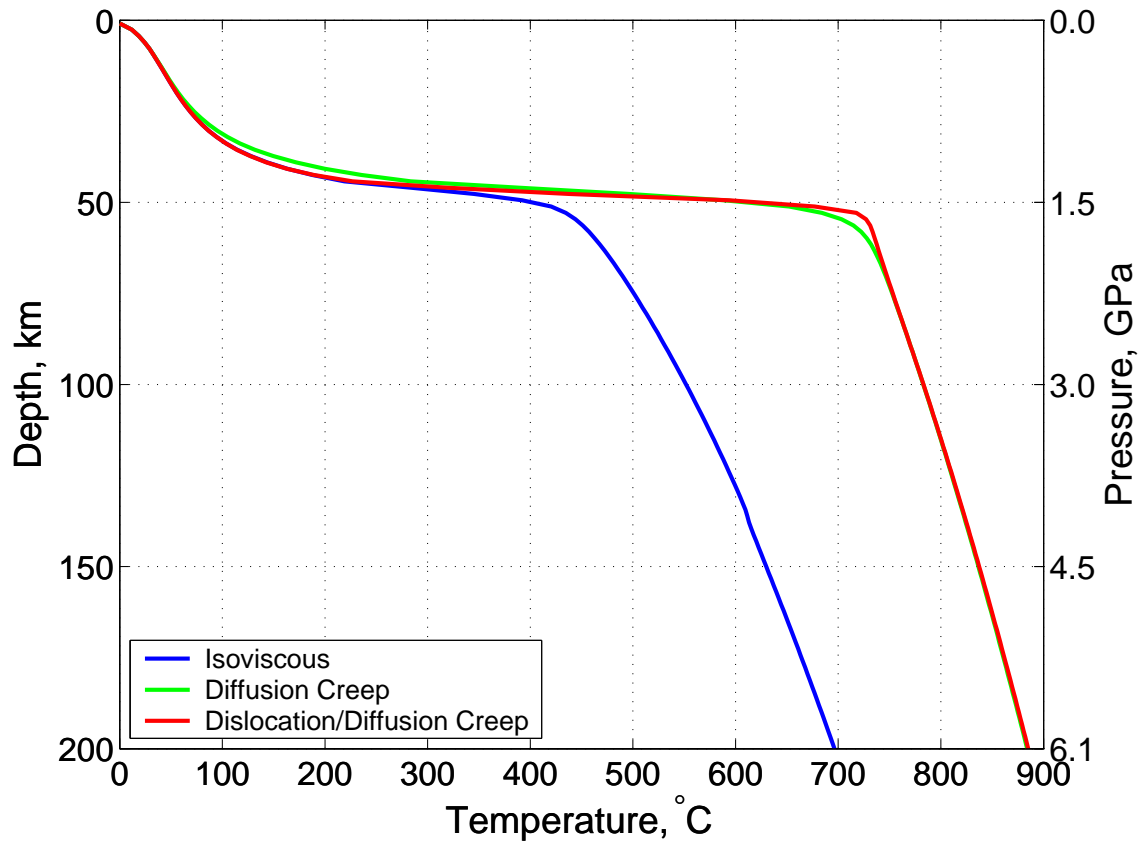


Figure 3-5: Slab surface temperature profiles for simulations shown in Figure 3-4a–c. These simulations all have a mantle potential temperature of 1300° C. The isoviscous flow model produces a slab surface temperature that is much lower than that of Newtonian and non-Newtonian temperature dependent viscosities.

fluid flow paths or distribution might provide a diagnostic for the style of deformation active in subduction zones.

The strongly sloping thermal boundary at the base of the lithosphere in subduction zone calculations may provide another means for focusing magma toward the corner. *Sparks and Parmentier* (1991) proposed a focusing mechanism for ridges in which rising magma encounters a permeability barrier at the base of the lithosphere where colder temperatures cause freezing and the reduction of porosity. They show that melt migration along this sloping boundary layer is directed toward the ridge and delivers sufficient melt to account for the observed crustal thickness. *Spiegelman* (1993a), *Magde and Sparks* (1997) and *Ghods and Arkani-Hamed* (2000) later confirmed these results in two and three dimensions although they also showed that the process is less efficient than previously assumed. The same mechanism may affect the trajectory of magma as it rises through the mantle beneath an arc. One question this raises is whether the magma would rise all the way to the hot nose of the wedge or whether it would traverse the cold boundary later at some point “downslope” from the nose.

Arc magmatism is localized in a volcanic front that is invariably 120 ± 40 km above the earthquakes in the slab (e.g. *Gill*, 1981; *Tatsumi*, 1986; *Jarrard*, 1986). Recent work by *England et al.* (2004) suggests that the depth to earthquakes is anti-correlated with slab convergence rate and dip-angle, but otherwise insensitive to most subduction parameters. This trend is consistent with thermal calculations where the penetration of the nose of hot mantle rock into the wedge corner increases with increasing convergence rate and slab dip (*England and Wilkins*, 2000). A comparison of two possible indicators of volcano position with data from *England et al.* (2004) is shown in Figure 3-7. Both of these, the position of the maximum degree of melting¹ F_{max} and the position of the “nose” of the 1225°C isotherm, vary with convergence rate (and slab dip) in the same way according to simulations. Hence it is possible that neither, one or both contribute to determining the depth of the slab beneath the volcanic arc. The important point here is that the observations by *England et al.*

¹The maximum degree of melting is computed by using the parameterization described in chapter 4 and assuming a constant bulk water content of 0.01 over the whole domain.

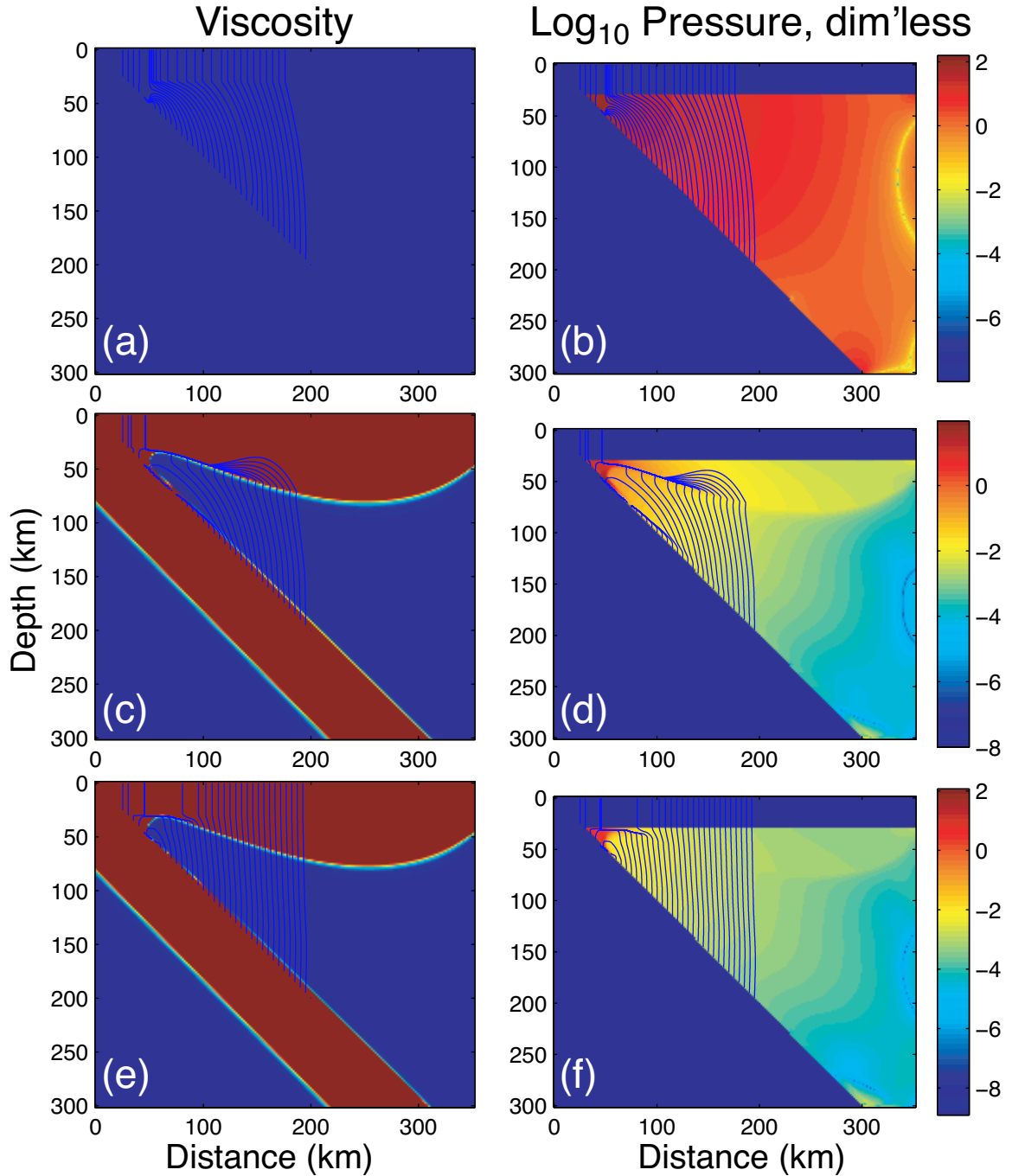


Figure 3-6: Simplified estimates of fluid flow in subduction zones. Following *Spiegelman and McKenzie* (1987), these calculations assume constant and uniform porosity and no melting and the following parameter values: $\phi = 0.01$, $\mu = 10^2$ Pa-s, $k_0 = 10^{-11}$ m², Blake-Kozeny-Carmen exponent $n = 2$ and $\Delta\rho = 500$ kg/m³. Together these parameters give a ratio of buoyancy-driven fluid velocity to slab-driven solid velocity, w_0/U_0 , of approximately 20 (although results are qualitatively similar for $10^{-12} \leq k_0 \leq 10^{-10}$). The left column shows the viscosity field and the right column shows the base-10 logarithm of the dimensionless pressure. Fluid flow streamlines are shown in blue. Fluid upwelling far from the pressure gradients of the wedge corner rises at about 15 cm/yr. **(a)-(b)** Isoviscous 10^{21} Pa-s solid flow and corresponding fluid flow. **(c)-(d)** Diffusion (T and P dependent) creep viscosity solid flow. **(e)-(f)** Full diffusion/dislocation creep viscosity.

(2004) are consistent with predictions from variable viscosity simulation of arc thermal structure.

3.5 Conclusions

A kinematic solid flow and thermal structure simulation is a critical component in any model of magma genesis and transport in subduction zones because it forms the context in which melting occurs. Recent work by *Kelemen et al.* (2002) has demonstrated the deficiencies associated with isoviscous models and has emphasized the importance of employing a viscosity that is at least temperature dependent. The simulations presented here use temperature, pressure and stress dependent viscosity that approximates the empirically derived flow laws for diffusion and dislocation creep of olivine. We show, however, that the difference in thermal structure between a Newtonian temperature dependent viscosity and a non-Newtonian one is small relative to the difference between isoviscous and variable viscosity simulations. The computational cost for non-Newtonian viscosity is at least a factor of five (more in some cases) greater than for Newtonian viscosity. On the other hand, calculations of melt flow in response to pressure gradients in this chapter and in chapter 2 show that melt organization is strongly dependent on the stress exponent of solid viscosity.

Simulations described here are consistent with the presence of three mechanisms of melting beneath arcs. Hydrous reactive melting is plausible in all solid flow and thermal structure models of subduction zones. Decompression melting and slab/sediment melting, however, depend on features of the simulations that are not present in isoviscous models. Variable viscosity simulations predict the presence of significant upwelling in sub-arc mantle flow and slab surface temperatures that cross the hydrous basalt solidus. Explicit melting and melt transport calculations are needed to resolve the contributions of each of these three melting mechanisms.

It remains a challenge to model both the slab-driven solid flow field and a consistent reactive fluid flow field simultaneously. With the added complexity of porosity dependent viscosity and reactive localization instabilities in the physics of porous

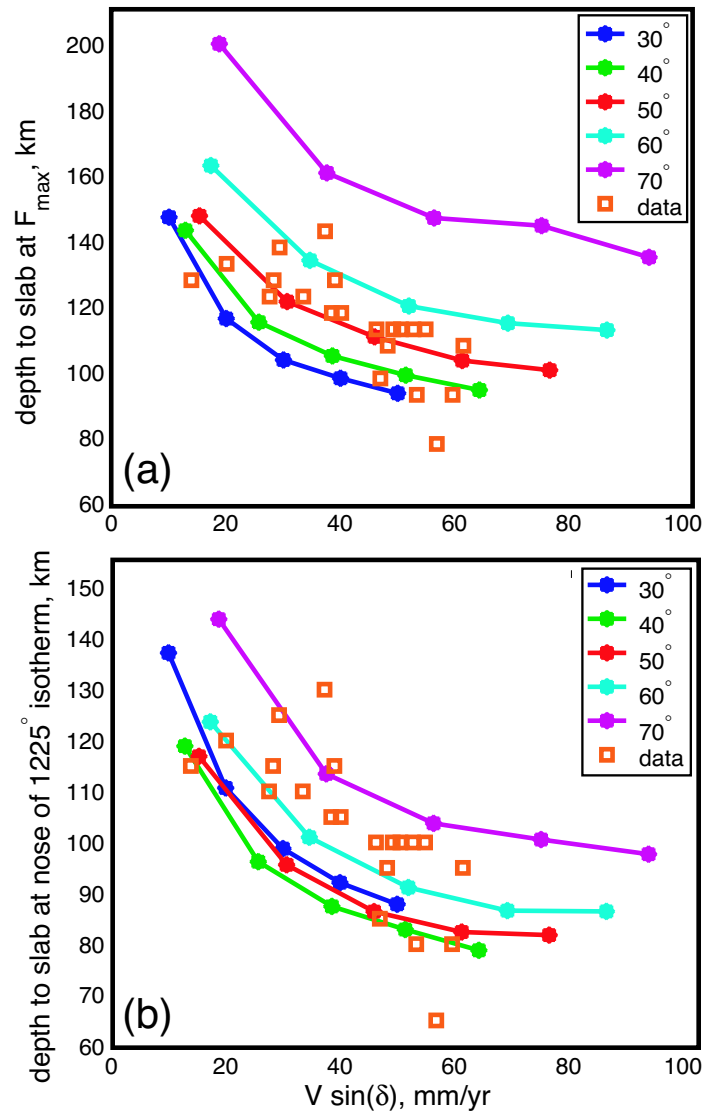


Figure 3-7: A comparison of two possible proxies for volcano position derived from numerical simulations with data from *England et al.* (2004). **(a)** Depth from the volcanic arc to the slab assuming that the arc is directly above the location of the maximum degree of melting, F_{max} . F_{max} is computed using the parameterization described in chapter 4 assuming a constant bulk water content everywhere in the domain. **(b)** Depth from the volcanic arc to the slab assuming that the arc is directly above the “nose” of the 1225°C isotherm. The nose is the point on the isotherm with the shortest horizontal distance to the trench. Its position may provide a proxy for the limit to lateral melt transport toward the wedge corner.

magmatic flow, such models will require significant computational power as well as grid and solver technologies more advanced than those used here. Nonetheless, these simulations will have solid flow field and thermal structure calculations at their core.

Chapter 4

A New Parameterization of Hydrous Mantle Melting

Richard F. Katz, Marc Spiegelman and Charles Langmuir

Geochem. Geophys. Geosyst. 4(9):1073, 2003

Copyright by the American Geophysical Union

Abstract

Modeling of melt formation and transport in all tectonic settings requires the inclusion of water, since water has large effects on mantle solidi as well as physical properties of liquids. To facilitate the inclusion of water in melting models this paper presents a new parameterization for melt fraction as a function of pressure, temperature, water content and modal cpx, based on knowledge gained from recent advances in the fields of thermodynamic modeling as well as experimental investigations of peridotite melting and hydrous equilibria. The parameterization is computationally efficient and can be modified easily as better experimental data become available. We compare it to other published parameterizations and test it in simple calculations of adiabatic decompression melting (mid-ocean ridge) and hydrous melting (subduction zone).

4.1 Introduction

Magma genesis and transport in subduction zones influence large scale chemical cycling in the mantle and provide the crucial link between mantle dynamics and geochemical signals observed in island arcs. Nevertheless, many aspects of these processes are still poorly understood. The challenge remains to integrate theory, experiment and observation into a consistent framework that permits inferences on subduction zone chemistry and dynamics from available observations. Quantitative models of

subduction zones provide such a framework. To consistently model both solid and fluid/melt processes, however, requires an accurate and computationally efficient parameterization of mantle melting that includes the effects of significant amounts of water. We present here a new parameterization that, while remaining mathematically simple, succeeds in capturing the important features of the behavior of this complex thermodynamic system.

While a full thermodynamically consistent treatment of melting might be preferred, current equilibrium thermodynamic models such as MELTS and pMELTS (*Ghiorso, 1994; Ghiorso and Sack, 1995; Ghiorso et al., 2002; Asimow and Stolper, 1999*) remain too computationally expensive for large time-dependent 2-D calculations (although see *Tirone and Ganguly, 2002*) that are necessary to create quantitative models applicable to ridges and convergent margins. Furthermore, these models do not cover the full range of pressure, temperature and composition conditions relevant to subduction zones. Thus melting parameterizations are a useful way to incorporate melting into tectonic models, and these parameterizations also have the advantage that they often better reproduce existing experimental data.

Thermodynamic constraints on such models, however, are also important. As we show, current experimental data for wet melting is sparse and experimental data for dry melting shows a large amount of scatter, even on nominally identical samples (see also *Hirschmann (2000)*). In order to make progress, here we take an approach that incorporates many of the theoretical concepts from thermodynamic models and also calibrates them against the current experimental database.

Other workers have produced various parameterizations (*McKenzie and Bickle, 1988; Davies and Bickle, 1991; Langmuir et al., 1992; Kinzler and Grove, 1992; Jha et al., 1994; Iwamori et al., 1995; Iwamori, 1997; Kinzler, 1997*); the discussion below presents a comparison of the different models. Overall, many of the parameterizations are qualitatively similar to each other with different biases in different parts of parameter space. Further progress in refining parametric melting functions will require either additional experiments or concerted efforts to better quantify the uncertainty in the experimental database.

4.1.1 Basic structure of the parameterization

Our parameterization is of the form $F = f(P, T, X_{\text{H}_2\text{O}}, M_{\text{cpx}})$ where F is the weight fraction of melt present, P is the pressure in GPa, T is the temperature in degrees Celsius, $X_{\text{H}_2\text{O}}$ is weight fraction of water dissolved in the melt and M_{cpx} is the modal cpx of the unmelted (or residual) peridotite. This parameterization incorporates the following concepts and principles:

1. The isobaric melting function, F should be monotonically increasing, concave upward, with isobaric productivity, $\partial F / \partial T|_{P, X_{\text{H}_2\text{O}}}$ increasing as a function of T (*Hirschmann et al.*, 1999), as long as the phase assemblage remains constant. We utilize this constraint despite the fact that existing experimental data do not clearly show the effect.
2. $F(T)$ should be kinked when major phases are exhausted from the residue, such as when $F = F_{\text{cpx-out}}$. In other words, productivity should decrease discontinuously at this point and then rise as it did for melting in the low- F regime (*Hirschmann et al.*, 1999).
3. For a peridotite with fertile mineral compositions, the melt reaction coefficient of cpx is a function of pressure only. Thus, $F_{\text{cpx-out}}$ can be predicted given the modal cpx of the peridotite being melted and the pressure of melting. (*Pickering-Witter and Johnston*, 2000; *Longhi*, 2002; *Walter*, 1998; *Walter et al.*, 1995)
4. Addition of water to a peridotite system should monotonically increase F at constant T and P . $F(X_{\text{H}_2\text{O}})$ at constant temperature and pressure should be an approximately linear increasing function for small $X_{\text{H}_2\text{O}}^{\text{bulk}}$. Furthermore, the slope should increase with increasing temperature, (*Hirschmann et al.*, 1999; *Hirose and Kawamoto*, 1995; *Hirose*, 1997; *Gaetani and Grove*, 1998)

$$\left. \frac{\partial F}{\partial X_{\text{H}_2\text{O}}^{\text{bulk}}} \right|_{P, T} = c(T), \quad c > 0. \quad (4.1)$$

5. Addition of water to a peridotite system should lower the solidus (except at atmospheric pressure) in proportion to $X_{\text{H}_2\text{O}}$. This seems to be uniform with P (*Burnham, 1979*). It should also lower the liquidus of the solid. However, for melt fractions near one and modest bulk water content, the weight percent dissolved water at the liquidus is small because it is diluted by silicate melt. Thus the liquidus is not lowered substantially, except by extreme water contents.
6. Assuming, after *Michael (1995)* and *Asimow and Langmuir (2003)*, that water may be treated as an incompatible element, addition of water to the system depresses the solidus until the melt becomes saturated. Of course the amount of water at saturation is strongly dependent on pressure. Because the amount of water in the liquid decreases progressively as melting proceeds, the influence of water progressively decreases, and hence productivity above the wet solidus remains low until a temperature near the dry solidus is reached (*Hirth and Kohlstedt, 1996; Hirschmann et al., 1999*).
7. Experiments show that $X_{\text{H}_2\text{O}}^{\text{sat}}^{\text{aturated}}$ is zero at atmospheric pressure, about 13 wt% at 1 GPa and continues to rise with increasing pressure. (*Dixon et al., 1995; Mysen and Wheeler, 2000*)

4.2 Mathematical Formulation

4.2.1 Anhydrous Melting

F_{cpx} is the degree of melting expected by equilibrium batch melting prior to the exhaustion of cpx. We parameterize it as a power-law of the rescaled temperature T' .

$$F_{\text{cpx}}(T') = [T'(T, P)]^{\beta_1}, \quad (4.2)$$

where

$$T'(T, P) = \frac{T - T_{solidus}(P)}{T_{liquidus}^{lherz}(P) - T_{solidus}(P)}. \quad (4.3)$$

is the fractional distance in temperature between the solidus and “lherzolite liquidus” (defined below). Here T is the temperature in Kelvin and the pressure dependence is hidden in $T_{solidus}$ and $T_{liquidus}^{lherz}$. Using the form suggested by *Hirschmann* (2000),

$$T_{solidus} = A_1 + A_2P + A_3P^2, \quad (4.4)$$

$$T_{liquidus}^{lherz} = B_1 + B_2P + B_3P^2, \quad (4.5)$$

for pressure in GPa (figure 4-1). The “lherzolite liquidus,” $T_{liquidus}^{lherz}$, in Eq. (4.2) is introduced as a means for creating a kinked melting function. It can be conceptualized as the temperature that the liquidus would have if melting continued according to Eq. (4.2) to $F = 1$, *i.e.* with cpx remaining in the residue. Cpx-out occurs at some $F < 1$, and at this point there is a discontinuous change in the productivity of the system. For simplicity, we do not consider the effect on melt productivity of the exhaustion of the aluminous phase, although *Walter* (1998) has shown that the exhaustion of garnet occurs before the exhaustion of cpx at pressures between 2 and 4 GPa. Furthermore, we ignore the loss of opx from the residue as this typically occurs at melt fractions beyond what we expect in an arc setting (thus we do not define a “hartzburgite liquidus”). For a closed (batch) system,

$$F_{cpx-out} = \frac{M_{cpx}}{R_{cpx}(P)}. \quad (4.6)$$

M_{cpx} is the weight fraction of cpx in the solid peridotite being isobarically melted. R_{cpx} is the reaction coefficient for cpx in the melting reaction. Following experimental results of *Longhi* (2002), *Walter* (1998), *Walter et al.* (1995) and *Pickering-Witter and Johnston* (2000), we give this reaction coefficient a pressure dependence of the form

$$R_{cpx}(P) = r_0 + r_1P. \quad (4.7)$$

There is evidence from *Walter (1998)* and *Kelemen et al. (1992)* that R_{cpx} reaches a maximum at about 3.5 GPa and decreases at higher pressures (in the garnet stability field). For simplicity, we neglect this effect but it may need to be reconsidered for applications where significant melting occurs at pressures greater than 3.5 GPa.

For $F > F_{cpx-out}$, the melting reaction changes to consume mostly opx and the melting function is:

$$F_{opx}(T) = F_{cpx-out} + (1 - F_{cpx-out}) \left[\frac{T - T_{cpx-out}}{T_{liquidus} - T_{cpx-out}} \right]^{\beta_2}, \quad (4.8)$$

where

$$T_{cpx-out} = F_{cpx-out}^{\frac{1}{\beta_1}} (T_{liquidus}^{lherz} - T_{solidus}) + T_{solidus} \quad (4.9)$$

and $T_{liquidus}$ is the true liquidus of the model peridotite system (Figure 4-1),

$$T_{liquidus} = C_1 + C_2P + C_3P^2. \quad (4.10)$$

The shape of the overall melting function at different pressures is shown in Figure 4-2. As mentioned in the introduction, $\partial^2 F / \partial T^2|_{P, X_{H_2O}} > 0$ for the isobaric melting curves and they are kinked at cpx out. The pressure dependence of R_{cpx} is evident in the melt fraction at which cpx is exhausted from the residue.

4.2.2 Hydrous Melting Extension

This parameterization of dry melting can be extended to include systems where the dissolved water fraction in the melt in weight fraction, X_{H_2O} , is specified (the weight fraction of *bulk* water is written as $X_{H_2O}^{bulk}$). Specifically, the changes are the following:

$$T_{solidus}(P) \rightarrow T_{solidus}(P) - \Delta T(X_{H_2O}) \quad (4.11)$$

$$T_{liquidus}^{lherz}(P) \rightarrow T_{liquidus}^{lherz}(P) - \Delta T(X_{H_2O}) \quad (4.12)$$

$$T_{liquidus}(P) \rightarrow T_{liquidus}(P) - \Delta T(X_{H_2O}) \quad (4.13)$$

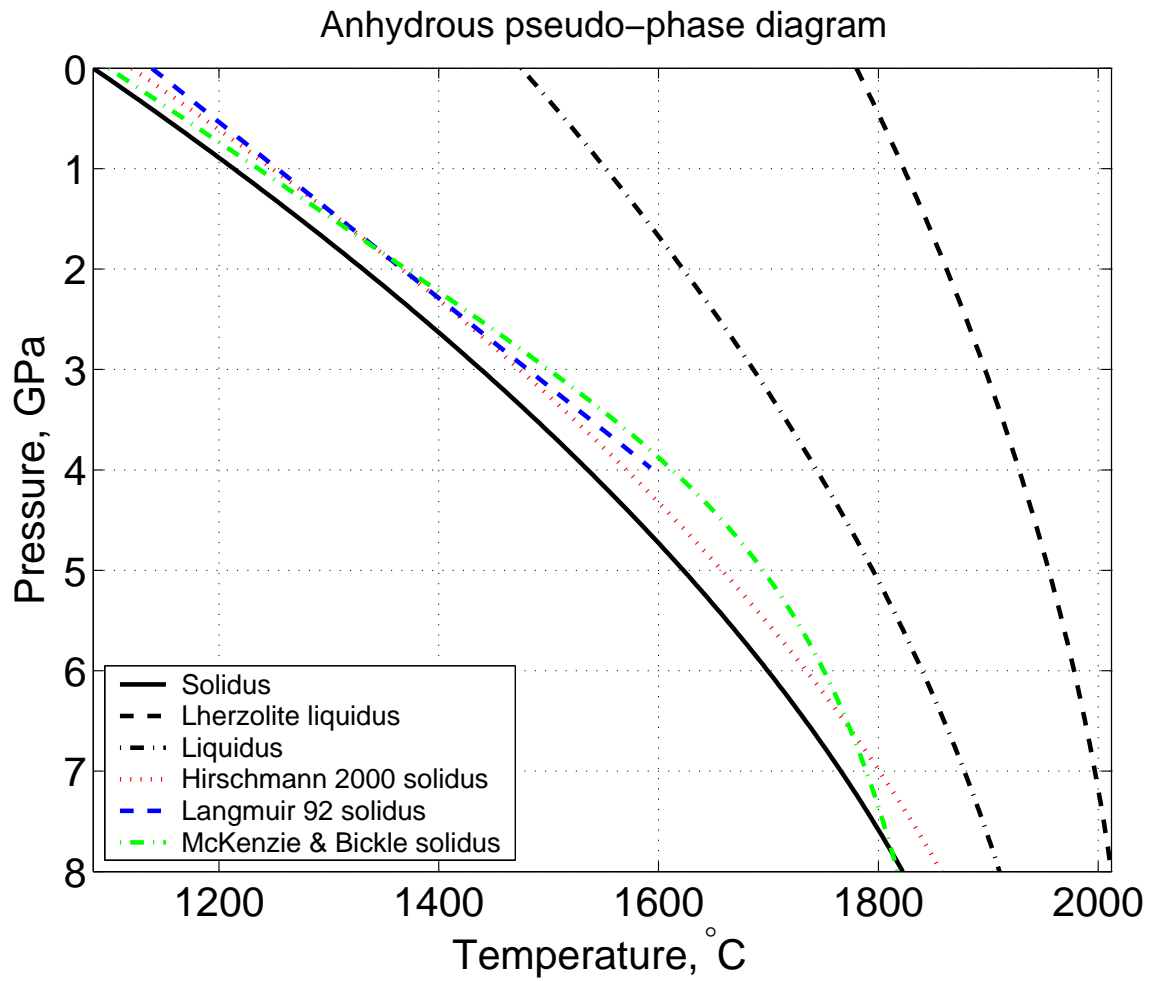


Figure 4-1: The anhydrous solidus, lherzolite liquidus (see text) and liquidus. Also shown, for comparison, the anhydrous solidi of *Hirschmann* (2000), *Langmuir et al.* (1992) and *McKenzie and Bickle* (1988).

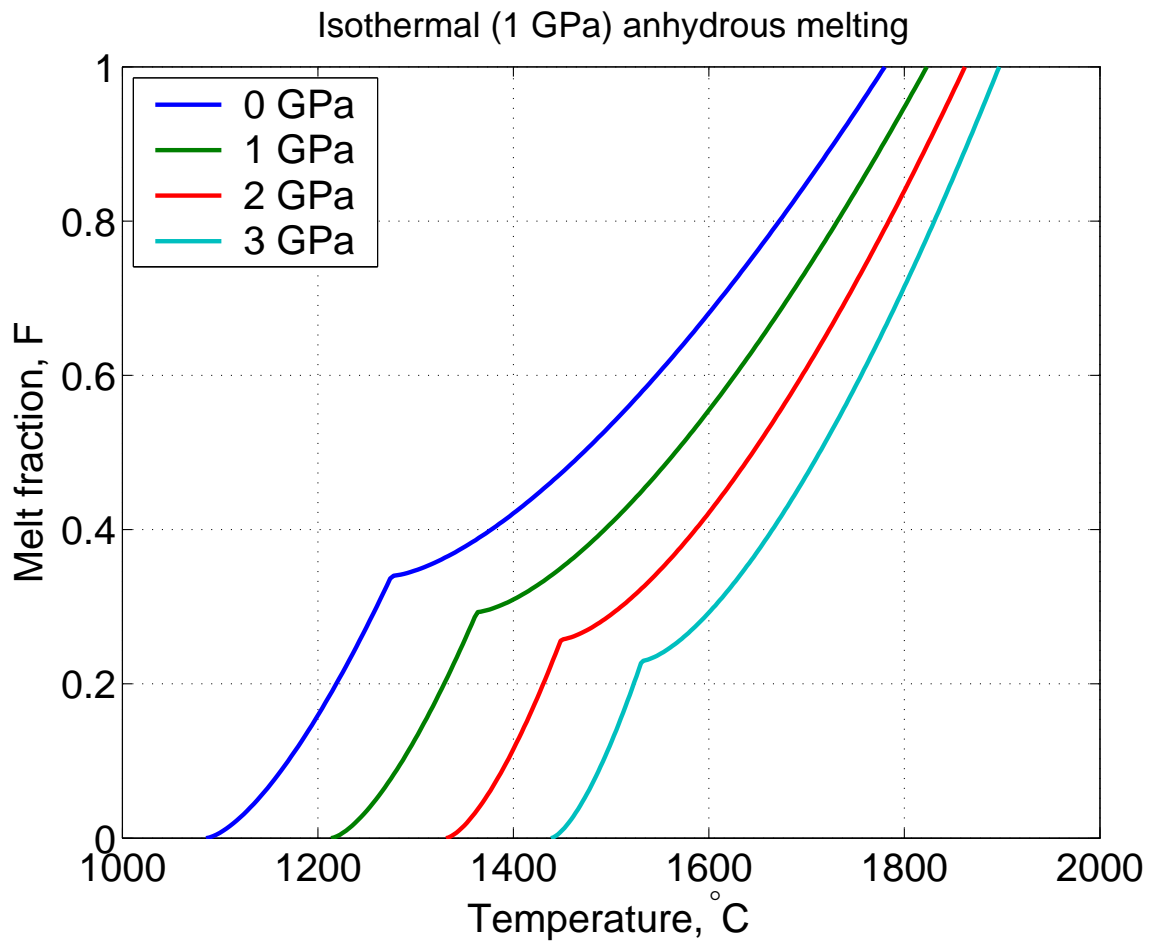


Figure 4-2: Isobaric anhydrous melting curves at different pressures with modal cpx of the unmelted rock at 15 wt%. For a comparison of these calculations to data, see Figure 4-6.

where $\Delta T(X_{\text{H}_2\text{O}})$ is the temperature decrease in the solidus caused by a water content $X_{\text{H}_2\text{O}}$ in the melt. This function, the same for the liquidus, lherzolite liquidus and solidus, may take a variety of forms as long as they satisfy:

$$\Delta T(X_{\text{H}_2\text{O}} = 0) = 0, \quad (4.14)$$

$$\Delta T(X_{\text{H}_2\text{O}} \geq X_{\text{H}_2\text{O}}^{\text{sat}}) = \Delta T(X_{\text{H}_2\text{O}}^{\text{sat}}). \quad (4.15)$$

where $X_{\text{H}_2\text{O}}^{\text{sat}}(P)$ is the weight percent of water in a completely saturated melt, which is principally a function of pressure. The criterion stated in equation (4.15) is necessary because of the way that we handle a free vapor phase. For computational simplicity, water present beyond the saturation of the melt is not computed as a separate vapor phase, it is accounted for as a part of the fluid phase which also includes the saturated silicate melt. The thermodynamic properties (*e.g.* liquidus) of the silicate melt are unaffected by water content beyond saturation. The utility of this simplification is that it permits the use of a standard two-phase fluid mechanical formulation for melt transport *McKenzie* (1984); *Spiegelman* (1993a).

The speciation of water dissolved in silicate melt has been a subject of debate (for a summary and references, see *Withers et al.* (1999)). *Stolper* (1989) and *Ihinger et al.* (1999) have reported that at temperatures near the water saturated rhyolite solidus, the first 1-2 wt% water dissolved into the melt exists mostly as hydroxyl ions (although see *Mosenfelder et al.* (2002)). For higher dissolved water contents, molecular water becomes the dominant species, however, increasing temperature diminishes the proportion of molecular water. The depolymerizing effect of hydroxyl ions on silicate melt exceeds that of molecular water because of its non-zero charge; depolymerization of the melt increases its entropy, stabilizing it at lower temperatures. Thus we choose a form for $\Delta T(X_{\text{H}_2\text{O}})$ that has a steep slope at low water contents and grows more slowly after that. This form is consistent with the data shown in figure 4-8a, within their uncertainties.

$$\Delta T(X_{\text{H}_2\text{O}}) = K X_{\text{H}_2\text{O}}^\gamma, \quad 0 < \gamma < 1 \quad (4.16)$$

The calibration of this function to find K and γ is discussed below. Figure 4-3 shows the solidus for a range of bulk water contents.

The saturation concentration of water in the melt is constrained at pressure below 2 GPa by the experiments of *Dixon et al.* (1995) and *Mysen and Wheeler* (2000). At higher pressure we estimate the saturation concentration of water by requiring that, in conjunction with $\Delta T(X_{\text{H}_2\text{O}}^{\text{sat}})$, it be consistent with the the results of *Grove* (2001) and *Kawamoto and Holloway* (1997) on the water saturated solidus.

$$X_{\text{H}_2\text{O}}^{\text{sat}} = \chi_1 P^\lambda + \chi_2 P, \quad 0 < \lambda < 1. \quad (4.17)$$

Calibration of this equation is discussed below.

The systematics of water abundances in MORB demonstrate that water behaves similarly to other moderately incompatible elements. *Michael* (1995) has shown that the water/Ce ratio changes little in MORB, and hence that water has approximately the same D as Ce for the melting conditions beneath ocean ridges. This behavior can be understood with the recognition that water is incorporated in solid mantle phases, like other trace components. Many workers have assumed that there is always a vapor phase at the solidus of materials that contain water [*T. Grove, pers. comm.*]. However, the treatment of water as a trace element in solution in solid phases suggests that this is not the case. Requiring water saturation at the solidus is similar to insisting on saturation of some rare earth element phase at the solidus. That only takes place if the concentration of the component exceeds the amount that can be taken into solution by the solid phases. Furthermore, partition coefficients can be used successfully even for major constituents of phases, and this use is thermodynamically valid (*Langmuir and Hanson*, 1981; *Weaver and Langmuir*, 1990). By considering water to behave as a regular trace element, its equilibrium partitioning between solid and silicate melt can be modeled with a bulk distribution coefficient:

$$X_{\text{H}_2\text{O}} = \frac{X_{\text{H}_2\text{O}}^{\text{bulk}}}{D_{\text{H}_2\text{O}} + F(1 - D_{\text{H}_2\text{O}})}. \quad (4.18)$$

The parameterization described here does not preclude the use of a bulk $D_{\text{H}_2\text{O}}$ for

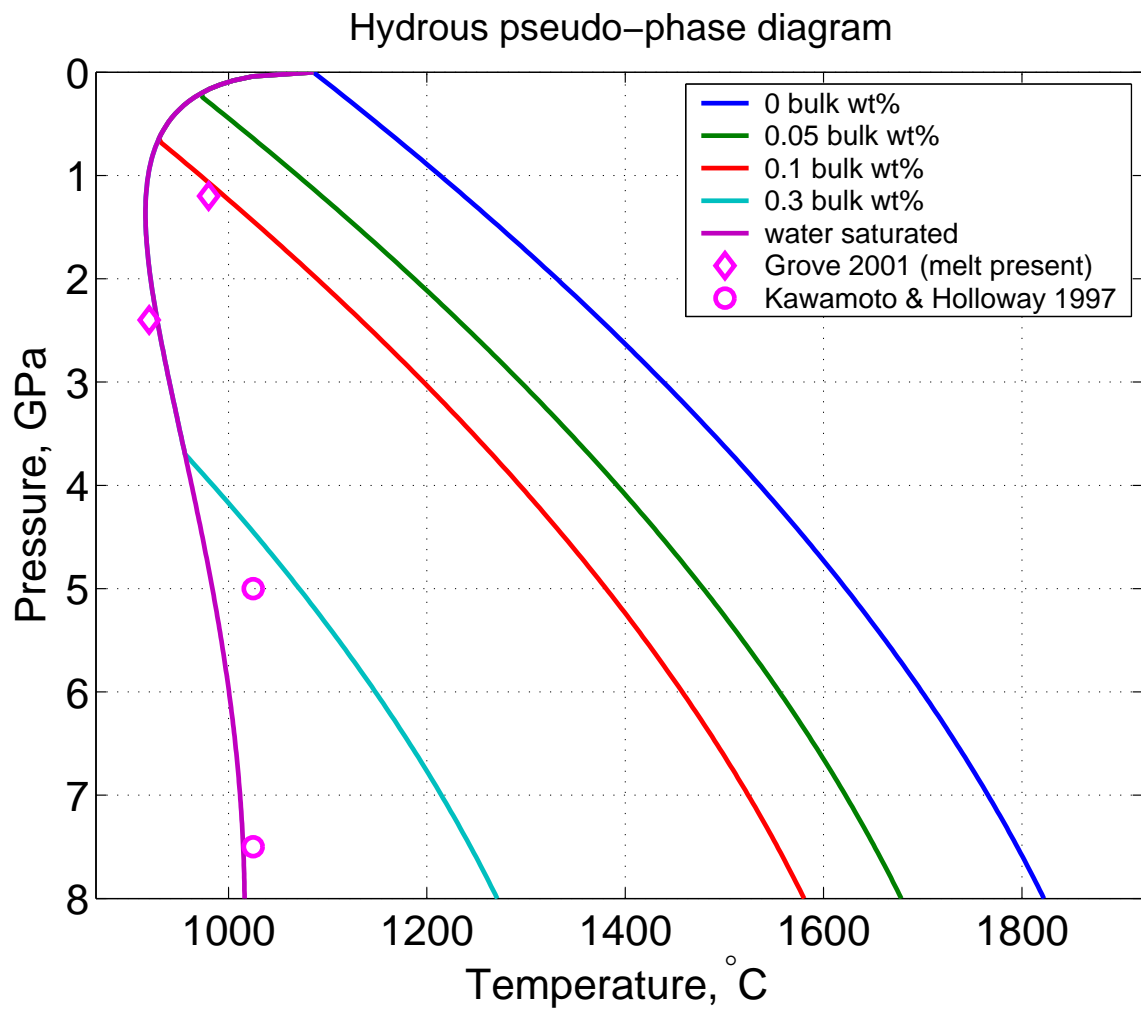


Figure 4-3: The solidus for different bulk water contents of the system. Solidus depression is linear with dissolved water. It is bounded by the saturation of water in the melt, a function of pressure.

water that varies with pressure. While such a variation is expected in natural systems and has been considered in past work by *Hirth and Kohlstedt* (1996), a quantitative estimate of $D_{\text{H}_2\text{O}}(P)$ for the range of water content and pressure relevant to arc melting has not been produced. Thus, in order to preserve the simplicity and transparency of the melting parameterization, we choose a constant bulk partitioning coefficient for the calculations described here. On the basis of its similarity in behavior to Ce, we use a D for water of 0.01. However, we do so with the recognition that this choice will have important implications for the volume and chemistry of melt produced near the wet solidus in arc melting simulations. Possible effects of variation in $D_{\text{H}_2\text{O}}$ need to be considered in the detailed application of the model.

Because ΔT depends on the melt fraction, F appears on both sides of equation (4.19) and no closed form analytical solution for F exists; however, a solution can be found numerically using a root-finder. The total melting function for $F \leq F_{\text{cpx-out}}$ is

$$F(P, T, X_{\text{H}_2\text{O}}^{\text{bulk}}) = \left[\frac{T - (T_{\text{solidus}} - \Delta T(X_{\text{H}_2\text{O}}^{\text{bulk}}, P, F))}{T_{\text{liquidus}}^{\text{herz}} - T_{\text{solidus}}} \right]^{\beta_1}. \quad (4.19)$$

Figure 4-4 shows isobaric melting curves with different bulk water content. Notice that small additions of water greatly depress the solidus and produce a prominent “low- F tail” without generating much additional melt. However, with water contents exceeding saturation at the solidus (0.3 wt% bulk water in figure 4-4), the melting function takes on a qualitatively different shape, ramping up sharply in F just above the solidus. This represents eutectic-like melting due to the overabundance of water acting as an additional phase: with each increment of new melting, more water can dissolve into the melt, pinning the solidus at its water saturated temperature until the reservoir of vapor phase water has been exhausted (*Gaetani and Grove*, 1998). At pressures below 2 GPa, water partitioning at the solidus is strongly affected by the presence of amphibole (*Schmidt and Poli*, 1998). A more sophisticated parameterization should take this into account.

Figures 4-5a and b show isobaric, isothermal melting curves. Progressive melting is achieved by adding water to the system. At $X_{\text{H}_2\text{O}}^{\text{bulk}}$ below saturation of the melt,

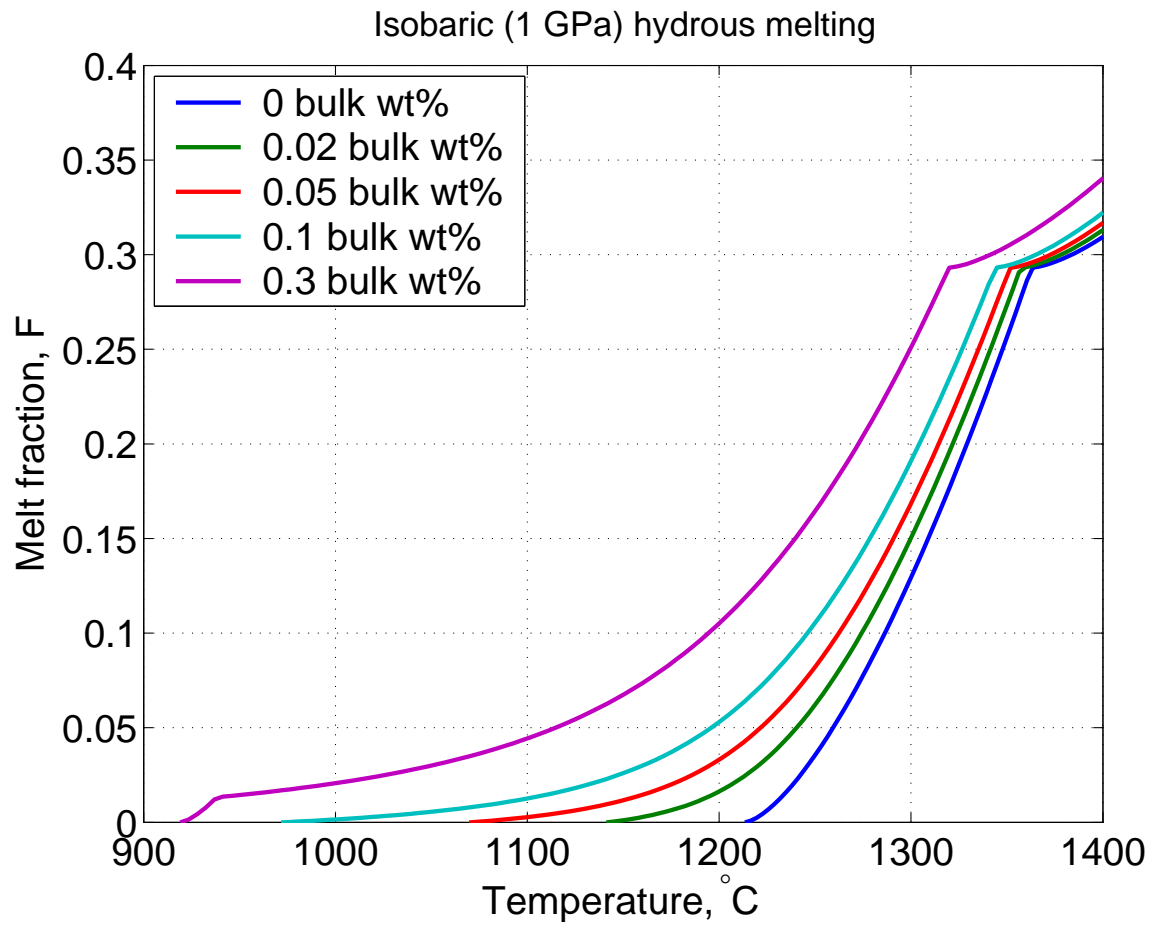


Figure 4-4: Isobaric melting curves (for 1 GPa) with different bulk water contents. The 0.3 wt% melting curve is saturated at the solidus.

most of the water goes into the melt, lowering the solidus and increasing the degree of melting. Figure 4-5a shows F as a function of bulk water content. This figure demonstrates that our parameterization achieves the objective stated in the introduction in item 4: the isobaric isothermal melting function has a roughly linear dependence on bulk water content, with a slope that is larger for higher temperature.

The equations described above provide a quantitative framework for equilibrium melting of peridotite in the presence of water. To make this framework useful we must specify values of the model parameters A_n , B_n , C_n , r_n , K , γ , χ_n , λ and β_n . This is done using a database of experimental results from the literature and comparison to other established models.

4.3 Experimental Database

4.3.1 Anhydrous

Calibration of the anhydrous model was performed on a set of experimental results on peridotite melting from various authors and labs. These results were compiled from publications from 1980 to the present. The peridotites used in melting experiments in the experimental database are compiled in table 4.1. Some of these studies contain results that are not included in the database due to undetermined or zero melt fraction.

A sampling bias of experiments especially relevant to this study is the lack of data at low melt fractions. Determining the compositions of melts at low melt fraction (below about 2 wt%) is difficult and unreliable and thus mass-balance estimates of F in this range can be inaccurate. However, understanding the beginning of melting is crucial because low- F melts control much of the trace element budget. The treatment of this problem is discussed in greater detail in the next section.

While typically reported experimental errors in P , T , and F are approximately 1 kb, 5° C and 1 wt% respectively, a glance at plots of the database reveal that there is significant variability between different experiments at different labs under nominally

<i>Identifier</i>	<i>Rock type</i>	<i>Modal cpx, %</i>	<i>Authors</i>
KLB-1	Spinel Lherzolite	15	<i>Hirose and Kushiro (1993)</i> <i>Iwamori et al. (1995)</i> <i>Takahashi et al. (1993)</i> <i>Takahashi (1986)</i>
HK66	Spinel Lherzolite	14	<i>Hirose and Kushiro (1993)</i>
KR4003	Spinel Lherzolite	15	<i>Walter (1998)</i>
MM3	Synthetic Spinel Lherzolite ^b	17	<i>Baker and Stolper (1994)</i> <i>Baker et al. (1995)</i> <i>Falloon et al. (1999)</i>
FER-B	Synthetic Spinel Lherzolite ^b	40	<i>Pickering-Witter and Johnston (2000)</i>
FER-C	Synthetic Spinel Lherzolite ^b	1	<i>Pickering-Witter and Johnston (2000)</i>
FER-D	Synthetic Spinel Lherzolite ^b	10	<i>Pickering-Witter and Johnston (2000)</i>
FER-E	Synthetic Spinel Lherzolite ^b	23.5	<i>Pickering-Witter and Johnston (2000)</i>
PHN1661	Garnet Lherzolite	16 ^a	<i>Kushiro (1996)</i>
KG1	Spinel Lherzolite + Basalt	16 ^a	<i>Kogiso et al. (1998)</i>
KG2	Spinel Lherzolite + Basalt	16 ^a	<i>Kogiso et al. (1998)</i>
Hawaiian	Pyrolite	16 ^a	<i>Jaques and Green (1980)</i>
Tinaquillo1	Spinel Lherzolite	16 ^a	<i>Jaques and Green (1980)</i> <i>Robinson et al. (1998)</i>
Tinaquillo8	Spinel Lherzolite	16 ^a	<i>Robinson et al. (1998)</i>

Table 4.1: Summary of experimental peridotites (anhydrous experiments only).

^a Modal cpx not known or not available. The mean of the other peridotites, 16%, is assumed for computations here. ^b Constructed by combining mineral separates from the Kilbourne Hole Xenolith.

the same conditions (see figure 4-6). For example, in figure 4-6a, pressure is known exactly (1 atm) and composition is constant across experiments—yet experiments conducted at 1175, 1200 and 1250° C each show a spread of about 10 wt% in melt fraction. Uncertainty in pressure, especially above ~ 4 GPa, and in temperature may be underestimated by experimentalists [*J. Longhi, pers. comm.*]. However, isothermal productivity only amounts to about -2 wt% per kilobar and so it is not able to explain all the variability. Hard to control experimental parameters such as oxygen fugacity, iron loss to the container, small amounts of water present in nominally anhydrous runs, run duration and physical properties of the starting materials probably all play a role in producing this disagreement. Until we have a better understanding of the formal error associated with experimental studies of melting, a partial reliance on theory and expectations is necessary.

4.3.2 Hydrous

Experiments on hydrous melting of peridotite are few. Fortunately there exist several sets of experiments that can be used as a foundation to calibrate the model. One set, from *Hirose and Kawamoto* (1995) is a direct melting type experiment where samples of peridotite with known bulk water are melted and the degree of melting is determined using mass balance of sodium¹. The second, by *Gaetani and Grove* (1998), is a set of peridotite melting experiments that do not attempt to measure an equilibrium degree of melting of a peridotite. Instead they use the fact that the degree of melting is an extensive property and maximize the yield of melt by varying the bulk composition, giving a large enough proportion of glass after quench to accurately determine the composition of the glass (see also *Kinzler and Grove*, 1992). Although this does not give the needed information, $F(X_{\text{H}_2\text{O}})$ directly, it is an advantageous approach because it allows an accurate analytical determination of the amount of water *dissolved in the melt* that is not dependent on assumptions regarding water

¹*Hirose and Kawamoto* (1995) assumed that sodium is completely incompatible when calculating the melt fraction. We recalculated the degree of melting after *Hirschmann* (2000) based on the assumption that Na has a small but non-zero partition coefficient when cpx is present.

loss to the capsule or partitioning of trace elements.

4.4 Model Calibration

4.4.1 Anhydrous melting

Calibration of the anhydrous model requires assigning numerical values to the parameters A_n , B_n , C_n , r_n , and β_n that provide a “best fit” to the assemblage of data, theory and expectations available (see table 4.2). This procedure is not an explicit inversion but occurs interactively by adjusting model parameters and comparing resulting curves to data and to expected trends such as productivity functions ($\partial F/\partial T|_{P, X_{H_2O}}$, $\partial F/\partial P|_{T, X_{H_2O}}$, and $\partial F/\partial X_{H_2O}|_{P, T}$) and how they vary with changes in the main variables.

The cpx reaction rate constants, r_0 and r_1 , are constrained on the basis of experiments on a simplified chemical system at 1% melting by *Longhi* (2002) and by batch melting experiments of lherzolite by *Pickering-Witter and Johnston* (2000); *Walter et al.* (1995) and *Walter* (1998). We fix values of r_n by informally fitting the anhydrous database.

Hirschmann (2000) and *Schwab and Johnston* (2001) show that significant variability in the solidus temperature between different compositions is due, at least in part, to the fertility of the peridotite. *Hirschmann* (2000) chose a set of experiments that represent an intermediate composition and formally inverted these for a solidus of best fit. This fit was performed using a melt present/absent criterion and did not utilize information on melt fraction for experiments with melt present. Using our database of melt fraction and melting parameterization, we find that a constant shift in the *Hirschmann* (2000) solidus of 35° down in temperature lowers the RMS residual of the model fit and better matches the data above the solidus (see figure 4-7). Because we expect a small “low-F tail” in the anhydrous isobaric melting function we assign a value of β_1 that is greater than 1. The anhydrous liquidii ($T_{liquidus}^{lherz}(P)$ and $T_{liquidus}(P)$) are constrained mainly by fitting the melting function $F(T')$ to the

anhydrous data set.

4.4.2 Hydrous melting

There are two components to the hydrous melting extension of our parameterization: the solidus shift as a function of water dissolved in the melt and the saturation water content of the silicate melt as a function of pressure.

At low pressures, both $\Delta T(X_{\text{H}_2\text{O}})$ and $X_{\text{H}_2\text{O}}^{\text{sat}}(P)$ are constrained by data. Water solubility measurements by *Dixon et al.* (1995) and *Mysen and Wheeler* (2000) on different melt compositions² are used to constrain the saturation water content of basaltic melt below two GPa.

We calibrate $\Delta T(X_{\text{H}_2\text{O}})$ using an approach similar to that sketched by *Gaetani and Grove* (1998). The calibration is performed using a model for magnesium partitioning between the residual olivine and the melt (*Langmuir et al.*, 1992; *Asimow*, 2000) that is able to give the liquidus temperature for the major element compositions of the experiments recalculated water free. Comparing this temperature to the water-bearing experiment gives the temperature change associated with the water content. *Gaetani and Grove* (1998) also give a calibration for dry olivine liquidus temperatures that they use for a similar purpose, but their form is essentially identical to that of *Langmuir et al.* (1992) and demonstrates the same compositional dependence. For this paper we calibrate the model based on a set of experimental melts encompassing a larger parameter space in P , T , and $X_{\text{H}_2\text{O}}$ [*P. Asimow, pers. comm.*]. The data generated using this inversion of chemistry are shown in figure 4-8a.

At pressures above two GPa we have no direct constraints on $X_{\text{H}_2\text{O}}^{\text{sat}}$. Instead we use an indirect constraint from measurements of the water saturated solidus by *Kawamoto and Holloway* (1997) and *Grove* (2001). In these experiments, however, the water content of the saturated melt is not reported. By taking the parameterized dry solidus minus the experimentally determined water saturated solidus we can estimate the ΔT of the solidus for each experiment. To estimate the water content of these saturated

²*Dixon et al.* (1995) uses basalt, *Mysen and Wheeler* (2000) uses haploandesite. The haploandesites have a higher silica content than the basalts.

melts we employ our parameterization of water solubility in the melt from equation (4.17) (which, unfortunately is not well constrained at high pressure). Data derived in this way, and the resulting fit for $\Delta T(X_{\text{H}_2\text{O}})$, is shown in figure 4-8a. As explained above, this does not limit the concentration of water in the fluid phase. It simply restricts the solidus lowering action of water to the range below the parameterized solubility of water in the silicate melt.

4.4.3 Free Parameters and Missing Constraints

Table 4.2 shows the large number of parameters in this model. This multitude of parameters exists because of a choice in the formulation of the model: each aspect of peridotite melting was parameterized separately resulting in separate “modules,” each with a fairly transparent physical meaning. These modules combine to form the melting model but retain their autonomy—each can be analyzed independently against existing or future data and theory. While certain modules are well constrained by existing data, others are poorly constrained at the present. Their values are determined as described above, until more data become available.

The anhydrous liquidii parameters, B_n and C_n , are not well constrained by currently available data. They are essentially fit parameters as described above. The reason for introducing three unconstrained parameters here instead of just one is that they provide greater flexibility to fit experimental data at moderate to high melt fraction, and they are consistent with other parts of the model.

Furthermore, there are sets of model parameters that can trade off to achieve a similar fit to data and constraints. For example, there is a trade-off between a higher curvature of the cpx-in isobaric melting function (β_1) and a lower mantle solidus temperature.

At high pressures, measures of the water saturated solidus constrain $\Delta T(X_{\text{H}_2\text{O}}^{\text{sat}})$ however the saturation water content at these pressures is unknown. We extrapolate the water saturation curve from low pressures and calibrate the solidus lowering curve to fit the experimentally determined water saturated solidus (see figures 4-8a and b). A different extrapolation of $X_{\text{H}_2\text{O}}^{\text{sat}}(P)$ would lead to a different $\Delta T(X_{\text{H}_2\text{O}})$

<i>Parameter</i>	<i>For calculating</i>	<i>Value</i>	<i>Units</i>
A_1	$T_{solidus}$	1085.7	$^{\circ}\text{C}$
A_2		132.9	$^{\circ}\text{C GPa}^{-1}$
A_3		-5.1	$^{\circ}\text{C GPa}^{-2}$
B_1	$T_{liquidus}^{lherz}$	1475.0	$^{\circ}\text{C}$
B_2		80.0	$^{\circ}\text{C GPa}^{-1}$
B_3		-3.2	$^{\circ}\text{C GPa}^{-2}$
C_1	$T_{liquidus}$	1780.0	$^{\circ}\text{C}$
C_2		45.0	$^{\circ}\text{C GPa}^{-1}$
C_3		-2.0	$^{\circ}\text{C GPa}^{-2}$
r_1	R_{cpx}	0.50	cpx/melt
r_2		0.08	cpx/melt/GPa
β_1	F	1.50	
β_2		1.50	
K	$\Delta T(X_{\text{H}_2\text{O}})$	43	$^{\circ}\text{C wt}\%^{-\gamma}$
γ		0.75	
$D_{\text{H}_2\text{O}}$		0.01	
χ_1	$X_{\text{H}_2\text{O}}^{sat}$	12.00	wt% $\text{GPa}^{-\lambda}$
χ_2		1.00	wt% GPa^{-1}
λ		0.60	
c_P	$\left.\frac{dF}{dP}\right _S$	1000	$\text{J kg}^{-1} \text{K}^{-1}$
α_s		40	$\times 10^{-6} \text{K}^{-1}$
α_f		68	$\times 10^{-6} \text{K}^{-1}$
ρ_s		3.30	$\times 10^3 \text{kg m}^{-3}$
ρ_f		2.90	$\times 10^3 \text{kg m}^{-3}$
ΔS		300	$\text{J kg}^{-1} \text{K}^{-1}$

Table 4.2: Summary of parameters and values.

that would satisfy the same constraint. This ambiguity represents a weakness in the parameterization, especially if it is applied for conditions of high water content and pressures above 2 GPa. This problem could be resolved by direct measurements of water solubility in basaltic melts at high pressure.

Experiments at high pressures indicate that the water-silicate melt solvus may close at about 4 GPa (*Bureau and Keppler, 1999*). If this is the case, it is incorrect to speak of a water-saturated solidus as there is no saturation point. We extend our parameterization above 4 GPa however, assuming that the parameterized saturation at high pressure is sufficiently high to effectively mimic the possible lack of a saturation point under naturally occurring water contents.

4.5 Comparison with other models

The parameterization of melting described here utilizes current theoretical and experimental results. Older parameterizations exist, however, and have proven useful so it is worth comparing the different parameterizations to each other and to the data. Figures 4-9 and 4-10 compare several parameterizations of hydrous and anhydrous melting. This comparison demonstrates that at moderate pressures the parameterizations agree to first order. There are, however, systematic differences at very low and very high degrees of melting. The increasing isobaric productivity above the solidus that is evident in pMELTS calculations and imposed on our parameterization is not present for other anhydrous parameterizations. With the addition of water, however, all of the isobaric melting functions show similar shape for low melt fractions (although the degree of melting can vary significantly between parameterizations). While we have not explored this effect in detail, it suggests that another approach to reconcile all of these models is to assume a linear function of T' for dry melting while employing addition of terms that include the solidus lowering effects of fertility due to fluxing elements such as water or alkalis.

A quantitative measure of the success of a dry melting parameterization is how much of the variance in experiments that it can explain. The parameterizations are

applied to each entry in the database using the experimental pressure, temperature (and modal cpx, for our model) to predict a degree of melting. The difference between the experimental and the predicted degree of melting is the residual. The variance reduction is then defined as the percentage of the total variance of experimentally determined F explained by a given parameterization. The variance reduction properties of each of the parameterizations are shown in table 4.3. Note that the *Langmuir et al.* (1992) model was not designed for pressures greater than 4 GPa and more than 40% melting.

Clearly a parameterization cannot reduce the variance beyond the experimental uncertainty. Figure 4-6a shows that under nominally identical conditions ($P \approx 1$ GPa) there is about a 4 wt% standard deviation in melt fraction. At higher pressures this deviation is likely to be greater.

4.6 Testing and validation

The intended application for this melting parameterization is the simulation of magma genesis in subduction zones that consider water release from the slab, fluid and solid flow, time dependent reactive melting and chemical transport. Here we concern ourselves with testing and validation of the parameterization by considering two highly simplified examples of magma genesis.

4.6.1 Adiabatic upwelling beneath mid-ocean ridges

A useful test of the melting model is to calculate the melt production of columns of adiabatically upwelling mantle. In this model, melt and solid upwell at the same velocity and do not separate. The melts from each vertical increment of the column may be ‘pooled’ for a simple approximation to a mid-ocean ridge basalt *Klein and Langmuir* (1987). A simplified version of the productivity function for pressure release

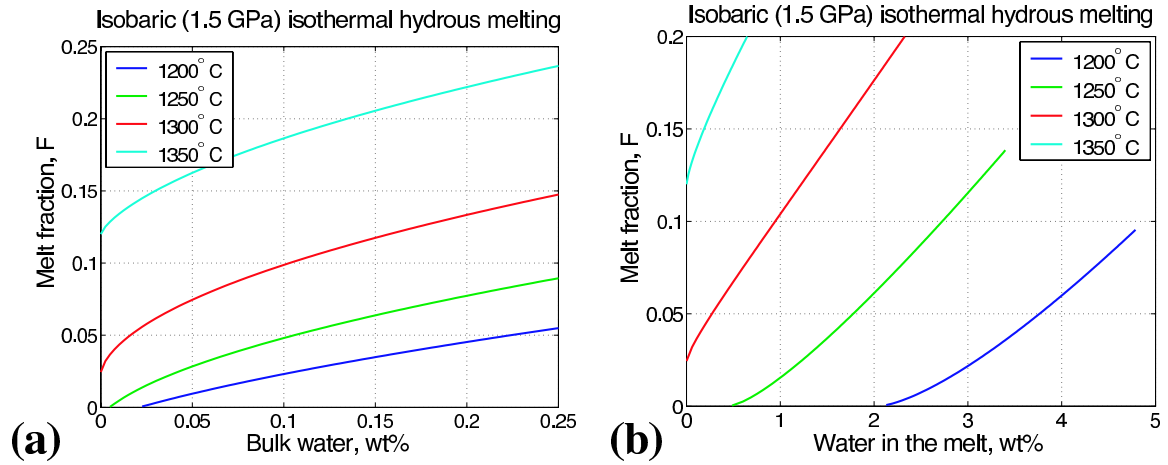


Figure 4-5: Degree of melting as a function of the water in the system, holding the temperature (see figure) and pressure (1.5 GPa) constant. Modal cpx is 17% in the unmelted solid. **(a)** F as a function of $X_{\text{H}_2\text{O}}^{\text{bulk}}$. Compare to *Gaetani and Grove (1998)* figure 13a. **(b)** F as a function of water dissolved in the melt. Bulk distribution coefficient of water is assumed to be 0.01.

<i>Parameterization</i>	<i>% reduction^a</i>	<i>% std. dev. of residual^a</i>
New model	85.0	9.1
Langmuir92	72.1	13.9
McKenzie & Bickle	74.7	11.0
Iwamori95	74.5	11.2

Table 4.3: Summary of variance reduction. ^a Using data from anhydrous experiments below 4 GPa and below 40% melting. The use of the entire data set yields lower variance reduction for all parameterizations.

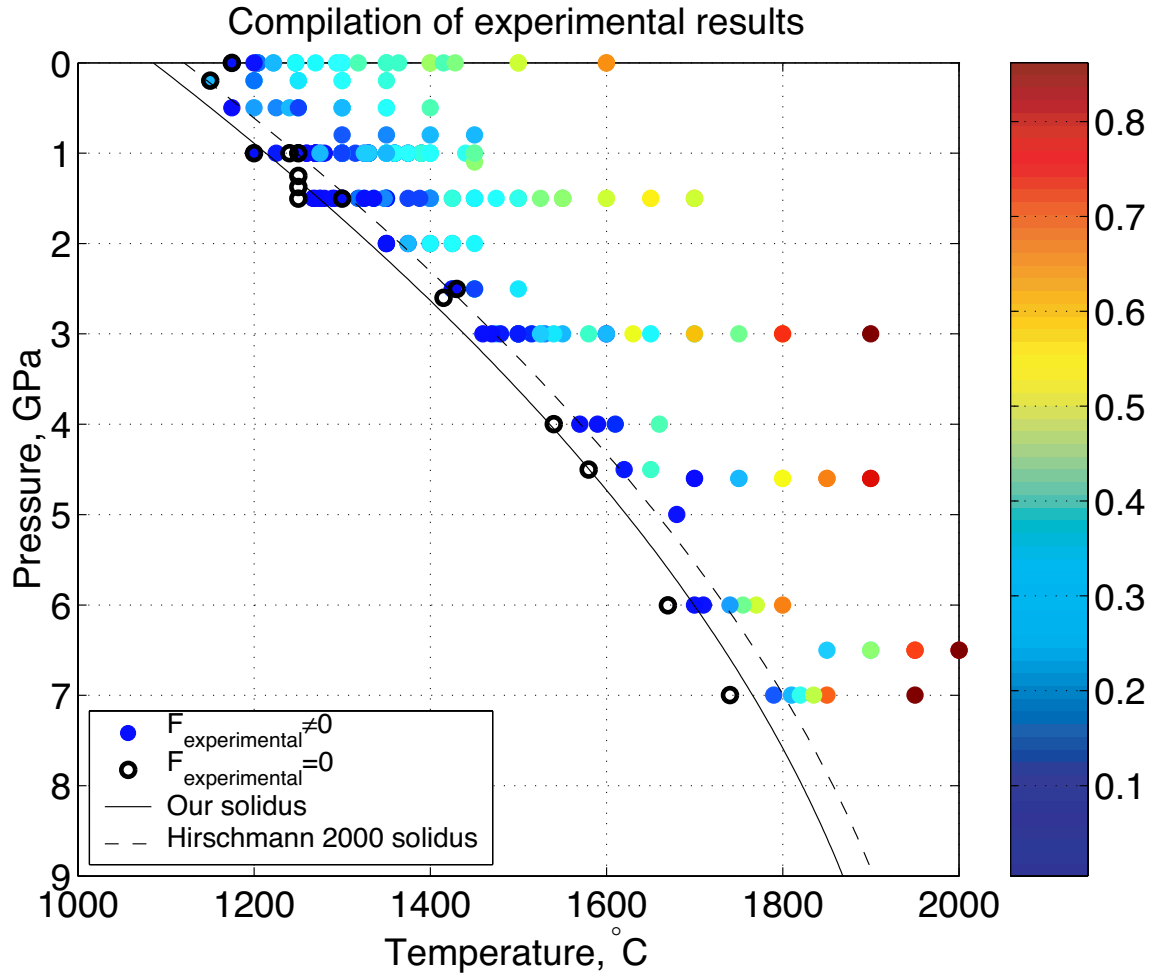


Figure 4-7: A plot of experimentally determined degree of melting as a function of pressure and temperature. The chosen solidus has an A_1 35 °C below that of *Hirschmann* (2000) to better fit the low melt fraction experiments but uses the same A_2 and A_3 that he reported. The 29 experiments within 10 °C of the *Hirschmann* solidus have an average degree of melting of 10 wt%. Of the 29, only 5 have no melting. This is due in part to our inclusion of experiments with more fertile source compositions (*e.g.* PHN-1611 and MPY) in the database.

melting at constant entropy is (McKenzie, 1984):

$$\left. \frac{dF}{dP} \right|_S = \frac{-\frac{c_P}{T} \left. \frac{\partial T}{\partial P} \right|_F + \left(F \frac{\alpha_f}{\rho_f} + (1-F) \frac{\alpha_s}{\rho_s} \right)}{\Delta S + \frac{c_P}{T} \left. \frac{\partial T}{\partial F} \right|_P}. \quad (4.20)$$

Asimow et al. (1997) pointed out that this equation does not account for variation in partial specific entropies of the various phases as a function of F . *Hirschmann et al.* (1999) demonstrated that just above the solidus, when incompatible elements are strongly concentrated in the melt, the effect of partial specific entropy variations may be significant. That said, we employ equation (4.20) here because we have no way to estimate the partial specific entropies of the solid and fluid phases. For $F < F_{cpx-out}$, the derivatives required for Eq. (4.20) are

$$\left. \frac{\partial T}{\partial F} \right|_P = \beta_1^{-1} F^{\frac{(1-\beta_1)}{\beta_1}} (T_{liquidus}^{lherz} - T_{solidus}), \quad (4.21)$$

$$\left. \frac{\partial T}{\partial P} \right|_F = F^{\frac{1}{\beta_1}} \left(\frac{\partial T_{liquidus}^{lherz}}{\partial P} - \frac{\partial T_{solidus}}{\partial P} \right) + \frac{\partial T_{solidus}}{\partial P}. \quad (4.22)$$

For the case where $F > F_{cpx-out}$ similar equations follow directly from Eq. (4.8). Equation (4.20) is numerically integrated using a fourth order Runge-Kutta scheme (*Press et al.*, 1992) from a given pressure and temperature at depth (where $F = 0$) to the surface. The P - T paths associated with these melting trajectories are shown in figure 4-11b. The P - T path of the adiabat is calculated by integrating

$$\left. \frac{dT}{dP} \right|_S = T \left(\frac{F \frac{\alpha_f}{\rho_f} + (1-F) \frac{\alpha_s}{\rho_s} - \Delta S \left. \frac{dF}{dP} \right|_S}{c_P} \right) \quad (4.23)$$

simultaneously with equation 4.20. Below the solidus at 1500 K this amounts to about 18 K/GPa.

We calculated adiabatic upwelling columns for 4 values of bulk water content from anhydrous to 200 wt ppm. *Hirth and Kohlstedt* (1996) estimated from the literature that the ambient water content in the mantle is about 125 ± 75 wt ppm. By assuming a potential temperature for the mantle of about 1350 °C and a standard activity model

for water in silicate melts, they predicted that melting should begin under ridges at about 115 km depth, well within the garnet stability field. Our calculations agree quite well with these estimates, as shown in Figure 4-11.

Figures 4-11a and b show 12 separate calculations, four bulk water contents at three different mantle potential temperatures. The results agree with the widely held view that water extends the depth interval of melting significantly, putting a larger portion of the total melt generation at higher pressures and increasing the average pressure of melting (*Asimow and Langmuir, 2003*). In figure 4-11c we quantify this effect by plotting the pressure interval over which the first one percent of melting occurs.

4.6.2 Arc Melting

As a first step toward applying this melting parameterization to subduction zone magma genesis simulations, we calculate a two dimensional melting field on an arc thermal structure with a specified mantle flow field. We apply a constant bulk water concentration evenly over a triangular region of the wedge. The thermal structure is determined by solving a time dependent advection-diffusion equation of energy conservation without melting (we use a Semi-Lagrangian Crank-Nicholson algorithm, see *Katz et al. (2003)*, in prep.). The thermal calculation is run to steady state and the resulting temperature field is used as an input to the melting calculation. Enthalpy is conserved at each grid point in this calculation according to the equation

$$c_P T_i = (c_P + F \Delta S) T_f. \quad (4.24)$$

Here, T_i is the temperature before melting and T_f the final temperature after melting. T_f must be consistent with the final degree of melting, F , according to the melt parameterization. Modal cpx is taken as 17 wt%. Results of an example calculation are shown in figure 4-12. We explore this model further in Langmuir et al. (in prep) to understand how subduction parameters such as convergence rate and slab dip will affect the degree of melting in the wedge and compare it to Na variations observed

in arc lavas.

4.7 Summary

We have presented a new parameterization of anhydrous and hydrous melting of mantle peridotite that takes into account the pressure, temperature, water content and modal cpx of a melting system to calculate the equilibrium degree of melting. Our parameterization includes many of the important features of hydrous melting of peridotite observed in experiments and predicted by theory. It remains mathematically simple, efficient to compute and flexible to modification as experiments and theory on peridotite melting evolve.

A comparison of isobars shows that all anhydrous parameterizations lie within the experimental variance at moderate pressure. All succeed to a similar degree in fitting the data. Furthermore, all of the parameterizations demonstrate concave upward low- F tails under hydrous conditions. An important difference between the models is their near-solidus behavior under anhydrous conditions.

The first preliminary test of the model, an adiabatic melting calculation, demonstrates that its predictions agree quantitatively with observations and theory (*Hirth and Kohlstedt*, 1996). An increasing pressure interval for the first 1% melting is consistent with expectations and has important implications for trace element partitioning. Application of the parameterization to a subduction zone thermal calculation gives reasonable results and will be coupled with full fluid and solid flow and geochemical transport in future work.

This parameterization is, of course, a simplification of the natural system that it aims to represent. For example, mineral composition, especially enrichment in easily fusible elements, plays an important role in determining the solidus and the shape of the melting function (*Pickering-Witter and Johnston*, 2000; *Schwab and Johnston*, 2001). This compositional variability is not captured by our parameterization.

To account for greater variability in the system would require a more complicated model. Given current uncertainties in experimental and theoretical constraints on

mantle melting, as well as the need to maintain computational efficiency, we feel that this parameterization contains an appropriate level of detail. It strikes a balance between efficiency and accuracy and delivers output that will be useful in tectonic scale models of magma genesis in subduction zones.

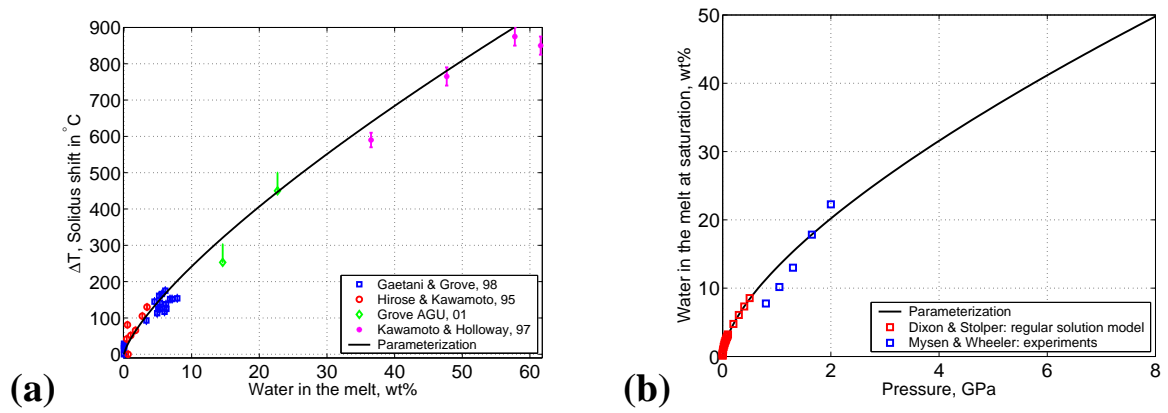


Figure 4-8: **(a)** The calibration of $\Delta T(X_{H_2O})$ for the parameters K and γ from equation 4.16. Data is derived from the experiments of *Hirose and Kawamoto* (1995), *Kawamoto and Holloway* (1997), *Gaetani and Grove* (1998), and *Grove* (2001). Result is given in table 4.2. **(b)** The saturation water content in wt% of the melt as a function of pressure from equation 4.17. Points are from *Dixon et al.* (1995), who report a regular solution model for basalt up to 0.5 GPa based on their and other experiments, and *Mysen and Wheeler* (2000), who report the saturation water content for three haploandesitic compositions (shown are results from the aluminum free composition that is 79% SiO_2).

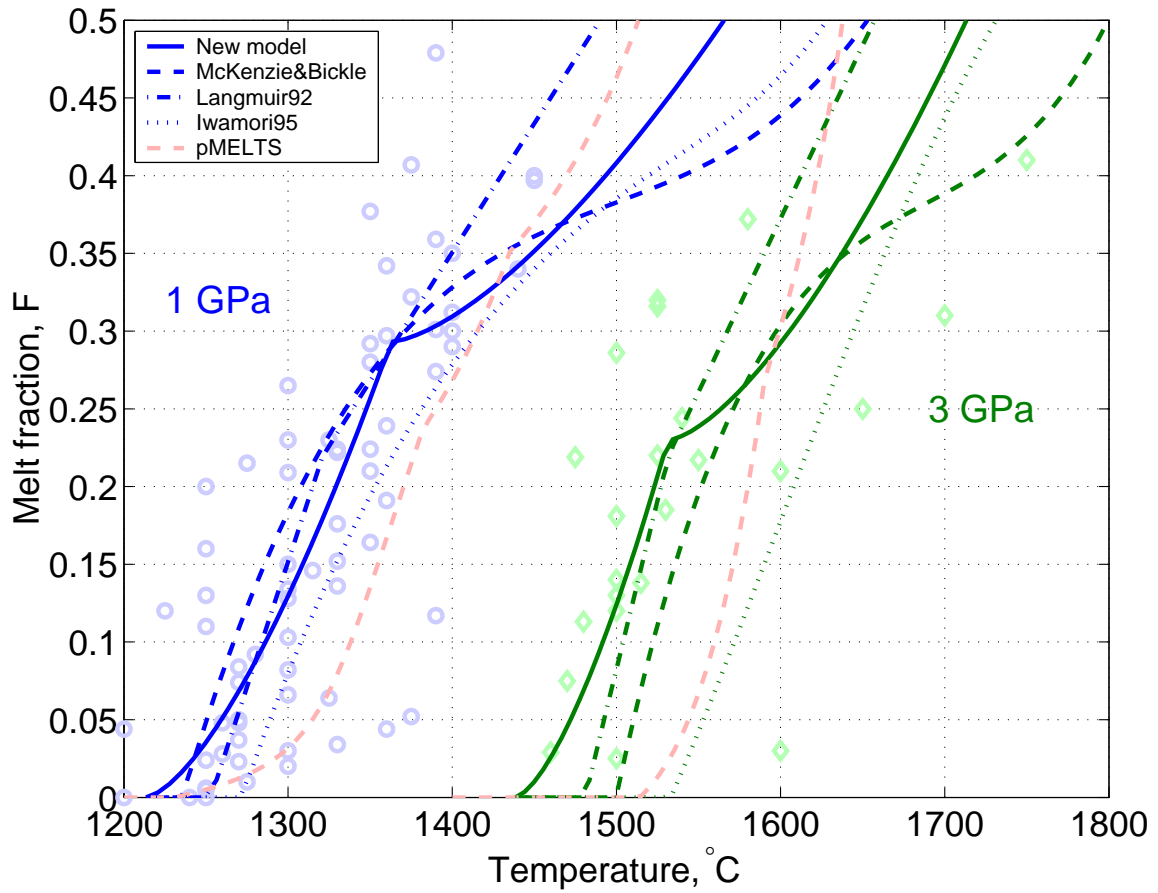


Figure 4-9: A comparison of the results of several parameterizations of dry melting and pMELTS calculations at 1 (in blue) and 3 (in green) GPa. The parameterizations are described by *Langmuir et al.* (1992), *McKenzie and Bickle* (1988) and *Iwamori et al.* (1995). pMELTS is described by *Ghiorso et al.* (2002). A commonly used parameterization by *Kinzler and Grove* (1992) is not considered because it requires the input of chemical information.

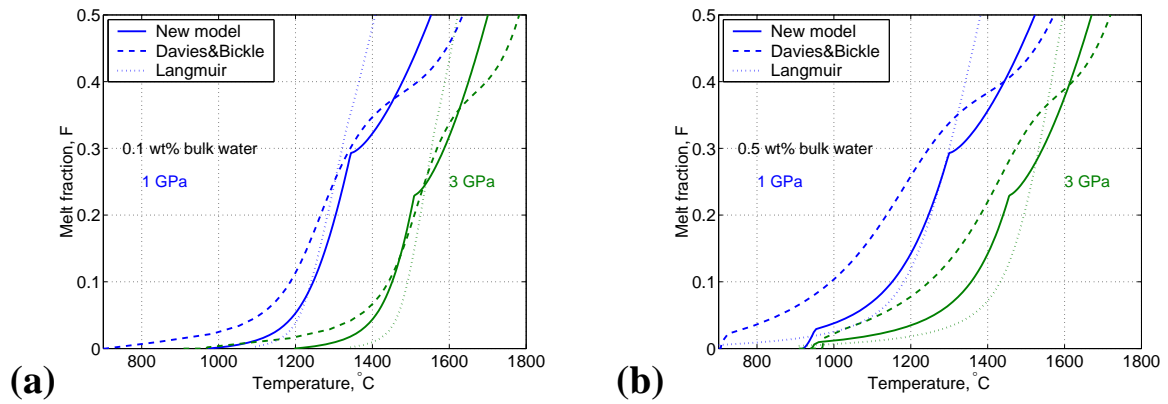


Figure 4-10: A comparison of parameterizations of mantle melting in the presence of water at 1 and 3 GPa. *Asimow and Langmuir* (2003) use a hydrous extension of the anhydrous parameterization described by *Langmuir et al.* (1992). *Davies and Bickle* (1991) extends the *McKenzie and Bickle* (1988) parameterization to handle wet melting. **(a)** For bulk water content of 0.1 wt%. **(b)** For bulk water content of 0.5 wt%.

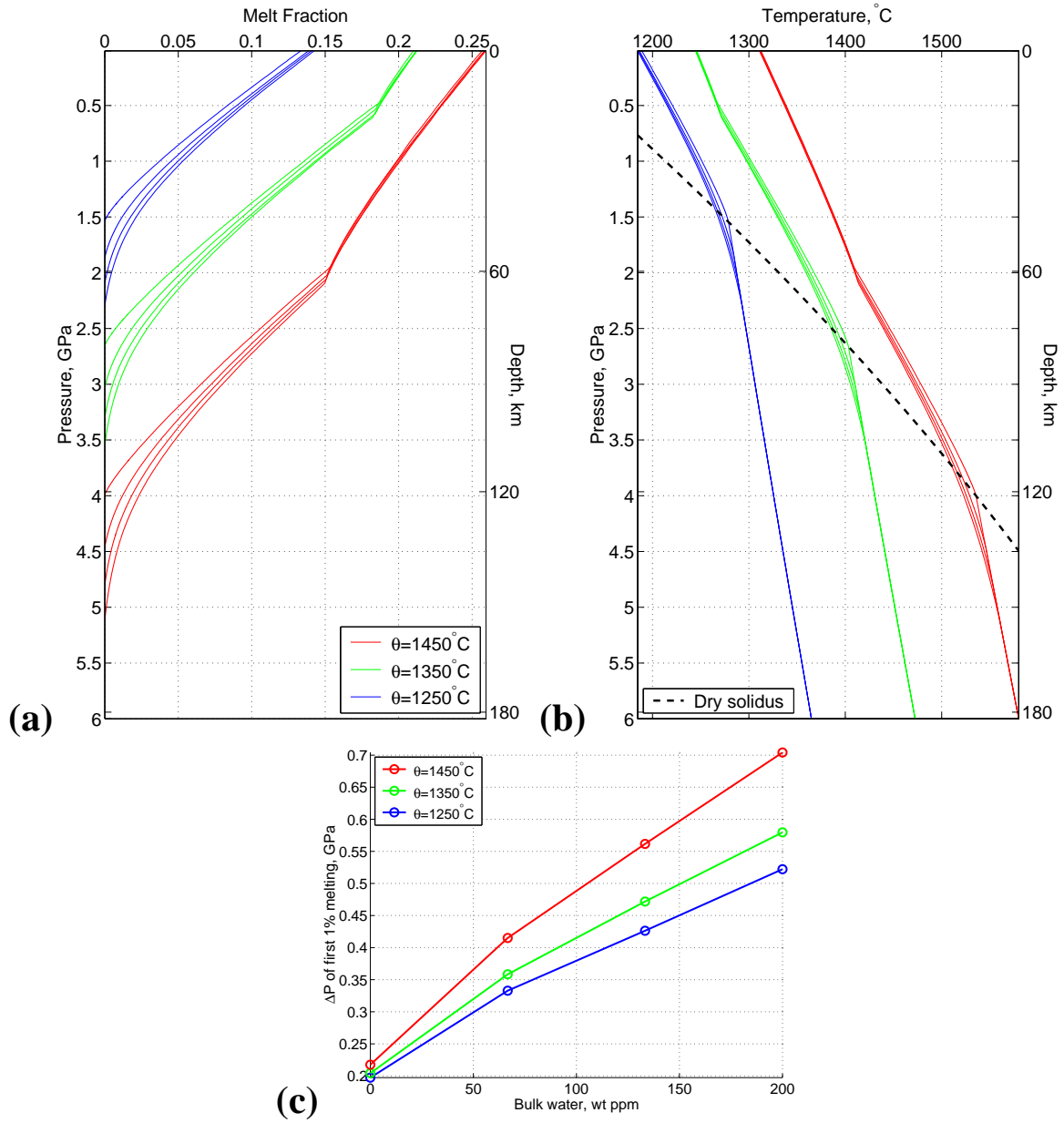


Figure 4-11: Results of the numerical integration of equations 4.20 and 4.23 for a mantle with bulk water ranging from 0 to 200 wt ppm and modal cpx of 10 wt%. Values of all melting model parameters are as given in table 4.2. Some of the curves show a kink due to cpx-out. **(a)** $F(P)$. **(b)** $T(P)$. **(c)** A quantification of the water induced low- F tails on adiabats. The pressure interval over which the first one percent of melting occurs is plotted as a function of bulk water in the system and potential temperature.

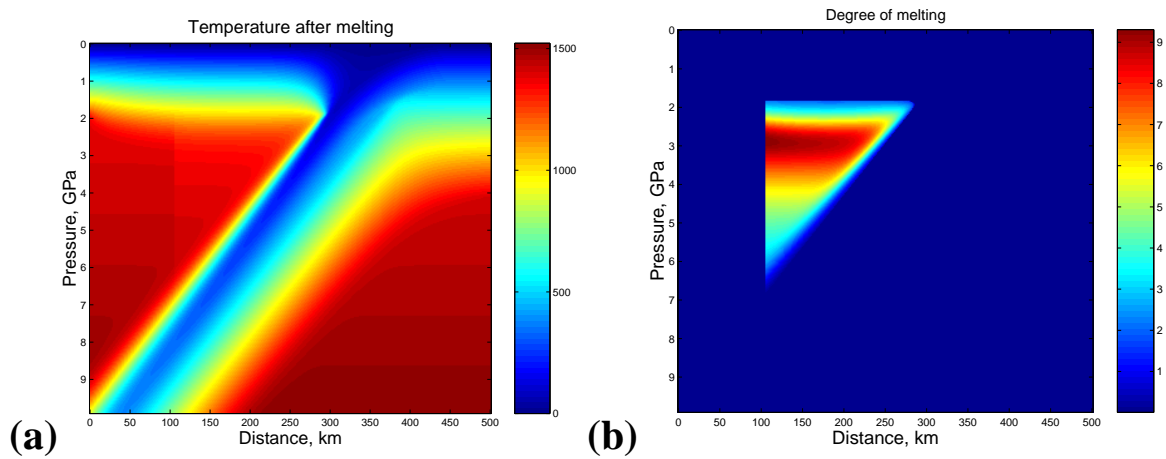


Figure 4-12: A representative example of a two dimensional static arc melting calculation. Bulk water of 0.5 wt% is applied only over the corner of the wedge shown in (b). The potential temperature of the mantle is taken to be 1350 °C. **(a)** Temperature of equilibration. **(b)** Equilibrium degree of melting in percent melt by mass. Maximum is 9.3%.

Chapter 5

Reactive hydrous melting and channelized melt transport in arcs

Abstract

Magma genesis in subduction zones has long been recognized as an open system process with fluxes of heat, mantle rock, hydrous fluids and magma moving along different paths through the system. Fluids released from the subducting slab interact with the mantle wedge and produce silicate melts that rise toward the lithosphere; some of this melt is eventually erupted from arc volcanoes. To develop a quantitative understanding of this process requires models capable of calculating both solid and fluid flow, adiabatic and reactive hydrous melting and temperature evolution. As a step toward such a model, we have parameterized a pseudo-phase diagram of a simplified rock–water system that describes the composition of water-bearing fluids in equilibrium with the silicate mantle. By extending a preexisting framework for reactive magma transport, we can use this pseudo-phase diagram to calculate reactive melting and freezing rates in a two dimensional model of a subduction zone. Our results show that channelization of fluid flux in the thermal boundary layer above the slab is an expected consequence of melting reactions in arcs. Furthermore, calculations suggest that when channels interact with the lithospheric thermal boundary layer they coalesce into bundles of channels that advect enough heat to modify the topography of the boundary layer. We discuss some implications of channelized melt transport predicted by the model and propose future work that would help to understand and quantify the results obtained here.

5.1 Introduction

Magma genesis in subduction zones has long been recognized as an open system process, from early conceptual diagrams (*Ringwood, 1974*) to recent computational models (e.g. *Gerya and Yuen, 2003; Iwamori, 1998*). The heat flux required for

sustained melting over geologic time is delivered by advection of hot mantle material into the wedge (*Kelemen et al.*, 2002; *van Keken et al.*, 2002). Volatiles, considered to be an essential component of subduction zone magma, are carried to depth by the subducting slab and liberated from it beneath the wedge by metamorphic reactions (*Stern*, 2002, and refs. therein). At least some of the magma which is produced leaves the system through the crust, carrying with it heat and volatiles as well as trace and major elements from a variety of sources at depth (*Miller et al.*, 1994).

Distinct geochemical evidence exists for two modes of melt generation in the mantle wedge: (1) Hydrous melting of mantle peridotite due to a flux of volatiles and (2) anhydrous melting of mantle peridotite due to adiabatic upwelling of mantle peridotite (*Sisson and Bronto*, 1998; *Kelley et al.*, 2004). Modern computational models of variable viscosity momentum and energy conservation in the mantle wedge produce flow and temperature fields consistent with simultaneous magma genesis in both of these modes (see chapter 3).

Temperature and solid flow fields in the mantle wedge hence constitute the context for melting. As such, they are of fundamental importance. However, to develop a quantitative understanding of magma genesis in subduction zones requires models that calculate melt transport as well as mass transfer reactions such as melting–freezing and hydration–dehydration. Previous authors have described models of porous fluid transport in subduction zones (*Davies and Stevenson*, 1992; *Iwamori*, 1998). Recent work by *Baker et al.* (2004) incorporates full mantle thermodynamics, as described by the MELTS algorithm (*Ghiorso et al.*, 2002), into an open system subduction model. These authors treat the hydrous fluid presumed to rise off the slab as a passive phase which is transported by solid advection and buoyancy–driven porous flow. By neglecting reactivity of the fluid and pressure forces arising from viscous compaction of the mantle matrix (described below), these models miss what may be a critical insight into the physics and chemistry of magma genesis in subduction zones. In this chapter I present a model that can address these deficiencies.

Such models of reactive transport in subduction zones are based on past work on mid-ocean ridges (*Spiegelman et al.*, 2001; *Spiegelman and Kelemen*, 2003). Exper-

iments and observations of mid-ocean ridge derived basalts shows that these melts are highly reactive as they rise toward the surface (*Kelemen et al.*, 1995a; *Liang and Morgan*, 2004), dissolving and reprecipitating mantle matrix phases. *Aharonov et al.* (1995) showed that the formation of high flux porous channels between low permeability compacted regions is a natural consequence of reactive porous flow up a solubility gradient. These channels seem to correspond to the tabular refractory dunite bodies surrounded by harzburgite observed in the Oman ophiolite (*Kelemen et al.*, 1995a; *Braun and Kelemen*, 2002).

Taken together, these calculations constitute a theoretical framework for modeling open system reactive melt transport. Here we describe an extension of that framework to the more complex case of magma genesis in subduction zones. We explicitly model the corrosive reactivity of an aqueous fluid rising from the top of the cool slab to the core of the hot mantle wedge and compute fluid transport using the full physics of porous flow in a viscously compatible medium as derived by *McKenzie* (1984) and outlined in chapter 1 of this thesis. As in the case of flow up a solubility gradient beneath mid-ocean ridges, fluids rising off the subducting slab react and localize into high flux channels. An example calculation is shown in 5-3. Channelized melts are predicted to have higher water contents and travel toward the Moho with greater speed. Furthermore, our calculations show that the heat transported by channelized fluids is sufficient to locally modify the temperature field.

5.2 Reactive melting

5.2.1 Chemistry

Experimental studies have shown that metamorphic reactions at depth in the subducting slab exsolve a dilute aqueous fluid (e.g. *Schmidt and Poli*, 1998; *Forneris and Holloway*, 2003; *Manning*, 2004). Subduction zone volcanics, on the other hand, are usually derived from silicate liquids with a small fraction of dissolved water. Between departure from the subducted slab and arrival at the volcano a vast change in silicate

content of the fluid must occur. This change has been attributed to hydrous melting, however it may equivalently be considered a reactive dissolution process. In this reactive framework an aqueous fluid rising from the slab through mantle of lower pressure and higher temperature becomes undersaturated in silicate components. It would thus be expected to dissolve silicate from the mantle matrix to reach equilibrium.

To formalize the reactive framework we must define a set of phases and components and specify the equilibrium state of the fluid phase (in terms of the concentrations of one or more components) as a function of temperature, pressure and composition. At its most complex, the set of phases would include all the mineral phases of the upper mantle, two immiscible liquid phases and a vapor phase, with the corresponding set of all mantle, slab, sediment and volatile components. In addition to incurring a prohibitive computational cost, the equilibrium state of such a system is not sufficiently constrained for our purposes (*Hirschmann et al.*, 1999). For efficiency, tightness of chemical constraints and ease of interpretation we choose the simplest possible system: two phases (solid and fluid) and two components (rock and water).

The equilibrium fluid state of binary monomineral–water systems at mantle-type pressures, temperatures and bulk water content has been studied extensively, especially the albite–water and quartz–water systems (*Manning*, 2004; *Hack et al.*, 2005, and references therein). Sub-solidus, these systems typically have low but variable solubilities of the mineral into the fluid and water into the solid. At low mantle pressures and higher temperature they melt eutectically. A solubility loop (and hence critical point) exists for systems that are more water-rich than the eutectic point. Figure 5-1a–b shows that with increasing pressure the eutectic and this critical point approach one another until they merge and the fluid concentration curve is continuous, representing a single, supercritical fluid phase which grades from aqueous fluid at low temperature to silicate melt at high temperature. *Hack et al.* (2005) generalizes this to rock–water systems. A transition to supercriticality has been shown to occur in the peridotite–water system at higher pressures (*Shen and Keppler*, 1997; *Bureau and Keppler*, 1999) and *Hack et al.* (2005) argue that their generalized rock–water phase diagram can be applied to approximately describe this more complex system. At

pressures below the transition to supercriticality this argument breaks down. However, as we show in Figure 5-1a–c and discussed below, the error resulting from this assumption is small.

A continuous solubility curve is convenient because it is consistent with past work on reactive flow modeling and because it stabilizes numerical solvers. Although the pressures relevant for subduction zone magma genesis are lower than those required for supercriticality in the peridotite-water system, we assume that for low bulk water contents a continuous solubility curve is a good approximation. This is supported by the observation that water and other incompatible elements present in low concentration cause a “low productivity tail” in the isobaric melting curve as a function of temperature (*Hirschmann et al.*, 1999). Furthermore, it is generally accepted that there is no eutectic for peridotite melting. Figure 5-1c shows that there is only a small difference in dissolved silica content as a function of temperature along a supercritical curve and a eutectic melting curve.

To parameterize the sigmoidal curve described by *Hack et al.* (2005), we specify the solubility of rock into the fluid as a function of temperature and pressure at fixed bulk water content. A convenient form is:

$$f(T') = (1 + \alpha T'^\beta) \tanh \frac{T'}{\lambda} \quad (5.1)$$

where $T' = 2T/T_{dry\ liquidus} - 1$. This definition for T' is chosen to control the position of the solidus in temperature by fixing it as one half the temperature of the liquidus, in degrees centigrade. For $T' > 0$, $\alpha = \alpha_1(P)$ and $\beta = \beta_1$ while for $T' < 0$, $\alpha = \alpha_2$ and $\beta = \beta_2$. α_1 is a linear function of pressure. The equilibrium concentration of rock in the fluid is then

$$C_f(T') = \frac{f(T') + 1 + \alpha_2}{2 + \alpha_1 + \alpha_2}. \quad (5.2)$$

The pressure dependence of solubility can be accounted for by giving $T_{dry\ liquidus}$ a quadratic dependence on pressure as in *Katz et al.* (2003). We then calibrate this function by fitting it (by inspection) to the output of a parameterization of hydrous melting (*Katz et al.*, 2003). The large number of parameters in this formulation arise

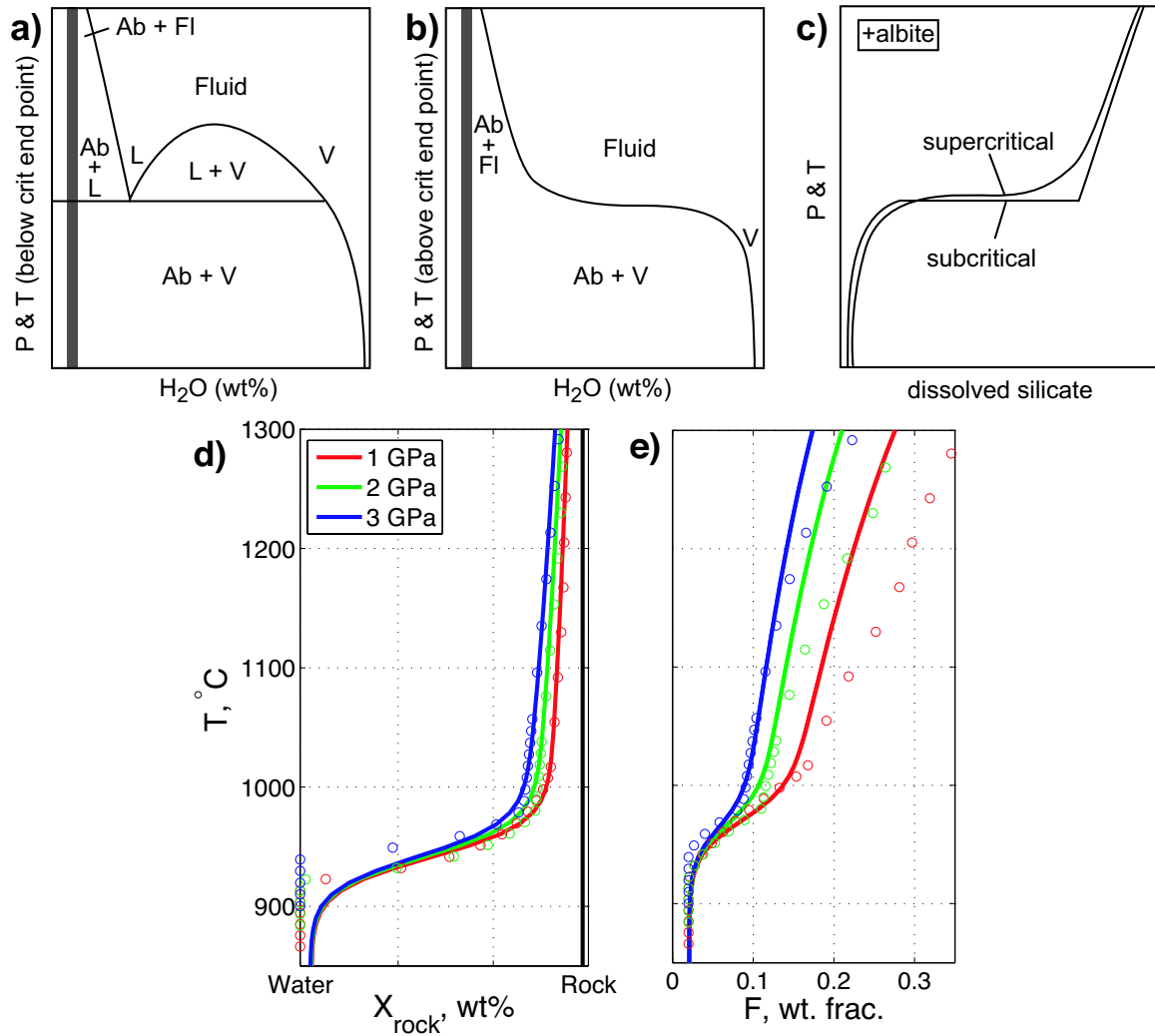


Figure 5-1: (a)-(c) Phase relations in the model system albite-H₂O along geothermal gradients in which P and T increase after *Manning* (2004), justifying the simple parameterization of hydrous mantle melting adopted in the initial stages of this study. Abbreviations: Ab, albite; L, liquid; Q, quartz; Fl, fluid; V, vapor. (a) and (b) illustrate relations along paths crossing respectively below and above the second critical end point in the system (*Shen and Keppler, 1997; Stalder et al., 2000; Manning, 2004*). The consequence of a critical end point is the change from a discrete solidus to a continuous melting interval. As shown in (c), this can be expressed in water-poor systems (dark-shaded compositions in (a) and (b)) in terms of the change in dissolved silicate in the fluid phase (H₂O-rich vapor or melt) with P and T. Comparison of the two paths indicates that there is little difference in the shape of these solubility curves. Our strategy has been to adopt a parameterization, shown in panel (d), that assumes melting behavior like that of a supercritical system. The resulting curves are then calibrated to the *Katz et al. (2003)* melting parameterization (points in panels (d) and (e)). There is a discrepancy between the two parameterizations in silicate content at low temperature because the melting parameterization of *Katz et al. (2003)* does not consider the small solubility of rock into water at temperatures below the solidus.

from designing an easily tuned curve that is specified in a symmetric manner around the solidus. A more careful study could reduce the number of parameters. The shape of the curve, however, and the eventual results obtained by using it in reactive melting calculations, would be largely unchanged.

Results of this calibration are shown in Figure 5-1d–e. Although we calibrate our parameterization of equilibrium solubility for a 2 wt% bulk water content system, we find that the solubility parameterization is in agreement with the melting parameterization for bulk water contents between 0.1 and 3 percent. The use of a pseudo-phase diagram to prescribe melting properties of the rock–water system produces a result inconsistent with observations (e.g. *Stolper and Newman, 1994*) and theoretical predictions (e.g. *Katz et al., 2003*), however. According to the pseudo-phase diagram parameterization, a system at a fixed temperature will vary in melt fraction with increasing bulk water to maintain *constant* water content of the melt. In contrast, the generally held view is that at a fixed temperature, addition of bulk water to the system will cause melt fraction to increase but less rapidly, such that the water content of the melt actually increases with increasing melt fraction. If the melting system indeed functions according to the latter scenario there may be consequences for predicted water content of melts that are not captured by the simulations described here.

With the solubility of rock in water expressed as a function of pressure and temperature and given a vertical temperature profile, a vertical profile of porosity and fluid composition can be calculated that is in a steady state, using the governing equations in the limit of zero compaction length. In this state, if we consider the high Damköhler number limit of the conservation of composition equation for the fluid and assume that the solid matrix is static and that there is an instantaneous balance between advection and reaction we find that the melting rate, Γ , scales as

$$\Gamma \propto \frac{\phi w}{C_R - C_f} \frac{\partial C_f^{eq}}{\partial P} \quad (5.3)$$

where ϕ is the volume fraction of melt, w is the vertical velocity of the melt, $C_R - C_f$

is the difference between the concentration of rock in the reaction product and in the fluid, and $\partial C_f^{eq}/\partial P$ is the slope of the equilibrium solubility curve along the arc geotherm. Figure 5-2 shows two temperature distributions and their resulting equilibrium and melting rate curves. The temperatures are imposed as an initial condition (and a reference state for the source term in equation (5.5)) but the melting rate and the equilibrium concentration of rock in the fluid are determined by solving the steady-state, zero compaction length approximation of the governing equations.

5.2.2 Physics

The physics of reactive open-system melt transport through a viscously deformable porous medium has been described by other authors (e.g. *Spiegelman et al.*, 2001). The conservation of mass equations for individual components, which augment the conservation equations in chapter 1, are presented by *Spiegelman et al.* (2001) and will not be repeated here. To extend this system for a temperature-dependent fluid equilibrium we require knowledge of temperature over the domain. Hence, in addition to the equations described by *Spiegelman et al.* (2001), we enforce the conservation of energy expressed as a temperature evolution equation. A conservation equation for the energy of a two-phase continuum with mass transfer representing magma-genesis in the mantle was derived by *McKenzie* (1984) and is given in expanded form in equation (1.7). We neglect changes in temperature due to (de)compression and differences in specific heat and thermal diffusivity between the solid and fluid phases. With these simplifications equation (1.7) becomes

$$\frac{\partial T}{\partial t} + \mathbf{v}_T \cdot \nabla T = \frac{-T\Delta S}{\bar{\rho}c_P}\Gamma + \kappa\nabla^2 T + S(\phi, T, \mathbf{x}), \quad (5.4)$$

where $\mathbf{v}_T = \frac{\rho_f\phi\mathbf{V} + \rho_s(1-\phi)\mathbf{V}}{\bar{\rho}}$ is the velocity at which heat is advected and $\bar{\rho} = \rho_f\phi + (1-\phi)\rho_s$ is the porosity-weighted density. This equation states that the temperature at a point fixed in the two-dimensional domain is controlled by advection, latent heat transfer, diffusion and a source term. Except for compaction and expansion, the solid is static in the simplified computations described here and thus advection of heat

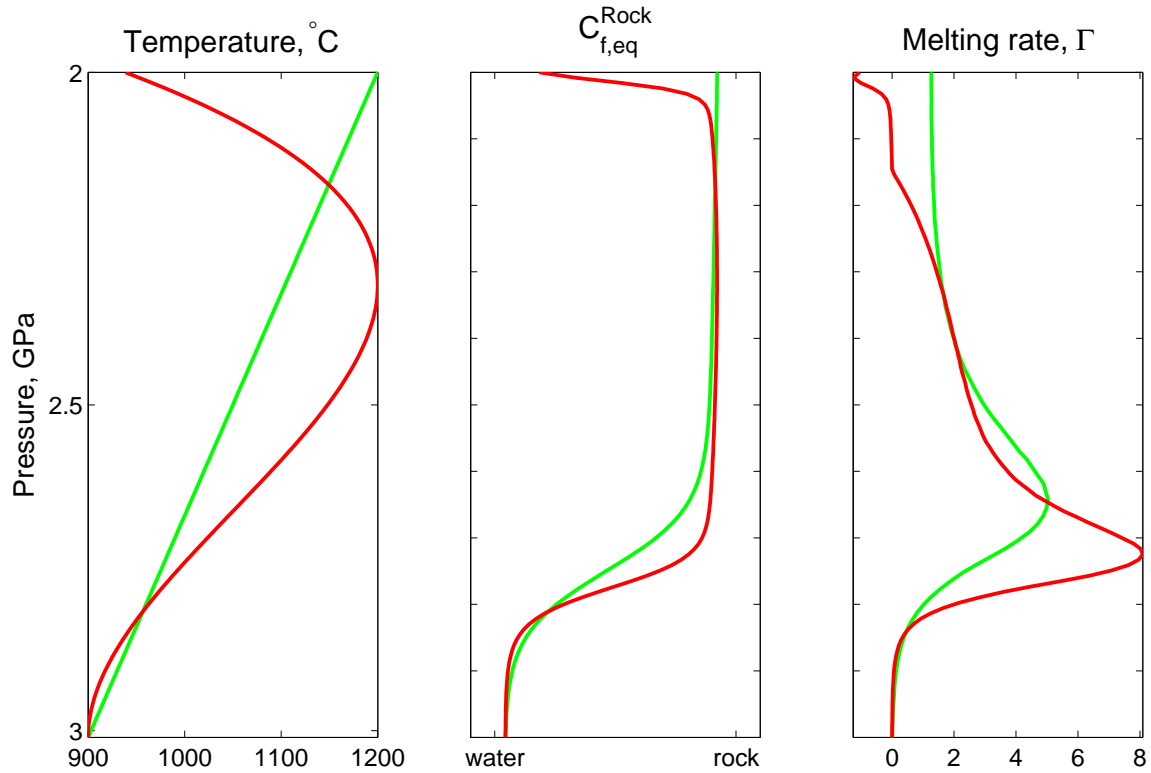


Figure 5-2: Two initial condition of vertical distribution of temperature and the resulting equilibrium content of rock in the fluid and dimensionless melting rate. The green line shows the initial condition for the calculation shown in Figure 5-3 and the red line shows the initial condition for Figure 5-4. **(a)** Imposed vertical temperature profile. The green line is a crude representation of the temperature field immediately above the slab: temperatures increase upward. The red line represents the temperature field between the slab and the bottom of the lithosphere. Both of these are simple approximations to a more realistic geotherm shown in Figure 5-6. **(b)** Equilibrium concentration of rock in the fluid given the temperature-pressure curve in panel (a). **(c)** Dimensionless melting rate given the temperature-pressure curve in panel (a). Note that precipitation is occurring at the bottom of the lithosphere in the simulation initiated with the red temperature profile. The curves in panels (b) and (c) are calculated by solving the steady-state, zero compaction length approximation of the governing equations.

is mainly by the fluid. Without transport of heat into the wedge by solid mantle flow, however, melting and melt transport would rapidly cool the wedge. We roughly approximate this advection of heat into the plane of the simulation with the source term S in equation (5.4). We assume that the solid mantle advected into the domain has the temperature structure of the initial T -field of the simulation and that its motion does not displace the pore fluids. With these assumptions the source term is

$$S(\phi, T, \mathbf{x}) = \tau(1 - \phi) [T(\mathbf{x}, t = 0) - T(\mathbf{x}, t)] \quad (5.5)$$

where τ has dimension of inverse time and is a number between zero and one parameterizing the fraction of the solid replaced with new solid advected in from outside the domain, carrying heat with it. The value of τ is typically set to be 0.03 kys^{-1} . The value of τ is set to keep the simulations from changing its temperature field too much from the initial temperature field. It should be noted, however, that this parameter is poorly constrained and the effect of variations has not been carefully explored.

The boundary conditions specified on the top boundary are very important for the behavior of the simulation. The vertical gradient in the compaction potential is set to zero across this boundary, although the horizontal gradient is not specified, allowing for compaction at and near the boundary. The gradient in concentration of the solid is also set to zero. This condition has little effect. The equilibrium fluid concentration is calculated as within the domain. The fluid concentration is also calculated as within the domain, however that fluid velocity on the boundary is calculated differently from inside the domain. The fluid velocity on the boundary is computed assuming zero dynamic pressure gradient—that is, the pressure gradient there is due to fluid buoyancy only. Finally, and most importantly for what is to follow, the temperature condition on the boundary is very loose: it specifies that there is no diffusion of temperature on the boundary by setting $d^2T/dz = 0$. It is only the effect of the source term, which acts as a “restoring force” on the temperature at every point in the domain, which forces the simulation to remain close to a given value of temperature at the boundary. This is, in effect, a mixed boundary condition. It

allows the advection of heat by the fluid to modify the temperature on the boundary.

Another important aspect of these calculations is how we treat the bulk viscosity. We adopt a form for the viscosity governing compaction proposed by *Sleep* (1988) and used by *Spiegelman et al.* (2001),

$$(\zeta + 4\eta/3) = \frac{(\phi_c/\phi)^m + 4/3}{\phi_c^m + 4/3}. \quad (5.6)$$

This equation states that the compaction viscosity $(\zeta + 4\eta/3)$ is nearly constant for porosities greater than the “compaction viscosity” ϕ_c , but becomes infinite for $\phi \ll \phi_c$.

We solve the magma dynamics equations plus conservation of energy and composition using the Portable Extensible Toolkit for Scientific computation (PETSc, *Balay et al.*, 1997, 2001, 2002) on a domain oriented parallel to the strike of the arc as shown in Figure 5-3a. The base of the domain sits just above the surface of the subducting slab and thus receives a flux of slab-derived fluids from below. The top of the domain is positioned either at the core of the wedge (green lines in Figure 5-2 and results in Figure 5-3) or above it in the upper thermal boundary layer of the wedge (red lines in Figure 5-2 and results in Figure 5-4). Orientation of the domain in this manner is convenient because it permits us to employ a simple, rectangular grid and a wrap-around boundary condition on the side boundaries.

5.3 Results

Fluid channelization is an expected consequence of the Reaction Infiltration Instability (*Chadam et al.*, 1986; *Daccord and Lenormand*, 1987; *Aharonov et al.*, 1995), which is active when a reactive fluid percolates through a soluble matrix from a zone of lower solubility to a zone of higher solubility. Regions with higher melt flux undergo more dissolution (as is evident in equation (5.3)) and thus a higher porosity, permeability and melt flux. Small perturbations grow and lead to a channelized porosity/permeability structure (*Aharonov et al.*, 1997; *Spiegelman et al.*, 2001).

5.3.1 Flow from the slab surface to the core of the mantle wedge

Models of reactive flow from the slab to the core of the wedge have results that are easy to interpret in terms of past work on reactive magmatic flow (*Spiegelman et al.*, 2001). The flux of magma in these calculations rapidly localizes into high porosity channels, shown at a late simulation time in Figure 5-3b. High rates of reaction are observed in calculations where fluid crosses the “wet solidus” of the rock phase. This is the temperature at which the equilibrium concentration of the fluid shifts sharply from water-rich to rock-rich, shown in Figure 5-1d. The corresponding increase of the reaction rate Γ with height is shown in Figure 5-2c. *Fang and Spiegelman* (2004) suggested that the rate of channelization in compactible systems is related to the change in solubility over a compaction length. Hence it is not surprising that channels in Figure 5-3b nucleate at a height in the domain where the reaction rate is at its peak.

In the calculation of hydrous reactive flow in Figure 5-3b, porosity in the channels is around 10% (although they grow larger than this with time) while inter-channel regions compact down to less than 1% porosity, although the latter depends on the details of the assumed bulk viscosity. Figure 5-3c shows that channels are marked by fast vertical velocities. Fluid in channels in these calculations moves about 10 times faster than fluids in diffuse porous flow calculations. This rapid ascent rate means that channel fluids remain further from equilibrium than inter-channel fluids. Contours in Figure 5-3b show the mass fraction of water content in the fluid and demonstrate that fluid rising rapidly through the channels is enriched in water relative to fluid outside the channels. This is not due solely to the disequilibrium between the rising fluid and the mantle matrix, however. Contours in Figure 5-3c show that the localized flux of fluids through the channels modifies the temperature field. Fluids flowing from colder to hotter temperatures cool the surrounding matrix rock. This cooling is enhanced by the removal of heat from the matrix to balance the latent heat of dissolution reactions, which are concentrated in the channels. In the calculations these effects are manifest

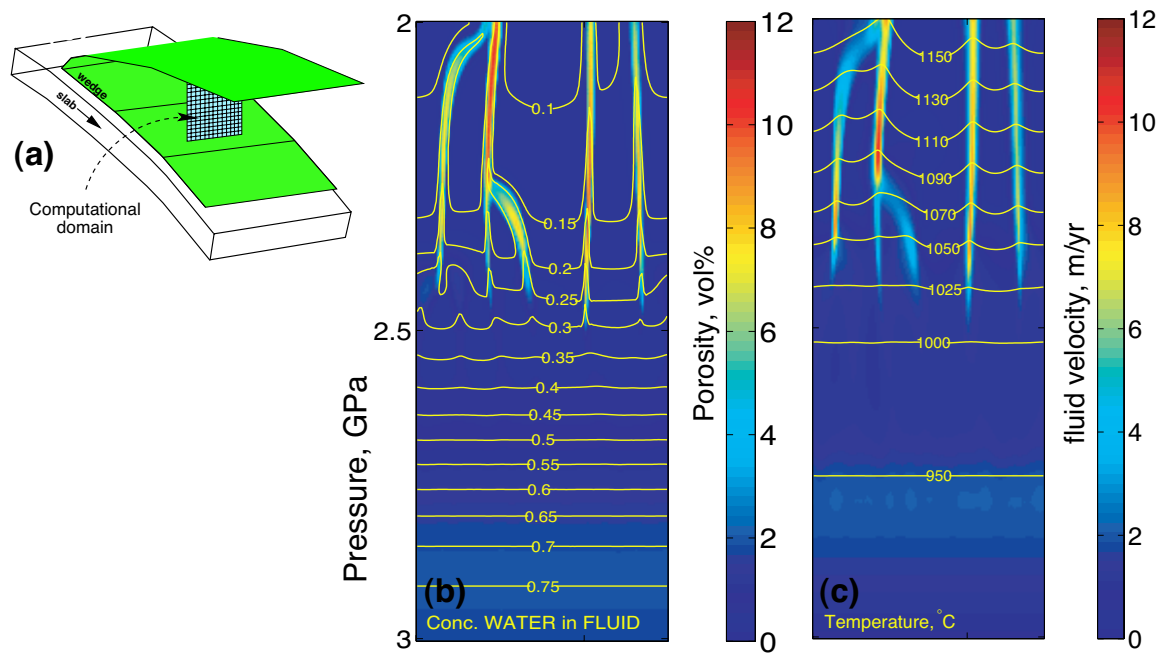


Figure 5-3: Results from one time-step of a simulation of hydrous reactive flow through the inverted thermal boundary layer in the mantle wedge above the subducting slab. **(a)** Schematic diagram illustrating position and orientation of the computational domain with respect to the trench and subducting slab. **(b)** Snapshot of porosity (colors) and weight fraction of water in the fluid (contours). **(c)** Vertical fluid velocity in cm/year (color) and temperature in degrees centigrade (contours).

in channels that are colder than the surrounding rock by about 20 degrees centigrade above the slab in the core of the wedge. The effect of lower temperatures in channels is to raise the equilibrium solubility of water, suppressing dissolution and making the channel fluids more water-rich. As we shall see below, the opposite occurs as fluids percolate from the wedge core to the colder lithosphere above.

The shape of channels is generally consistent with previous calculations by *Spiegelman et al.* (2001), however in the calculations described above, there seems to be comparatively less upward coalescence of channels. This may be due to the fact that calculations by *Spiegelman et al.* (2001) used a linear solubility curve with a constant slope and an approximately constant compositional difference between the equilibrium fluid composition and the composition of fluid generated by dissolution, yielding a channelization rate that is approximately constant with height in the box. Here, a strongly non-linear solubility curve is used (Figure 5-1d), which yields a reaction rate with a peak at the height where temperatures cross the solidus. Above this height in the core of the wedge, steady-state fluid solubility is roughly constant with height and reaction rates are lower. Channels that nucleated below in the reactive zone “coast” through this unreactive zone, neither decaying nor coalescing. As we shall see below, however, the situation changes when we consider the case of fluid flow from the cold slab through the hot wedge and into the cold lithosphere.

5.3.2 Flow from the slab surface to the lithosphere overlying the wedge

Magma erupted from arc volcanoes must traverse not just the hot wedge but also the cold lithosphere. The base of the lithosphere is clearly visible in Figure 3-3 where viscosity changes by several orders of magnitude over a small distance. The temperature at which this transition occurs is much higher than the temperature at which peridotite becomes brittle. Thus, at least over a portion of the thickness of the lithosphere, magma may travel via porous flow, as in the asthenospheric mantle. One caveat to this logic is that if fluid pressures are high enough, they can cause the rock

to hydrofracture, even if it is hot. Lower temperatures in the lithosphere would be expected to cause freezing (or equivalently, precipitation) of components of the rising magma, enriching it in water. Volcanoes erupt lava, however; evidently magma must traverse the mantle lithosphere to arrive at the brittle crust in some manner.

Simulations that impose an initial temperature field that increases with height and then decreases show interesting and unexpected results. A time series of porosity and temperature fields from a simulation is shown in Figure 5-4. In this simulation an initial temperature profile given by the red curve in Figure 5-2a was prescribed. The curve is not a profile derived from a thermal structure simulation (as in Figure 5-6) but the two share an important characteristic, namely that they are cold at the depth of the slab-wedge interface, increase in temperature with height to a maximum and then decrease back to colder temperatures below the surface.

Figure 5-4 shows a simulation that starts with a horizontally uniform porosity field. With time, high porosity channels emerge. These channels coalesce into bundles of channels. The coalescence point begins near the base of the cold lithosphere and propagates downward. The result is a wide channel that carries a very high flux of melt derived from ~ 5 smaller channels that feed it. Contours in Figure 5-4 demonstrate how the temperature field is affected by fluid flow and melting in the channel bundle: below the core of the wedge the channel is cooler than its surroundings, above it is warmer. The fluid advects enough heat to create a high temperature pathway through the lithosphere. It traverses this pathway precipitating less rock than it would have if it crossed the same height interval without a hot pathway. To understand this result it is important to recall that the local temperature within the domain is controlled by the balance of diffusion, (fluid) advection and a source term that represents heat flow in the 3rd dimension. In the lithosphere where fluid advection acts to add heat and increase the temperature, the source term acts to decrease the temperature. To maintain a hot pathway through the lithosphere the flux of magma must transport enough heat to balance losses. This is discussed further below.

Another noteworthy feature of the results, shown in Figure 5-5, is that the channel bundles are capped, near the base of the upper thermal boundary layer, with a pod-

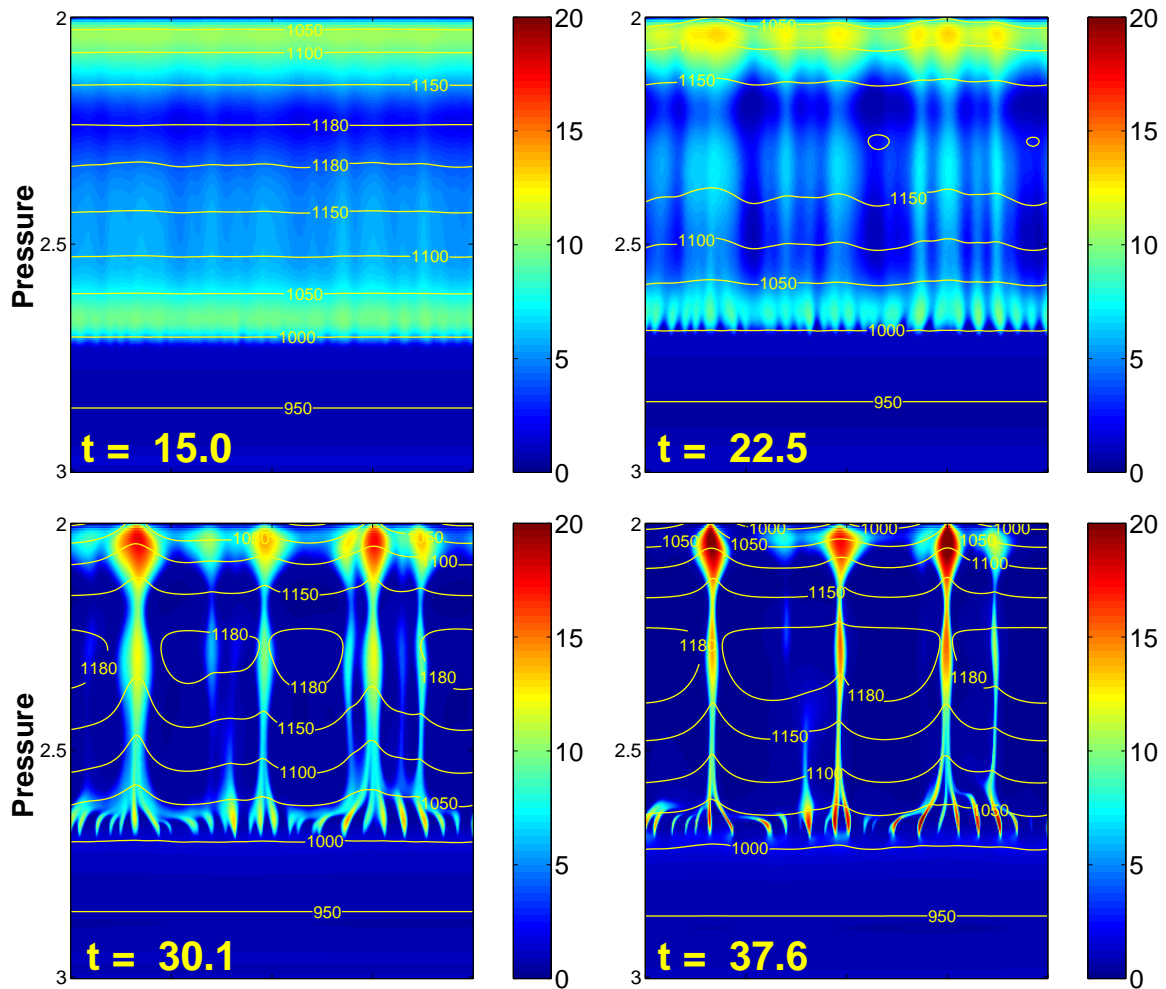


Figure 5-4: Porosity (color) and temperature (contours) at four non-dimensional times in a hydrous reactive melting simulation. Temperature increases above the bottom of the domain into the wedge core and then, unlike in Figure 5-3, decreases with height toward the surface. Channels form and immediately begin to coalesce into bundles that tighten with time. These channel bundles carry a large flux of melt and are able to significantly perturb the temperature field. Freezing melt near the top boundary lowers the permeability and confines outflow to narrow, high porosity gaps. Below these gaps, melt pools in high porosity zones. We are exploring hypotheses for the mechanism of coalescence.

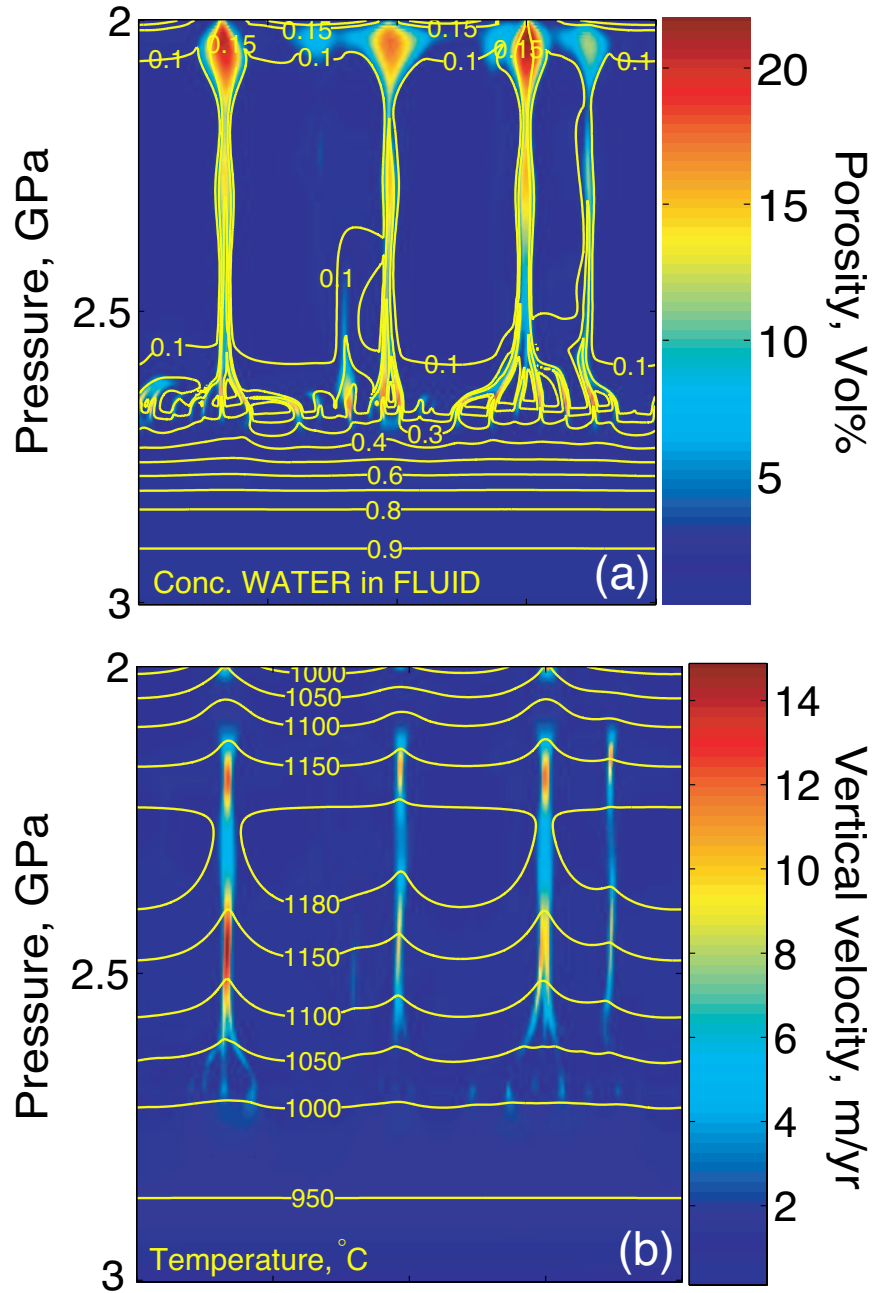


Figure 5-5: Results from the same calculation as in Figure 5-4 comparing porosity, fluid composition, vertical fluid velocity and temperature fields. **(a)** Porosity field (color) with overlaid contours of water concentration in the fluid. Rapid flow through the channel bundles leads to high water concentrations in the bottom half of the domain and that can persist through to the top of the domain. **(b)** Vertical fluid velocity (color) with overlaid contours of temperature. Fluid velocities are calculated assuming a velocity scale w_0 of 1 m/yr after *Spiegelman et al.* (2001). This is a conservative estimate and may be low by 2 orders of magnitude. (Since time in this calculation is scaled by δ/w_0 , all rates scale with this ratio as well. So the input flux, the melting rate and the melt velocity all vary together with changes in w_0 .) Note the stagnation of melt in the high porosity “pods” at the base of the cold thermal boundary layer.

shaped zone of high porosity where magma stagnates before moving rapidly through the top of the domain. This may be a feature observable in seismic images of the sub-arc lithosphere and mantle.

5.4 Discussion

The calculations described in this chapter indicate that flux channelization in subduction zones is an expected consequence of the gradient in the solubility of rock into the aqueous fluids that are released from the subducting slab. *Fang and Spiegelman* (2004) show that for reactive melting beneath mid-ocean ridges, channelization is expected only if the ratio of melt upwelling velocity to solid upwelling velocity is high and that the solubility gradient is sufficiently large (*i.e.* the solid viscosity is sufficiently high). Rapidly upwelling fluids traverse the solubility gradient driving reaction faster, yielding larger reaction rates relative to the adiabatic melting rate. In subduction zones, upwelling of solid mantle may occur but its geometry is such that flow is not directly upward, but sub-parallel to the slab, and hence not likely to be as fast as melt upwelling rates. Furthermore, the solubility gradient of rock is very steep as fluids cross the sharp temperature gradient above the slab (see Figure 5-6). Here the amount of dissolution per compaction length rise is much larger than expected beneath ridges and hence the growth rate of the channelization instability is very high. If the solubility model presented here is roughly correct, high permeability channels are likely to be present in subduction zones. To further test this hypothesis, however, many more calculations are needed.

Assuming that this model of fluid flux channelization in arcs is correct, it is interesting to consider the predicted consequences for lava chemistry. The observation of Radium disequilibria in young arc lavas by *Turner et al.* (2001), for example, and the positive correlation of Radium disequilibria with Barium–Thorium ratios suggest rapid transit of fluids from the slab to volcanoes in subduction zones (*Turner*, 2002). The transport of fluids through high permeability channels could provide a pathway for bringing radioactive nuclides from the subducting slab to volcanoes about an or-

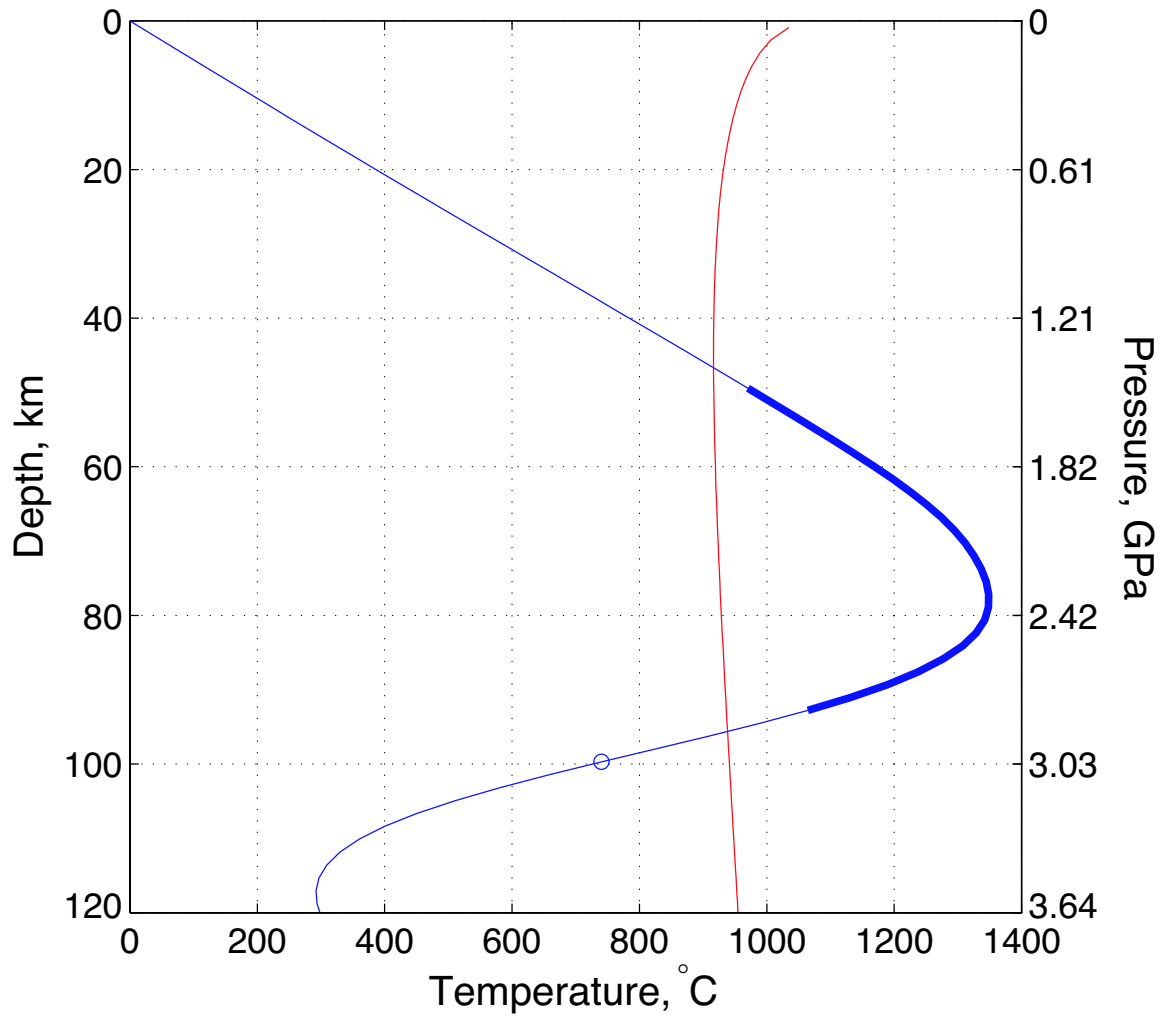


Figure 5-6: Subduction zone geotherm (blue) and solidus (red, assuming 1 wt% bulk water) taken at 100 km from the “trench” from the temperature field shown in Figure 3-2b. The thick section of the blue line marks the section of the geotherm that passes through viscosities below 10^{22} Pa-s in the wedge. The open circle on the blue line marks the point where the geotherm crosses the slab surface.

der of magnitude more rapidly than by diffuse flow. Assuming $w_0 = 1$ m/yr, channel velocities could be about 10 m/yr and 100 km of mantle could be traversed in 10^4 years (about 6 half-lives of Radium-226). If w_0 is larger by an order of magnitude then this time would be reduced to 1000 years. 10^3 - 10^4 years is within the range of transit times preferred by *Turner* (2002).

Results shown in Figure 5-3 suggest that unlike diffuse porous flow, channelized flow can modify the temperature structure of the two-phase medium. This has also been observed in experiments by *Solomon and Hartley* (1998) on convection in a mushy layer. In these experiments the Reactive Infiltration Instability produces open chimneys that transport undersaturated melts at a different temperature than the ambient surrounding permeable mush. The modification of local temperatures by fluid flow has implications for equilibrium fluid composition as well as for arc heat flow. Most significantly, models (e.g. Figure 5-4) predict that fluid flow can modify the thermal structure at the base of the lithosphere, leading to focusing of flow, melt pooling and high-temperature shallow equilibration. One can speculate that the focusing that causes channels to coalesce into bundles is caused by an instability in the interaction with a cold thermal boundary layer. This is illustrated schematically in Figure 5-7. Channel-induced fluctuations in the thermal boundary layer topography could reinforce magmatic focusing. This would occur according to a mechanism proposed by *Sparks and Parmentier* (1991) whereby melt moves laterally along a cold, sloping thermal boundary because colder temperatures directly above cause crystal precipitation and decreased permeability. A feedback could result if melt focusing modifies the local slope of the base of the lithosphere, leading to more focusing. If such a focusing mechanism is active, the depth at which melts last equilibrate with the mantle may be buffered by the extent to which advective heat transport can preserve the ductile flow regime to shallow depths. Testing these ideas will require the use of simplified computational models coupled with physical experiments.

Another interesting speculation that can be made about channel bundles and their penetration into the lithosphere is that this process selects the along-arc spacing of volcanoes. If coalescence of channels into bundles occurs by a thermal erosion

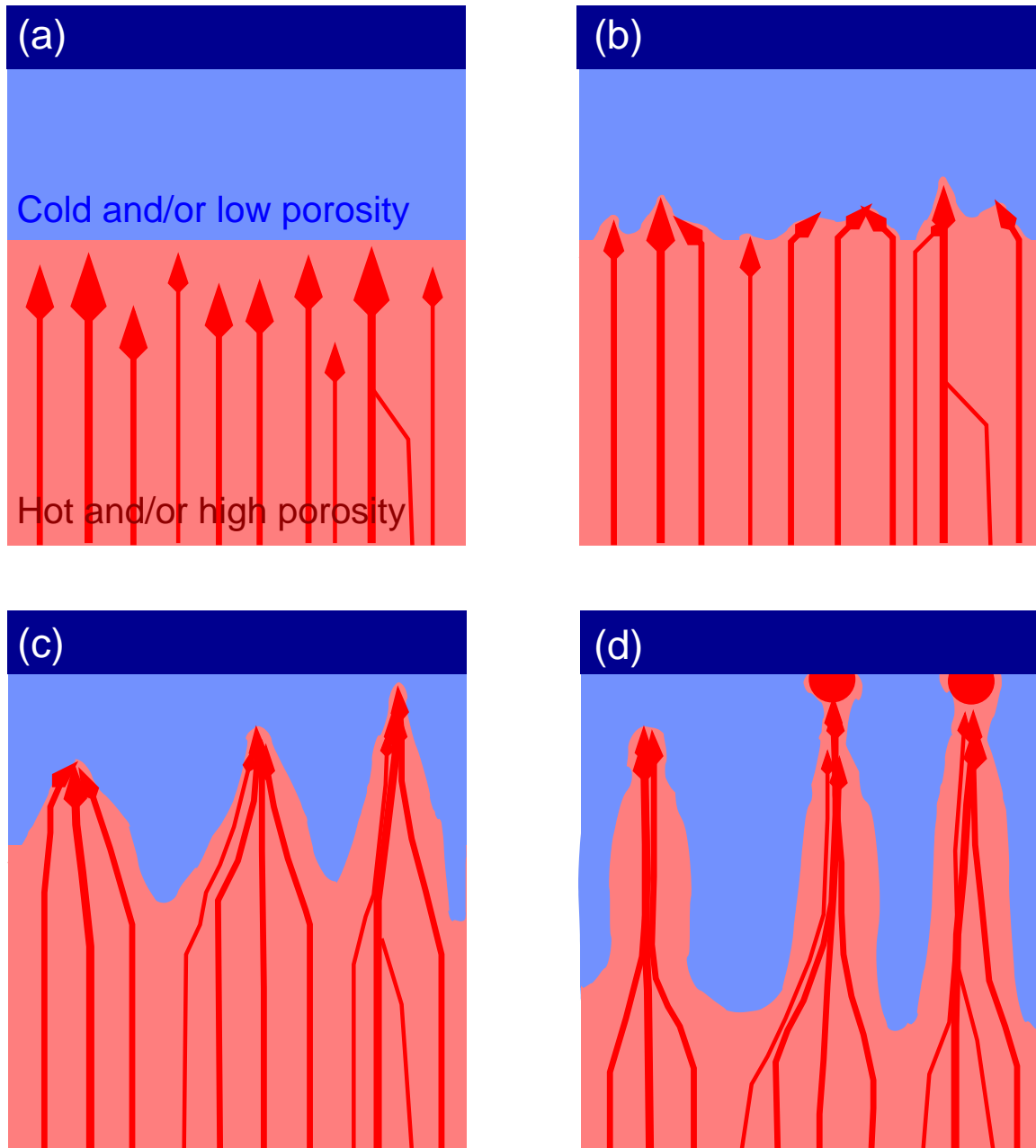


Figure 5-7: A schematic illustration of the proposed magmatic focusing instability. The blue regions represent cold, compact mantle. The pink areas represent hot, porous mantle. Red arrows represent highly porous channels. Channels impinge on the thermal boundary layer and perturb its topography. Melt follows upward along the sloping boundary by the mechanism proposed by *Sparks and Parmentier* (1991). This focusing produces more efficient thermal erosion of the boundary layer and coalescence of channels. As localized thermal erosion advances upward, regions between the channel bundles compact and become almost impermeable, pushing the coalescence point downward and forcing horizontal melt transport into the high-flux channel bundles.

process then the separation of these bundles may be controlled by thermal properties of the magma/mantle system. For example, the diffusivity and heat capacity of the lithosphere and the latent heat of freezing could all contribute to determining the total flux of magma that must be focused in order to deliver enough heat to penetrate the lithosphere. Then the spacing of volcanoes would reflect this required flux. Uncertainties in the parameters that go into determining the compaction length, especially the reference mantle viscosity and permeability, however, leads to variation in the predicted spacing of bundles by 2-3 orders of magnitude. Before simulations of the complexity described here can be confidently interpreted, simpler models must be used to test the validity of the focusing hypothesis.

5.5 Future work

Much work is required to better understand and quantify the results described here. It can be divided into three general projects, however, that may each be undertaken separately. The first two involve stripping complexity from the current model to investigate the basic controls on channelization and channel coalescence. The third project involves adding complexity to the model in order to generate testable geochemical predictions.

We have shown that under reasonable assumptions regarding the compositional equilibrium between a hydrous fluid and mantle, reactive flow calculations produce channelized melt flux. The sensitivity of the result to these assumptions, both in terms of the existence and characteristics of the channels, has not been investigated. It would thus be useful to perform an exploration of parameter space associated with the solubility gradient and equilibrium parameterization: the steepness and profile of the temperature gradient itself, as well as the sharpness of the solidus transition in the pseudo-phase diagram in Figure 5-1d. These calculations would be done on a domain that extends from the slab to the wedge core, as in Figure 5-3. Furthermore, simplifications to the physics and parameterized chemistry could be made to eliminate parameters from the problem and isolate the fundamental controls

on the channelization instability in this system.

The coalescence of channels into channel bundles as shown in Figure 5-4 is an intriguing result of our calculations. Although this behavior was observed in a number of model runs with cold lithospheric thermal boundary layers above the melting region, we can only hypothesize about the mechanism and relevant controls. Many more simulations and analysis are needed to explore how the initial temperature structure, temperature source term and thermodynamic parameters affect the predicted channel structures. This should be done using the current model as well as a reduced model. The domain of the reduced model would extend from the wedge core below through the cold thermal boundary layer above. Equilibrium fluid inflow would be prescribed at the base of the domain as either channelized flux or uniform flux. The reduced model would incorporate a simplified parameterization of equilibrium fluid composition with a more gentle solidus transition to improve numerical convergence. This model would permit an exploration of the physics of channel coalescence and melt focusing through the lithosphere by isolating parameters that may be important such as channel existence, spacing and flux, structure of the initial temperature profile and the strength of the temperature source term.

Future calculations intended to explore melt–lithosphere interaction should be accompanied by physical analog experiments like those carried out by *Kelemen et al.* (1995b) that recreate the situation of precipitating reactive porous flow through a cold thermal boundary layer. Experiments would provide a means for investigating the focusing hypothesis described in Figure 5-7 without the assumptions that are associated with a computational simulation of relatively high complexity.

A model capable of making predictions of geochemistry (such as an estimate of Radium disequilibrium, discussed above) would be a useful tool for testing hypotheses on the dynamics of subduction zones. It will necessarily be more complex than the model described in this chapter. Simpler models are still essential for developing an understanding of the basic behavior of the hydrous reactive system. The first step in building a geochemical transport model is combining reactive flow calculations with arc solid flow and thermal structure calculations from chapter 3 in a 2D domain ori-

ented perpendicular to the trench. This model would also need a parameterization for fluid release from the subducting slab as well as a parameterization to calculate adiabatic melting. With these components it would provide a self-consistent framework for tracing the flow of energy and chemistry, including radiogenic isotopes, from the slab to the base of the crust. There are many technical challenges that must be overcome to build such a model, however, and therefore this project is a significant undertaking.

5.6 Conclusion

The calculations presented here are a preliminary investigation into the consequences of reactive flow in a subduction zone setting. Results show that channelization of fluid flux is a physically plausible scenario in subduction zones and that channelized flux is different in significant ways from diffuse porous flow. Some of these differences may have observable consequences, such as rates of fluid transport from the slab to the arc.

We have developed a new approach to modeling hydrous melting in arcs, one that is based on experimental investigations of rock–water equilibrium and is well suited to open-system reactive flow calculations. The parameterization of water content in the fluid is formally consistent with previous work on reactive modeling of magma transport (*Spiegelman et al.*, 2001). However, it prescribes an equilibrium state that is a function of both pressure and temperature, where previous work used a pressure-dependent equilibrium. To supply temperature values to the parameterization we solve the conservation of energy equation for the two-phase medium. This allows us to explore thermal effects of reactive flow that had not previously been modeled. We show that a channelized flux of fluids can modify the temperature field and hence the equilibrium transport of solutes. We also show how advected heat delivered to the base of the lithosphere can change the topography of this thermal boundary layer, possibly resulting in magmatic focusing.

The results obtained here are qualitative. They show that by making a large

number of reasonable assumptions about the physics, chemistry and thermodynamics of the magma/mantle system in subduction zones, a predicted instability leads to channelization of fluid flux. The details of this process, including the spacing of channels and their porosity, width and flux, are not quantitatively predicted by these calculations. Numerical and analytical investigations conducted for this thesis as well as elsewhere (*Aharonov et al.*, 1995, 1997; *Spiegelman et al.*, 2001; *Fang and Spiegelman*, 2004) all suggest that the instability is robust: it occurs under a wide range of parameters and mechanical assumptions. While much work remains to be done to understand the characteristics and implications of channelized melt flow in subduction zones, work presented here has demonstrated its physical plausibility for the first time.

Chapter 6

Discussion

6.1 Summary

Much work is needed before models that are capable of addressing the questions raised about subduction in the Introduction can be developed and interpreted. The chapters of this thesis describe my research on general magma dynamics and subduction-related dynamics that will be useful in reaching that long-term goal. Chapter 2 shows that mechanical interactions between magma and mantle rock can lead to localization of porosity and shear. The orientation of these localizations, if present in the Earth, would affect the permeability structure of the mantle and have important implications for seismic anisotropy (*Holtzman et al.*, 2003b). This orientation is shown to be governed by the balance between porosity and strain rate-weakening mechanisms of the two phase aggregate. The localization places significant demands on the computational method and grid resolution of models. Preparations must be made to handle these challenges if their presence is expected in large-scale magma dynamics simulations.

Chapter 3 reports work on a single phase model of creeping mantle flow through a subduction zone and the resulting temperature field. The results are similar to those obtained by other investigators (*van Keken*, 2003b) and show the importance of employing (at least) temperature-dependent viscosity. The role of stress and pressure-dependence of viscosity in determining the flow field and thermal structure of arcs (in steady-state), seems to be minor. The flow of fluids in a simple, constant porosity

model after *Spiegelman and McKenzie* (1987), however, is shown to be sensitive to the inclusion of stress-dependence of viscosity, however. Stress-dependence was shown in chapter 2 to have an important effect of melt flow and organization. In general, variable viscosity models of arc thermal structure are consistent with the presence of three modes of melting in subduction zones: adiabatic, reactive hydrous and slab melting. Such models can serve only as the context for melting, however, because they do not explicitly track fluids and interphase reactions.

A framework for reactive porous flow of fluids through the mantle exists (*Spiegelman et al.*, 2001) but a simple, computationally efficient parameterization of hydrous mantle melting that is accurate relative to current theoretical and experimental knowledge was lacking. Chapter 4 addresses this gap and provides a means for rapidly calculating equilibrium melt fractions and compositions in a simplified system of rock (composed of olivine and pyroxene) and water. This work is useful not only for models of subduction, however, but as a general tool for geodynamic models of mantle melting (see Appendix A, for example).

The melting parameterization presented in chapter 4 enabled the development of the first model of reactive hydrous flow and melting in arcs described in chapter 5. It is used to calibrate the rock–water pseudo-phase diagram critical for the adaptation of previous work on reactive flow. Chapter 5 shows that the reactive flow of hydrous fluids rising off the subducting slab into the mantle wedge may lead to channelization of fluid/magma flux with consequences for predictions of the temperature field, rates of fluid transport and fluid compositions in subduction zones. Furthermore, reactive interactions with the lithosphere may lead to channel coalescence and could be related to the along-arc spacing of arc volcanoes. The conclusions and speculations in this chapter are exciting but need much more work to be understood and quantified. The model described in this chapter may serve as a basis for the development of more comprehensive models of subduction zone magma dynamics. Like the work in chapter 2 on mechanical localization, these calculations require high resolution computational grids and advanced solvers. Further progress will require a reconsideration of the numerical methods used here.

6.2 Open questions

Many interesting questions about the dynamics of volcanic source regions remain unanswered. Several were listed in the introduction of this thesis. While this thesis has attempted to address questions about magma dynamics in the mantle beneath arcs, it has raised new questions about volcanic systems in subduction zones and other tectonic settings. What follows is a review of some of the questions about the dynamics of volcanic source regions that interest me.

6.2.1 Buoyancy effects

Buck and Su (1989) suggested that melting could cause active, focused upwelling at mid-ocean ridges by lowering the density and viscosity of the solid–fluid aggregate beneath the ridge. This would clearly be very important as a mechanism of melt production at ridges as well as arcs and hot spots. Its plausibility, however, depends quantitatively on the porosity–permeability relationship. If melt were easily drained from the pores of the solid then melt would separate from the mantle under gravity and would not drive upwelling of solid mantle. On the other hand, if the permeability of the mantle were zero independent of porosity then melting would produce horizontal buoyancy gradients of the two-phase aggregate and hence solid convection. The permeability of the mantle lies somewhere between these extremes and hence to test the hypothesis of *Buck and Su* (1989) requires a computational model with melting, Darcy flow of magma and buoyancy-driven flow of the solid mantle. Such a study is likely to be complicated by the presence of magmatic solitary waves, however.

Even if porosity-driven buoyancy is not important for upwelling and melting of the mantle, active convection may be occurring in subduction zones. *Kelemen et al.* (2002) showed that for a temperature-dependent viscosity and sufficiently large Rayleigh number, cold lithospheric downwellings can perturb steady-state corner flow and give it a time-dependent component. Calculations by *Gerya and Yuen* (2003) suggest that cold plumes of chemically buoyant material could rise off the subducting slab into the mantle wedge. While provocative, this latter hypothesis seems to rely on

low prescribed viscosities of hydrated mantle, slab and sediments. Furthermore, these calculations do not account for the separation of fluids from solids and hence assume that all fluid buoyancy is available for driving upwelling of the solid. A computational study that incorporates these effects and also allows for separation of fluid and solid through porous flow would enhance our understanding of the role of buoyancy in magma genesis in subduction zones.

6.2.2 Rheological effects

Chapter 2 of this thesis (as well as experiments and theory on melt localization going back to *Stevenson* (1989)) demonstrated that the predicted behavior of a deforming two-phase aggregate is drastically different depending on whether the aggregate is modeled as porosity-weakening. To date, however, the effects of porosity weakening of viscosity have only been explored in laboratory experiments and models of those experiments. The important question of how porosity-weakening viscosity modifies the predicted mantle and magmatic flow fields beneath an island arc, mid-ocean ridge or hot-spot has not been addressed. Are strain rates in the partially molten regions of the mantle large enough to produce porosity banding like that seen in experiments? If so, where? What is the orientation of the emergent bands and how do they interact with gravitationally driven magmatic flow? If strain rates are too slow then the mechanical porosity band instability may not produce localization, however high porosity channels resulting from a reactive dissolution instability would presumably localize shear just as effectively, if they are suitably oriented.

6.2.3 Experimental constraints

Whether or not the mechanical instability discussed in chapter 2 is active in the mantle, experiments by *Holtzman et al.* (2003a) provide a rare opportunity to directly test the continuum theory of magma migration because they produce internal patterns that can be compared with simulation. The analysis of those experiments raises questions about the rheology of the partially molten mantle and is thus an important

contribution to the dialog between experimentalists and geodynamic modelers. An important question is then, what other experiments exist or could be performed that would help to constrain the fluid dynamics of magma migration? Also, how can technical obstacles in the simulation of magma–mantle dynamics and localization be overcome? It would be very useful to run simulations of porosity band formation to larger strains, for example, however this has remained impossible because simulations fail to converge as spatial gradients in porosity and strain rate becomes pronounced.

6.2.4 Magmatic focusing

One of the most robust observations of island arcs is the position of volcanoes with respect to the slab: 120 ± 40 km above the earthquakes (e.g. *Gill*, 1981; *Tatsumi*, 1986; *Jarrard*, 1986). This fundamental observation is not well understood, although several hypotheses have been proposed. Many processes are likely to be at play: melt transport along the sloping thermal boundary layer at the base of the lithosphere (*Sparks and Parmentier*, 1991), the depth of coupling of slab–wedge coupling and the resulting wedge dynamics (see chapter 3), the down-dip distribution of fluid-releasing metamorphic reactions in the slab (*Schmidt and Poli*, 1998; *Forneris and Holloway*, 2003; *Manning*, 2004), and the dynamics of reactive transport of fluids and heat through the mantle wedge to the base of the lithosphere (see chapter 5). To resolve the contributions of each of these factors requires a predictive model that self-consistently represents all of them. Such a model could be preliminarily formulated in 2D as long as the domain is oriented perpendicular to the strike of the trench.

It is interesting to ask a more general question about volcanic systems: how is magma that is produced over a large volume of mantle focused down to a narrow vent in the Earth’s crust? Undoubtedly, dikes and other brittle pathways through the crust contribute to the highly localized nature of volcanoes relative to their source regions. Crustal faults are ubiquitous and their spacing is often much smaller than volcano spacing (e.g. in the Cascades and Aleutians, volcanoes have a spacing of about 50 km (*Wood and Kienle*, 1990) along the arc). Furthermore, there is a substantial temperature difference between the base of the brittle section of the lithosphere ($\sim 350^\circ\text{C}$)

and the solidus of hydrous magma ($\sim 1000^\circ\text{C}$). Melt must travel across this temperature difference as it passes through the lower lithosphere. To preserve its heat from conductive loss, magmatic flow must be focused as it crosses the lithospheric mantle. Thus there must be a mantle process that focuses magmatic flow near the base of the thermal boundary layer. This process should be governed by the magma migration equations. One possibility, demonstrated in calculations of magmatic flow in chapter 3, is that the interaction of channelized melt flux with the cold thermal boundary layer induces coalescence of channels in channel bundles that thermally erode the base of the lithosphere. Further work is required to address this suggestion.

6.3 Conclusions

The goal of this thesis has been to develop theoretical and computational tools and insights that contribute to the developing understanding of the source regions of volcanoes. Specific conclusions have been offered at the end of each of the chapters presented here. Two general conclusions can be drawn:

1. The behavior of geodynamic models is strongly dependent on the constitutive law used to define the relationship between stress and strain rate. This is true of large-scale models of mantle flow beneath ridges and arcs as well as in small-scale models of magma–mantle interaction under shear. Chapter 3 and appendix A demonstrate the importance of temperature dependent viscosity in determining a realistic mantle flow field and associated thermal structure. Full solutions to fluid flow in a deforming two-phase aggregate in chapter 2 expose the influence of the strain rate-dependence of viscosity on magma–mantle interactions. Simpler fluid flow calculations in chapter 3 underscore this finding. From these results it can be concluded that models of magma/mantle dynamics should consider the full complexity of the rheology of the mantle. More generally, geodynamic models that are designed to be compared to observations must account for the best available knowledge of mantle rheology. Given experiments such as those discussed in chapter 2, geodynamic simulations can also contribute to our

understanding of rheology.

2. Localization of porosity and magmatic flux into narrow channels surrounded by compacted rock occurs through instabilities in the magma–mantle system. Chemical instability can occur when magma flows up a solubility gradient, dissolving mantle rock as it moves. Aqueous fluids rising off the subducting slab beneath arcs are an example of such a situation. Mechanical instability may also contribute to the formation of magma localizations in two-phase regions with sufficiently high strain rates. In subduction zones, this might be expected just above the slab or below the lithosphere. Chemical and mechanical localization mechanisms, if present in the same place at the same time, would almost certainly interact and reinforce each other. Hence it seems likely that magmatic flux through the mantle in subduction zones, as well as in other tectonic/volcanic settings, is channelized.

While geochemical models of mid-ocean ridges have incorporated ideas of channelized melt flux through parameterized models (*Jull et al.*, 2002) and direct calculations (*Spiegelman and Kelemen*, 2003), the chemical consequences of channelized flow in subduction zones has not been considered. For example, predictions of Uranium series disequilibria depend on melt transit times and porosity where melting and equilibration occurs. High porosity/permeability channels that allow rapid transport of fluids from the slab to the base of the lithosphere would thus be expected to produce a different disequilibrium signature from models in which magma flow is diffuse and occurs at low porosity/permeability.

Direct prediction of such geochemical tracers from models that calculate both solid mantle flow and reactive magmatic flow would be very useful for connecting observations available at the surface with dynamic processes at depth. Such models could be used to interpret observations or to constrain geodynamic processes, or both. These models are inherently complex and represent a significant challenge to construct. They will require significant computational resources to run. Developments reported in this thesis are a step in the construction of such models, however.

Bibliography

- Aharonov, E., J. Whitehead, P. Kelemen, and M. Spiegelman (1995), Channeling instability of upwelling melt in the mantle, *J. Geophys. Res.*, *100*(B10), 20,433–20,450.
- Aharonov, E., M. Spiegelman, and P. Kelemen (1997), Three-dimensional flow and reaction in porous media: implications for the earth's mantle and sedimentary basins, *J. Geophys. Res.*, *102*(B7), 14,821–14,833.
- Albers, M. (2000), A local mesh refinement multigrid method for 3-D convection problems with strongly variable viscosity, *J. Comp. Phys.*, *160*, 126–150.
- Asimow, P. (2000), Modeling hydrous melt production and fractionation at mid-ocean ridges: application to the Azores region, *Journal of Conference Abstracts*, *5*(2), Goldschmidt Meeting 2000, #164.
- Asimow, P., and C. Langmuir (2003), The importance of water to oceanic mantle melting regimes, *Nature*, *421*, 815–820.
- Asimow, P., and E. Stolper (1999), Steady-state mantle-melt interactions in one dimension: I. Equilibrium transport and melt focusing, *J. Petrol.*, *40*(3), 475–494.
- Asimow, P., M. Hirschmann, and E. Stolper (1997), An analysis of variations in isentropic melt productivity, *Phil. Trans. R. Soc. London A*, *355*(1723), 255–281.
- Baker, L., C. Hall, P. Asimow, P. Smith, and M. Gurnis (2004), Subduction dynamics and mass transfer: A synthesis model, in *EOS Trans. Amer. Geophys. Union*, vol. 85, fall Meet. Suppl., Abstract V12A-08.
- Baker, M., and E. Stolper (1994), Determining the composition of high-pressure mantle melts using diamond aggregates, *Geochim. Cosmochim. Acta*, *58*(13), 2811–2827.
- Baker, M., M. Hirschmann, M. Ghiorso, and E. Stolper (1995), Compositions of near-solidus peridotite melts from experiments and thermodynamic calculations, *Nature*, *375*(6529), 308–311.
- Baker, M. G. T., and R. Price (1994), Primitive basalts and andesites from the Mt. Shasta region, N. California - products of varying melt fraction and water-content, *Contrib. Mineral. Petrol.*, *118*(2), 111–129.

- Balay, S., W. Gropp, L. McInnes, and B. Smith (1997), Efficient management of parallelism in object oriented numerical software libraries, in *Modern Software Tools in Scientific Computing*, edited by E. Arge, A. M. Bruaset, and H. P. Langtangen, pp. 163–202, Birkhauser Press.
- Balay, S., K. Buschelman, W. Gropp, D. Kaushik, M. Knepley, L. McInnes, B. Smith, and H. Zhang (2001), PETSc home page, <http://www.mcs.anl.gov/petsc>.
- Balay, S., K. Buschelman, W. D. Gropp, D. Kaushik, M. Knepley, L. C. McInnes, B. F. Smith, and H. Zhang (2002), PETSc users manual, *Tech. Rep. ANL-95/11 - Revision 2.1.5*, Argonne National Laboratory.
- Batchelor, G. (1967), *An Introduction to Fluid Mechanics*, Cambridge University Press.
- Bear, J. (1972), *Dynamics of Fluids in Porous Media*, Elsevier.
- Becker, T., C. Faccenna, R. O’Connell, and D. Giardini (1999), The development of slabs in the upper mantle: insights from numerical and laboratory experiments, *J. Geophys. Res.*, *104*(B7), 15,207–15,226.
- Bercovici, D., Y. Ricard, and G. Schubert (2001), A two-phase model for compaction and damage 1. general theory, *J. Geophys. Res.-Solid Earth*, *106*(B5), 8887–8906.
- Billen, M., and M. Gurnis (2001), A low viscosity wedge in subduction zones, *Earth Plan. Sci. Lett.*, *193*(1–2), 227–236.
- Billen, M., and G. Hirth (2004), Rheologic controls on the dynamic evolution of slabs in the upper mantle, in *EOS Trans. Amer. Geophys. Union*, vol. 85, fall Meet. Suppl., Abstract T23D-03.
- Blackwell, D., R. Bowen, D. Hull, J. Riccio, and J. Steele (1982), Heat-flow, arc volcanism, and subduction in northern Oregon, *J. Geophys. Res.*, *87*(NB10), 8735–8754.
- Bourdon, B., S. Turner, and A. Dosseto (2003), Dehydration and partial melting in subduction zones: constraints from U-series disequilibria, *J. Geophys. Res.*, *108*(B6).
- Braun, M., and P. Kelemen (2002), Dunite distribution in the Oman ophiolite: Implications for melt flux through porous dunite conduits, *Geochem. Geophys. Geosys.*, *3*(8603).
- Briggs, W., V. Henson, and S. McCormick (2000), *A Multigrid Tutorial*, 2 ed., SIAM.
- Buck, W., and W. Su (1989), Focused mantle upwelling below mid-ocean ridges due to feedback between viscosity and melting, *Geophys. Res. Letts.*, *16*(7), 641–644.
- Buck, W., L. Lavier, and A. Poliakov (2005), Modes of faulting at mid-ocean ridges, *Nature*, *434*(7034), 719–723.

- Bureau, H., and H. Keppler (1999), Complete miscibility between silicate melts and hydrous fluids in the upper mantle: experimental evidence and geochemical implications, *Earth Plan. Sci. Lett.*, *165*, 187–196.
- Burnham, W. (1979), The importance of volatile constituents, in *The evolution of igneous rocks: fiftieth anniversary perspectives*, chap. 16, pp. 439–482, Princeton University Press.
- Cai, X., D. Keyes, and V. Venkatakrishnan (1997), Newton-Krylov-Schwarz: An implicit solver for CFD, in *Proceedings of the Eighth International Conference on Domain Decomposition Methods*, pp. 387–400.
- Carbotte, S., C. Small, and K. Donnelly (2004), The influence of ridge migration on the magmatic segmentation of mid-ocean ridges, *Nature*, *429*, 743–746.
- Chadam, J., D. Hoff, E. Merino, P. Ortoleva, and A. Sen (1986), Reactive infiltration instabilities, *IMA Journal Of Applied Mathematics*, *36*(3), 207–221.
- Cheadle, M. (1989), Properties of texturally equilibrated two-phase aggregates, Ph.D. thesis, Cambridge University.
- Cheadle, M., M. Elliott, and D. Mckenzie (2004), Percolation threshold and permeability of crystallizing igneous rocks: the importance of textural equilibrium, *Geology*, *32*(9), 757–760.
- Clark, S., M. Reagan, and T. Plank (1998), Trace element and U-series systematics for 1963-1965 tephras from Irazu Volcano, Costa Rica: Implications for magma generation processes and transit times, *Geochim. Cosmochim. Acta*, *62*(15), 2689–2699.
- Conder, J. (2005), A case for hot slab surface temperatures in numerical viscous flow models of subduction zones with an improved fault zone parameterization, *Phys. Earth Planet. In.*, *149*(1–2), 155–164.
- Conder, J., D. Forsyth, and E. Parmentier (2002a), Asthenospheric flow and asymmetry of the East Pacific Rise, MELT area, *J. Geophys. Res.*, *107*(B12, 2344).
- Conder, J., D. Wiens, and J. Morris (2002b), On the decompression melting structure at volcanic arcs and back-arc spreading centers, *Geophys. Res. Letts.*, *29*(15).
- Cooper, R. (1990), Differential stress induced melt migration: an experimental approach, *J. Geophys. Res.*, *95*(B5), 6979–6992.
- Currie, C., K. Wang, R. Hyndman, and J. He (2004), The thermal effects of steady-state slab-driven mantle flow above a subducting plate: the Cascadia subduction zone and backarc, *Earth Plan. Sci. Lett.*, *223*(1–2), 35–48.
- Daccord, G., and R. Lenormand (1987), Fractal patterns from chemical dissolution, *Nature*, *325*(6099), 41–43.

- Daines, M., and D. Kohlstedt (1997), Influence of deformation on melt topology in peridotites, *J. Geophys. Res.*, *102*, 10,257–10,271.
- Davies, J., and M. Bickle (1991), A physical model for the volume and composition of melt produced by hydrous fluxing above subduction zones, *Philos. Trans. R. Soc. Lond. Ser. A-Math. Phys. Eng. Sci.*, *335*(1638), 355–364.
- Davies, J., and D. Stevenson (1992), Physical model of source region of subduction zone volcanics, *J. Geophys. Res.*, *97*(2), 2037–2070.
- Davis, E., and J. Karsten (1986), On the cause of the asymmetric distribution of seamounts about the Juan de Fuca ridge: Ridge crest migration over a heterogeneous asthenosphere, *Earth Plan. Sci. Lett.*, *79*, 385–396.
- DeMets, C., R. Gordon, D. Argus, and S. Stein (1994), Effect of recent revisions to the geomagnetic reversal time scale on estimates of current plate motions, *Geophys. Res. Letts.*, *21*, 2191–2194.
- Dixon, J., E. Stolper, and J. Holloway (1995), An experimental study of water and carbon dioxide solubilities in mid ocean ridge basaltic liquids: I. Calibration and solubility models, *J. Petrol.*, *36*(6), 1607–1631.
- Elliott, T., T. Plank, A. Zindler, W. White, and B. Bourdon (1997), Element transport from slab to volcanic front at the Mariana arc, *J. Geophys. Res.*, *102*(B7), 14,991–15,019.
- England, P., and C. Wilkins (2000), A simple analytical approximation to the temperature structure in subduction zones, *Geophys. J. Int.*, *142*.
- England, P., R. Engdahl, and W. Thatcher (2004), Systematic variation in the depths of slabs beneath arc volcanoes, *Geophys. J. Int.*, *156*(2), 377–408.
- Evans, R., et al. (1999), Asymmetric electrical structure in the mantle beneath the East Pacific Rise at 17 degrees S, *Science*, *286*, 752–756.
- Falloon, T., D. Green, L. Danyushevsky, and U. Faul (1999), Peridotite melting at 1.0 and 1.5 GPa: an experimental evaluation of techniques using diamond aggregates and mineral mixes for determination of near-solidus melts, *J. Petrol.*, *40*(9), 1343–1375.
- Fang, Y., and M. Spiegelman (2004), Consequences of adiabatic decompression melting on magmatic channeling instabilities, *EOS Trans. Amer. Geophys. Union*, *85*(47), fall Meet. Suppl., Abstract V21A-0595.
- Forneris, J., and J. Holloway (2003), Phase equilibria in subducting basaltic crust: implications for H₂O release from the slab, *Earth Plan. Sci. Lett.*, *214*(1–2), 187–201.

- Forsyth, D., S. Webb, L. Dorman, and Y. Shen (1998a), Phase velocities of Rayleigh waves in the MELT experiment on the East Pacific Rise, *Science*, *280*, 1235–1238.
- Forsyth, D., et al. (1998b), Imaging the deep seismic structure beneath a mid-ocean ridge: The MELT experiment, *Science*, *280*, 1215–1218.
- Fowler, A. (1985), A mathematical model of magma transport in the asthenosphere, *Geophys. Astrophys. Fluid Dyn.*, *33*, 63–96.
- Fowler, A. (1990), A compaction model for melt transport in the Earth's asthenosphere. I. The basic model., in *Magma Transport and Storage*, edited by M. Ryan, pp. 3–14, John Wiley.
- Furukawa, Y. (1993a), Magmatic processes under arcs and formation of the volcanic front, *J. Geophys. Res.*, *98*(B5), 8309–8319.
- Furukawa, Y. (1993b), Depth of the decoupling plate interface and thermal structure under arcs, *J. Geophys. Res.*, *98*, 20,005–20,013.
- Gaetani, G., and T. Grove (1998), The influence of water on melting of mantle peridotite, *Contrib. Mineral. Petrol.*, *131*(4), 323–346.
- George, R., S. Turner, C. Hawkesworth, J. Morris, C. Nye, J. Ryan, and S. Zheng (2003), Melting processes and fluid and sediment transport rates along the Alaska-Aleutian arc from an integrated U-Th-Ra-Be isotope study, *J. Geophys. Res.*, *108*(B5).
- Gerya, T., and D. Yuen (2003), Rayleigh-taylor instabilities from hydration and melting propel 'cold plumes' at subduction zones, *Earth Plan. Sci. Lett.*, *212*(1–2), 47–62.
- Ghiorso, M. (1994), Algorithms for the estimation of phase-stability in heterogeneous thermodynamic systems, *Geochim. Cosmochim. Acta*, *58*, 5489–5501.
- Ghiorso, M., and R. Sack (1995), Chemical mass transfer in magmatic processes. IV. A revised and internally consistent thermodynamic model for the interpolation and extrapolation of liquid-solid equilibria in magmatic systems at elevated temperatures and pressures, *Contrib. Mineral. Petrol.*, *119*, 197–212.
- Ghiorso, M., M. Hirschmann, P. Reiniers, and V. Kress (2002), pMELTS: A revision of MELTS for improved calculation of phase relations and major element partitioning related to partial melting of the mantle to 3 GPa, *Geochem. Geophys. Geosys.*, *3*(5).
- Ghods, A., and J. Arkani-Hamed (2000), Melt migration beneath mid-ocean ridges, *Geophys. J. Int.*, *140*(3), 687–697.
- Gill, J. (1981), *Orogenic Andesites and Plate Tectonics*, Springer, 390 pp.

- Green, D. (1973), Experimental melting studies on a model upper mantle composition at high-pressure under water-saturated and water-undersaturated conditions, *Earth Plan. Sci. Lett.*, *19*(1), 37–53.
- Gropp, W., L. McInnes, M. Tidriri, and D. E. Keyes (1998), Parallel implicit PDE computations: Algorithms and software, in *Proceedings of Parallel CFD '97*, pp. 333–334, Elsevier.
- Grove, T. (2001), Vapor-saturated melting of fertile peridotite revisited: A new experimental approach and re-evaluation of the hydrous peridotite solidus, *EOS Trans. Amer. Geophys. Union*, *82*(47), fall Meet. Suppl., Abstract T31F-05, ©2001 American Geophysical Union.
- Gurnis, M., C. Hall, and L. Lavier (2004), Evolving force balance during incipient subduction, *Geochem. Geophys. Geosys.*, *5*.
- Gutscher, M., and S. Peacock (2003), Thermal models of flat subduction and the rupture zone of great subduction earthquakes, *J. Geophys. Res.*, *108*(B1).
- Hack, A., J. Hermann, and J. Mavrogenes (2005), Insights into deep earth hydrothermal phenomena from internally consistent phase relations and solubility surfaces: A critical look at $\text{NaAlSi}_3\text{O}_8\text{--H}_2\text{O}$ and $\text{SiO}_2\text{--H}_2\text{O}$ and application to more complex rock– H_2O systems, *in review*.
- Hager, B., and R. O’Connell (1978), Subduction zone dip angles and flow driven by plate motion, *Tectonophysics*, *50*(2–3), 111–133.
- Hall, C., and E. Parmentier (2000), Spontaneous melt localization in a deforming solid with viscosity variations due to water weakening, *Geophys. Res. Letts.*, *27*(1), 9–12.
- Hawkesworth, C., K. Gallagher, J. Hergt, and F. McDermott (1993), Mantle and slab contributions in arc magmas, *Ann. Rev. Earth Planet. Sci.*, *21*, 175–204.
- Hirose, K. (1997), Melting experiments on lherzolite KLB-1 under hydrous conditions and generation of high-magnesian andesitic melts, *Geology*, *25*(1), 42–44.
- Hirose, K., and T. Kawamoto (1995), Hydrous partial melting of lherzolite at 1 GPa - the effect of H_2O on the genesis of basaltic magmas, *Earth Plan. Sci. Lett.*, *133*(3–4), 463–473.
- Hirose, K., and I. Kushiro (1993), Partial melting of dry peridotites at high-pressures — determination of compositions of melts segregated from peridotites using aggregates of diamond, *Earth Plan. Sci. Lett.*, *114*, 477–489.
- Hirschmann, M. (2000), Mantle solidus: experimental constraints and the effect of peridotite composition, *Geochem. Geophys. Geosys.*, *1*(2000GC000070).

- Hirschmann, M., P. Asimow, M. Ghiorso, and E. Stolper (1999), Calculation of peridotite partial melting from thermodynamic models of minerals and melts. III. Controls on isobaric melt production and the effect of water on melt production, *J. Petrol.*, *40*(5), 831–851.
- Hirth, G., and D. Kohlstedt (1995a), Experimental constraints on the dynamics of the partially molten upper mantle: Deformation in the diffusion creep regime, *J. Geophys. Res.*, *100*(2), 1981–2002.
- Hirth, G., and D. Kohlstedt (1995b), Experimental constraints on the dynamics of the partially molten upper mantle 2. deformation in the dislocation creep regime, *J. Geophys. Res.*, *100*(8), 15,441–15,052.
- Hirth, G., and D. Kohlstedt (1996), Water in the oceanic upper mantle: implications for rheology, melt extraction and the evolution of the lithosphere, *Earth Plan. Sci. Lett.*, *144*(1–2), 93–108.
- Hirth, G., and D. Kohlstedt (2003), Rheology of the upper mantle and the mantle wedge: A view from the experimentalists, in *The Subduction Factory*, edited by J. Eiler, AGU Geophysical Monograph, Amer. Geophys. Union.
- Holtzman, B., N. Groebner, M. Zimmerman, S. Ginsberg, and D. Kohlstedt (2003a), Stress-driven melt segregation in partially molten rocks, *Geochem. Geophys. Geosyst.*, *4*, art. No. 8607.
- Holtzman, B., D. L. Kohlstedt, and J. P. Morgan (2005), Viscous energy dissipation and strain partitioning in partially molten rocks, *J. Petrol.*, doi:10.1093/petrology/egi065.
- Holtzman, B. K., D. L. Kohlstedt, M. E. Zimmerman, F. Heidelbach, T. Hiraga, and J. Hustoft (2003b), Melt segregation and strain partitioning: Implications for seismic anisotropy and mantle flow, *Science*, *301*(5637), 1227–1230.
- Ihinger, P., Y. Zhang, and E. Stolper (1999), The speciation of dissolved water in rhyolitic melt, *Geochim. Cosmochim. Acta*, *63*(21), 3567–3578.
- Iwamori, H. (1997), Compression melting in subduction zones, *Terr. Nova*, *9*(1), 9–13.
- Iwamori, H. (1998), Transportation of H₂O and melting in subduction zones, *Earth Plan. Sci. Lett.*, *160*(1–2), 65–80.
- Iwamori, H., D. McKenzie, and E. Takahashi (1995), Melt generation by isentropic mantle upwelling, *Earth Plan. Sci. Lett.*, *134*(3–4), 253–266.
- Jaques, A., and D. Green (1980), Anhydrous melting of peridotite at 0–15 kb pressure and the genesis of tholeiitic basalts, *Contrib. Mineral. Petrol.*, *73*(3), 287–310.

- Jarrard, R. (1986), Relations among subduction parameters, *Rev. Geophys.*, *24*(2), 217–284.
- Jellinek, A., R. Gordon, and S. Zatman (2005), Experimental tests of simple models of oceanic intraplate deformation, *Geophys. J. Int.*, submitted.
- Jha, K., E. Parmentier, and J. Phipps Morgan (1994), The role of mantle-depletion and melt-retention buoyancy in spreading-center segmentation, *Earth Plan. Sci. Lett.*, *125*, 221–234.
- Jull, M., P. Kelemen, and K. Sims (2002), Consequences of diffuse and channelled porous melt migration on Uranium series disequilibria, *Geochim. Cosmochim. Acta*, *66*(23), 4133–4148.
- Karato, S., and P. Wu (1993), Rheology of the upper mantle: A synthesis, *Science*, *260*(5109), 771–778.
- Katz, R., and M. Spiegelman (2004), Progress towards an integrated computational model of magma genesis and transport in subduction zones, in *EOS Trans. Amer. Geophys. Union*, vol. 85, fall Meet. Suppl., Abstract V12A-04.
- Katz, R., M. Spiegelman, and C. Langmuir (2003), A new parameterization of hydrous mantle melting, *Geochem. Geophys. Geosys.*, *4*(9).
- Kawamoto, T., and J. Holloway (1997), Melting temperature and partial melt chemistry of H₂O-saturated mantle peridotite to 11 gigapascals, *Science*, *276*(5310), 240–243.
- Kay, R. (1978), Aleutian magnesian andesites - melts from subducted pacific ocean crust, *J. Volcanol. Geothermal Res.*, *4*(1–2), 117–132.
- Kay, S., V. Ramos, and M. Marquez (1993), Evidence in Cerro-Pampa volcanic-rocks for slab-melting prior to ridge-trench collision in southern South-America, *J. Geol.*, *101*(6), 703–714.
- Kelemen, P., K. Johnson, R. Kinzler, and A. Irving (1990), High-field-strength element depletions in arc basalts due to mantle magma interaction, *Nature*, *345*(6275), 521–524.
- Kelemen, P., H. Dick, and J. Quick (1992), Formation of harzburgite by pervasive melt rock reaction in the upper mantle, *Nature*, *358*(6388), 635–641.
- Kelemen, P., N. Shimizu, and V. Salters (1995a), Extraction of mid-ocean-ridge basalt from the upwelling mantle by focused flow of melt in dunite channels, *Nature*, *375*(6534), 747–753.
- Kelemen, P., J. Whitehead, E. Aharonov, and K. Jordahl (1995b), Experiments on flow focusing in soluble porous-media, with applications to melt extraction from the mantle, *J. Geophys. Res.*, *100*(B1), 475–496.

- Kelemen, P., M. Parmentier, J. Rilling, L. Mehl, and B. Hacker (2002), Thermal convection of the mantle wedge, *Geochim. Cosmochim. Acta*, 66(15A), A389–A389.
- Kelemen, P., G. Yogodzinski, and D. Scholl (2003), Along-strike variation in the Aleutian island arc: Genesis of high mg# andesite and implications for continental crust, in *Inside the Subduction Factory, Geophysical Monograph Series*, vol. 138, edited by J. Eiler, p. 223, American Geophysical Union.
- Kelley, K., E. Hauri, and T. Sisson (2004), Melt inclusion evidence for both water-fluxed and decompression melting at Galunggung, Indonesia, in *EOS Trans. Amer. Geophys. Union*, vol. 85, fall Meet. Suppl., Abstract V12A-07.
- Kincaid, C., and R. Griffiths (2004), Variability in flow and temperatures within mantle subduction zones, *Geochem. Geophys. Geosys.*, 5.
- Kincaid, C., and I. Sacks (1997), Thermal and dynamical evolution of the upper mantle in subduction zones, *J. Geophys. Res.*, 102(B6), 12,295–12,315.
- King, S. (2001), Subduction zones: observations and geodynamic models, *Phys. Earth Planet. In.*, 127(1–4), 9–24.
- Kinzler, R. (1997), Melting of mantle peridotite at pressures approaching the spinel to garnet transition: Application to mid-ocean ridge basalt petrogenesis, *J. Geophys. Res.*, 102(B1), 853–874.
- Kinzler, R., and T. Grove (1992), Primary magmas of midocean ridge basalts 1. Experiments and methods, *J. Geophys. Res.*, 97(B5), 6885–6906.
- Klein, E. M., and C. H. Langmuir (1987), Global correlations of ocean ridge basalt chemistry with axial depth and crustal thickness, *J. Geophys. Res.*, 92, 8089–8115.
- Knepley, M., R. Katz, and B. Smith (2006), Developing a geodynamics simulator with PETSc, in *Numerical Solution of Partial Differential Equations on Parallel Computers, Lecture Notes in Computational Science and Engineering*, vol. 51, edited by A. Bruaset and A. Tveito, Springer-Verlag.
- Kogiso, T., K. Hirose, and E. Takahashi (1998), Melting experiments on homogeneous mixtures of peridotite and basalt: application to the genesis of ocean island basalts, *Earth Plan. Sci. Lett.*, 162(1–4), 45–61.
- Kushiro, I. (1972), Effect of water on composition of magmas formed at high pressures, *J. Petrol.*, 13(2), 311.
- Kushiro, I. (1996), Partial melting of a fertile mantle peridotite at high pressures: An experimental study using aggregates of diamond, in *Earth Processes: Reading the Isotopic Code, Geophysical Monograph*, vol. 95, pp. 109–122, American Geophysical Union.

- Kushiro, I., Y. Syono, and S. Akimoto (1968), Melting of a peridotite nodule at high pressures and high water pressures, *J. Geophys. Res.*, *73*(18), 6023.
- Langmuir, C., and G. Hanson (1981), Calculating mineral-melt equilibria with stoichiometry, mass balance, and single-component distributions, in *Thermodynamics of Minerals and Melts, Advances in Physical Geochemistry*, vol. 1, edited by R. Newton, A. Navrotsky, and B. Wood, pp. 247–272, Springer-Verlag.
- Langmuir, C., E. Klein, and T. Plank (1992), Petrological systematics of mid-oceanic ridge basalts: constraints on melt generation beneath ocean ridges, in *Mantle flow and melt generation at mid-ocean ridges, Geophysical Monograph*, vol. 71, edited by J. Phipps Morgan, D. Blackman, and J. Sinton, pp. 183–280, Amer. Geophys. Union.
- Liang, Y., and Z. Morgan (2004), An experimental study of the kinetics of lherzolite reactive dissolution: Implications for contrasting styles of melt transport in the mantle, in *EOS Trans. Amer. Geophys. Union*, vol. 85, fall Meet. Suppl., Abstract V24A-04.
- Lin, J., and J. Morgan (1992), The spreading rate dependence of 3-dimensional mid-ocean ridge gravity structure, *Geophys. Res. Letts.*, *19*(1), 13–16.
- Longhi, J. (2002), Some phase equilibrium systematics of lherzolite melting: I, *Geochem. Geophys. Geosys.*, *3*(3).
- Macdonald, K., P. Fox, L. Perram, M. Eisen, R. Haymon, S. Miller, S. Carbotte, M. Cormier, and A. Shor (1988), A new view of the mid-ocean ridge from the behavior of ridge-axis discontinuities, *Nature*, *335*(6187), 217–225.
- Magde, L., and D. Sparks (1997), Three-dimensional mantle upwelling, melt generation, and melt migration beneath segment slow spreading ridges, *J. Geophys. Res.*, *102*(B9), 20,571–20,583.
- Manning, C. (2004), The chemistry of subduction-zone fluids, *Earth Plan. Sci. Lett.*, *223*(1–2), 1–16.
- Martin, H., R. Smithies, R. Rapp, J. Moyen, and D. Champion (2005), An overview of adakite, tonalite-trondhjemite-granodiorite (TTG), and sanukitoid: relationships and some implications for crustal evolution, *Lithos*, *79*(1–2), 1–24.
- McKenzie, D. (1969), Speculations on consequences and causes of plate motions, *Geophys. J.*, *18*, 1–32.
- McKenzie, D. (1984), The generation and compaction of partially molten rock, *J. Petrol.*, *25*(3), 713–765.
- McKenzie, D., and M. Bickle (1988), The volume and composition of melt generated by extension of the lithosphere, *J. Petrol.*, *29*(3), 625–679.

- Mei, S., W. Bai, T. Hiraga, and D. Kohlstedt (2002), Influence of melt on the creep behavior of olivine-basalt aggregates under hydrous conditions, *Earth Plan. Sci. Lett.*, *201*, 491–507.
- Michael, P. (1995), Regionally distinctive sources of depeleted MORB: Evidence from trace elements and H₂O, *Earth Plan. Sci. Lett.*, *131*, 301–320.
- Miller, D., S. Goldstein, and C. Langmuir (1994), Cerium lead and lead-isotope ratios in arc magmas and the enrichment of lead in the continents, *Nature*, *368*(6471), 514–520.
- Morris, J., W. Leeman, and F. Tera (1990), The subducted component in island arc lavas: constraints from Be isotopes and B-Be systematics, *Nature*, *344*, 31–36.
- Mosenfelder, J., N. Deligne, A. P.D., and G. Rossman (2002), Incorporation of OH in olivine at high pressure: new experimental results, in *EOS Trans. Amer. Geophys. Union, Fall Meet. Suppl.*, vol. 83, abstract T22C-07.
- Mysen, B., and K. Wheeler (2000), Solubility behavior of water in haploandesitic melts at high pressure and high temperature, *Am. Mineral.*, *85*, 1128–1142.
- Peacock, S. (1990), Fluid processes in subduction zones, *Science*, *248*(4953), 329–337.
- Pickering-Witter, J., and A. Johnston (2000), The effects of variable bulk composition on the melting systematics of fertile peridotitic assemblages, *Contrib. Mineral. Petrol.*, *140*(2), 190–211.
- Plank, T., and C. Langmuir (1993), Tracing trace elements from sediment input to volcanic output at subduction zones, *Nature*, *362*, 739–743.
- Plank, T., E. Benjamin, J. Wade, and T. Grove (2004), A new hygrometer based on the europium anomaly in clinopyroxene phenocrysts in arc volcanic rocks, *EOS Trans. Amer. Geophys. Union*, *85*(47), fall Meet. Suppl., Abstract V12A-05.
- Press, W., S. Teukolsky, W. Vetterling, and B. Flannery (1992), *Numerical Recipes in FORTRAN: the art of scientific computing*, 2nd ed., Cambridge University Press, Cambridge, U.K.
- Renner, J., K. Viskupic, G. Hirth, and B. Evans (2003), Melt extraction from partially molten peridotites, *Geochem. Geophys. Geosyst.*, *4*(5), 8606, doi:10.1029/2002GC000369.
- Richards, M., S. Morris, F. Busse, and A. Lenardic (2003), Towards a physical understanding of the effects of depth-dependent rheology on mantle convection, *EOS Trans. Amer. Geophys. Union*, *84*(46), fall Meet. Suppl., Abstract S11G-06.
- Richardson, C. (1998), Melt flow in a variable viscosity matrix, *Geophys. Res. Letts.*, *25*(7), 1099–1102.

- Ringwood, A. (1974), The petrological evolution of island arc systems, *J. Geol. Soc. London*, *130*, 183–204.
- Robinson, J., B. Wood, and J. Blundy (1998), The beginning of melting of fertile and depleted peridotite at 1.5 GPa, *Earth Plan. Sci. Lett.*, *155*(1–2), 97–111.
- Rudnicki, J., and J. Rice (1975), Conditions for localization of deformation in pressure-sensitive dilatant materials, *J. Mech. Phys. Solids*, *23*(6), 371–394.
- Schmidt, M., and S. Poli (1998), Experimentally based water budgets for dehydrating slabs and consequences for arc magma generation, *Earth Plan. Sci. Lett.*, *163*(1–4), 361–379.
- Schouten, H., H. Dick, and K. Klitgord (1987), Migration of mid-ocean ridge volcanic segments, *Nature*, *326*, 835–839.
- Schwab, B., and A. Johnston (2001), Melting systematics of modally variable, compositionally intermediate peridotites and the effects of mineral fertility, *J. Petrol.*, *42*(10), 1789–1811.
- Scott, D., and D. Stevenson (1984), Magma solitons, *Geophys. Res. Letts.*, *11*, 1161–1164.
- Scott, D., and D. Stevenson (1986), Magma ascent by porous flow, *J. Geophys. Res.*, *91*, 9283–9296.
- Shen, A., and H. Keppler (1997), Direct observation of complete miscibility in the albite-H₂O system, *Nature*, *385*, 710–712.
- Sisson, T., and S. Bronto (1998), Evidence for pressure-release melting beneath magmatic arcs from basalt at Galunggung, Indonesia, *Nature*, *391*(6670), 883–886.
- Sisson, T., and G. Layne (1993), H₂O in basalt and basaltic andesite glass inclusions from four subduction-related volcanoes, *Earth Plan. Sci. Lett.*, *117*, 619–635.
- Sleep, N. (1988), The tapping of melt by veins and dykes, *J. Geophys. Res.*, *93*, 10,255–10,272.
- Small, C., and L. Danyushevsky (2003), Plate-kinematic explanation for mid-ocean ridge depth discontinuities, *Geology*, *31*(5), 399–402.
- Sobolev, A., and M. Chaussidon (1996), H₂O concentrations in primary melts from supra-subduction zones and mid-ocean ridges: Implications for H₂O storage and recycling in the mantle, *Earth Plan. Sci. Lett.*, *137*(1–2), 45–55.
- Solomon, T., and R. Hartley (1998), Measurements of the temperature field of mushy and liquid regions during solidification of aqueous ammonium chloride, *J. Fluid Mech.*, *358*, 87–106.

- Sparks, D., and E. Parmentier (1991), Melt extraction from the mantle beneath spreading centers, *Earth Plan. Sci. Lett.*, *105*(4), 368–377.
- Spiegelman, M. (1993a), Flow in deformable porous-media. part 1. Simple analysis, *J. Fluid Mech.*, *247*, 17–38.
- Spiegelman, M. (1993b), Flow in deformable porous media. part 2. Numerical analysis—The relationship between shock waves and solitary waves, *J. Fluid Mech.*, *247*, 39–63.
- Spiegelman, M. (1993c), Physics of melt extraction: theory, implications, and applications, *Phil. Trans. R. Soc. London A*, *342*, 23–41.
- Spiegelman, M. (2003), Linear analysis of melt band formation by simple shear, *Geochem. Geophys. Geosys.*, *4*(9), article 8615, doi:10.1029/2002GC000499.
- Spiegelman, M., and R. Katz (2005), A semi-lagrangian crank-nicolson algorithm for the numerical solution of advection-diffusion problems, *Geochem. Geophys. Geosys.*, submitted.
- Spiegelman, M., and P. Kelemen (2003), Extreme chemical variability as a consequence of channelized melt transport, *Geochem. Geophys. Geosys.*, *4*.
- Spiegelman, M., and D. McKenzie (1987), Simple 2-D models for melt extraction at mid-ocean ridges and island arcs, *Earth Plan. Sci. Lett.*, *83*, 137–152.
- Spiegelman, M., P. Kelemen, and E. Aharonov (2001), Causes and consequences of flow organization during melt transport: the reaction infiltration instability in compactible media, *J. Geophys. Res.*, *106*(B2), 2061–2077.
- Stalder, R., P. Ulmer, A. Thompson, and D. Günther (2000), Experimental approach to constrain second critical end points in fluid/silicate systems: near-solidus fluids and melts in the system albite-H₂O, *Am. Mineral.*, *85*, 68–77.
- Staniforth, A., and J. Cote (1991), Semi-Lagrangian advection schemes for atmospheric models - a review, *Monthly Weather Review*, *119*(9), 2206–2223.
- Stern, R. (2002), Subduction zones, *Reviews of geophysics*, *40*(4), art. No. 1012.
- Stevenson, D. (1989), Spontaneous small-scale melt segregation in partial melts undergoing deformation, *Geophys. Res. Letts.*, *16*(9), 1067–1070.
- Stolper, E. (1989), The temperature dependence of the speciation of water in rhyolitic melts and glasses, *Am. Mineral.*, *74*, 1247–1257.
- Stolper, E., and S. Newman (1994), The role of water in the petrogenesis of Mariana Trough magmas, *Earth Plan. Sci. Lett.*, *121*(3–4), 293–325.
- Su, W., and W. Buck (1993), Buoyancy effects on mantle flow under midocean ridges, *J. Geophys. Res.*, *98*(B7), 12,191–12,205.

- Takahashi, E. (1986), Melting of a dry peridotite KLB-1 up to 14 GPa - implications on the origin of peridotitic upper mantle, *J. Geophys. Res.*, *91*(B9), 9367–9382.
- Takahashi, E., T. Shimazaki, Y. Tsuzaki, and H. Yoshida (1993), Melting study of a peridotite KLB-1 to 6.5 GPa, and the origin of basaltic magmas, *Philos. Trans. R. Soc. Lond. Ser. A-Math. Phys. Eng. Sci.*, *342*(1663), 105–120.
- Tanton, L., T. Grove, and J. Donnelly-Nolan (2001), Hot, shallow mantle melting under the cascades volcanic arc, *Geology*, *29*(7), 631–634.
- Tatsumi, Y. (1986), Formation of volcanic front in subduction zones, *Geophys. Res. Letts.*, *13*, 717–720.
- Tatsumi, Y., M. Sakuyama, H. Fukuyama, and I. Kushiro (1983), Generation of arc basalt magmas and thermal structure of the mantle wedge in subduction zones, *J. Geophys. Res.*, *88*(NB7), 5815–5825.
- Tirone, M., and J. Ganguly (2002), Thermodynamic control on thermo-fluid dynamic mantle flow model, in *Goldschmidt Conference Abstracts*, p. A776.
- Toomey, D., S. Wilcock, S. Solomon, W. Hammond, and J. Orcutt (1998), Mantle seismic structure beneath the MELT region of the East Pacific Rise from P and S wave tomography, *Science*, *280*, 1224–1227.
- Toomey, D., W. Wilcock, J. Conder, D. Forsyth, J. Blundy, E. Parmentier, and W. Hammond (2002), Asymmetric mantle dynamics in the MELT region of the East Pacific Rise, *Earth Plan. Sci. Lett.*, *200*, 287–295.
- Trompert, R., and U. Hansen (1996), The application of a finite volume multigrid method to 3d flow problems in a highly viscous fluid with variable viscosity, *Geophys. Astrophys. Fluid Dyn.*, *83*, 261.
- Turcotte, D., and J. Schubert (2002), *Geodynamics, Second Edition*, Cambridge University Press.
- Turner, S. (2002), On the time-scales of magmatism at island-arc volcanos, *Phil. Trans. R. Soc. London A*, *360*, 2853–2871.
- Turner, S., P. Evans, and C. Hawkesworth (2001), Ultrafast source-to-surface movement of melt at island arcs from Ra-226-Th-230 systematics, *Science*, *292*(5520), 1363–1366.
- Turner, S., S. Black, and K. Berlo (2004), Pb-210-Ra-226 and Ra-228-Th-232 systematics in young arc lavas: implications for magma degassing and ascent rates, *Earth Plan. Sci. Lett.*, *227*(1–2), 1–16.
- van Keken, P. (2003a), The structure and dynamics of the mantle wedge, *Earth Plan. Sci. Lett.*, *215*(3–4), 323–338.

- van Keken, P. (2003b), Benchmark for subduction zone modeling, web page, <http://www.geo.lsa.umich.edu/~keken/subduction/benchmark.html>.
- van Keken, P., B. Kiefer, and S. Peacock (2002), High-resolution models of subduction zones: implications for mineral dehydration reactions and the transport of water into the deep mantle, *Geochem. Geophys. Geosys.*, *3*.
- von Bargen, N., and H. Waff (1986), Permeabilities, interfacial-areas and curvatures of partially molten systems - results of numerical computation of equilibrium microstructures, *J. Geophys. Res.*, *91*(B9), 9261–9276.
- Walter, M. (1998), Melting of garnet peridotite and the origin of komatiite and depleted lithosphere, *J. Petrol.*, *39*(1), 29–60.
- Walter, M., T. Sisson, and D. Presnall (1995), A mass proportion method for calculating melting reactions and application to melting of model upper mantle lherzolite, *Earth Plan. Sci. Lett.*, *135*, 77–90.
- Wark, D., and E. Watson (1998), Grain-scale permeabilities of texturally equilibrated, monomineralic rocks, *Earth Plan. Sci. Lett.*, *164*, 591–605.
- Weaver, J., and C. Langmuir (1990), Calculation of phase equilibrium in mineral-melt systems, *Comput. Geosci.*, *16*(1), 1–19.
- Withers, A., Y. Zhang, and H. Behrens (1999), Reconciliation of experimental results on H₂O speciation in rhyolitic glass using in-situ and quenching techniques, *Earth Plan. Sci. Lett.*, *173*, 343–349.
- Wood, C., and J. Kienle (Eds.) (1990), *Volcanoes of North America: United States and Canada*, Cambridge University Press.
- Zhu, W., and G. Hirth (2003), A network model for permeability in partially molten rocks, *Earth Plan. Sci. Lett.*, *212*, 407–416.
- Zimmerman, M., S. Zhang, D. Kohlstedt, and S. Karato (1999), Melt distribution in mantle rocks deformed in shear, *Geophys. Res. Letts.*, *26*(10), 1505–1508.

Appendix A

Ridge Migration, Asthenospheric Flow and the Origin of Magmatic Segmentation in the Global Mid-Ocean Ridge System

Richard F. Katz, Marc Spiegelman and Suzanne Carbotte

Geophys. Res. Letts. 31:15605, 2004

Copyright by the American Geophysical Union

Abstract

Global observations of mid-ocean ridge (MOR) bathymetry demonstrate an asymmetry in axial depth across ridge offsets that is correlated with the direction of ridge migration. Motivated by these observations, we have developed two-dimensional numerical models of asthenospheric flow and melting beneath a migrating MOR. The modification of the flow pattern produced by ridge migration leads to an asymmetry in melt production rates on either side of the ridge. By coupling a simple parametric model of three dimensional melt focusing to our simulations, we generate predictions of axial depth differences across offsets in the MOR. These predictions are quantitatively consistent with the observed asymmetry.

A.1 Introduction

Global observations of the bathymetry of intermediate and fast spreading mid-ocean ridges (MOR) by *Carbotte et al.* (2004) demonstrate that differences in axial depth across ridge offsets are correlated with the direction of ridge migration in the fixed hot-spot reference frame. They show that the shallower segment across an offset is

usually the segment *leading* with respect to the direction of ridge migration (Figure A-1a). The systematic connection with plate kinematics, global scope and ubiquity of this observed asymmetry suggests that it might yield to a simple explanation related to plate induced dynamics. Changes in ridge morphology along a MOR are commonly attributed to differences in the volume of melt delivered from the mantle although the origin of these variations in magma supply are poorly understood (*Macdonald et al.*, 1988; *Lin and Morgan*, 1992). *Carbotte et al.* (2004) suggest a conceptual model of melt generation and 3D focusing to account for their observations. They propose that ridge migration leads to asymmetry in mantle upwelling and melt generation with melt production augmented beneath the leading plate and diminished beneath the trailing plate. We quantify this suggestion by calculating the influence of ridge migration on mantle melt production using 2D numerical simulations of asthenospheric flow and adiabatic melting.

Previous authors have considered the possible effect of ridge migration on MOR processes. A kinematic model of asthenospheric flow beneath a migrating ridge was used by *Davis and Karsten* (1986) to explain the asymmetric distribution of seamounts about the Juan de Fuca ridge and by *Schouten et al.* (1987) to study the migration of non-transform offsets at spreading centers. Modeling studies (*Conder et al.*, 2002a; *Toomey et al.*, 2002) of the MELT region of the EPR (*Forsyth et al.*, 1998b) found the dynamic effect of ridge migration could produce an asymmetry in melt production, but not of the magnitude inferred from across-ridge differences in P, S and Rayleigh wave velocities (*Forsyth et al.*, 1998a; *Toomey et al.*, 1998) and in electrical conductivity (*Evans et al.*, 1999). These studies attribute the observed asymmetry in mantle structure to enhanced horizontal flow from a large-scale pressure gradient in the asthenosphere from the distant South Pacific Superswell and additionally, by *Toomey et al.* (2002), to an anomalous asthenospheric temperature inflow. Such considerations may be necessary to explain the large asymmetry seen in the MELT region (assuming the asymmetry is due to melt production) but they represent a geographically special case.

We show that the more general situation of asymmetry generated by ridge mi-

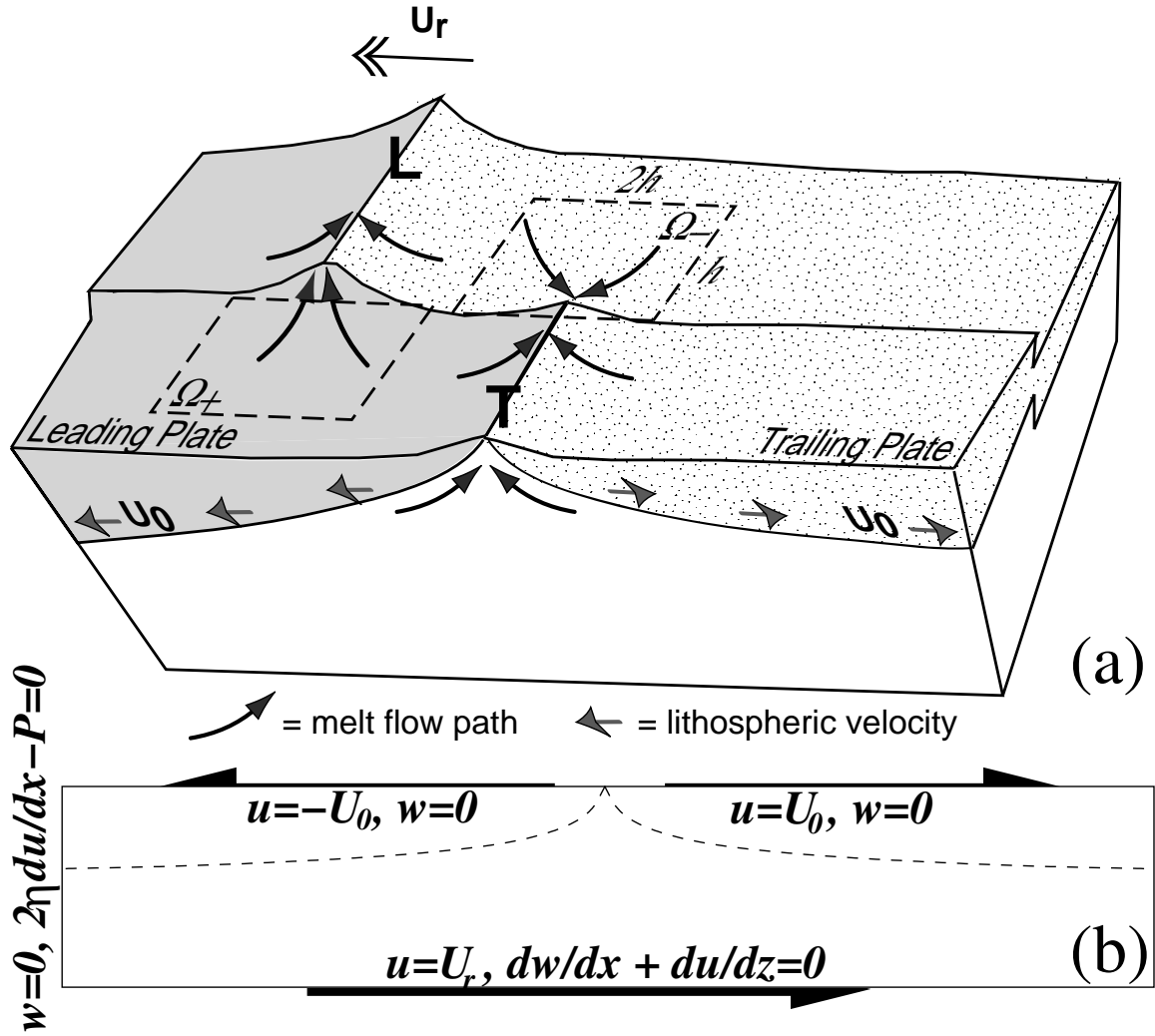


Figure A-1: (a) Schematic diagram illustrating a discontinuity in the spreading ridge modified from *Carbotte et al.* (2004). The ridge-normal rate of ridge migration is given by the vector U_r . The leading segment is labeled **L** and the trailing one **T**. Black arrows show assumed paths of melt focusing beneath the lithosphere. Grey arrows show lithospheric motion. Focusing regions Ω_+ and Ω_- used in equation (A.3) are dashed rectangles with sides of length h and $2h$. (b) Schematic diagram illustrating the model domain and boundary conditions. Half spreading rate is U_0 .

gration alone is sufficient to explain the global observations of variation in ridge bathymetry. We describe how shear induced by the relative motion of the lithosphere over the mantle produces an asymmetric perturbation of melt production rates. Furthermore, our model quantitatively predicts the observed relationship between axial depth differences across an offset in the ridge and the length of the offset (Figure A-2). Our model is different from those used in previous studies in that it employs a non-Newtonian combined diffusion and dislocation creep viscosity. This viscosity enhances the melting rate asymmetry by a factor of 3 to 4 over diffusion creep alone.

A.2 Model description and solution

Figure A-1a shows a conceptual model of three-dimensional melt focusing from the upwelling zone of two adjacent ridge segments separated by a discontinuity. Delivery of melt to the ridge axis is assumed to occur by buoyant flow along a sloping, thermally imposed impermeable barrier (*Magde and Sparks, 1997*). If the symmetry of the lithospheric thermal structure is not affected by ridge migration, one would expect that the focusing process would be equally efficient to both ridge segments across a ridge discontinuity. Thus, an asymmetry in magma supply inferred from ridge morphology requires a difference in melt production in the regions from which the melt is drawn.

While computing melt focusing near a ridge offset requires a 3D model, the asymmetric production of melt can be investigated in 2D. Here we solve the equations,

$$\nabla P = \nabla \cdot [\eta (\nabla \mathbf{V} + \nabla \mathbf{V}^T)] , \quad \text{s.t. } \nabla \cdot \mathbf{V} = 0; \quad (\text{A.1})$$

$$\mathbf{V} \cdot \nabla \theta = \kappa \nabla^2 \theta, \quad (\text{A.2})$$

for the thermal and flow structure in the reference frame of the migrating ridge. Here P is the dynamic pressure, θ is the potential temperature and \mathbf{V} is the two dimensional velocity. The viscosity is given by $\eta = (1/\eta_{dist} + 1/\eta_{difu})^{-1}$ where η_{dist} and η_{difu} correspond to P and T -dependent dislocation creep and P , T and strain

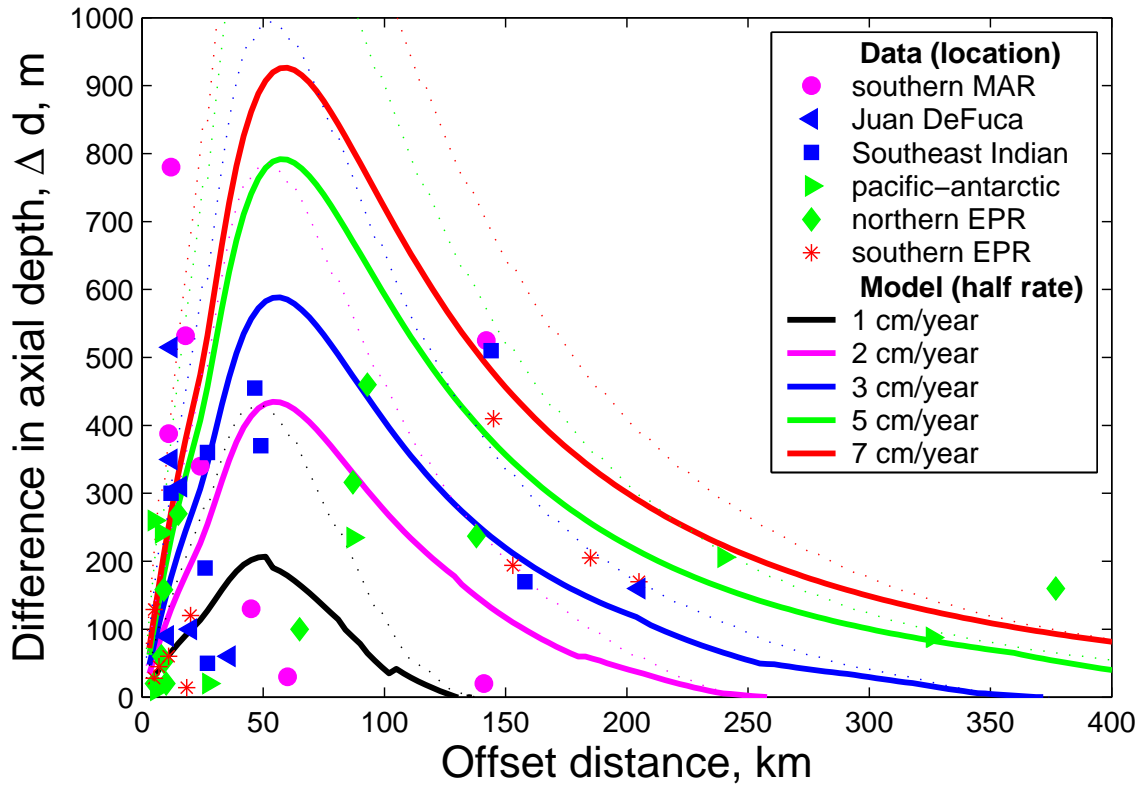


Figure A-2: Model results and observations of morphological asymmetry versus offset length of discontinuities in the MOR. **Symbols:** difference in axial depth of two adjacent ridge segments across ridge-axis discontinuities (Δd) restricted to those cases where the leading ridge segment is shallower than the trailing segment. Data for fast and intermediate spreading ridges from *Carbotte et al.* (2004). Also shown are previously unpublished data from the slow spreading southern MAR 23°-36°S measured as the difference in axis elevation at mid-points of adjacent segments. Along the 11000 km of MOR examined in the combined data set, the leading ridge segments are shallower at 76% of all discontinuities with offsets greater than 5 km. Symbols for each ridge are colored to correspond to the closest model half rate. Mean half rates in cm/year are 1.9 (southern MAR), 2.8 (Juan de Fuca), 3.7 (Southeast Indian), 4.3 (Pacific Antarctic), 4.6 (northern EPR) and 7.0 (southern EPR) (*DeMets et al.*, 1994). **Curves:** Δd from equation (A.3) for a range of spreading rates. Solid curves represent a conservative estimate of 670 km for the asthenospheric depth and recover a reasonable melt focusing region, Ω (shown in Figure A-1a), determined by approximate “by eye” fitting of the curves to the data. This procedure gives a characteristic dimension h of 24 km, although this solution is non-unique (see text). Dotted curves were computed for an asthenospheric depth limit of 300 km and the same focusing region.

rate-dependent diffusion creep (*Karato and Wu, 1993; Hirth and Kohlstedt, 2003*). We use values of 14 and 5 cm³/mole for V_{disl}^* and V_{difn}^* .

In our simulations the asthenospheric depth is equal to the domain depth. The underlying mantle has zero horizontal velocity in the fixed hot-spot frame. A large drop in horizontal mantle velocity with increasing depth is expected across the transition zone for mantle convection with a low viscosity asthenosphere (*Richards et al., 2003*). The horizontal velocity on the bottom boundary, however, is set to the ridge migration rate, U_r , because we solve for the flow field in a reference frame fixed to the migrating ridge. Other boundary conditions are illustrated in Figure A-1b. The full system of equations and boundary conditions is solved iteratively with a Newton-Krylov-Schwarz method (*Cai et al., 1997; Gropp et al., 1998*) available through the Portable Extensible Toolkit for Scientific Computation (PETSc) (*Balay et al., 2001, 2002, 1997*).

Observations by *Small and Danyushevsky (2003)* show that the mean ratio of the ridge-perpendicular migration rate to the half spreading rate at all ridges studied in Figure A-2 is 0.95 with a standard deviation of 0.33. Thus we set the ridge migration rate U_r equal to the half spreading rate U_0 for all model runs. The flow perturbation caused by ridge migration is extracted by subtracting the flow field calculated for a non-migrating ridge from that of an identical calculation with non-zero U_r . Example output is shown in Figure A-3.

A.3 Melting and melt focusing

Assuming mantle upwelling to be an isenthalpic process we compute the melting rate *anomaly* due to ridge migration (kg m⁻³ sec⁻¹ per kilometer in the along axis direction) as $\Gamma'(x, z) = \rho_m W' dF/dz|_s$ where ρ_m is the density of solid mantle, W' is the vertical velocity perturbation, and $dF/dz|_s$ is the adiabatic productivity. The productivity is computed using a parameterization of mantle melting by *Katz et al. (2003)*, assuming a mantle potential temperature of 1300°C. Because this productivity is nearly constant at 0.2 %/km over the melting region and for each of the runs, Γ' can

be considered a function of W' only. To estimate the axial depth anomaly expected across a discontinuity (e.g. Figure A-1a), we integrate Γ' over an area Ω where melt is assumed to be focused to the axis. The predicted difference in crustal thickness, ΔH , is then the difference between the crustal thickness anomalies at leading and trailing segment ends given by:

$$\Delta H = \int \left(\frac{\int_{\Omega+} \Gamma' dA - \int_{\Omega-} \Gamma' dA}{2\rho_c U_0} \right) dz \quad (\text{A.3})$$

where ρ_c is the density of the crust and U_0 is the half spreading rate. Assuming isostatically compensated topography and crustal density of 2700 kg/m^3 , the difference in axial depth, Δd , is equal to approximately $0.26\Delta H$ (*Turcotte and Schubert, 2002*).

A.4 Results

Figure A-3 shows that ridge migration produces asymmetry in the melting rate in 2D calculations. The difference in melt production across the ridge axis increases with spreading rate. For a domain of 670 km depth it ranges from 1% of the total melt production rate for U_0 of 1 cm/yr, to 5% at 3 cm/yr, to 11% at 7 cm/yr. Predicted asymmetry in axial depth computed from these simulations are shown with global ridge data in Figure A-2. The curves in this figure are generated using equation (A.3), adjusted for isostatic compensation. For moderate to fast spreading (greater than 3 cm/year half rate), the model predicts that asymmetry in axial depth has a maximum when the offset length is about 50 km and is still evident when offsets are greater than 200 km. Slower spreading rates result in a peak asymmetry at slightly smaller distances and zero asymmetry beyond an offset of about 100 km. These model results are consistent with observed differences in ridge elevation as a function of ridge offset length from the moderate to fast spreading ridges examined in *Carbotte et al. (2004)* as well as from the slowly spreading southern Mid Atlantic Ridge (MAR) (Figure A-2). The largest contrasts in ridge elevation for the southern MAR occur at transform offsets of less than 50 km and rapidly diminish at longer

offsets. Faster spreading ridges show a maximum asymmetry in ridge morphology at longer transform faults of about 50-100 km and smaller amounts of asymmetry at longer offsets.

The solid curves in Figure A-2 are computed with a pooling region Ω of size $h=24$ km, chosen to roughly fit the data (h is defined in Figure A-1a). Although there is scatter in the data, our model can account for the general trend and amplitude. The amplitude of the model curves scales inversely with the asthenosphere depth and directly with the area within the pooling region. Both of these parameters are poorly constrained and may vary considerably over the global mid-ocean ridge system. Our estimate of the characteristic distance of melt focusing, h , is thus non-unique. It depends on our assumption of asthenospheric depth of 670 km. A thinner asthenosphere would produce a greater 2D melting asymmetry and thus require a smaller melt focusing region, Ω . The sensitivity of amplitude could be a source of the observed scatter in the data, along with mantle fertility, local spreading rate, deviation of the ratio of half spreading rate to migration rate from unity, *etc.* However, the shape of the curves and the position of their maxima are independent of these poorly constrained parameters.

A.5 Discussion

The behavior of the model is readily understood by considering just the component of mantle flow induced by ridge migration (Figure A-3b). If there were no lithospheric plates, this additional flow would be simple shear with no vertical velocity component. However, because the lithosphere provides a boundary that curves upward beneath the ridge, the perturbed flow has a vertical component with upwelling on the leading side of the ridge and downwelling on the trailing side. This enhanced vertical flow translates to more melt production on the leading side (Figure A-3c). Note that with increasing depth, the location of the maximum (or minimum) of the perturbed melting rate field moves away from the ridge axis along the bold lines shown in Figure A-3c. The maximum excess melt production occurs near the intersection of this line

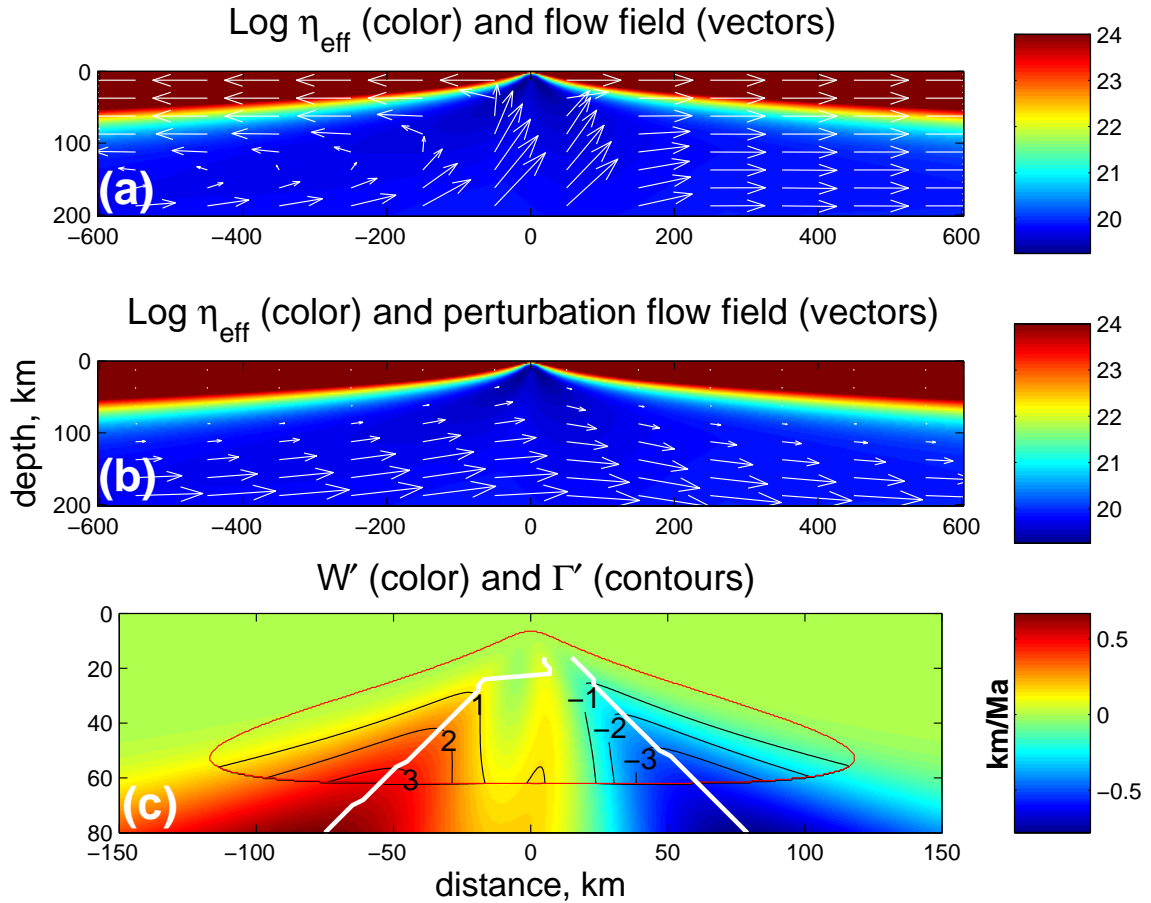


Figure A-3: Output from a sample calculation with $U_0 = U_r = 1$ cm/year and domain size of 200 km depth by 1200 km width. **(a)** Colored field is \log_{10} of the viscosity field. Vectors represent the flow pattern beneath the migrating ridge. **(b)** Colored field as in (a). Vectors represent the perturbations of the solid flow field caused by ridge migration. *The scaling of the vectors is slightly different in (a) and (b).* **(c)** Colored field is W' , the vertical component of the velocity perturbation field in km/Ma. The red contour shows the boundary of the melting region and black contours map Γ' , the melting rate perturbation, in $\text{kg m}^{-3} \text{Ma}^{-1}$. White lines mark the location of the maximal values of W' as a function of depth, as in Figure A-4a.

with the depth of the solidus, which in this calculation occurs about 50 km off axis.

Figure A-4a shows the positions of the extremal lines and the lithospheric thickness for a range of spreading rates from a simplified model that calculates only the perturbed flow due to ridge migration. This figure suggests that for a constant depth solidus, the position of the peak in excess melt production is reasonably insensitive to spreading rate (and should occur roughly at a distance comparable to the depth of the solidus). This result explains the stable position of the peak in Figure A-2.

The amplitude of the perturbation in melt production, however, depends on the rate of ridge migration and spreading. Figure A-4b shows the value of $|W'|$ as a function of depth along the extremal lines. The magnitude of the perturbed upwelling scales with U_r . When $U_r = U_0$, increasing spreading rate is associated with increasing magnitude of W' at all depths (light lines in Figure A-4b). The increase in Δd with spreading rate shown in Figure A-2 stems from this effect. However, for a fixed U_r , slower spreading results in a larger enhancement of upwelling because slower spreading ridges have a more pronounced thinning of the lithosphere. Finally, the offset at which Δd goes to zero is controlled by the geometry of the base of the lithosphere which limits the width of the region above the solidus. Fast spreading ridges have thinner lids which allow melting due to the perturbed flow to extend further away from the ridge axis.

A.6 Conclusions

Models described here show that plate-induced mantle dynamics is a plausible explanation for the morphological changes observed along MOR. The perturbation in asthenospheric flow caused by ridge migration generates an asymmetry in melt production rates which, under reasonable assumptions of 3D melt focusing, leads to an asymmetry in predicted axial depth (crustal thickness) across ridge segment boundaries. These results are consistent with models by *Conder et al.* (2002a) and *Toomey et al.* (2002) but they do not depend on an inferred large-scale plume-related asthenospheric flow and temperature anomaly. The correspondence between observed

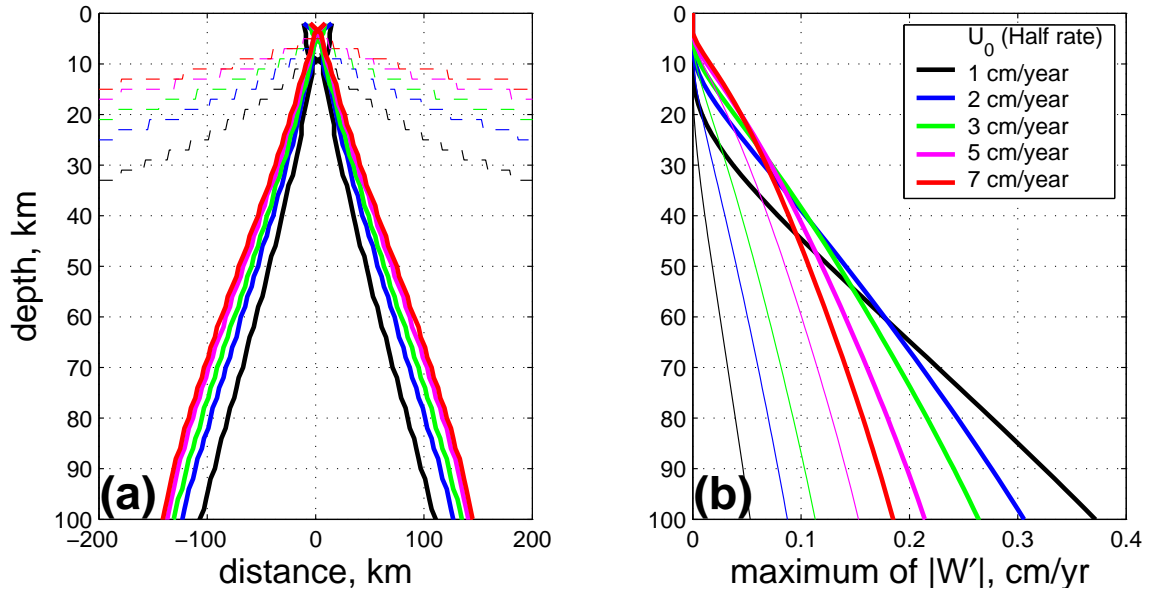


Figure A-4: Results from a simplified model for the perturbed flow, showing the effect of spreading rate on the position and magnitude of the peak upwelling perturbation. Model domain is 200 km deep by 800 km wide. (a) Dashed curves show the position of the bottom of the lithosphere for calculations at different spreading rates and $U_r = 7$ cm/year (see legend in b). Solid curves show the position, at each depth, of the maximum and minimum in the vertical component of the velocity perturbation field (e.g see Fig. 3). Note that the W' field contracts slightly with decreasing spreading rate which explains the change in the maxima seen in Figure A-2. (b) Heavy curves represent the maximum in W' as a function of depth for a fixed rate of ridge migration, $U_r = 7$ cm/yr. Light curves are the maxima in W' for $U_r = U_0$.

and modeled changes in axial depth asymmetry with offset length supports the assumption of plate-driven asthenospheric flow above a high viscosity, zero horizontal velocity mantle. The amplitude of the data can be fit using a conservative estimate of asthenosphere depth and a parametric model of melt focusing. Future models can place better constraints on the scale of melt focusing and upwelling geometry by computing 3D flow and temperature fields.

Appendix B

A Semi-Lagrangian Crank-Nicolson Algorithm for the Numerical Solution of Advection-Diffusion Problems

Marc Spiegelman and Richard F. Katz

Submitted to *Geophys. Geochem. Geosyst.* July 18, 2005

Abstract

We present a hybrid algorithm for the numerical solution of advection-diffusion problems that combines two standard algorithms; Semi-Lagrangian schemes for hyperbolic advection-reaction problems and Crank-Nicolson schemes for purely diffusive problems. We show that the hybrid scheme is identical to the two end-member schemes in the limit of infinite and zero Peclet number and remains accurate over a wide range of Peclet numbers. This scheme does not have a CFL stability criterion allowing the choice of time step to be decoupled from the spatial resolution. We present a numerical test against an analytic solution and compare the results of both an operator split version of the algorithm and a combined algorithm that solves advection and diffusion simultaneously. We also compare results to simple explicit and implicit schemes and show that the SLCN scheme is both faster and more accurate on the same problem. Finally we also introduce a variable order interpolation scheme for the semi-Lagrangian schemes that reduces interpolation artifacts for sharp fronts without introducing additional numerical diffusion.

B.1 Introduction

Advection-diffusion problems are ubiquitous in physical sciences and engineering and can pose significant challenges for accurate numerical solution. Typical problems arise

where the Peclet number varies strongly across the domain, for example in convection problems which are predominantly advective but develop narrow diffusive boundary layers, or for problems where advective stirring significantly steepens concentration gradients enhancing diffusion. These problems can also prove difficult for operator splitting approaches when advection modifies gradients on time-scales comparable to diffusion time scales. We have also encountered problems in advection-diffusion-reaction problems (e.g. *Spiegelman et al.*, 2001; *Spiegelman and Kelemen*, 2003) where the three processes are so closely balanced that small amounts of excess numerical diffusion (or even operator splitting) can change the numerical results. Ideally we would like a efficient numerical solver that can handle a wide range of Peclet numbers and solve both advection and diffusion simultaneously.

Here, we describe a numerical scheme with these properties that we have found useful for solving chemical transport in reactive media. This scheme is a hybrid that combines Crank-Nicolson schemes for diffusion and semi-Lagrangian schemes for advection, drawing on advantages of both algorithms. We show that this scheme reduces identically to the two end-member schemes in the limits of zero and infinite Peclet number and is accurate for a wide range of Pe numbers in between. Furthermore, SLCN has no inherent stability criterion and therefore it decouples the resolution in space from the resolution in time, reducing the computational cost of increasing the grid size. We present a numerical test of the scheme against an analytic solution that couples advection and diffusion and shows that, for this problem, the combined scheme is more accurate and faster than simple explicit or implicit schemes. We also discuss existing short-comings of this scheme and some approaches to correcting them.

B.2 Algorithms

Before developing the hybrid Semi-Lagrangian Crank-Nicolson scheme it is worth briefly reviewing the component schemes and their behavior.

B.2.1 Basic Algorithms

Crank-Nicolson scheme A d -dimensional Crank-Nicolson scheme for solution of the diffusion equation

$$\frac{\partial u}{\partial t} = \nabla^2 u \quad (\text{B.1})$$

can be written as

$$\frac{\mathbf{u}^{n+1} - \mathbf{u}^n}{\Delta t} = \frac{1}{2} [\mathcal{L}\mathbf{u}^{n+1} + \mathcal{L}\mathbf{u}^n] \quad (\text{B.2})$$

where \mathbf{u}^n is the discrete solution to Eq. (B.1) at time step n and \mathcal{L} is the discrete diffusion operator (Laplacian). Rearranging Eq. (B.2) yields

$$\left[I - \frac{\Delta t}{2} \mathcal{L} \right] \mathbf{u}^{n+1} = \left[I + \frac{\Delta t}{2} \mathcal{L} \right] \mathbf{u}^n \quad (\text{B.3})$$

which is a sparse linear system (assuming \mathcal{L} is a linear operator) for \mathbf{u}^{n+1} which we solve rapidly using a standard geometric multi-grid solver (e.g. *Briggs et al.*, 2000) for Cartesian geometries. The Crank-Nicolson scheme is unconditionally stable for all time steps.

Semi-Lagrangian Schemes Semi-Lagrangian schemes solve the advection-reaction problem

$$\frac{\partial u}{\partial t} + \mathbf{v} \cdot \nabla u = f(u, \mathbf{x}, t) \quad (\text{B.4})$$

using the method of characteristics for *each* point in a regular mesh. Unlike fully Lagrangian (particle tracking schemes), which will take an initially regular mesh and distort it, Semi-Lagrangian schemes are effectively particle tracking schemes between two regular meshes that preserve the regularity of the mesh from time-step to time-step. *Staniforth and Cote* (1991) provides an excellent introduction and details for these schemes. The basic idea of Semi-Lagrangian schemes is that they actually solve the equation

$$\frac{Du}{Dt} = f(u, \mathbf{x}, t) \quad (\text{B.5})$$

as an ordinary differential equation along the trajectory that connects from some take-off point \mathbf{x}_* at time t to the *regular grid point* \mathbf{x} at time $t + \Delta t$. In general they can be written as

$$\mathbf{u}^{n+1} = \mathbf{u}_*^n + \int_t^{t+\Delta t} f(\mathbf{u}(\tau), \mathbf{x}(\tau), \tau) d\tau \quad (\text{B.6})$$

where \mathbf{u}^{n+1} is the solution on the regular grid at time step $n + 1$. $\mathbf{u}_*^n = \mathbf{u}^n(t, \mathbf{x}_*)$ is the value of the solution at the take-off point (which is generally not on the grid). The final term is the line integral of the source terms along the trajectory. The take-off point \mathbf{x}_* is found by solving the ODE particle tracking problem

$$\frac{d\mathbf{x}}{dt} = -\mathbf{v} \quad (\text{B.7})$$

starting at the grid point \mathbf{x} and moving back in time. Once the take-off point is located, the value of the function and any attendant source terms are found at this point by interpolation from the *regular* mesh \mathbf{u}^n . Semi-Lagrangian schemes have considerable flexibility in their choice of particle tracking and interpolation schemes. We use the simplest, second-order two-level scheme which uses an iterated mid-point scheme to find the take-off point and bi-cubic interpolation (in 2-D) to interpolate values at time step n (see *Staniforth and Cote, 1991*, for details). Lower order interpolants such as bi-linear interpolation introduce systematic errors similar to the numerical diffusion introduced by low-order up-wind schemes and are not acceptable. However, higher-order interpolants can produce systematic overshoots near sharp edges that remain localized to the edges but grow with time. Section B.5.1 describes a hybrid interpolation scheme that preserves high-order interpolation for smooth fields but prevents over-shoots near discontinuities.

To complete Eq. (B.6) requires an approximation to the final integral. For the second-order two-level scheme we use a trapezoidal rule so that the full algorithm can be written

$$\mathbf{u}^{n+1} = \mathbf{u}_*^n + \frac{\Delta t}{2} [\mathbf{f}_*^n + \mathbf{f}^{n+1}] \quad (\text{B.8})$$

where $\mathbf{f}_*^n = f(\mathbf{x}_*, t)$ is the value of the source term (usually interpolated) at the

take-off point.

For pure advection problems with no source terms, the Semi-Lagrangian scheme reduces to $\mathbf{u}^{n+1} = \mathbf{u}_*^n$, i.e. the value of the function remains constant on the characteristic and the old value is simply copied into its new position on the regular grid. As long as the take-off point and the old value can be found accurately, there is no stability limit to the length of the time step. In practice, the second-order accuracy of the mid-point scheme restricts the time step to $\sim 4 - 5$ times the Courant number although for simpler flow fields, time steps greater than 10 times the Courant condition are possible.

B.2.2 Hybrid Schemes

Given these two schemes for advection and diffusion, we combine them to solve the scaled, constant diffusivity advection-diffusion problem

$$\frac{\partial u}{\partial t} + \mathbf{v} \cdot \nabla u = \nabla^2 u \quad (\text{B.9})$$

where the maximum scaled velocity $\|\mathbf{v}\|_{max}$ is order the Peclet number, $\text{Pe} = \frac{Lv_0}{\kappa}$.

Operator splitting OS-SLCN The first approach simply uses the Semi-Lagrangian scheme to advect the quantity for a time Δt such that $\mathbf{u}^{n'} = \mathbf{u}_*^n$ and then diffuses for a time Δt using the CN scheme. The operator split semi-Lagrangian Crank-Nicolson scheme for Eq. (B.9) is then

$$\left[I - \frac{\Delta t}{2} \mathcal{L} \right] \mathbf{u}^{n+1} = \left[I + \frac{\Delta t}{2} \mathcal{L} \right] \mathbf{u}^{n'} \quad (\text{B.10})$$

Note that $\mathbf{u}^{n'}$ has first been moved onto the regular grid before the diffusion operator is applied. For small time-steps or for flows that do not significantly distort gradients over a time-step, the operator split SLCN scheme can produce accurate solutions for large time steps (see Section B.3). However, for strongly distorting flows where advection and diffusion operate simultaneously, we find that a small

modification to this scheme is more reliable.

Operator Combined SLCN In the operator combined SLCN scheme, we consider the problem slightly differently as

$$\frac{Du}{Dt} = \nabla^2 u \quad (\text{B.11})$$

and treat it in the same manner as Eq. (B.5) with the diffusion as a “source term.” Using the same discretization that leads to Eq. (B.8) we write the SLCN scheme as

$$\mathbf{u}^{n+1} = \mathbf{u}_*^n + \frac{\Delta t}{2} [(\mathcal{L}\mathbf{u}^n)_* + \mathcal{L}\mathbf{u}^{n+1}] \quad (\text{B.12})$$

where $(\mathcal{L}\mathbf{u}^n)_*$ is the diffusion operator acting at the *take-off point* \mathbf{x}_* before advection has distorted the gradients. If \mathcal{L} is the discrete Laplace operator and \mathcal{C}_* is the bicubic interpolation operator at point \mathbf{x}_* then it is straightforward to show that on a regular cartesian grid that the order of interpolation and diffusion is interchangeable i.e. $(\mathcal{L}\mathbf{u}^n)_* = \mathcal{L}\mathcal{C}_*\mathbf{u}^n = \mathcal{C}_*\mathcal{L}\mathbf{u}^n$. Thus, in practice, it is usually easier to apply the Laplacian on the regular grid at time step n and then interpolate the resulting field. With these definitions Eq. (B.12) can be rearranged to yield

$$\left[I - \frac{\Delta t}{2} \mathcal{L} \right] \mathbf{u}^{n+1} = \mathbf{u}_*^n + \frac{\Delta t}{2} (\mathcal{L}\mathbf{u}^n)_* \quad (\text{B.13})$$

or

$$\left[I - \frac{\Delta t}{2} \mathcal{L} \right] \mathbf{u}^{n+1} = \mathcal{C}_* \left[\left(I + \frac{\Delta t}{2} \mathcal{L} \right) \mathbf{u}^n \right] \quad (\text{B.14})$$

In the limit of no motion ($\text{Pe} = 0$ or $\mathbf{v} = \mathbf{0}$), Eq. (B.14) is identical to a Crank-Nicolson scheme (Eq. (B.3)) as $\mathcal{C}_* = I$ (or $\mathbf{u}_*^n = \mathbf{u}^n$ and $(\mathcal{L}\mathbf{u}^n)_* = \mathcal{L}\mathbf{u}^n$). It is less obvious that in the limit of no diffusion ($\text{Pe} \rightarrow \infty$), this scheme reduces identically to the semi-Lagrangian scheme.

To see this, we first note that although none of these schemes have stability criteria, we still have to choose a time step Δt based on some accuracy criterion. For mixed advection-diffusion problems we choose a time step based on the fastest process and

an accuracy criterion based on either the maximum number of grid points we want to move in a time step or the smallest wavelength that we want to decay accurately. For example we set

$$\Delta t = \min \left(\frac{\alpha \Delta x}{\|\mathbf{v}\|_{\max}}, (\beta \Delta x)^2 \right) \quad (\text{B.15})$$

where Δx is a measure of the grid spacing, α is the maximum number of grid points to move in a time step (i.e. the maximum Courant number) and $\lambda = \beta \Delta x$ is the minimum wavelength to resolve for diffusion at long times. In the limit of large velocities ($\text{Pe} \rightarrow \infty$), the time it takes to move α grid-points is negligible (i.e. $\Delta t = O(\epsilon)$). In the limit $\Delta t \rightarrow 0$ Eq. (B.13) reduces to $\mathbf{u}^{n+1} = \mathbf{u}_*^n$ which is just the semi-Lagrangian advection scheme.

For strongly advectively dominated problems, it usually makes more sense to scale by the advection time so that the dimensionless velocities are order 1, in which case the problem becomes

$$\frac{Du}{Dt} = \frac{1}{\text{Pe}} \nabla^2 u \quad (\text{B.16})$$

and the combined SLCN scheme becomes

$$\left[I - \frac{\Delta t}{2\text{Pe}} \mathcal{L} \right] \mathbf{u}^{n+1} = \mathbf{u}_*^n + \frac{\Delta t}{2\text{Pe}} (\mathcal{L} \mathbf{u}^n)_* \quad (\text{B.17})$$

and the Peclet number enters into the operator (thus the operator becomes poorly scaled when the Peclet number is small and is singular for $\text{Pe} = 0$).

B.3 An analytic test problem

Strictly speaking, the method of characteristics does not work for advection-diffusion problems because the diffusion operator moves information between particle trajectories such that characteristics do not exist for all times. However, in practice, this numerical scheme works well because it only considers the particle trajectories for a single time-step and just provides a more accurate method to map a uniform grid \mathbf{u}^n at time t to another uniform grid \mathbf{u}^{n+1} at time $t + \Delta t$. We have not proved this

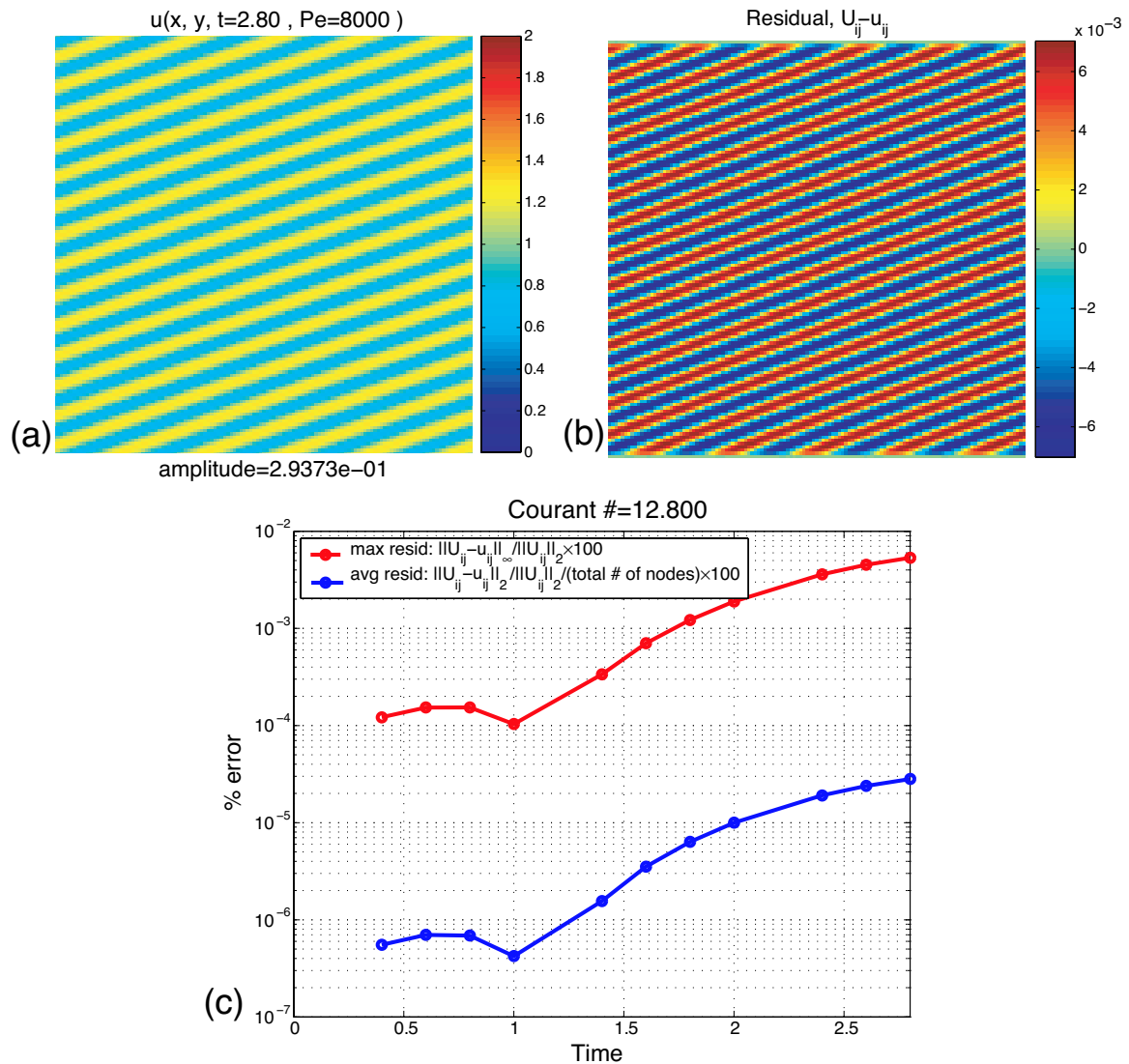


Figure B-1: Results of an example calculation using the combined operator SLCN scheme. (a) The u field at model time $t = 2.8$. (b) The residual, analytic minus numerical, at the same time. (c) The residual over model time. The red curve shows the maximum residual normalized by the L2 norm of the discrete analytic solution. The blue curve is the grid averaged L2 norm of the residual, normalized in the same way.

rigorously, but provide a useful test of the algorithm for an analytic solution that combines both advection and diffusion in a non-separable way.

This problem considers the solution of Eq. (B.9) in an infinite domain with velocity field

$$\mathbf{v}(\mathbf{x}, t) = U(y) = \text{Pe}y\mathbf{i} \quad (\text{B.18})$$

and initial condition

$$u(\mathbf{x}, 0) = e^{i\mathbf{k}\cdot\mathbf{x}} \quad (\text{B.19})$$

Physically, this problem corresponds to advection-diffusion of a plane wave in a shearing flow field (see Fig. B-1)

In the absence of diffusion, this problem can be solved by characteristics for any initial condition $u(\mathbf{x}, 0) = f(\mathbf{x})$ such that $u(\mathbf{x}, t) = f(x - \text{Pe}yt, y)$. In the case of a plane wave initial condition, the solution is

$$u(\mathbf{x}, t) = e^{i[k_x(x - \text{Pe}yt) + k_y y]} \quad (\text{B.20})$$

which can be written more physically as $u(\mathbf{x}, t) = e^{i\mathbf{k}(t)\cdot\mathbf{x}}$ where

$$\mathbf{k}(t) = k_x\mathbf{i} + (k_y - k_x\text{Pe}t)\mathbf{j}$$

is a time dependent wave-number. Thus any initial plane wave remains a plane wave but changes wavelength with time. For an initially vertical plane wave ($k_y = 0$), shear increases the wave-number with time and should enhance diffusion.

An analytic solution to the full advection-diffusion problem can be found by seeking solutions of the form

$$u(\mathbf{x}, t) = e^{i(\mathbf{k}(t)\cdot\mathbf{x}) + s(t)} \quad (\text{B.21})$$

Substituting Eqs. (B.18) and (B.21) into Eq. (B.9) and solving for $s(t)$ gives

$$s(t) = -[k^2 t - \text{Pe}k_x k_y t^2 + (\text{Pe}k_x)^2 t^3 / 3] \quad (\text{B.22})$$

where $k^2 = k_x^2 + k_y^2$. In the absence of advection ($\text{Pe} = 0$), this solution is simply

the exponential decay of a static plane wave. When $Pe > 0$ and initially $k_y = 0$, the shear enhances the decay rate of the amplitude as expected.

We test both the operator split and combined versions of the SLCN scheme against the real part of this solution for a computational domain $x \in [-1/2, 1/2]$, $y \in [-1/2, 1/2]$. Boundary conditions are periodic in the x -direction and dirichlet in y ; we prescribe the analytical solution at $y = \pm 1/2$ for all x . The initial condition that we use is $k_y = 0$, $k_x = 10\pi$ for five full cycles in the x -direction.

In addition to the two schemes described above, we also compare results with numerical solutions using a Forward-time centered-space (FTCS) scheme as well as a semi-implicit Crank-Nicolson centered-space (CNCS) scheme that discretizes the advection term as

$$Pe y \frac{\partial u}{\partial x} \sim \frac{Pe y}{2} [u_{i+1,j}^n - u_{i-1,j}^n] = A \mathbf{u}^n$$

and solves the linear system

$$\left[I + \frac{\Delta t}{2}(A - \mathcal{L}) \right] \mathbf{u}^{n+1} = \left[I - \frac{\Delta t}{2}(A - \mathcal{L}) \right] \mathbf{u}^n \quad (\text{B.23})$$

using a multigrid solver. The FTCS is a straw-man scheme: its CFL condition limits it to very small time-steps and even under these conditions its accuracy and efficiency are poor. The CNCS scheme is better than FTCS however it too has a stability criterion that limits the time-step size.

B.4 Results

For each run of the benchmark problem we measure the process time (on a Sun Blade 100 with 250 KB RAM and a 500 MHz processor) and the accuracy of the solution. Accuracy is measured by comparing the numerical solution to a discretized version of the exact solution \mathbf{u}_{true}^n :

$$\% \text{ error} = \frac{\|\mathbf{u}_{true}^n - \mathbf{u}^n\|_{2 \text{ or } \infty}}{\|\mathbf{u}_{true}^n\|_2} \times 100 \quad (\text{B.24})$$

Figure B-1 shows the results of an example calculation using operator combined SLCN. In this example the Peclet number is chosen to be 4000 and final shear strain is .625. This combination of parameters results in the decay of the signal to 30% of its initial amplitude. The L2 norm percent error is observed to parallel the infinity norm in our calculations; for the rest of the paper, percent error is reported in terms of the infinity norm.

Figure B-2 shows the comparison of accuracy as a function of Peclet number for the SLCN scheme in operator split and combined versions with the CNCS scheme. Each simulation is run to approximately one e-folding time in amplitude, thus the amount of final shear increases with Peclet number. For small Peclet number, all the schemes give the same results. This is as expected: they all reduce to pure Crank-Nicolson for $Pe \rightarrow 0$. For large Peclet number runs where final shear is higher (advection is more important), SLCN performs better than CNCS, with a significant advantage for the combined operator version of SLCN.

Figure B-3 shows the results of a set of simulations for different h and Δt . It is clear that even for time steps an order of magnitude longer, the SLCN schemes perform significantly better than the other schemes. For example, in Figure B-3c, with 12 grid intervals per initial wavelength and a Courant number of about 10, the error is 0.03%, around an order of magnitude smaller than for the CNCS scheme can achieve.

The computational time required for each of the calculations performed is shown in Figure B-4. Computation time for the CNCS scheme and the SLCN schemes are comparable for a given courant number. However, the SLCN scheme is stable to much higher Courant number, so it is capable of accelerating the simulation significantly. For the example given above, the SLCN scheme is about five times faster than the CNCS scheme for an order of magnitude improvement in accuracy.

A comparison of operator split and operator combined SLCN shows that while the operator combined SLCN scheme has a wide stability range where accuracy is approximately constant, the operator split version has two regimes of accuracy dependence on Courant number. In the first regime, at lower Courant numbers, the performance

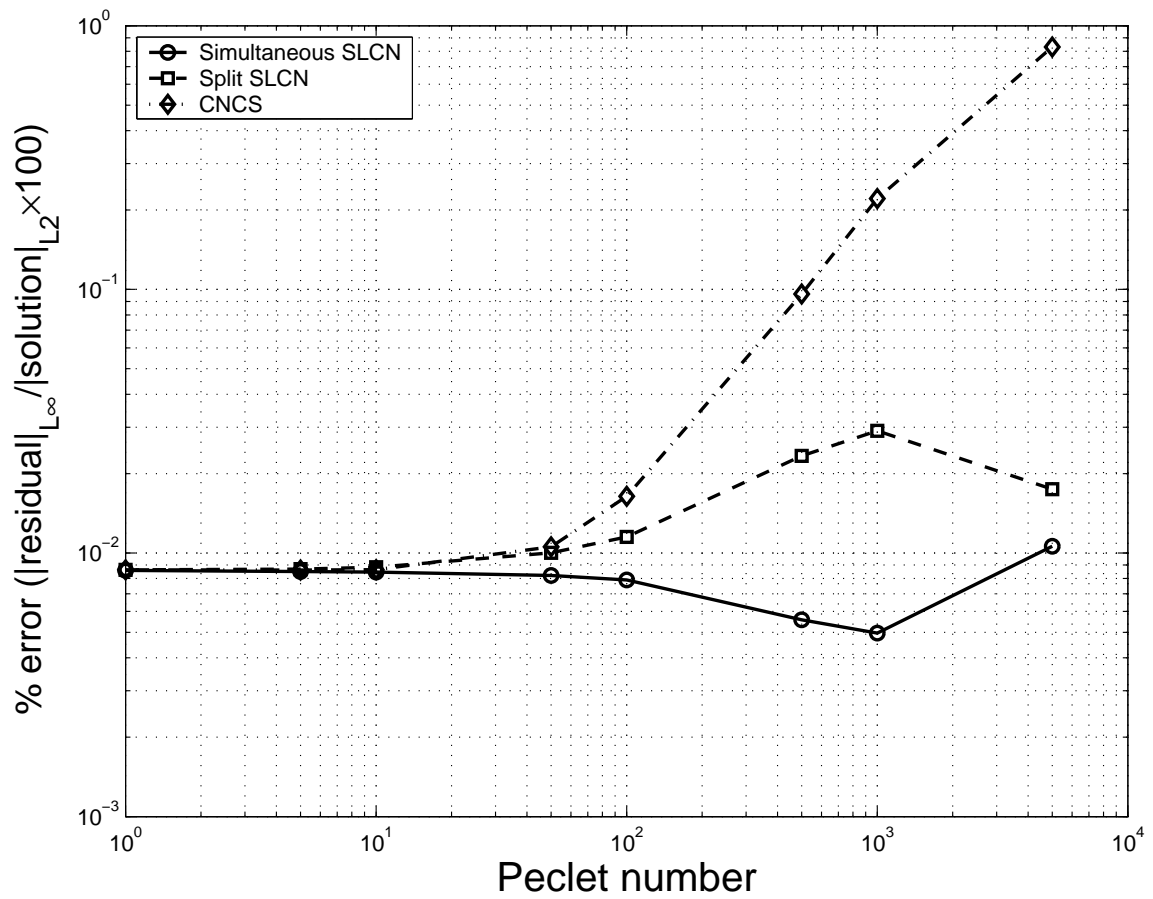


Figure B-2: L^∞ percent error as a function of Peclet number for CNCS, operator split SLCN and operator combined SLCN. The time step is set according to equation (B.15), with $\beta = 0.7$ and $\alpha = 6$ for the semi-Lagrangian algorithms and $\alpha = 1$ for the CNCS scheme.

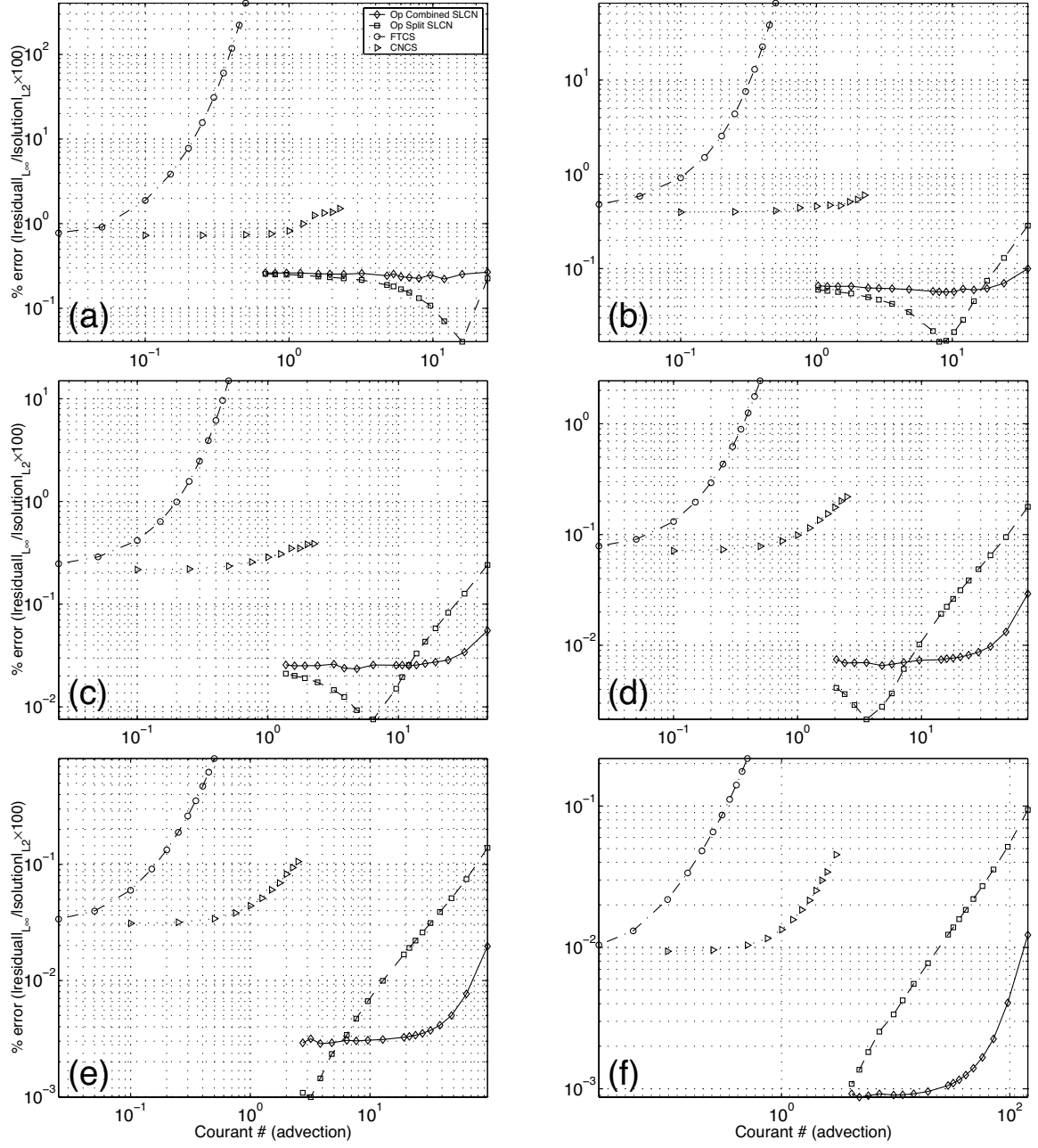


Figure B-3: L^{∞} % Error (as defined in Eq. (B.24)) as a function of courant number, $\frac{Pe v_{max} \Delta t}{\Delta x}$. Each graph represents a different grid spacing. These are, in terms of grid points per wavelength of the initial q field: (a) 6 (b) 9 (c) 12 (d) 19 (e) 25 (f) 38

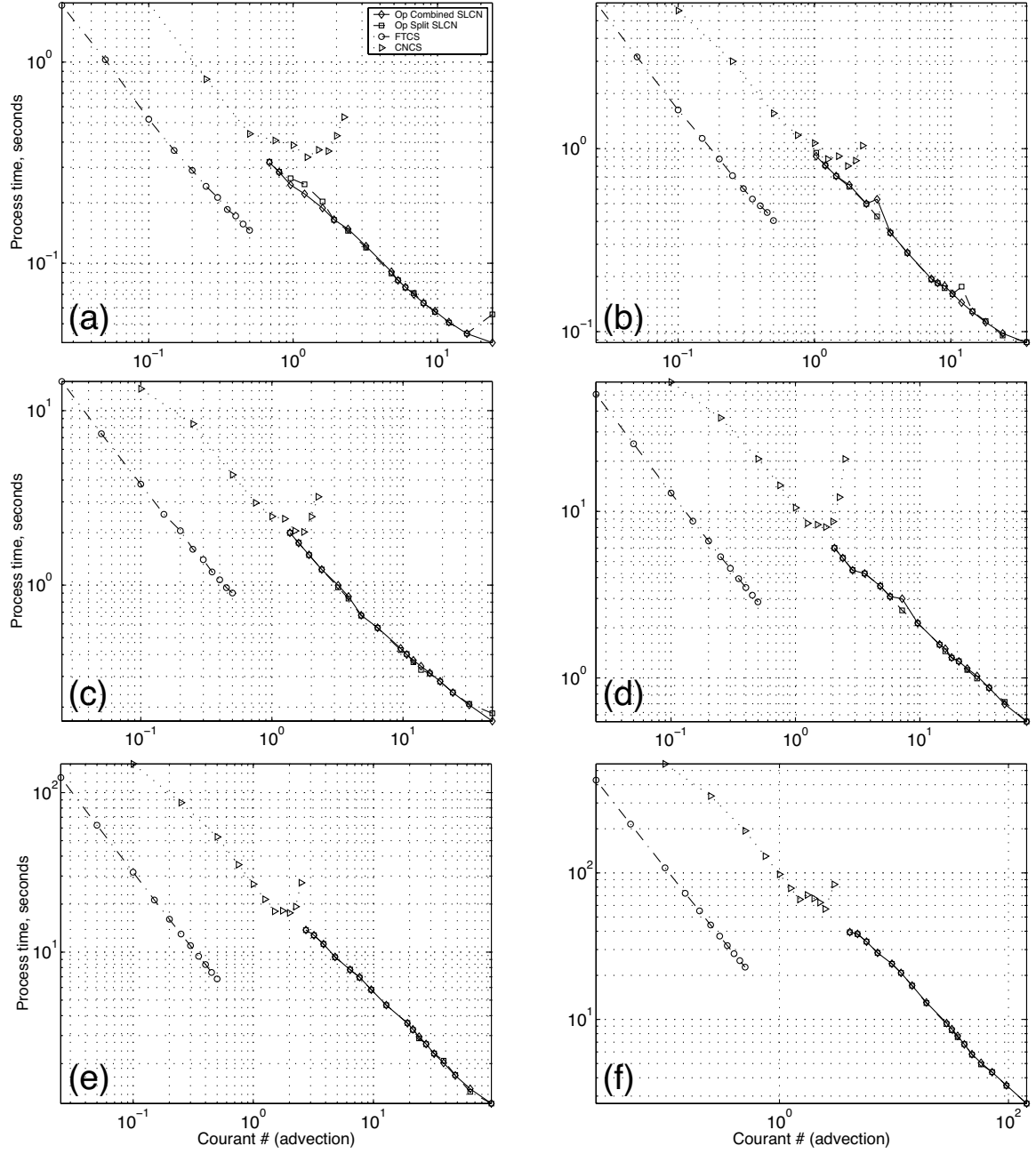


Figure B-4: Computational time (in seconds) as a function of Courant number, $\frac{Pe v_{max} \Delta t}{\Delta x}$. All computations performed on a Sun Blade 100 with 250 KB RAM and a 500 MHz processor. Each graph represents a different grid spacing. These are, in terms of grid points per wavelength of the initial q field: (a) 6 (b) 9 (c) 12 (d) 19 (e) 25 (f) 38

of the scheme improves with increasing time-step size. The second regime shows a rapid degeneration of the performance as the time-step size continues to increase.

B.5 Discussion

The strengths of the shearing, diffusing plane wave as a benchmark problem are that it couples advection and diffusion and that it has a non-separable analytic solution. Our tests were successful in distinguishing the different schemes. The SLCN scheme confers a significant advantage over the other schemes considered, both in terms of accuracy and efficiency. The performance of the operator split SLCN scheme compares favorably with the simultaneous operator version for some values of the Courant number, but its accuracy is highly variable. We cannot explain this marked variability.

There are limitations of the benchmark problem with respect to testing the SLCN scheme. First, all advection is in one dimension and thus the calculated characteristics are exact. A problem with a more complex flow field, *e.g.* curved particle trajectories or stagnation points, would present a more demanding test of the SLCN scheme and would degrade its accuracy at higher Courant numbers. Second, because characteristics are parallel to the x -direction of the grid, interpolation is needed only in one dimension (however computation times given above are for full bicubic interpolation).

A third limitation of the chosen benchmark problem is that the quantity being transported varies smoothly in space. It is often necessary, in high Peclet number advection-diffusion problems, to encounter shocks or fronts in the transported quantity. A known problem with the semi-Lagrangian advection scheme arises under these circumstances. The bicubic interpolant, chosen to reduce numerical diffusion without incurring too great a computational cost, tends to overshoot near discontinuities in the field. We have developed an adaptive interpolation method that retains the advantages of bicubic interpolation while avoiding its associated overshoot problems. To demonstrate this problem, and our solution, we performed a classic test of the semi-Lagrangian advection scheme, solid body rotation of a square bordered with a

discontinuity.

B.5.1 Adaptive Interpolation Method

The adaptive interpolation method makes use of the fact that a bicubic interpolation is executed by doing five cubic interpolations on four points each. Avoiding overshooting on each of these five one dimensional interpolation steps is thus required for avoiding overshooting in the overall bicubic interpolation.

In constructing the one dimensional cubic overshoot detection algorithm we make the assumption that the field is sufficiently well resolved on the grid that there are no oscillations at the grid scale. Thus we expect that over a set of four points, the first derivative of the field can change signs at most once. Given a set of field values y_i with local index $i \in \{0, 1, 2, 3\}$ and a real-valued interpolation target in local grid coordinates $x = i\Delta x$, $1 \leq x \leq 2$, we detect an overshoot using the following steps:

1. For each i , compute the slope, y'_i , of the cubic interpolant at $x = i\Delta x$.
2. There are oscillations in the interpolant over the grid segment if $\text{SIGN}(y'_3)$ equals $\text{SIGN}(y'_0)$ and $\text{SIGN}(y'_2)$ does not equal $\text{SIGN}(y'_3)$.

Because this test is fairly expensive, it is performed only if the set of points y meets two conditions. First, the absolute range of y must be greater than a specified fraction of the range in values over the whole domain. If the set of interpolation points is constant to a within this fraction it may still have features in the noise that cause detectable but small overshoots that do not damage the solution. Second, the cubic interpolant must fall outside of a specified envelope around the linear interpolant. This envelope is defined by a tolerance on the normalized difference between the cubic and the linear interpolants, as shown in Figure B-5.

The results of the solid body rotation test are shown in Figure B-6 for three full rotations around a corner of the box. The overshoots evident in the pure bicubic interpolation run are suppressed by the adaptive interpolation method. Bilinear interpolation is included for comparison (but tends to show large amounts of numerical diffusion)..

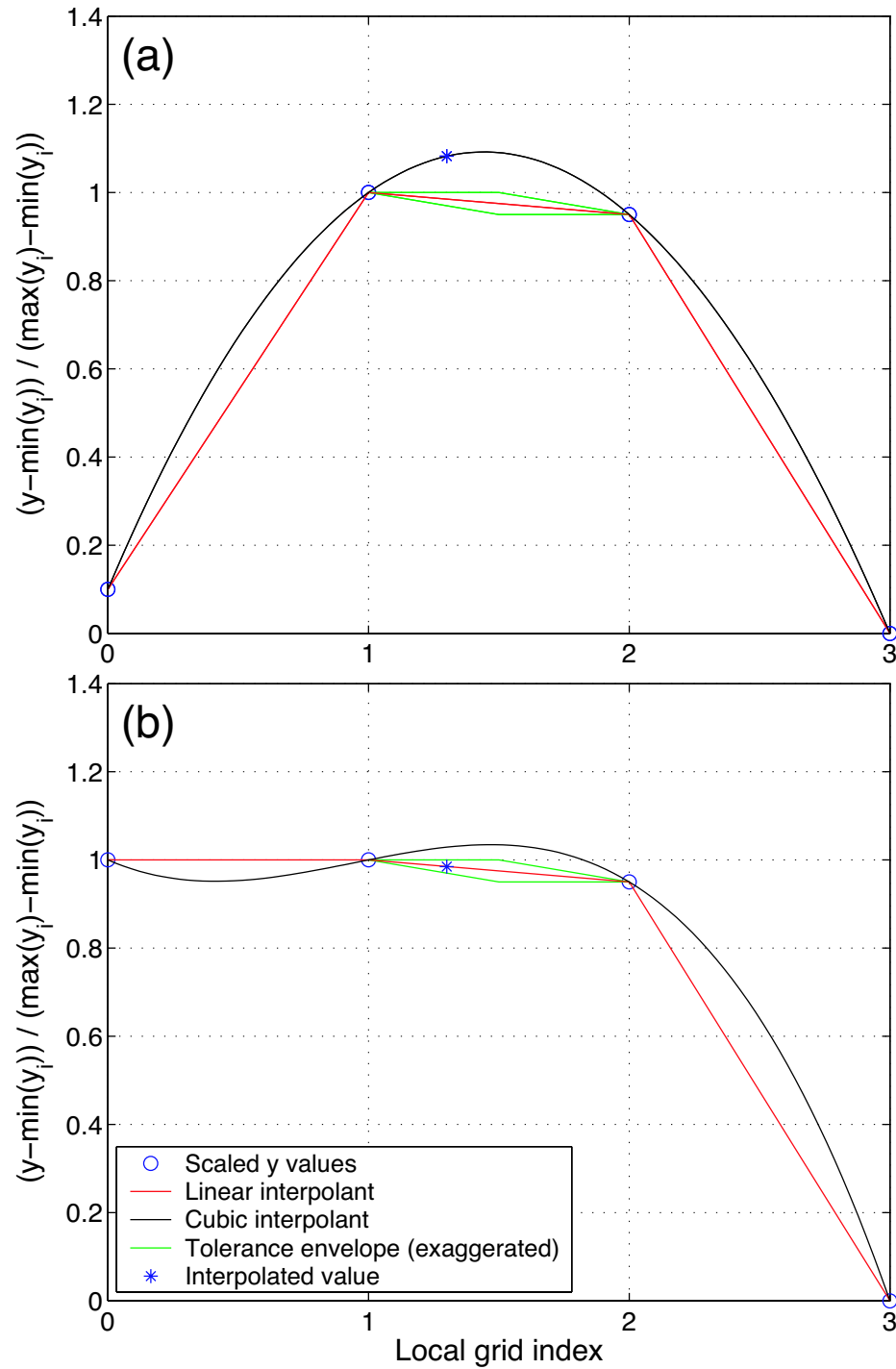


Figure B-5: Two examples of adaptive interpolation with overshoot detection, both with $x = 1.3$. The green lines delineate the tolerance envelope, the thickness of which is exaggerated for clarity. **(a)** In this case, assuming that the field is smooth, the cubic interpolant is a better approximation than the linear one. The overshoot detection algorithm correctly returns false. **(b)** This figure shows the overshoots that characterize the cubic interpolant near an edge. The overshoot detection algorithm returns true and thus the linear interpolant is chosen.

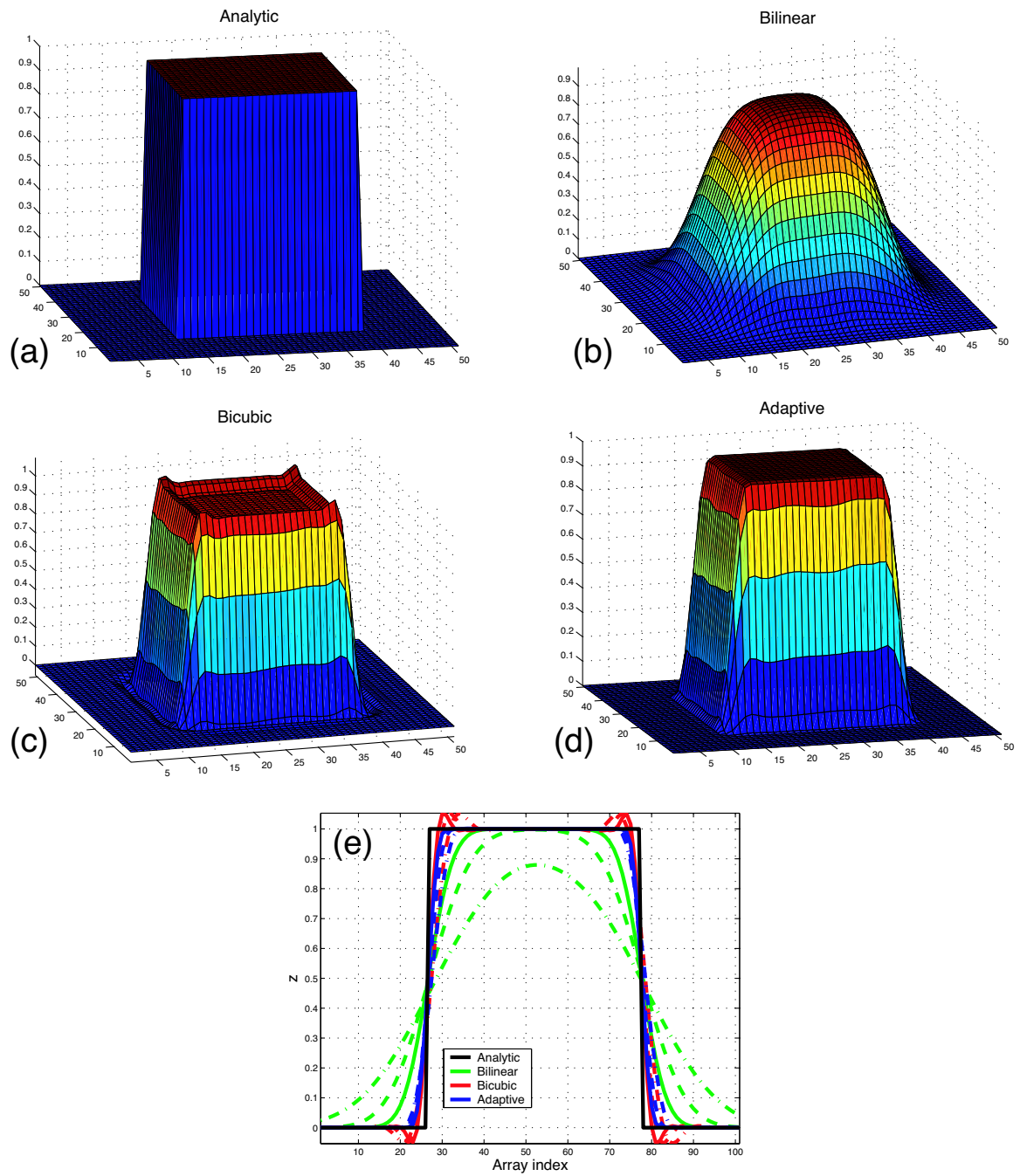


Figure B-6: Results for three interpolation methods for the semi-Lagrangian advection scheme, compared with the analytic solution after three full rotations. (a) Analytic solution. (b) Bilinear interpolation (c) Bicubic interpolation (d) Adaptive interpolation. (e) Profiles across the box after 1 (solid line), 3 (dashed line) and 9 (dash-dotted line) full revolutions.

B.6 Conclusions

A general numerical solver for advection-diffusion problems must be capable of handling pure advection, pure diffusion and any combination of the two. The accuracy and stability of such a solver becomes especially critical in the case of advectively dominated problems with sharp spatial gradients in the transported quantity. The SLCN algorithm draws on the strengths of the Crank-Nicolson scheme for diffusion and the semi-Lagrangian scheme for advection. Since neither of these have time-steps limited by a stability criterion, the SLCN scheme is also unconditionally stable. We have shown that when the advection and diffusion operators act simultaneously on the transported field the SLCN scheme is accurate and efficient over a broad range of time step sizes relative to two other advection-diffusion schemes. Furthermore, by employing our adaptive interpolation method, the SLCN scheme is able to handle discontinuities while reducing the problems of cubic interpolant overshooting, and maintaining its low numerical diffusivity.